UNIVERSITY COLLEGE LONDON

Faculty of Mathematics and Physical Sciences

Department of Physics & Astronomy

LASER INDUCED MOLECULAR AXIS ALIGNMENT: MEASUREMENT AND APPLICATIONS IN ATTOSECOND SCIENCE

Thesis submitted for the Degree of Doctor of Philosophy of the University College London

by

Immacolata Procino

I, Immacolata Procino, confirm that the work presented in this thesis is my own. Where information has been derived from other sources, I confirm that this has been indicated in the thesis.

Immacolata Procino

Abstract

This thesis reports the measurement and applications of molecular axis alignment induced by strong non-resonant linearly polarised laser fields. The spatial alignment of gas phase molecules overcomes the loss of information that results from averaging angle-dependent quantities over all the possible orientations of an isotropic sample. Therefore, laser-induced molecular alignment techniques are an essential component in new experiments aimed at measuring the structure of molecules with attosecond time resolution.

In the first part of this thesis an experiment to measure molecular axis alignment is described. This experiment is based on the velocity map imaging technique in conjunction with time-resolved femtosecond laser Coulomb explosion of the molecular sample by an intense circularly polarised laser beam. A circularly polarised beam is needed to ensure a uniform detection efficiency for each possible orientation of the molecular axis in the polarisation plane. However, such a polarisation produces ion distributions that are not cylindrically symmetric, preventing the use of the standard Abel inversion technique to retrieve the three-dimensional ion distributions from the detected two-dimensional images. A new inversion algorithm is presented that allows the retrieval of molecular axis distributions from angular distributions of ions without cylindrical symmetry.

The second part of the thesis focuses on the application of laser-induced molecular alignment to retrieve molecular structure and dynamics from high-order harmonic generation (HHG) experiments. HHG with a mid-infrared laser source (1300 nm) from aligned molecular samples of CO_2, N_2, C_2H_2, and N_2O are presented. The use of a laser source with a wavelength longer than that used in previous experiments (800 nm) has increased the amount of information obtainable from such experiments. These experiments have provided insight into the hole dynamics of CO_2 following ionisation, and reveal for the

first time structural features in the HHG spectra of molecules with low ionisation potentials such as C_2H_2.

Acknowledgements

I would like to express my gratitude to all the people who made possible and unforgettable this experience. First of all to Dr. Jonathan Underwood for giving me the opportunity to pursue a PhD and for his supervision. I also thank my secondary supervisor Prof. Peter Barker for his availability, and for reading my thesis.

My sincere thanks go also to Chiara, Ana, Edward, and Maria with who I had fun during lunch, orange and ice cream breaks when our brains were "switched off".

During my PhD I have had the pleasure of working also at the Laser Consortium at Imperial College London. Here I carried out some experiments under the supervision of Prof. Jonathan Marangos. I would like to thank him for his infectious enthusiasm and passion for research, and most of all for giving me the opportunity to join his great group. My gratitude goes to Sarah who first introduced me to the laboratory. She has been a great guide, always capable at boosting up my confidence with encouraging and appreciating words about the work I was carrying out. I also would like to thank Marco for bringing a Neapolitan touch to the laboratory during the long afternoons spent acquiring data, and for the great time we had. A huge thanks goes to Ricardo who has been a solid reference point and a fantastic guide during the whole PhD process. He has been very generous with his time and patience, always available for fruitful discussions and ready to give me great advices, even once he left Imperial College. I also thank him for being so kind to give me his room and sleep in R 70 during the experiment at the Rutherford Appleton Laboratory (RAL). There I spent a lovely time working also with Leonardo and Thomas on the high-order harmonic generation experiments. I thank them for that and also for their help with the Red Dragon laser at Imperial College. My gratitude goes also to Amelle for always bringing enthusiasm and positivity to the lab, and for her availability

in helping with experimental issues. I would like to thank all the other members of the Laser Consortium I have had the pleasure of working with or simply with whom I enjoyed scientific and non-scientific discussions during lunch and coffee breaks, especially Omair, Delphine, Natty, and Richard.

A sincere thanks goes to Prof. Carlo Altucci and Prof. Raffaele Velotta who first introduced me to the realm of experimental physics being them my supervisors during my undergraduate studies. It was very great working with them again during the RAL experiments.

I also acknowledge Jochen Maurer and Prof. Henrik Stapelfeldt for letting me test the inversion algorithm with high quality VMI images they acquired.

Outside the work, I would like to thank all my friends, especially Elvira, Clelia and Pavlina for being present whenever I needed them.

No thanks will be ever enough for my Mum, Dad and my brother Vincenzo, who supported and encouraged me over these years. I particularly thank my Mum for never complaining about my choice to leave my sunny country.

Finally, I would love to thank my boyfriend Michele for being such a special person. I really could not have done all of this without you.

List of Publications

1. R. Torres, T. Siegel, L. Brugnera, I. Procino, J. G. Underwood, C. Altucci, R. Velotta, E. Springate, C. Froud, I. C. E. Turcu, S. Patchkovskii, M. Yu. Ivanov, O. Smirnova and J. P. Marangos, *"Revealing molecular structure and dynamics through high-order harmonic generation driven by mid-IR fields"*, Phys. Rev. A **81**, 051802(R) (2010).

2. R. Torres, T. Siegel, L. Brugnera, I. Procino, J. G. Underwood, C. Altucci, R. Velotta, E. Springate, C. Froud, I. C. E. Turcu, M. Yu. Ivanov, O. Smirnova and J. P. Marangos, *"Extension of high harmonic spectroscopy in molecules by a 1300 nm laser field"*, Opt. Expr. **18**, 3174 (2010).

3. T. Siegel, R. Torres, D. J. Hoffmann, L. Brugnera, I. Procino, A. Zaïr, J. G. Underwood, E. Springate, I. C. E. Turcu, L. E. Chipperfield and J. P. Marangos, *"High harmonic emission from a superposition of multiple unrelated frequency fields"*, Opt. Expr. **18**, 6853 (2010).

4. N. Kajumba, R. Torres, J. G. Underwood, J. S. Robinson, S. Baker, J. W. G. Tisch, R. de Nalda, W. A. Bryan, R. Velotta, C. Altucci, I. C. E. Turcu, I. Procino, and J. P. Marangos, *"Measurement of electronic structure from high harmonic generation in non-adiabatically aligned polyatomic molecules"*, New J. Phys. **10**, 025008 (2008).

Contents

List of Figures

List of Tables

Chapter 1

Introduction

The spatial orientation of a molecule is of fundamental importance for its interaction with other molecules, atoms or electromagnetic fields. Measurements on gas phase molecules, performed on an isotropic sample, suffer in fact an averaging over all molecular orientations that can result in a loss of information. In order to avoid this averaging it is necessary to define the molecular orientation at the point of making a measurement, that is one or more molecular axes need to be confined in the laboratory frame where measurements are made. This confinement which brings the molecular frame, where the molecular processes occur, into the laboratory frame is called "molecular axis alignment". In particular, if only one axis is confined the molecule is said to be one-dimensionally (1D) aligned, if three-axes are confined it is three-dimensionally (3D) aligned. Due to its crucial role in chemistry and physics, this process has been widely studied both theoretically and experimentally in the last few decades, and different techniques to align molecules have been developed.

The first approaches to molecular axis alignment relied on the use of static electric fields. In 1979 Brooks *et al.* [1] gave experimental evidence of the dependence of chemical reactions on the orientation of the reactants. They used six alternately charged parallel rods in a hexagonal configuration to generate an electrostatic hexapole field. In such a field molecules experienced a radial force determined by the first-order Stark effect, which allowed focusing molecules in the same rotational quantum state $|J\,M\,K\rangle$ onto a small spot on the hexapole axis. Molecules so selected were given a preferential orientation in the laboratory frame by applying a homogeneous electric field. This technique, has been used

in many other experiments [2–7]. However, an important drawback is that this technique is not general and can be used only to orient polar symmetric-top molecules [8].

A more general technique, also based on the use of a static electric field, was first proposed by Loesch *et al.* in 1990 [9], and then used also in other experiments [10, 11]. This technique, called "Brute Force orientation", relies on the fact that when a polar molecule is placed in an electric field, the field will induce a torque on the molecule that forces the permanent dipole moment of the molecule to orient along the direction of the field. The electric field can be generated in a very practical way, by applying voltages on two parallel highly charged electrode plates mounted perpendicularly to the plane of the molecular beam [9]. This technique in principle is applicable to any polar molecule. However, due to an upper limit to the strength of a static electric field that can be applied to a molecule, this method works well only for polar molecules that have a large dipole moment, and that have been rotationally cooled through supersonic expansion into vacuum [12]. Thus, the main drawback of both the techniques described above is that none of them is general. However, they have the advantage of orienting the molecules, i.e arranging the molecules in a head-versus-tail order, beside aligning them. A schematic showing the difference between alignment and orientation of a sample of diatomic molecules is shown in Fig. 1.1.

A strong electric field, such as the one created by an intense laser beam ($I \approx 10^{12} - 10^{13}$ W cm^{-2}) is able to induce a dipole moment on molecules, thus overcoming the need of a permanent dipole moment to align them. Historically, the first experimental evidence of molecular axis alignment induced by a laser field interacting with a sample of CS_2 molecules was obtained by Heritage *et al.* in 1975 [13]. In the same period, a theoretical study on the behaviour of a symmetric-top molecule in an intense laser field was presented by Zon *et al.* [14]. The first rigorous theoretical treatment of molecular axis alignment induced by a strong non-resonant linearly polarised laser pulse was presented in the mid 90's by Friedrich and Hershbach [15, 16], and by Seideman [17]. They showed that a strong electric field supplied by a linearly polarised laser beam can polarise a molecule with an anisotropic polarisability tensor, inducing a dipole moment which causes the molecule to experience a torque of its most polarisable axis towards the polarisation axis of the laser beam. Friedrich and Hershbach treated the molecular alignment only for a laser pulse much longer than the rotational period of the molecule. In this case, the molecules are aligned in the presence of the laser field and return to the original isotropic field-

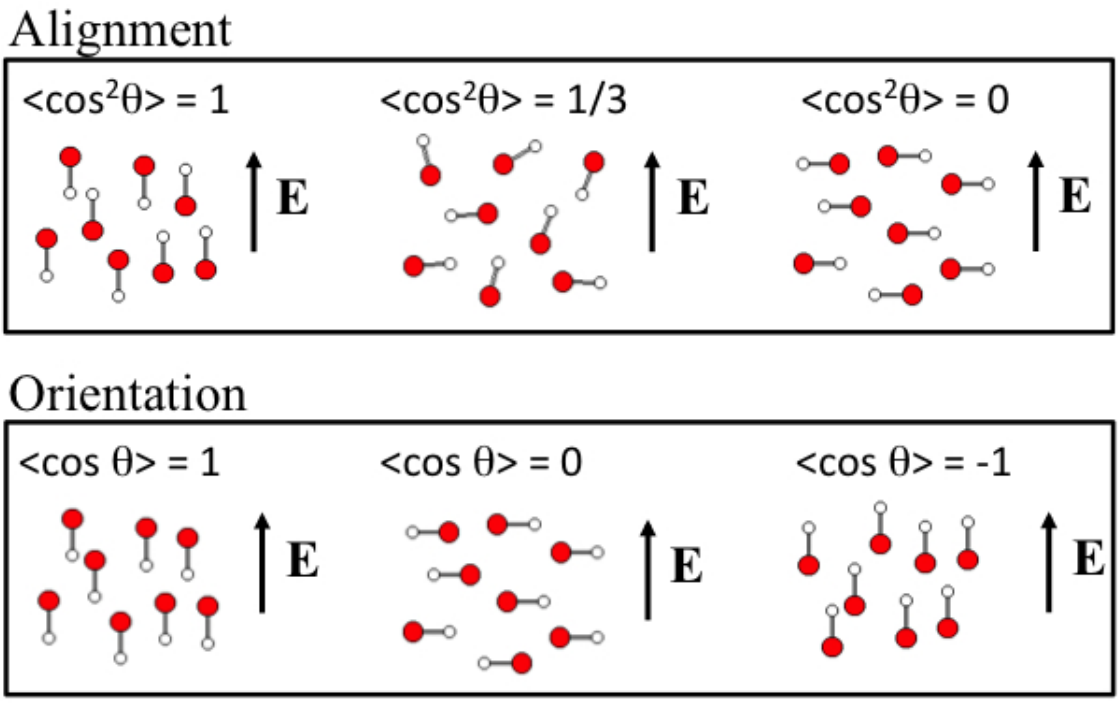

Figure 1.1: Schematic of a sample of diatomic molecules placed in an electric field E. In the top panel the molecules are: aligned along the field (left), isotropic (middle), anti-aligned, i.e. their molecular axes are perpendicular to the electric field (right). In the bottom panel the molecules are: oriented along the field (left), isotropic (middle), oriented in the opposite direction with respect to the electric field (right). The values of $\langle \cos^2 \theta \rangle$ and $\langle \cos \theta \rangle$ quantify the degree of alignment and orientation, respectively. The angle θ is the angle between the electric field and the molecular axis.

free rotor states once the laser pulse is over. Since in this regime the molecules follow adiabatically the evolution of the laser pulse, the process is called "adiabatic alignment". The first experimental demonstration of adiabatic alignment was reported by Felker *et al.* in 1996 [18]. A different process may be found when a laser pulse shorter than the classical rotational period of the molecule is used. In this regime, the molecules cannot adiabatically adapt to the laser pulse which leaves the system in a coherent superposition of rotational states, resulting in a time-dependent field-free alignment. This process is called either "non-adiabatic alignment" or "impulsive alignment". A theoretical treatment of this technique has been presented by Seideman [17] in 1995, while the first experimental demonstration of impulsive alignment has been given by Rosca-Pruna *et al.* in 2001 [19]. The great advantage of impulsive alignment is the absence of the alignment field when the molecules are aligned. The presence of the field can critically distort the molecules under investigation, while the molecules are aligned.

The interest in laser induced molecular axis alignment field has grown in the last decade spurred by the availability of ultrashort (few femtosecond) high intensity lasers, resulting in rapid theoretical [20–29] and experimental [30–40] developments. Particular attention has also been dedicated to the realisation of techniques that allow to obtain simultaneously alignment and orientation of a molecular sample [41–48].

Evidence of molecular axis alignment has been obtained in laser induced electron diffraction [49], high harmonic generation [50–61], and in other kinds of experiments [18, 62–69]. In order to experimentally detect and measure the degree of laser induced molecular axis alignment, different techniques have been used over the years. One of the first methods was based on the measurement of the birefringence of the molecular gas, which increases with the degree of alignment [13, 70]. Another technique commonly used to detect molecular axis alignment is laser induced Coulomb Explosion Imaging (CEI) [19, 33–35, 37, 38, 46, 48, 71–75]. This technique is based on the fact that the fragments generated from a Coulomb explosion of a molecule include information about the position of the nuclei before the explosion, and thus information about the molecular axis distribution. Coulomb explosion of aligned molecules is usually induced by a short intense probe laser pulse which, stripping off the molecule's electrons, causes strong Coulomb repulsion between the nuclei. In many experiments the fragments generated from the Coulomb explosion are accelerated in a velocity map imaging system (VMI) consisting of an electrostatic lens and a 2D detector [76]. The VMI images formed on the detector are projections of the 3D Coulomb explosion cloud of charged particles on a two dimensional (2D) detection plane. In order to extract all the information available, like as the energy and angular distributions of the charged particles, an inversion of the VMI image is necessary. Inversion methods make use of the fact that if the original 3D distribution has an axis of cylindrical symmetry, its 2D projection parallel to this axis contains enough information to reconstruct the full 3D distribution [77]. Therefore, if the cloud of ions generated in a CEI - VMI experiment has an axis of cylindrical symmetry lying in a plane parallel to the detection plane, the VMI image can be inverted by using one of the many inversion algorithms available [78–86]. However, the angular distribution of ions retrieved with those algorithms corresponds to the convolution of the molecular axis distribution and the molecular orientation dependence of the Coulomb explosion probe. This is because the probe laser pulse does not ionise all the molecules with the same probability due to an orientational dependence of ionisation [87]. Therefore, to date it is not possible to

extract the true molecular axis distribution from CEI-VMI images.

In this thesis we present an inversion algorithm that overcomes this problem. The algorithm allows the inclusion of a non-uniform detection function, leading to the retrieval of the molecular axis distribution deconvoluted from the molecular orientation dependence of the Coulomb explosion probe. Therefore, this algorithm is capable of retrieving the molecular axis distribution from a 2D VMI image even when the image corresponds to a Coulomb exploded cloud of ions without a cylindrical symmetry.

The growing interest in molecular alignment is related to its influence on strong field phenomena, which have opened the possibility of performing ultrafast measurements of molecular dynamics with unprecedented time resolution [49, 53–56, 88–93]. Among these strong field processes, we are particularly interested in high harmonic generation (HHG) spectroscopy. In the last years it has been shown that HHG is highly sensitive to molecular structure [53–56, 94], and allows measuring dynamics [91–93, 95, 96], including subfemtosecond rearrangements of nuclei [91, 92, 95] and electrons [93, 96]. To date most of the experiments have been performed using a 800 nm driving laser pulse. We discuss the advantages of using a longer wavelength and present the results of an experiment carried out by using a mid-infrared laser source (1300 nm) to generate high harmonics from aligned molecular samples of CO_2, N_2, C_2H_2, and N_2O.

In the next sections the theoretical bases of the experiments presented in the thesis will be introduced. Specifically, the main concepts and theory behind laser induced alignment will be presented in section 1.1. An overview of the different ionisation processes for atoms and molecules will be given in section 1.2. Section 1.3 will present a classical treatment of the free electron accelerated by the laser field. The electron recollision with the parent ion will be discussed in section 1.4, where more attention is dedicated to the high-order harmonic generation process. The Coulomb explosion process will be introduced in section 1.5. Finally, an outline of the thesis will be given in section 1.6.

1.1 Molecular axis alignment

A strong linearly polarised laser field can be used to align non-polar molecules. The electric field generated by such a laser field can be expressed as:

$$\mathbf{E}(t) = \hat{e} E_0 f(t) \cos(\omega t) \tag{1.1}$$

where $\hat{e}$ is a unit vector along the polarisation direction of the laser pulse, E_0 is the field amplitude, $f(t)$ is the pulse envelope, and ω is the laser angular frequency. A molecule placed in such an electric field will experience a potential $V(\theta)$ depending on the angle θ between the field and the molecular axis, given by:

$$V(\theta) = V_\mu(\theta) + V_\alpha(\theta) \tag{1.2}$$

The potentials $V_\mu(\theta)$ and $V_\alpha(\theta)$ are due to the interaction of the electric field with the permanent dipole moment μ (for non-polar molecule $\mu = 0$), and the induced dipole moment $\mathbf{p}$ of the molecule, respectively. The induced dipole moment is related to the polarisability tensor $\bar{\bar{\alpha}}$ through the expression $\mathbf{p} = \epsilon_0 \bar{\bar{\alpha}} \cdot \mathbf{E}$, where ϵ_0 is the permittivity of free space. In the simplest case of a linear molecule, the polarisability tensor has a component along the direction of the molecular axis, $\alpha_\parallel$, and a component perpendicular to the molecular axis, $\alpha_\perp$. In this case, the potentials experienced by the molecule have the following expressions [15]:

$$V_\mu(\theta) = -|\mu||\mathbf{E}|\cos(\theta) \tag{1.3}$$

$$V_\alpha(\theta) = -\frac{1}{2}|\mathbf{E}(t)|^2 \left(\alpha_\parallel \cos^2(\theta) + \alpha_\perp \sin^2\theta\right) \tag{1.4}$$

Since the laser oscillation (2.66 fs for a 800 nm laser pulse) is much faster than the rotational motion of the molecules (few ps), the molecules cannot follow the oscillations of the electric field and are only sensitive to the envelope. The potentials averaged over the field cycle are $\bar{V}_\mu(\theta) = 0$ which excludes the possibility of orienting the molecules, and:

$$\bar{V}_\alpha(\theta) = -\frac{f(t)^2 E_0^2}{4}\left(\Delta\alpha \cos^2(\theta) + \alpha_\perp\right) \tag{1.5}$$

where $\Delta\alpha = \alpha_\parallel - \alpha_\perp$ is the difference between the components of the polarisability parallel and perpendicular to the molecular axis, and it is called *polarisability anisotropy* of the molecule. In order to study the dynamics of the interaction between the laser pulse and the molecule, it is necessary to solve the time-dependent Schrödinger equation:

$$i\hbar\frac{\partial\Psi}{\partial t} = (H_0 + \bar{V}_\alpha(\theta))\Psi \tag{1.6}$$

where $H_0 = B\mathbf{J}^2$ is the field free rotational Hamiltonian of the molecule, B the rotational constant and $\mathbf{J}^2$ the squared angular momentum operator. Its eigenstates $|JM\rangle$ are represented in the angular space by the spherical harmonics $Y_{JM}(\theta,\ \phi)$ and its eigenvalues are given by $E_J = BJ(J+1)$ [23]. The solution of Eq. 1.6 can be written as a superposition of the field free rotational states of the molecule, generated through a series of Raman transitions whose selection rules are $\Delta J = 0, \pm 2$ and $\Delta M = 0$ for a linearly polarised field [23]:

$$|\Psi_{J_i M_i}\rangle = \sum_{J \geq |M_i|} F_{J_i J}(t)\, |JM_i\rangle \tag{1.7}$$

where J_i and M_i are the quantum numbers of the initial rotational state. The expansion coefficients $F_{J_i J}(t)$ are complex in general, and both their phase and moduli can vary during the interaction with the laser, depending on the relation between the laser pulse duration and the molecular rotational constant of the molecule.

When the duration of the laser pulse is significantly longer than the rotational period of the molecule the alignment takes place adiabatically [23]. The essential requirement for alignment under this condition is that the potential well induced by the laser field is large as compared to the rotational energy. Thus, when the laser pulse interacts with the molecule, the initial wavefunction (field free rotor state) $|JM\rangle$ transforms into an eigenstate of the complete Hamiltonian $|\tilde{J}M\rangle$, i.e a pendular state that librates about the polarisation axis [20, 97, 98]. When the laser turns off, the molecule returns to the field free rotor eigenstate from which the pendular state originated [99].

In contrast, when the laser pulse is much shorter than the period for molecular rotation, the molecule is not able to adiabatically adjust to the laser pulse, rather the interaction can be viewed as a "kick" imparted to the molecule that transfers a large amount of angular momentum setting the molecule in a rotating motion [12]. In this limit the moduli of the component of the wave packet remain constant whilst the phases keep evolving as they would in a field-free rotor. Upon the time evolution of the wave packet the different components of the wave packet dephase and rephase leading to recurrences of the alignment at times multiple of the fundamental rotational period. These recurrences of molecular field-free axis alignment are called *rotational revivals*. For example, the first experimental rotational revival structure observed by Rosca-Pruna *et al.* [19] in the alignment of I_2 molecules is shown in Fig. 1.2.

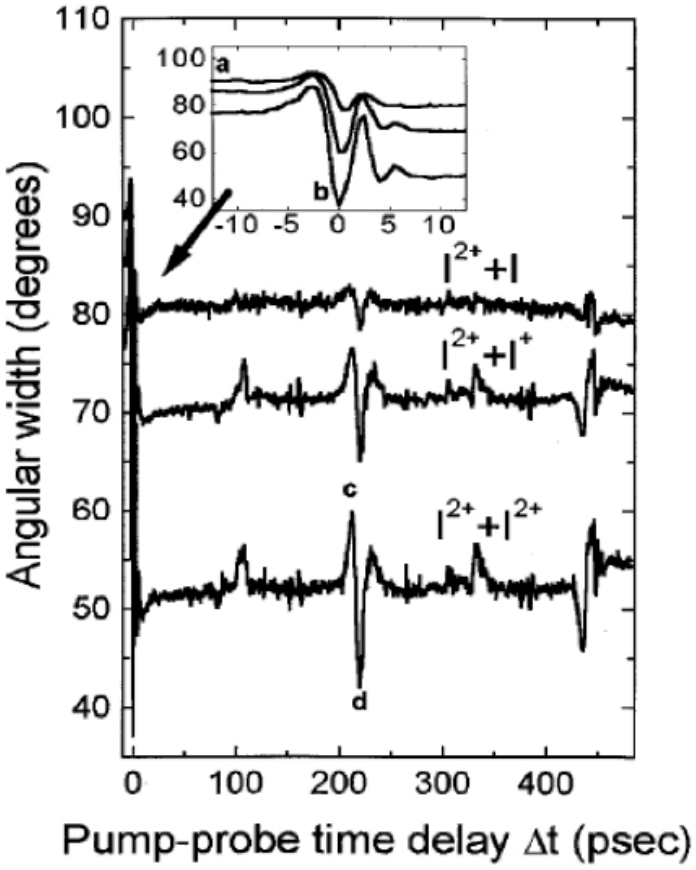

Figure 1.2: Pump-probe time delay scan, showing the angular width of the I^{2+} + I, the I^{2+} + I^{+}, and the I^{2+} + I^{+} channels, recorded using a 3.8 mJ 2.8 ps pump pulse and a 1.2 mJ 10 fs probe pulse. The measurements show alignment of the molecule during the pump pulse (see inset), residual alignment at the end of the pump pulse, and the occurrence of rotational revivals. Taken from [19].

The degree of alignment of a molecular sample is characterised by the expectation value of $\cos^2\theta$, and ranges from 0, corresponding to the case where all the molecules are delocalised in a plane perpendicular to the polarisation axis (maximal anti-alignment), to 1 for a perfectly aligned sample of molecules. The value of $\langle\cos^2\theta\rangle$ corresponding to an isotropic sample is 1/3 [23]. A schematic of a sample of aligned, anti-aligned and isotropic diatomic molecules is shown in the top panel of Fig. 1.1. If an ensemble of molecules in thermal equilibrium having a rotational temperature T_r is considered, then the expectation value of $\cos^2\theta$ has to be averaged over the Boltzmann distribution of the initial rotational states J_i. Here the degree of alignment is given by [15]:

$$\left\langle\left\langle\cos^2\theta\right\rangle\right\rangle = Z_r^{-1}\sum_{J_i}\exp\left[-\frac{B}{kT_r}J_i\left(J_i+1\right)\right]\sum_{M_i=-J_i}^{J_i}\left\langle\Psi_{J_iM_i}|\cos^2\theta|\Psi_{J_iM_i}\right\rangle \tag{1.8}$$

where Z_r is the rotational partition function and k is the Boltzmann's constant. Therefore, the degree of alignment depends on the temperature of the ensemble of the molecules, decreasing when the temperature increases.

The degree of alignment depends also upon the intensity of the interacting laser field, increasing with the laser intensity [20]. However, the laser intensity used to align molecules has to be low enough not to ionise or dissociate the molecules. Typical intensities used to induce impulsive molecular axis alignment vary in the range of $10^{12} - 10^{13}$ W cm^{-2}.

1.2 Ionisation processes

Atoms or molecules which experience an intense laser field (I$> 10^{13}$ W cm^{-2}), will suffer some ionisation [100–102]. Depending on the intensity and frequency of the laser pulse and on the ionisation potential of the molecule, different ionisation processes can take place such as multiphoton ionisation (MPI), above-threshold ionisation (ATI), tunnel ionisation (TI), and over the barrier ionisation (OTBI) [103–105].

It is crucial to have a good understanding of the ionisation mechanisms, since tunnel ionisation is the first step in other important strong field phenomena like HHG, non-sequential double ionisation, laser-induced electron diffraction, etc. The mechanisms of ionisation by strong laser fields are described in this section, first in the case of atoms, and then the same approach will be extended to the case of molecules, and the similarities and differences between the two cases will be discussed.

1.2.1 Atomic ionisation

If the electric field generated by the laser is not able to distort the Coulomb potential experienced by the electrons, it can be considered as a perturbation to the system. In this case the only way for an electron to escape the Coulomb barrier and reach the continuum is to absorb a number N of photons such that $N\hbar\omega > I_p$. The absorption of the photons occurs as a series of transitions through virtual states until the electron reaches the continuum [106–108]. Each virtual state can be thought as a real state whose lifetime is determined by the energy-time uncertainty relation $\tau = \hbar/E_v$ where E_v is the energy of the virtual state. The N-photon ionisation rate Γ_N, depends on the laser intensity I to

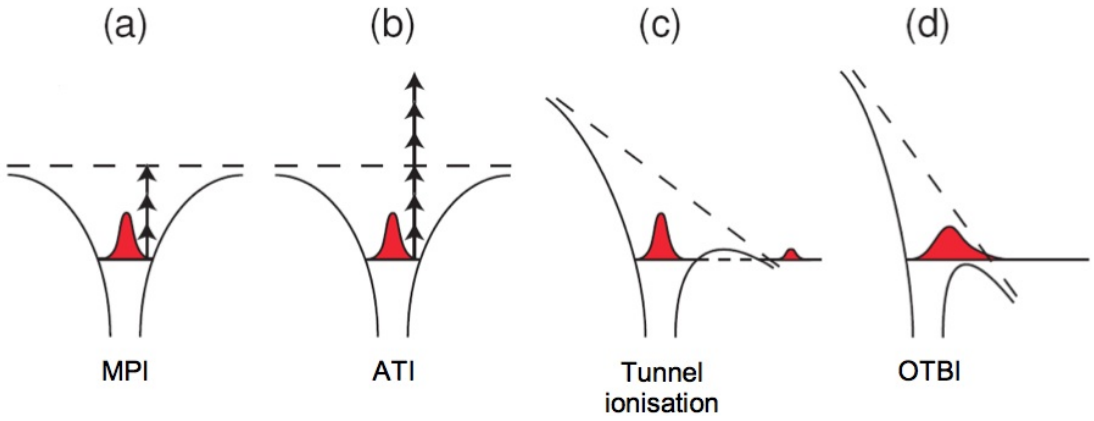

Figure 1.3: Laser induced ionisation processes: a) mutiphoton ionisation (MPI); b) above-threshold ionisation (ATI); c) tunnel ionisation (TI); d) over the barrier ionisation (OTBI). The solid lines represent the potential in presence of the laser field. In (a) and (b) the Coulomb potential experienced by the electrons is not distort by the laser pulse.

the power N and is given by [109, 110]:

$$\Gamma_N = \sigma_N \, I^N \tag{1.9}$$

where N is the minimum number of photons needed for ionisation, σ_N is the generalised cross section that can be calculated with perturbation theory [111]. This process is known as *multiphoton ionisation*, and is schematised in Fig. 1.3 (a).

At higher intensities ($\approx 10^{14}$ W cm^{-2}) more photons than necessary for ionisation can be absorbed by an atom, leading to photoelectrons with kinetic energies much higher than the photon energy, and separated each other by one photon energy. In this case, the intensity dependence of the ionisation rate is given by [112]:

$$\Gamma_{(N+S)} = \sigma_{(N+S)} \, I^{(N+S)} \tag{1.10}$$

where S is the number of excess photons absorbed. This process is called *above-threshold ionisation*, and is schematised in Fig. 1.3 (b).

As the intensity of the laser field increases ($> 10^{14}$ W cm^{-2}), the electric field of the laser cannot be considered as a perturbation to the atom anymore. In fact, the potential due to the electric field of the laser, V_L, is able to distort the Coulomb potential experienced by the valence electron of the atom [87, 113]. The distortion of the potential barrier leads to a raising of the potential on one side of the well and a lowering of the barrier on the

other side (see Fig. 1.3 (c)). In correspondence of the peak of V_L, the bound electron will see a barrier of finite width through which there is a finite probability of quantum mechanical tunnelling. The electron can tunnel the barrier if the tunnelling time is less than half of the optical period. In this way the ionisation happens before the electric field of the laser reverses and the barrier raises again [114]. The tunnelling ionisation rate Γ, can be calculated in quasi-static approximation with the Ammosov, Delone and Krainov theory (ADK) [115], and is given in atomic units by:

$$\Gamma \approx 4I_p \left[\frac{2\,(2I_p)^{3/2}}{E}\right]^{2n^*-|m|-1} \exp\left(-\frac{2\,(2I_p)^{3/2}}{3E}\right) \tag{1.11}$$

where I_p is the ionisation potential of the atom, n^*, l, and m are the effective principal quantum number and the angular and magnetic quantum numbers of the ionising electron, and E is the electric field experienced by the electron. This ionisation process is known as *tunnel ionisation* and is schematised in Fig. 1.3 (c).

An approximate indicator of whether the MPI or the TI mechanism dominates is the Keldysh parameter γ, which is defined as [116, 117]:

$$\gamma = \sqrt{\frac{I_\mathrm{p}}{2\,U_\mathrm{p}}} \tag{1.12}$$

where I_p is the ionisation potential, and U_p is the ponderomotive energy representing the mean kinetic energy acquired by a free electron in the oscillating laser field. The ponderomotive energy depends on the wavelength λ and on the intensity I of the laser pulse according to the following equation [103]:

$$U_p = \frac{1}{4}\frac{E_0^2 e^2}{m_e \omega^2} \propto \lambda^2\, I \tag{1.13}$$

where E_0 is the amplitude of the electric field supplied by the laser pulse, ω is the angular frequency of the laser, e and m_e are the charge and the mass of the electron. If $\gamma > 1$ then the external electric field is weak compared to the Coulomb potential experienced by the valence electron in the atom or molecule, and the multiphoton dynamics are most significant, whereas if $\gamma < 1$ the TI mechanism dominates.

For very high laser intensities ($> 10^{15}$ W cm^{-2}), the Coulomb potential barrier is lowered so much that the electron is not longer bound, so it is free to reach the continuum.

The intensity needed to remove the potential barrier is given by [118]:

$$I_{OTBI} = 4 \times 10^9 (I_p)^4 Z^{-2} \tag{1.14}$$

where I_{OTBI} is expressed in W cm^{-2}, I_p is the ionisation potential in eV and Z is the charge state of the resulting ion. This process is known as *over the barrier ionisation* and is represented in Fig. 1.3 (d).

1.2.2 Molecular ionisation

As an atom, a molecule placed in an intense laser field can be ionised through different mechanisms: multiphoton, above-threshold, tunnelling, and over-the-barrier ionisation. However, in the case of molecules the ionisation rate depends strongly on the molecular symmetry and on the spatial orientation of the molecules with respect to the laser field [63–65, 119–123]. While the dynamics of MPI, ATI, and OTBI for molecular ionisation are similar to the case of atomic ionisation, tunnel ionisation from molecules presents new phenomena due to the multiple-well nature of the ionic potential. In particular, the tunnelling ionisation rates are very sensitive to the separation of nuclei in a molecular ion [100, 104, 124–132]. The dependence of the ionisation rate on the internuclear distance can be understood by considering the Coulomb potential experienced by a valence electron of a diatomic molecule, shown in Fig. 1.4. In this figure, the Coulomb potential experienced by a valence electron of a diatomic molecule in the absence (a) and the presence (b) of a laser field linearly polarised along the direction parallel to the molecular axis, are shown for different internuclear separations [124]. It can be seen that in a diatomic molecule the ability of an electron to move between the two ions (wells) in response to an external laser field depends on the internal potential barrier between the ions [124]. For a short internuclear distance R (dashed curves), the internal barrier is below the ground state energy. Therefore, to escape the molecule, the electron needs to tunnel only through one external barrier, like in an atom. A similar situation occurs for a very large internuclear distance (dot-dashed curves), where an electron cannot move easily from one ion to the other because of the large internal Coulomb barrier and therefore, in order to escape the molecule, the electron has to tunnel through potential barriers that are atomic like. Between these two cases there is a critical internuclear distance R_c (solid curves), where the electron is partially trapped by the internal barrier in the absence of field (see Fig. 1.4 (a)),

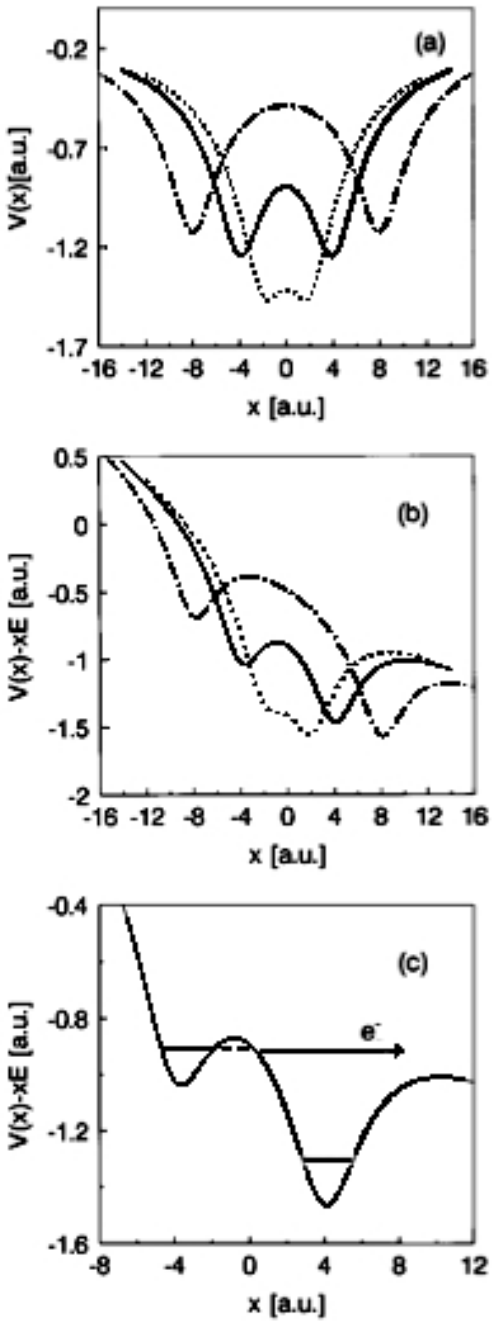

Figure 1.4: Schematic of the electronic potential in a generic diatomic molecule at several internuclear separations R: dotted line $R < R_c$, solid line $R = R_c$, dot-dashed line $R > R_c$, being R_c the critical internuclear distance. a) without electric field; b) with electric field; c) tunnelling ionisation through internal barrier. Taken from [124]

then in the presence of a field, as the field becomes large, the internal barrier is lowered (see Fig. 1.4 (b)). Therefore, as illustrated in Fig. 1.4 (c), the electron needs only tunnel through the small internal barrier in order to escape the molecule. This mechanism is a new ionisation process and the corresponding ionisation rate is much higher compared with

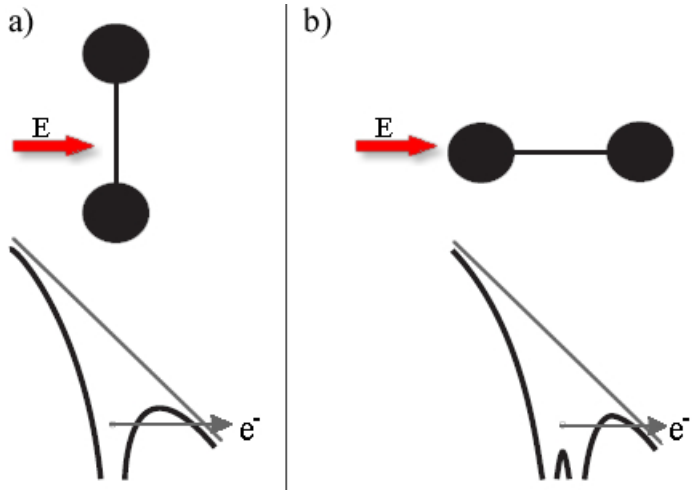

Figure 1.5: Schematic of the potential curve for an electron in a diatomic molecule at an internuclear distance smaller than the critical distance in an intense laser field polarised (a) perpendicular or (b) parallel to the internuclear axis.

larger or smaller internuclear separations, that is why this process is known as *enhanced ionisation* [104, 126].

It must be highlighted that this process occurs only if the laser field is linearly polarised along the internuclear axis. For example in the case of a polarisation direction perpendicular to the internuclear axis, the valence electron experiences only a single-well potential in the field direction, as experimentally obtained by Constant *et al.* [129]. A schematic of the potential experienced by a valence electron of a molecule, placed in an intense laser field which is polarised perpendicular (a) or parallel (b) to the molecular axis is shown in Fig. 1.5.

1.3 Free electron in the electric field

Once the electron has escaped from the atom/molecule, it appears in the continuum where it is accelerated by the laser field following an oscillatory motion. If the laser pulse is linearly polarised, there is a high probability that the electron returns to the parent ion when the electric field reverses, as shown in Fig. 1.6. Since we are interested in the different processes that take place during the recollision of the electron with the parent-ion, we consider a linearly polarised laser field, whose electric field is given by:

$$\mathbf{E}(t) = E_0 \cos \omega t \, \hat{e} \tag{1.15}$$

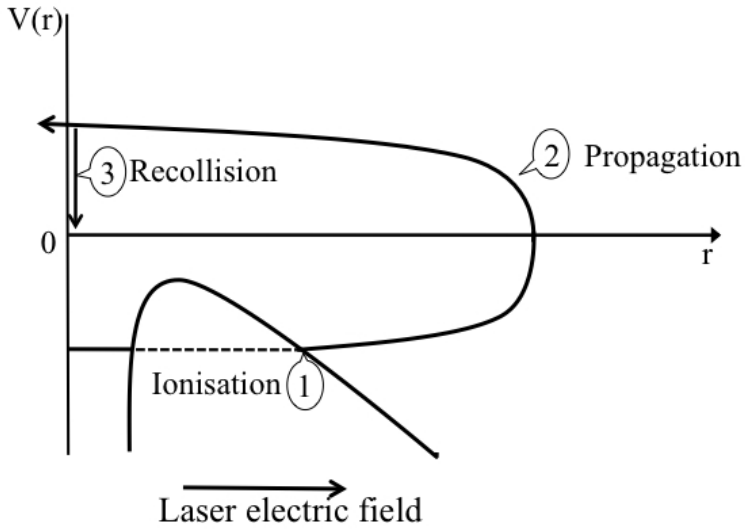

Figure 1.6: Schematic of the three step process: 1. The electron reaches the continuum trough tunnel ionisation; 2. The electron is accelerated back by the laser electric field; 3. The electron recollides with the parent ion.

where E_0 is the amplitude of the electric field, ω is the frequency of the laser field and $\hat{e}$ is a unit vector along the polarisation direction of the laser pulse. In the simplest possible approximation followed by Corkum *et al.*, the electron dynamics is treated classically with the initial condition that it reaches the continuum at time $t = t_0$ with zero velocity [133]. In these conditions, the force $\mathbf{F}$ experienced by the electron in the laser field is given by:

$$\mathbf{F} = -e\left(\mathbf{E} + \mathbf{v} \times \mathbf{B}\right) \simeq -e\mathbf{E} \tag{1.16}$$

where e is the charge of the electron, $\mathbf{v}$ is the electron velocity, and $\mathbf{B}$ is the magnetic field of the laser, which has been neglected since non relativistic pulse intensities are considered. Thus, the equation of the motion of the electron is obtained by integrating Newton's equation:

$$m_e \frac{\partial^2 \mathbf{r}}{\partial t^2} = -e\mathbf{E} \tag{1.17}$$

where m_e is the mass of the electron. The solution of the previous equation, with the initial conditions stated above is:

$$\mathbf{r}(t) = \alpha\left(\cos\omega t + \omega t \sin\omega t_0 - \omega t_0 \sin\omega t_0 - \cos\omega t_0\right)\ \hat{e} \tag{1.18}$$

where t_0 is the time of ionisation and α is the classical oscillation amplitude, given by:

$$\alpha = e\,E_0/m_e\,\omega^2. \tag{1.19}$$

The corresponding electron velocity is given by:

$$\mathbf{v}(t) = (-\alpha\omega\ \sin\omega t + \alpha\omega\ \sin\omega t_0)\ \hat{e} = \mathbf{v}_O(t) + \mathbf{v}_D \tag{1.20}$$

where $\mathbf{v}_O(t)$ is the oscillating term, and $\mathbf{v}_D$ is the drift velocity which depends only on the time of ionisation t_0. Therefore, the velocity of a "direct electron", which is an electron that is detected without recolliding with the parent ion, is given by $\mathbf{v}_D$. The maximum value of the drift velocity is given by $v_{\max} = \alpha\omega$, implying that the maximum kinetic energy $T_{\max}$ acquired by a direct electron is:

$$T_{\max} = \frac{m_e}{2} v_{\max}^2 = \frac{e^2\,E_0^2}{2\,m_e\,\omega^2} = 2\,U_p \tag{1.21}$$

where U_p is the ponderomotive potential defined in Eq. 1.13. The maximum kinetic energy gained during the propagation by an electron returning to the parent ion corresponds to the maximum velocity of the electron at the time of recombination t_1, which is determined by solving the equation $\mathbf{r}(t) = 0$, where $\mathbf{r}(t)$ is given by Eq. 1.18. This energy results to be 3.17 U_p [133].

By treating the electron dynamics classically an important quantum effect is neglected. In reality, the electron is not born with exactly zero momentum in the continuum. Rather, there is a distribution of initial momenta, giving rise to the spreading of the electron wave packet after ionisation [134]. This suppresses the efficiency of recollision [135], but guarantees that the returning wave packet will sweep over the entire molecule rather than covering only part of the molecule, allowing to gain information about the molecular structure [94, 136, 137].

1.4 Electron recollision

Only half of the electrons that are ionised during half optical cycle of the linearly polarised laser pulse pass the position of the ion once when the electric field of the laser reverses [133]. These are the electrons emitted immediately after the peak of the laser field. These

electrons can inelastically or elastically scatter from the parent ion, or they can recombine with the parent ion yielding a high-order harmonic photon. All of these processes generated in molecules have been widely explored in the last decades since the product of the electron-ion recollision incorporates information about the molecular structure [52–59, 138–143].

When inelastic scattering happens, the electron returns to the parent ion with a sufficient energy to excite or further ionise it, causing non-sequential double ionisation and therefore triggering the fragmentation process [144–148].

If the returning electron is elastically rescattered from the parent ion it is deflected by a certain angle, but with unchanged absolute value of the velocity. This electron is re-accelerated by the laser electric field, gaining further kinetic energy. Paulus *et al.* obtained numerically that the maximum kinetic energy gained by a rescattered electron during the propagation in the laser field is approximately 10 U_p, and it is achieved only by the back-rescattered electrons (i.e electrons scattered at 180°) [149–151]. They also showed that rescattered electrons are manifested in ATI photoelectron spectra from atoms. These spectra can be seen as divided in two parts corresponding to low-energy and high-energy electrons, respectively. The low energy electrons are those reaching the detector without returning to the ion-parent, which are thus called direct electrons. The maximum energy that a direct electron can gain in the laser field has been obtained in Eq. 1.21 and is 2 U_p. The high energy part of the spectrum is due to the rescattered electrons and presents a plateau-like structure, i.e., an ionisation probability independent of the photoelectrons energy up to a rather sudden cutoff [152]. In the case of elastic electron rescattering from molecules, the angular distribution of the rescattered electrons present a typical interference structure that has encoded in it molecular structure information [138, 139, 141, 142]. Such a feature in the angular distribution is due to diffraction of the returning electron [90] by the molecule.

If the returning electron recombines with the parent ion it can emit light at a multiple of the laser frequency. The frequency of the emitted light and so the order of the generated harmonic depends on the acquired energy of the electron and on the ionisation potential I_p of the molecule. The typical harmonic spectrum falls off for the first few harmonics then exhibits a plateau over many orders before a sharp cutoff is reached where the intensity drops again, as shown in Fig.1.7. The plateau of harmonics with nearly equal amplitude is due to the fact that all possible recollision energies up to the cutoff energy have roughly the same probability. The cutoff energy is the energy emitted following the recombination

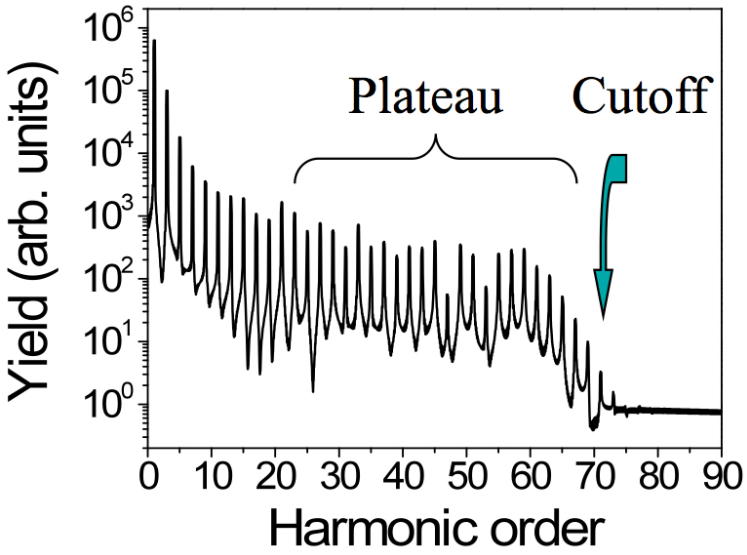

Figure 1.7: Schematic of a typical HHG spectrum simulated by Ricardo Torres.

of the electron that has gained the maximum kinetic energy during his propagation in the laser field (3.17 U_p), and is given by [134]:

$$\epsilon_{\text{cutoff}} = 3.17\,\text{U}_\text{p} + \text{I}_\text{p} \tag{1.22}$$

The cutoff energy is gained by the electron emitted at an optimum ionisation time corresponding to $\omega_0 t_0 = 17°$ after the peak. The further away from that time an electron is born the lesser its return energy. Electrons born after that time return to the core sooner and are therefore called short trajectory electrons. Ones born before return later and are therefore called long trajectory electrons [153]. Each harmonic in the plateau is therefore emitted at two different times which join up for cut-off harmonics where no distinction between trajectories can be made, as shown in Fig. 1.8.

As the electron ionisation and recombination happen twice every laser period T, the HHG process period time is $T/2$. In the frequency domain this corresponds to a periodicity of $2\omega_0$, where ω_0 is the frequency of the laser pulse. Therefore in a centrosymmetric system, only odd harmonics are produced because even harmonics from each half cycle cancel each other out. The applications of HHG in molecular imaging will be discussed in Chapter 5.

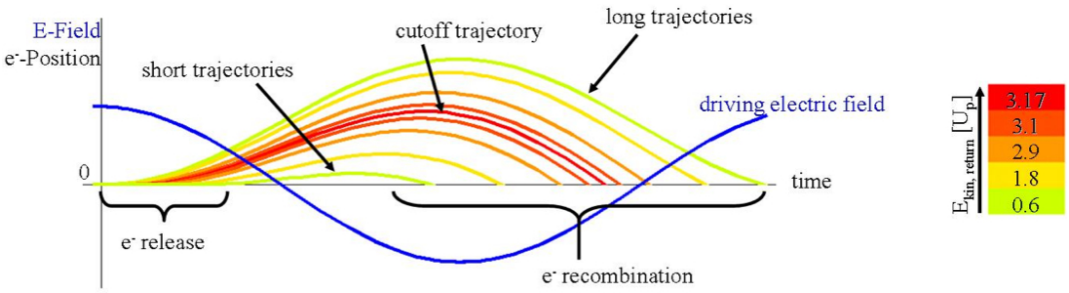

Figure 1.8: Schematic of the trajectories of some of the electrons that recombine with the parent ion. The trajectory in red corresponds to the maximum kinetic energy gained by the electron in the laser field (3.17 U_p). Taken from [224].

1.5 Coulomb Explosion Imaging

When a molecule is exposed to a very intense laser field ($I > 10^{15}$ W cm^{-2}) many of its electrons can be stripped during the brief duration of the laser pulse. The highly charged molecular ion resulting from such an interaction dissociates quickly due to a large Coulomb repulsion between the nuclei [71, 104]. If the ionising pulse is short enough (< 15 fs) to freeze even highly charged molecular ions by their own inertia for the duration of the ionising pulse [154], then by measuring the momenta of the positively charged fragments, the initial position of the nuclei and thus the structure of the parent molecule [74, 104, 154–157], as well as the energy and angular distributions of the sample of molecules can be reconstructed [35, 36, 73, 75, 127, 158–160]. For this reason, this technique, first investigated by Frasinski *et al.* in 1987 [71] and known as "Coulomb explosion imaging" (CEI) is widely used to detect molecular axis alignment [19, 33–35, 37, 38, 46, 48, 71–75].

Before the experiment performed by Frasinski *et al.*, collision-induced Coulomb explosion was already used for imaging static molecular structures. In collision induced CEI, molecular ions are accelerated by an electromagnetic field towards a stationary target, usually a thin gold foil. As the molecules pass through the foil many electrons are stripped from each molecule which thus Coulomb explods [161–163]. Since the transit time of the ions through the foil is less than 1 fs, the nuclear motion can be considered "frozen" during the process. In order to obtain the same situation in optical induced CEI, the use of a laser pulse short on the timescale of molecular motion needs to be used. During a slow ionisation, in fact, the molecule expands as it ionises. As the molecule approaches a critical internuclear distance, the ionisation is enhanced along the direction parallel to the laser field, as discussed in section 1.2.2. As a consequence, the angular distribution of the

Coulomb explosion fragments cannot be ascribed only to the alignment of the molecules induced by a previous laser pulse, but depends also on the enhancement of the ionisation rate along the direction of the laser field [104, 164, 165].

Therefore, in order to have a reliable measurement of molecular axis alignment an ultrashort laser pulse must be used to induce Coulomb explosion of the aligned sample of molecules [38, 39, 46].

1.6 Outline of the thesis

The thesis is organised as follows. Chapter 2 describes the experimental apparatus used for a pump-probe experiment aiming to detect molecular axis alignment by using a combination of CEI and VMI. In Chapter 3 a regularised version of the matrix inversion method developed by T Cho and S-J Na [86] is introduced. This regularised algorithm has been used to extract the probe molecular orientation dependence from images acquired from an isotropic sample of molecules. Chapter 4 presents the inversion algorithm that we have implemented to retrieve the molecular axis distribution deconvoluted from the molecular orientation dependence of the Coulomb explosion probe. Chapter 5 presents and discusses the results of the HHG experiments performed on aligned sample of molecules. Finally, a summary of the thesis is presented in Chapter 6.

Chapter 2

Experimental apparatus

In this chapter the experimental apparatus designed for two different experiments is described in detail. One is a pump-probe experiment that aims to detect molecular axis alignment by looking at the angular distribution of the Coulomb exploded ions from aligned molecules, the other aims at the detection of rescattered electrons from atoms or molecules. Measurements of molecular axis alignment are reported in chapters 3 and 4, whilst preliminary results from the rescattered electron experiment are shown in the last section of this chapter. A schematic overview of the experimental apparatus comprising both the optical setup and the vacuum system is given in Fig. 2.1, and all the aspects of the experiment are explained in detail in the following sections (2.1 - 2.5).

2.1 Optical setup

The laser system employed was a chirped pulse amplification (CPA, [166]) Ti:Sapphire laser system comprising a regenerative amplifier pumped by a frequency doubled Nd:YLF laser (Legend-HE, Coherent). The system operated with a repetition rate of 1 kHz. The output pulses have a central wavelength of 800 nm with a 12-15 nm bandwidth, a near transform limited duration of about 45 fs, and an energy up to 2.5 mJ.

The laser output was divided in two by a 60/40 beam splitter. In the molecular axis alignment experiment the transmitted 40% was used as the pump beam to align the molecules, whilst the reflected 60% was used as the probe beam; in the rescattered

electron experiment only the reflected 60% beam was used. The optical path followed by the reflected beam is the same in both experiments.

After the beam splitter, the pump beam diameter was reduced by 1/3 using a Galilean telescope, which allowed adjustment of relative beam sizes and consisted of a -250 mm and a 750 mm focal length lenses. Then, the pump beam was sent through a motorised delay stage in order to control its delay with respect to the probe beam. A half waveplate, was used to control the linear polarisation direction of the pump laser beam.

The beam reflected by the beam splitter was designed either to ionise atoms/molecules for the rescattered electron detection experiment or to initiate Coulomb explosion of the aligned molecules. Therefore, as explained in the previous chapter, the temporal duration of this laser pulse has to be very short (< 20 fs). A well established technique called hollow fibre pulse compression was used to reduce the duration of the probe laser pulses [168–170]. In this technique the optical spectrum is first broadened inside a gas-filled hollow fiber by self-phase modulation (SPM) occurring through the nonlinear interaction of the laser with the gas medium [171–173]. Then, since the spectrally broadened beam transmitted through the fibre is not transform limited, a subsequent optical pulse compression, based on dispersion compensation of the broadened pulse, is performed. The dispersion compensation is usually obtained by use of negatively dispersive chirped mirrors [174] or a prism-pair [168, 169, 175].

The probe laser beam was focused through a 1 m focal length lens into a 50 cm long hollow fibre having an inner radius of 125 μm. In order to avoid ionisation of the gas at the entrance of the hollow fibre, which could cause defocusing and then reduction of the coupling efficiency, the hollow fibre was differentially pumped [174, 176, 177], i.e pressurised at the fibre exit and evacuated at the fibre entrance, with $0.7 - 0.8$ bar of argon. Using an input laser pulse with an average energy of 900 μJ, a transmitted energy of (450 ± 10) μJ, corresponding to a transmission of about 50%, was routinely achieved. The transmitted beam was collimated using a 2 m focal length concave mirror. The focal length of this mirror, which determines the size of the beam, was chosen in order to obtain the biggest possible beam propagating without clipping on any optics. The chirp of the collimated beam was compensated by using eight chirped mirrors [178], each of which introduced a group velocity dispersion of -50 fs^2 per reflection. The compressed pulse had a temporal duration of 14.5 ± 0.7 fs, as measured by a single-shot second-harmonic frequency-resolved optical grating (SHG FROG) [167].

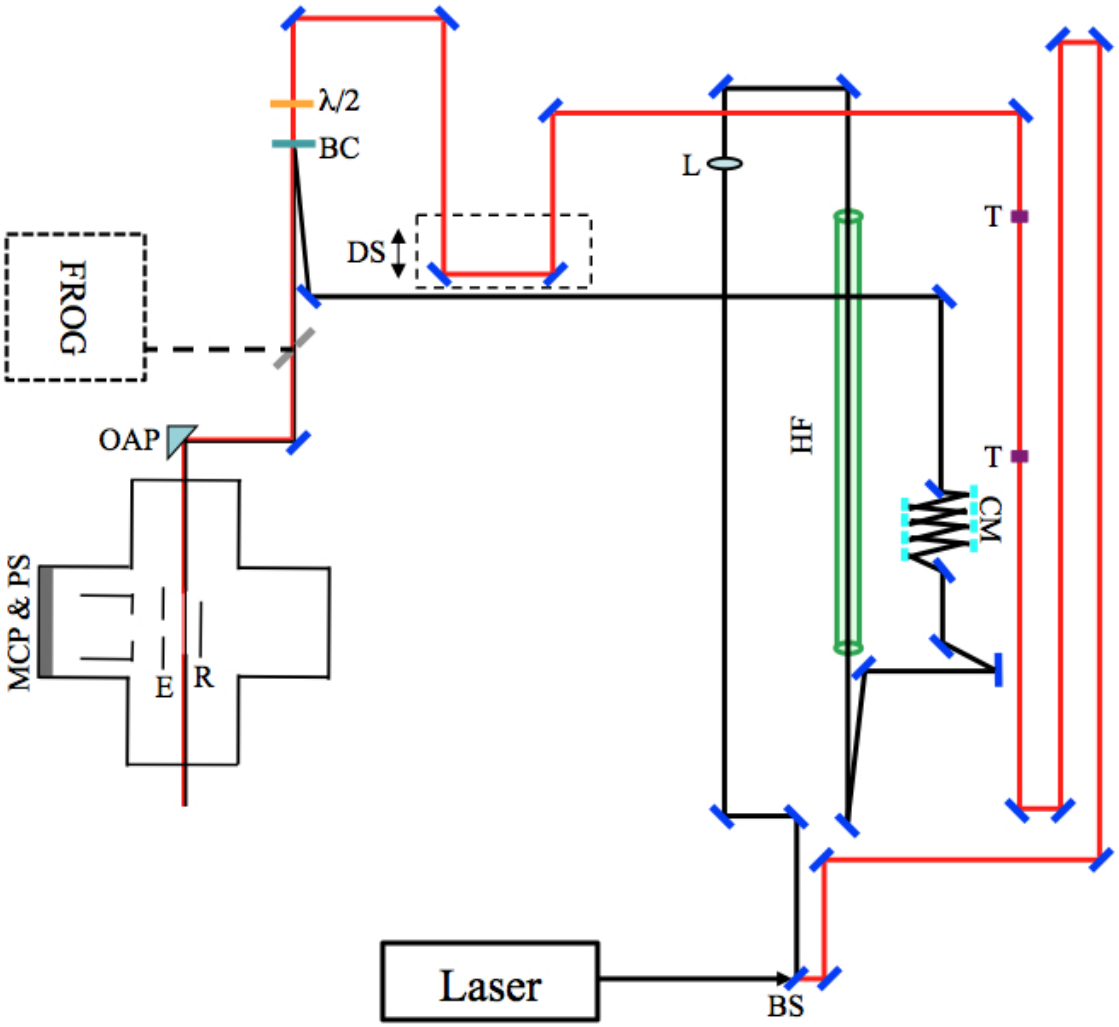

Figure 2.1: Schematic of the experimental setup. The pump beam is represented with the red line, while the probe beam is represented with the black line. Both beams can be deviated through a flip mirror towards the FROG [167] for pulse duration measurements (dashed line). Abbreviations: BS beam splitter (60/40); L lens with a focal length $f =$ 1000 mm; HF hollow fibre; CM chirped mirrors; T telescope composed of two lenses with focal lengths $f = -250$ mm and $f = 750$ mm (represented in purple); DS motorised delay stage; $\lambda/2$ half waveplate; BC beam combiner (80/20); OAP off axis parabolic mirror; R and E repeller and extractor electrodes of the VMI system; MCP multichannel plates; PS phosphor screen.

A $\lambda/4$ waveplate was used to control the polarisation of the laser beam in the rescattered electron experiment. In particular, the polarisation of the laser beam was converted from linear to circular by passing once through the waveplate, or was rotated by 90° by passing twice through the waveplate. In the alignment experiment, in order to be able to compare the results obtained by using circularly or linearly polarised probe laser beams, it is necessary that the intensity of the probe pulse along the direction of polarisation parallel to the polarisation of the pump laser beam is the same in both cases. In order to satisfy this requirement, a $\lambda/4$ waveplate was used to obtain circular polarisation of the probe laser beam, whilst a combination of the $\lambda/4$ waveplate and a dielectric thin film multilayer polariser was used to rotate the polarisation of the probe laser beam. The use of the polariser after the waveplate allowed transmitting only one linearly polarised component of the circularly polarised laser beam. The dispersion introduced by the polariser was the same as the waveplate, so in both experiments in the case of circular polarisation a glass plate of the same thickness as the waveplate was added to the beam path to equalise the material dispersion introduced in the case of linear polarisation.

Finally, the pump and probe beams were recombined by a normal incidence 80% reflective mirror. The beams were focused into the interaction region in the vacuum chamber through a 20 cm focal length, gold coated, 45° incidence angle, off-axis parabolic mirror (OAP). The use of a reflective focusing optic instead of a lens avoided any effects of material and chromatic dispersion, allowing the ultrashort probe laser beam to be focused without being temporally stretched. The OAP was mounted on a system of translation stages that allowed moving the mirror along the directions of the propagation of both the incident and reflected beams in order to focus the beams to the correct position in the chamber. The focal spot sizes of the pump and probe beams, which were found to be slightly astigmatic, were measured with a WinCam (Laser200 GmbH). The focal spot of the pump had $1/e^2$ diameters of (65 ± 5) μm along the direction of vertical polarisation, and (50 ± 5) μm along the other direction, and the focal spot of the probe had $1/e^2$ diameters of (55 ± 5) μm along the direction of vertical polarisation, and (45 ± 5) μm along the other direction.

Since the experiments aimed either to detect molecular axis alignment or to investigate rescattered electrons from aligned molecules, the pump and probe beams needed to be spatially and temporally overlapped. It was critical to ensure that the probe beam interacted only with molecules aligned by the pump beam. So, ideally the focal size of

the pump beam should have been much larger than the focal size of the probe beam. Since this was not the case in these experiments where the focal sizes of the two beams were comparable, the beams had to be very precisely overlapped spatially. The overlap was checked by diverting the beams at the entrance of the chamber through an optical wedge that reflected 5% of the beams towards a CCD camera. This CCD camera allowed overlapping the foci of the two beams within a precision of 5 μm.

The temporal overlap was obtained by observing the interference fringes created in the FROG trace when the two beams, already spatially overlapped, arrived on the CCD camera of the FROG at the same instant ("time zero").

2.2 Pulsed molecular beam source

A molecular beam is created by supersonic expansion of a gas from a high-pressure gas source, into a low-pressure ambient background [179], which corresponds to the expansion chamber in the experimental setup described in this chapter (see Fig. 2.3).

Continuous or pulsed molecular beams can be generated. The advantages of using a pulsed molecular beam in comparison with a continuous molecular beam are that a pulsed molecular beam strongly reduces the pumping requirements [180], it minimises the interference with gas reflected back into the beam by surrounding walls [181], and also it reduces the signal due to background thermalised gas.

A piezoelectric pulsed valve, whose sketch is shown in Fig. 2.2, was used in the experiments performed with the setup described in this chapter. The body of the valve, made of stainless steel, was filled with molecular or atomic gas at a backing pressure (P_b) of a few bars through a gas inlet. The main component of the valve is a piezoelectric disk on which a small "poppet" is attached, and a vacuum seal is achieved by the use of o-rings at the end of the poppet. The application of a voltage signal to the piezoelectric disk, causes the poppet to retract, allowing the gas to flow through a 300 μm diameter nozzle. The displacement of the poppet, and so the amount of gas that flows through the nozzle depends on the amplitude of the voltage signal applied to the piezo. This voltage signal was generated by a pulse generator (Physik-Instrumente), which was triggered by a signal generated by a delay generator (DG535, Stanford Research) in order to synchronise the pulsed valve with the laser. This trigger signal allowed control over the opening time and the repetition rate of the valve, which can fire at a repetition rate up to 1 kHz with opening

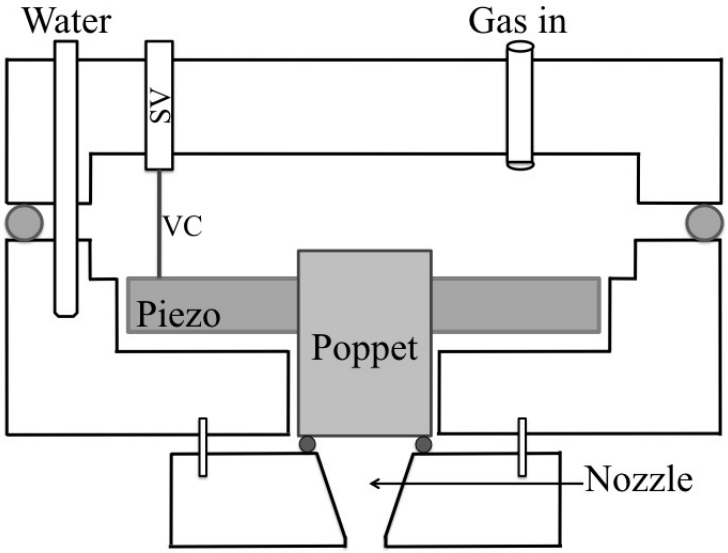

Figure 2.2: Schematic representation of the home-made piezoelectric pulsed valve. Abbreviations: SV voltage signal feedthrough; VC voltage connector.

times below 150 μs. At such a high repetition rate, there is a substantial thermal load on the piezo that can deteriorate the shot-to-shot stability unless cooling is implemented. For this reason the body of the valve was cooled by an internal water circuit. The pulsed valve was mounted on a three-dimensional translation stage that allows positioning of the molecular beam relative to the skimmer.

The gas jet expanded from the pulsed valve into the expansion chamber, whose schematic view is shown in Fig. 2.3. The vacuum system comprised two sections separated by a 1 mm diameter skimmer, which maintained the two chambers at different pressures when the gas jet was firing, and also collimated the molecular beam. The expansion chamber contained both the nozzle and the skimmer separated by 10 cm. This chamber was evacuated by two turbo-molecular pumps with a total pumping speed of 600 l/s (Turbovac 351, Oerlikon Leybold Vacuum and TPU 261 PC, Pfeiffer), that allowed the pressure in this chamber to be kept just below 10^{-4} mbar during operation of the gas jet. The second section, the target chamber, was located below the skimmer and was evacuated by two turbo-molecular pumps with a total pumping speed of approximately 400 l/s (Turbovac 151, Oerlikon Leybold Vacuum, and V551, Varian). The pressure was kept at about 4×10^{-7} mbar during operation of the gas jet. The resulting density of the nitrogen gas in the interaction region for this configuration of the pulse valve and vacuum chamber was estimated to be $\rho \approx 1.6 \times 10^{11}$ molecules cm^{-3} [179].

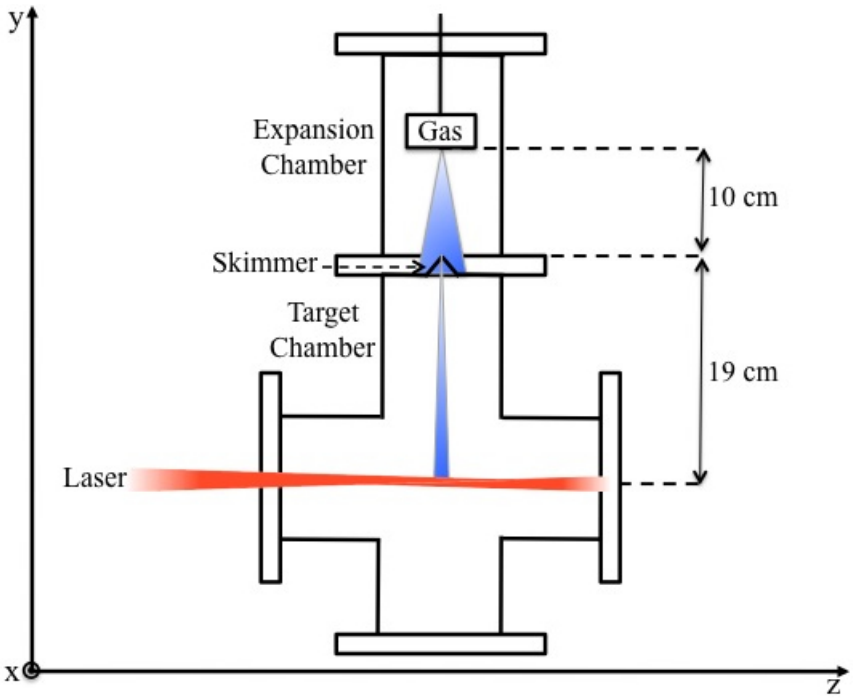

Figure 2.3: Schematic representation of the vacuum chamber designed for electrons and ions VMI detection. The chamber consists of two main sections (expansion and target chambers) separated from each other by a 1 mm diameter skimmer. The skimmer lies 10 cm below the nozzle of the pulsed valve that generates the molecular beam (represented in blue). The molecular beam travels through the skimmer toward the interaction point (19 cm below the skimmer) where it interacts with the laser pulses (represented in red).

The interaction between the laser and the molecular beam occurred in the target chamber 29 cm below the nozzle. The target chamber also hosted the velocity map imaging (VMI) spectrometer and the detection system that will be described in the next sections.

2.3 Velocity Map Imaging spectrometer

The VMI spectrometer described in this section was capable of detecting either electrons or ions, depending on the experiment. However, the design of the VMI device was dictated by the need for detection of rescattered electrons with energies in the 50-200 eV range.

The image formed on the detector is a projection of the expanding Newton sphere. Since the radius of the sphere at the detector depends linearly on the flight time and the square root of the energy [76], the maximum detectable particle energy depends on: the detector size, the distance of the detector from the interaction point, and the voltages applied to the electrodes.

According to these considerations, a VMI spectrometer, whose schematic is shown in

Electrode	Shape	Thickness (mm)	Outer diameter (mm)	Inner diameter (mm)
Repeller	plate	2	60	0
Extractor	disc	2	90	20
Ground	disc	2	74	24

Table 2.1: VMI electrode physical dimensions

Fig. 2.4, was built. The electrostatic lens assembly consisted of three electrodes: repeller (R), extractor (E), and ground (G), whose physical dimensions are listed in table 2.1. Since the ground electrode was connected directly to the flight tube, in order to further increase the maximum kinetic energy detectable, its inner diameter (corresponding to the aperture in the time-of-flight (TOF) tube) was increased with respect to the inner diameter of the extractor. The ground electrode aperture and the TOF tube did not limit the detectable solid angle of electrons, which was instead limited by the radius of the MCP. Both the ground electrode and the TOF tube were grounded via the chamber wall. High voltages were applied to the repeller and extractor electrodes through two spring-loaded bars that connected the electrodes to a feedthrough flange. This feedthrough was connected in its turn to two high voltage generators. It was found that the highest voltages that could be applied to the repeller and extractor electrodes were -14 kV and -11 kV, respectively. If higher voltages were applied for more than a few minutes, there was a risk of electrical breakdown. The two electrodes were insulated from each other and from the ground through a mounting structure made of an electric insulator (MACOR), which also held the electrodes in position. The components to which the high voltage was applied were made from electro-polished stainless steel.

The entire grid assembly was enclosed in a cylindrical, open ended magnetic shield consisting of two layers of 2 mm thick mu-metal shield spaced by 5 mm. Four holes of 15 mm of diameter were made in order to allow the laser and the molecular beams into this region, and to facilitate pumping. The magnetic shield was earthed through the chamber wall.

The whole assembly was housed within the 15.2 cm diameter tube of the target chamber. The same chamber housed also the detector that was mounted as close to the interaction point (151 mm) as was made possible by the geometry of the vacuum chamber. The detector is described in the next section.

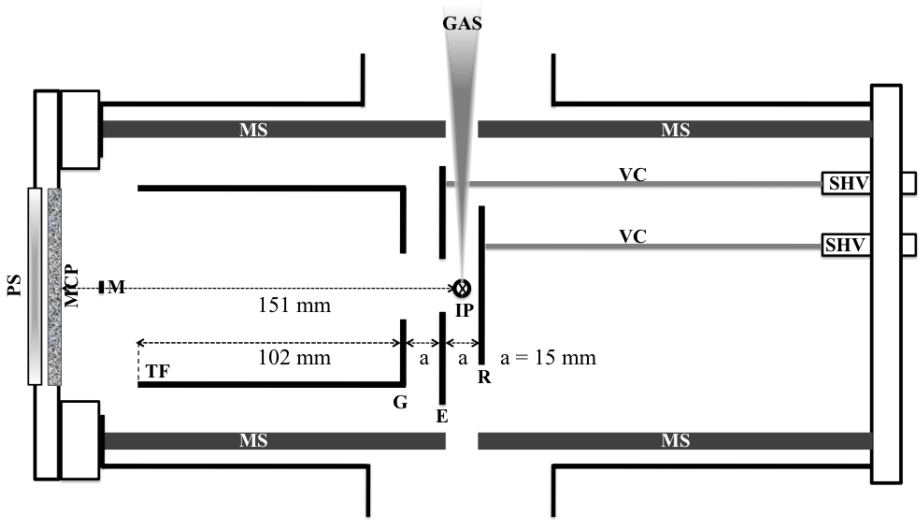

Figure 2.4: Schematic of the VMI spectrometer. Abbreviations: SHV high voltage signal supplied to electrodes through the voltage connectors VC; R repeller electrode; IP interaction point where the molecular beam and the laser pulses interact; E extractor electrode; G ground electrode; TF flight tube; M mask to protect the MCP multichannel plates; PS phosphor screen; MS magnetic shield.

2.4 Detection and data acquisition system

The position sensitive detector employed comprised two 75 mm diameter imaging microchannel plates (MCPs) mounted in a Chevron configuration, (MCP, Burle Industries, APD3075FM 12/10/8 I EDR 60:1) followed by a P47 phosphor screen (PS), which emitted blue light and had a decay time of the order of 50 ns. A CCD camera (Pixelfly, PCO AG) with an optical lens of 8 mm focal length (pentax TV lens 8.5 mm 1:1.5) was placed behind the PS in order to record the electron/ion images and store them on a computer. These images were then analysed with the program described in chapters 3 and 4.

In order to prevent damage to the centre of the MCP a 5 mm diameter mask made of copper and earthed through the chamber wall was placed in front of the centre of the MCP at a distance of 15 mm from it. This mask was held in position by two 0.5 mm wide copper wires. The damage to the MCP is caused by the large amount of electrons arriving at the centre of the MCP for each laser shot. This signal is not only due to low energy electrons, but has also a contribution from all electron energies generated, since the image on the MCP is a 2D projection of the original 3D sphere of electrons.

During the measurements of molecular axis alignment, the detection time of the MCP was gated in order to obtain efficient detection only in a narrow time window assuring that only ions with the same mass to charge ratios were recorded. This was done by

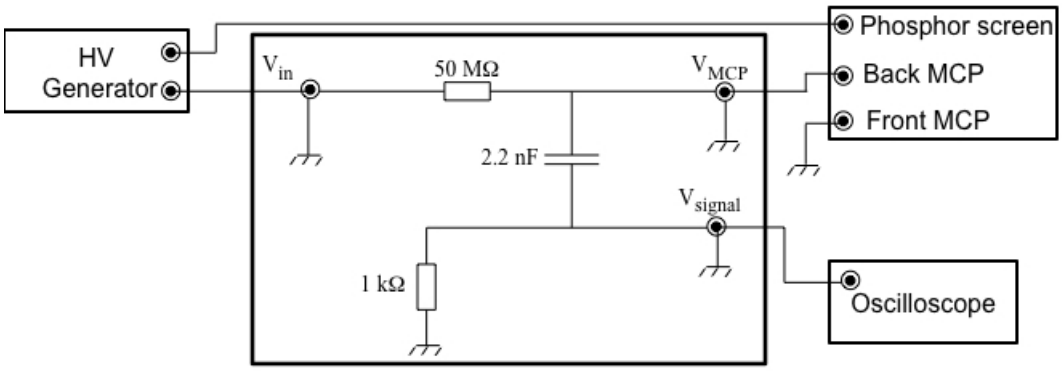

Figure 2.5: Schematic of the decoupling circuit used to monitor the charge on the back MCP plate.

switching the voltage on the back plate of the MCP from 0 V to 1450 V while maintaining a constant difference of voltage between the back MCP plate and the phosphor screen. The signal to the MCP was generated by a high voltage pulse generator (PVX-4140, IXYS Colorado) that was externally triggered with a signal generated by a delay generator (DG535, Stanford Research).

The same detector system (MCP and PS) was used in conjunction with a home made decoupling circuit in order to acquire time-of-flight traces. A sketch of the decoupling box is illustrated in Fig. 2.5. By decoupling the high voltage supplied to the back MCP plate (V_{in}), it was possible to monitor the charge on the back MCP plate (V_{signal}), and record the corresponding TOF trace by connecting V_{signal} to an oscilloscope. The other output signal of the decoupling circuit, V_{MCP}, is connected to the back MCP plate. The usual voltages applied in TOF configuration are the input voltage into the circuit $V_{in} = 1.7$ kV and the voltage to the phosphor screen $V_{PS} = 1.9$ kV.

2.5 Operation of the VMI spectrometer

2.5.1 Synchronisation of the experiment

The molecular axis alignment experiment was performed by using a MCP gating pulse and a gas jet repetition rates of 100 Hz. Gating the detector allowed operating the MCP at 100 Hz, preventing any contribution to the images from laser pulses before or after the one interacting with the molecular beam. Furthermore, an advantage of using a gas jet repetition rate of 100 Hz instead of 1 kHz in the molecular axis alignment experiment was that a better rotational cooling of the molecular beam, and so a better degree of alignment,

was obtained [179]. The rescattered electron experiment, instead, was performed by using a gas jet repetition rate of 1 kHz since in this case it was not possible to gate the detection time of the MCP due to the very short electron TOF (few ns).

In order to ensure the interaction of the laser beam with the molecular beam, they need to be synchronised. Furthermore, in order to detect the images generated from this interaction, also the MCP gating time has to be synchronised with the laser pulse in the molecular axis alignment experiment. A schematic diagram of the trigger timing implemented for both experiments is shown in Fig. 2.6. The laser pulse signal was taken from the delay line generator that controlled the switching time of the Pockels cells of the regenerative amplifier in the laser system, which determine the instant that the laser pulse is emitted from the cavity. This signal triggered a first delay generator (DG535, Stanford Research), which in the alignment experiment was used for the triggering of the MCP gating (channel A⊓B, where channel A controlled the delay and channel B the opening time), and for the control of the repetition rate of the generated signals (channel D). In order to obtain a repetition rate of 100 Hz, the longest delay (channel D) was set at $\approx$ 10 ms, since all of the outputs return to zero about 800 ns after the longest delay, according to the operation of the delay generator used. Channel D was used also for the triggering of a second delay generator, identical to the first one, which was used for the triggering of the gas jet (channel A'⊓B', where channel A' controlled the timing and channel B' the opening time). In the rescattered electron experiment only one delay generator was needed and it was used for the triggering of the gas jet (channel A⊓B, where channel A controlled the timing and channel B the opening time). In this case the longest delay (channel D) was chosen $<$ 1 ms in order to generate signals with a repetition rate of 1 kHz. Since the molecular beam spent a certain amount of time to propagate from the nozzle to the interaction region, the trigger signal for the gas needed to be ahead of the laser pulse.

The CCD camera used for the acquisition of the images formed on the phosphor screen was not synchronised to the laser pulse since a long exposure time, (0.4 - 0.5) s, was used during both experiments.

In order to find the time corresponding to the synchronisation of the molecular beam with the laser beam, TOF traces at different delays between the gas jet trigger and the laser pulse were acquired. A molecular beam of nitrogen gas (P_b = 1 bar) was produced by the pulsed valve operating with an opening time of 200 μs. Two different repetition

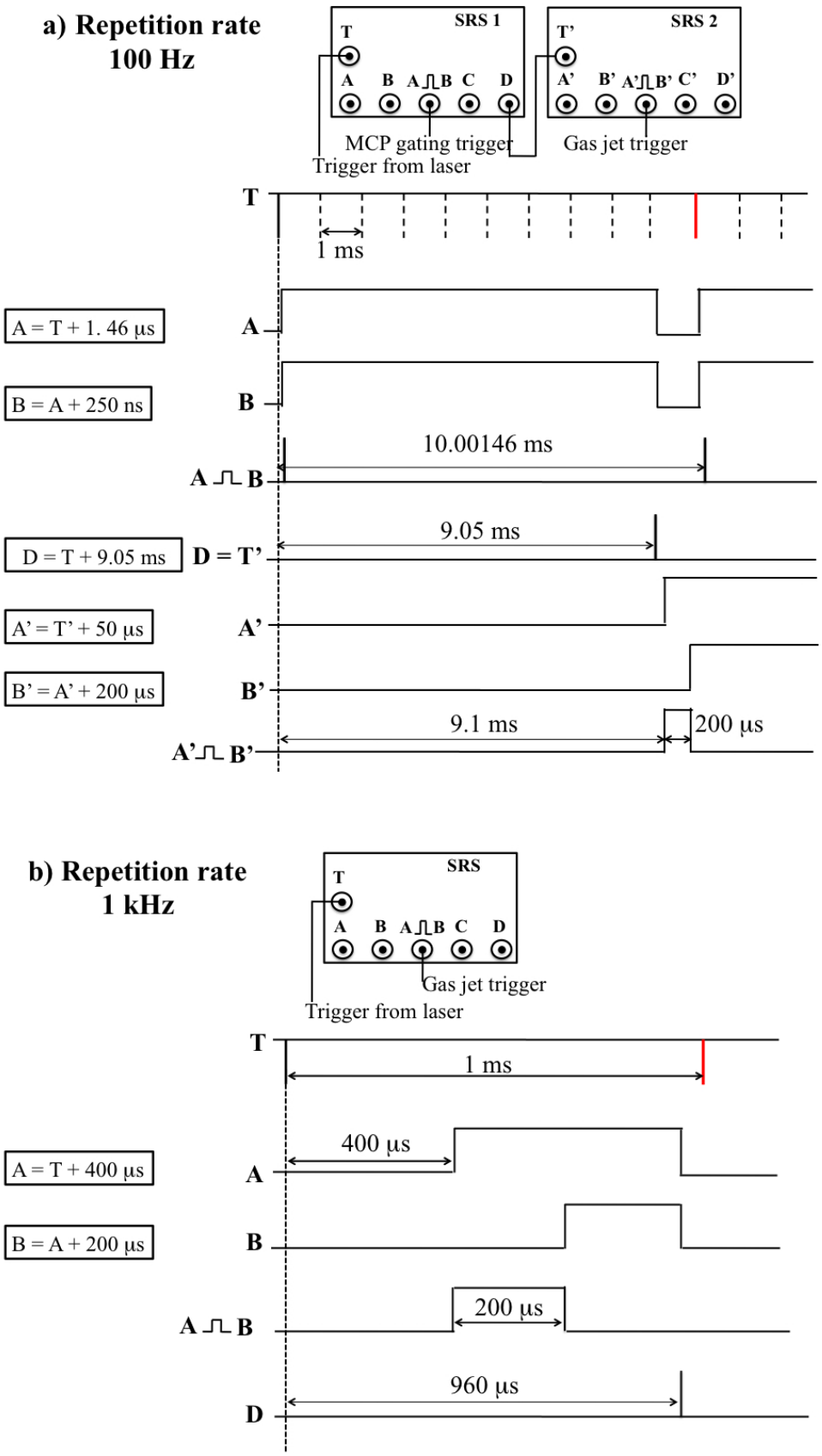

Figure 2.6: Schematic drawing of the trigger timing implemented for the molecular axis alignment experiment (a) and the rescattered electron experiment (b). The trigger T represents the laser pulse signal: the laser pulse interacting with the molecular beam is indicated with a red line, whilst the other pulses are represented by dashed lines.

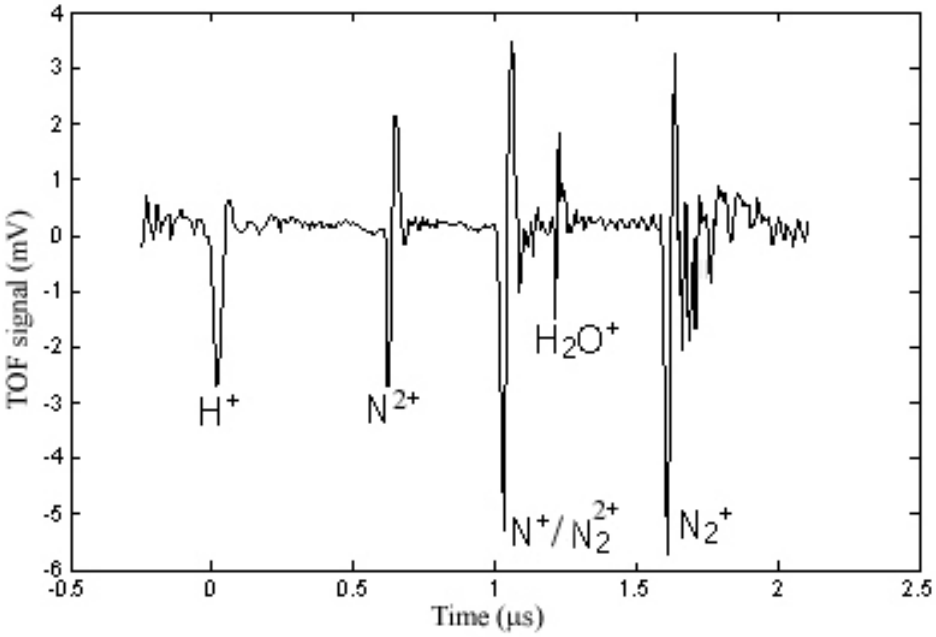

Figure 2.7: Time-of-flight spectrum, averaged over 1200 gas pulses, obtained by the interaction of the linearly polarised probe laser beam ($I = 8.7 \times 10^{13}$ W cm^{-2}, $\tau \approx 15$ fs) with a nitrogen molecular beam ($P_b = 1$ bar, opening time gas jet 200 μs, repetition rate 100 Hz). The voltages applied to the electrodes were $V_R = 1.5$ kV, $V_E = 0.8$ kV, and the voltages on the back MCP plate $V_{MCP} = 1.7$ kV and on the phosphor screen $V_{PS} = 1.9$ kV.

rates, 100 Hz or 1 kHz, were used. The molecular beam interacted with the probe laser beam having an intensity of $I \approx 9 \times 10^{13}$ W cm^{-2} and linearly polarised along a direction perpendicular to the time-of-flight axis. The ions generated from this interaction were accelerated in the electric field created by applying a voltage $V_R = 1.5$ kV to the repeller and $V_E = 0.8$ kV to the extractor. The resulting TOF signal was sent to the oscilloscope and the trace, averaged over 1200 gas pulses, was recorded. A typical TOF trace acquired in these conditions with a 100 Hz repetition rate of the gas valve is shown in Fig. 2.7. The TOF trace consists of peaks which correspond to ions generated from nitrogen and other peaks generated from background gas present in the chamber. Both the N^{2+} and N^+ ions result from the dissociation of the N_2 molecules. However, since the N^+ ions have the same TOF as the N_2^{2+} ions, the amplitude of the N^{2+} peak was measured as a function of the delay between the gas jet trigger and the laser pulse for both the repetition rates considered. The resulting plots are shown in Fig. 2.8. A higher contrast ratio of the signal (50%) was obtained for a repetition rate of a 100 Hz compared to that obtained for a repetition rate of 1 kHz (25%), since in the first case the pumps had more time to evacuate the target chamber between gas pulses.

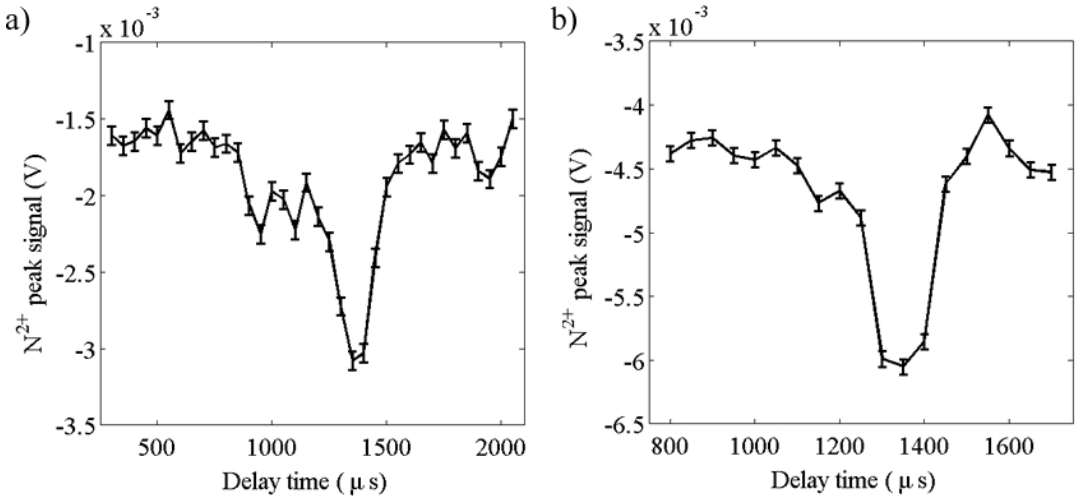

Figure 2.8: Plot of the amplitude of the N^{2+} TOF peak, averaged over 1200 laser shots, as a function of the delay time between the gas jet trigger and the laser pulse for a gas jet repetition rate of 100 Hz (a), and 1000 Hz (b).

The same procedure was followed for synchronisation of the laser pulse with each of the gas species used during the experiments.

2.5.2 Aligning the laser beams into the spectrometer

The laser beams need to be focused in the centre of the VMI device in z (direction of propagation of the laser pulse) and y (axis perpendicular to z and lying in a plane parallel to the detector) directions. In fact, only if the electrons or ions are created in the central position between the repeller and extractor electrodes, will the image created on the detector remain centred in the same position independently of the ratio between the voltages applied to the electrodes. In this case, by changing the voltage ratio the image on the detector will contract or expand from the same point.

Since the pump and probe beams are overlapped during the experiments, and since it is important that the charged particles are generated in the centre of the VMI spectrometer, only the probe beam, linearly polarised along a direction parallel to the y axis and with an intensity sufficiently high to induce ionisation, $I \approx 9 \times 10^{13}$ W cm^{-2}, was used during the alignment procedure. The alignment was obtained by adjusting both the OAP and the previous mirror positions, and it was considered satisfactory when the image formed on the detector by the parent ions created through the interaction of the laser beam with a nitrogen molecular beam, was centred in the same position for two particular sets of VMI electrode voltages. The first set was given by $V_R = V_E$ while in the second set V_R was kept

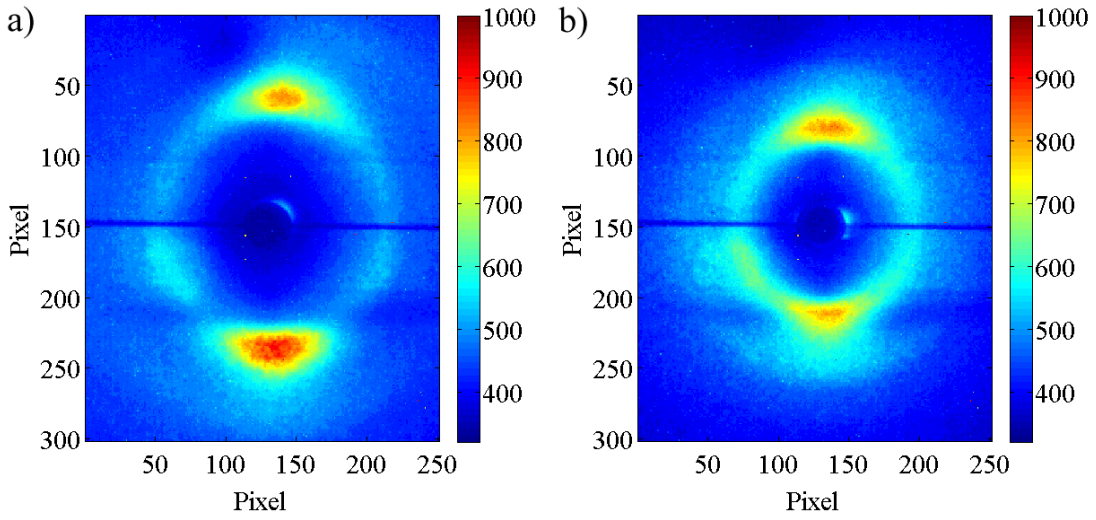

Figure 2.9: VMI images obtained from a sample of nitrogen molecules with a) $V_R/V_E = 74\%$; b) $V_R/V_E = 89\%$.

at the same value and $V_E = 0$ V. With these voltages, the VMI spectrometer operates in a spatial imaging mode, focusing ions originating from a given spatial position to a point on the detector. Therefore, in both cases the image on the detector corresponded to an image of the laser focus, consisting of a line parallel to the laser propagation. These configurations proved to be the easiest for assessing the alignment, particularly along the propagation direction of the laser pulse due to the presence of the mask that prevented from detecting the ions at the centre of the MCP. The gas jet used in this measurements operated at 100 Hz with an opening time of 200 μs.

Once this procedure was completed, images were acquired with different voltage ratios and it was observed that the ion distributions were asymmetric with respect to the centre of the image. Two of these images obtained for ratios $V_R/V_E = 74\%$ and $V_R/V_E = 89\%$, averaged over 51200 laser shots (corresponding to 5120 gas pulses for the gas jet operating at 100 Hz), and acquired with an exposure time of the CCD of 0.4 s, are illustrated in Fig. 2.9 (a) and (b), respectively. In the left image (a), the distribution of ions seems to be more intense on the bottom part of the image, whilst in the right image (b) the asymmetry seems to reverse. This phenomenon suggests that the asymmetry could be related to a non uniform gain of the detector, since the illuminated area changes with the ratio V_R/V_E.

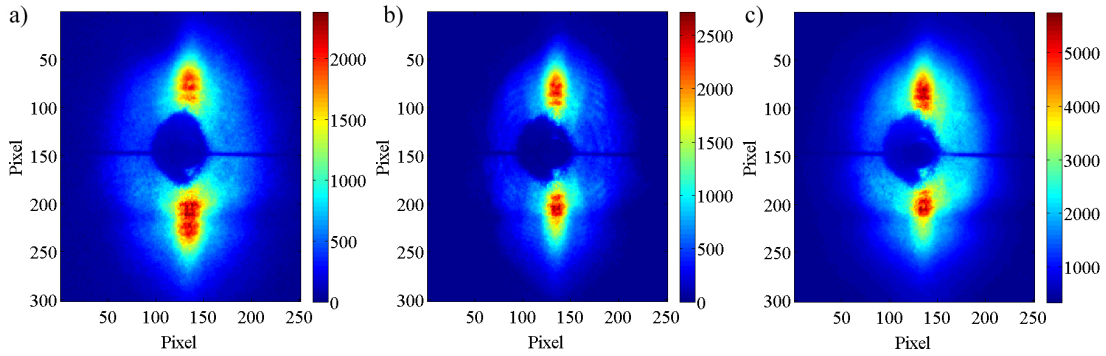

Figure 2.10: VMI images of ATI rings of xenon with background subtracted, acquired with the pump laser beam (long pulse $\tau = 45$ fs) corresponding to different ratios: a) $V_E/V_R = 67\%$; b) $V_E/V_R = 75.3\%$; c) $V_E/V_R = 80\%$. The best voltage ratio corresponds to the image b) having the sharpest ATI rings.

2.6 VMI of high energy photoelectrons

As discussed in the previous sections, the VMI device was designed primarily to detect high energy rescattered electrons. Thus, some preliminary measurements were done in order to test the performance of the VMI spectrometer.

2.6.1 Tuning the VMI lens voltages

The voltages applied to the repeller and extractor electrodes were chosen in order to ensure the velocity mapping of the photoelectrons onto the detector [76]. Optimal focusing voltage was found by looking at the Above Threshold Ionisation (ATI) photoelectrons generated from the interaction of the pump laser beam with a xenon atomic beam. The pump beam was preferred to the probe beam for this procedure since its pulses are longer ($\tau = 45$ fs), and as a consequence, the separation between the ATI rings is not blurred by the broad spectral bandwidth of the laser pulse, as would happen in the case of the ultrashort probe beam. Images were acquired for different voltage ratios between the electrodes. In particular, the repeller voltage was kept constant at the value $V_R = -2.9$ kV, whilst the extractor voltage was changed between -2.0 kV and -2.3 kV, giving a ratio V_E/V_R in the range of (67-80)%. The best voltage ratio, which corresponded to the image having the sharpest ATI rings was found to be 75.3%. The blurring of the image when the detector plane is out of focus, can be seen in Fig. 2.10 (a) and (c). Fig. 2.10 shows three images acquired at V_E/V_R equals to 67%, 75.3% and 80% respectively. Background images (acquired without the gas jet firing) have been subtracted from the images shown.

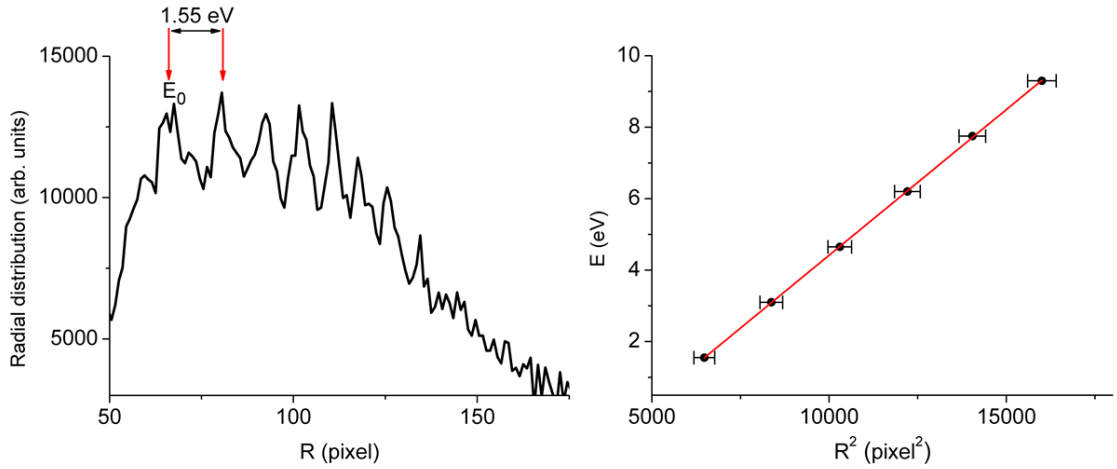

Figure 2.11: The image on the left shows the ATI peaks of the xenon. It is a plot of the radial distribution of the inverted image acquired for V_R = 1.5 kV. The first peak is considered as the reference point E_0 from where the energies of the other rings are calculated. The difference in energy between two consecutive rings is 1.55 eV. In the image on the right the differences between the energies of the ATI peaks and E_0 is plotted as a function of R^2, where R is the radial position of the peaks expressed in pixels. The red line represents the linear fit to the data. The slope of the linear fit is found to be $B = 8.15 \times 10^{-4} \pm 0.03 \times 10^{-4}$ eV pixel^{-2}

2.6.2 Calibration of the VMI spectrometer

In order to assign an energy to the detected charged particles, it is necessary to calibrate the VMI spectrometer. The conversion factor B between the radial position R and the energy E of the detected particles is given by the equation:

$$E = B\ R^2 \tag{2.1}$$

For this purpose, since the difference in energy between two consecutive ATI peaks is a known value corresponding to the energy of one photon ($E_{\text{photon}} = \hbar\omega = 1.55$ eV), low order ATI photoelectrons were generated by letting the pump laser beam interact with a sample of xenon atoms. The ATI photoelectrons were accelerated towards the detector with a given value of V_R and a ratio V_E/V_R = 75.3%. The 3D radial distribution was obtained from the 2D image formed on the detector, by using an inversion process described in the next chapter. The corresponding energy of the ATI peaks was plotted as a function of R^2 and the conversion factor B was obtained by applying a linear fit, represented by Eq. 2.1, to the data. The key steps of this process are illustrated in Fig. 2.11.

The maximum repeller voltage that produced visible low order ATI rings was -4.5 kV. However, since the VMI spectrometer was designed to detect high energy electrons, the

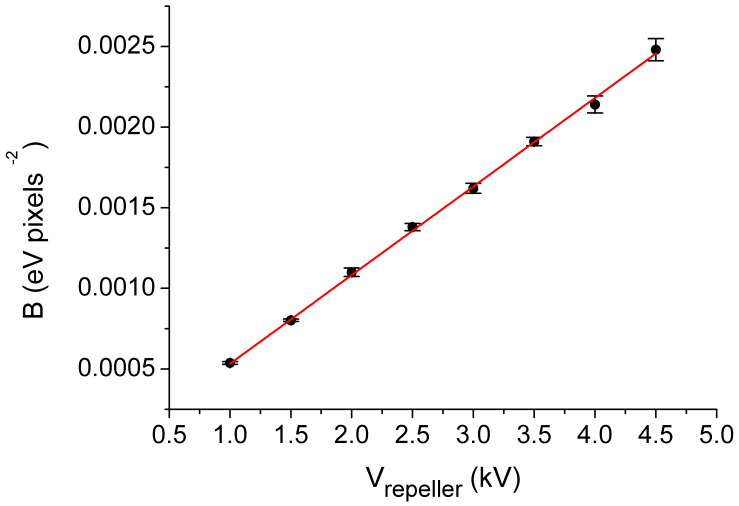

Figure 2.12: Plot of conversion factors B, obtained for a fixed ratio V_E/V_R and different V_R as a function of the repeller voltage. The red line represents the linear fit, $B = C\,V_R$. The constant C allows to calibrate the VMI device for high electrode voltages.

spectrometer needed to be calibrated for higher electrode voltages. In order to do this, it was considered that for a fixed ratio V_E/V_R the conversion factor B is linearly related to the repeller voltage by a multiplicative constant C through the equation $B = C\,V_R$ [76]. Therefore, by knowing C, the conversion factor B can be calculated for whatever value of the repeller voltage. To find C, the calibration procedure described above was repeated for eight different pair of electrode voltages, by keeping the ratio $V_E/V_R = 75.3\%$. Then, the resulting values of B were plotted as a function of V_R, and the coefficient C was obtained by applying a linear fit to the data. The plot is shown in Fig. 2.12.

2.6.3 Detecting rescattered high energy electrons

In order to test the high energy photoelectron performance of the VMI spectrometer and to check what the maximum electron energy detectable is, rescattered electrons in xenon were studied, since they are manifested in ATI spectra at the highest energies, as discussed in section 1.4 of Chapter 1.

Only the 60% of the main beam, reflected by the beam splitter and compressed through the hollow fibre technique, and having a temporal duration at the interaction point of 16 fs, was used in this experiment. Different intensities of the laser beam, obtained by aperturing down the beam before the OAP, were used. For each intensity, measurements with linear polarisation in the detector plane, and circular polarisation of the laser pulse were carried out. The gas jet operated at 1 kHz repetition rate, with an opening time of

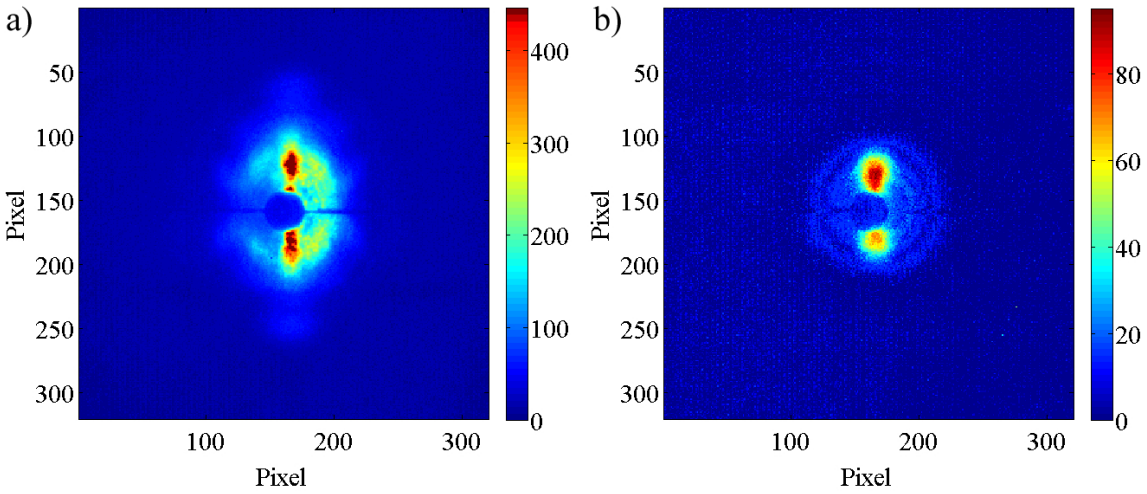

Figure 2.13: Images obtained from a sample of xenon with: a) linear polarisation; b) circular polarisation of the laser pulse. The estimated average intensity of the laser pulse, based on beam characterisation measurements, is $I_1 = (2.0 \pm 0.6) \times 10^{14}$ W cm^{-2}.

200 μs, and $P_b = 1.2$ bar. The potentials applied to the electrodes where $V_R = -10$ kV and $V_E = -7.53$ kV. The images were acquired with the CCD camera operating with an exposure time of 0.5 s. Each image corresponded to an average over 1280 camera acquisitions, i.e 640000 laser shots.

First, images were acquired with an intensity of $I_1 = (2.0 \pm 0.6) \times 10^{14}$ W cm^{-2} (estimated from the focal spot measurement) in order to see if rescattered electrons were detected. The images with the background (image acquired without the gas jet firing) subtracted, obtained respectively with linear (a) and circular (b) polarisations of the laser beam are shown in Fig. 2.13. These images were inverted with the regularised algorithm described in chapter 3 in order to retrieve the energy and angular distributions of the photoelectrons. For both polarisations the angular distribution was plotted as a function of the angle θ, which is defined as the angle between the photoelectron position and the polarisation vector in the case of linear polarisation, and as the complementary of the angle between the photoelectron position and the laser propagation direction (i.e the angle out of the plane of polarisation), in the case of circular polarisation.

Since the maximum kinetic energy of rescattered electrons is obtained when the electrons are back-scattered [150, 151], the energy spectra were obtained by integrating the signal of the inverted images over a small range of θ angles, $\theta \in [0°, 10°]$. By restricting the range of integration, the contribution to the spectra of the high energy electrons was not washed out by the other electrons. The resulting energy spectra for both polarisations

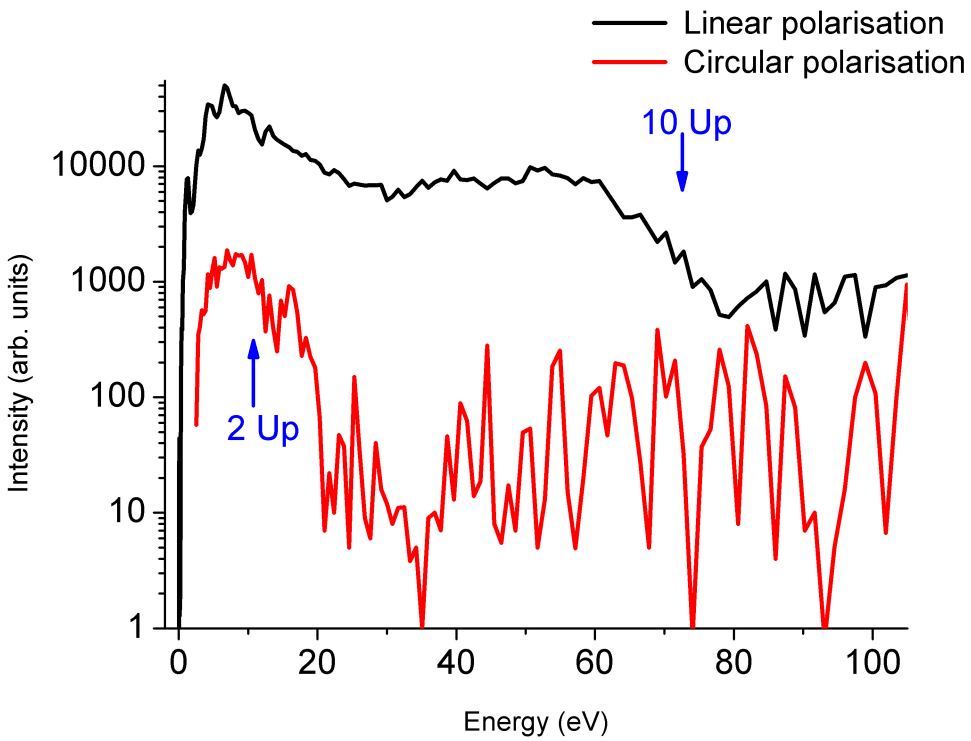

Figure 2.14: Retrieved electron energy distributions obtained by integrating the signal of the inverted images over $\theta \in [0°, 10°]$. The estimated average intensity of the laser pulse, based on beam characterisation measurements, is $I_1 = (2.0 \pm 0.6) \times 10^{14}$ W cm^{-2}. The black curve refers to the linearly polarised laser pulse and the red curve to the circularly polarised laser pulse. The arrows mark ATI cut-offs at around 70 eV and 14 eV corresponding to 10 U_p and 2 U_p, respectively.

are plotted on the same graph for comparison, and are shown in Fig. 2.14. For the linear polarisation case (black line), the energy spectrum has the typical shape obtained when rescattering plays a role [152]. In fact the ATI energy distribution exhibits a sharp fall in signal at low energies, followed by a plateau due to electrons returning to the ion core during the ionisation process and rescattering elastically [152]. This plateau ends with a sharp cut-off at around 70 eV. For the circular polarisation case, the electron signal has a similar shape at low energies, but the ATI plateau disappears in this case since the additional component of the electric field prevents electrons from returning to the ion core. However, in this case, the position of a cut-off, which allows quantification of the maximum electron energy detected, is not very clear. To be able to characterise the cut-off position, the angular distributions of the photoelectron signal at various energies, reconstructed from the inverted image, were analysed. Each angular distribution was obtained by integrating the signal of the inverted image over an energy range of 3 eV. Furthermore, to confirm that

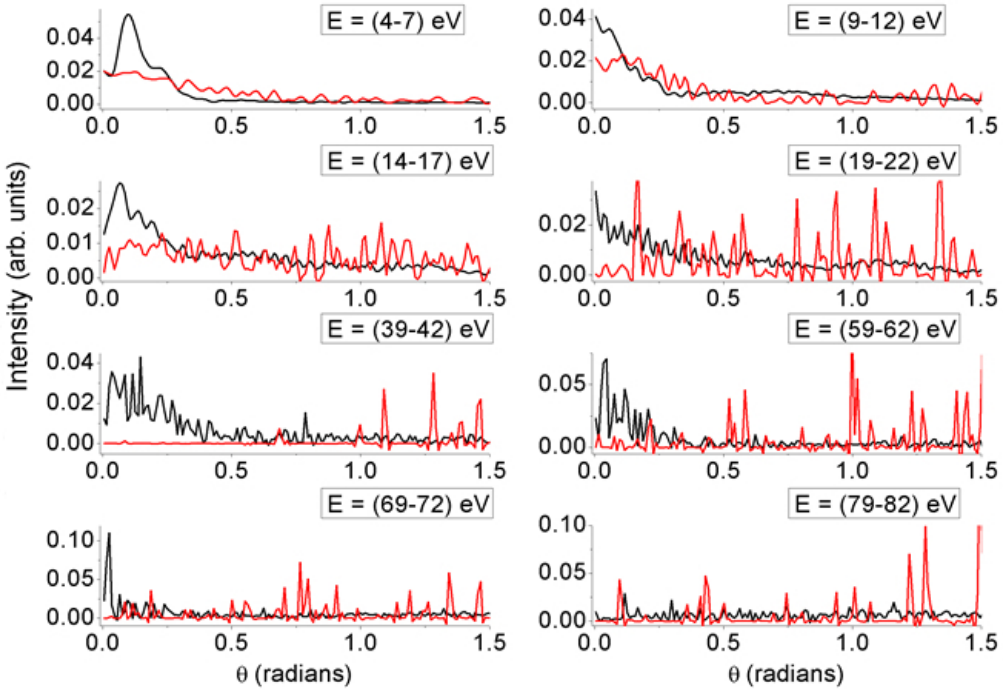

Figure 2.15: Retrieved angular distributions for the circularly polarised (red lines) and linearly polarised (black lines) pulses for various electron energies. The estimated average intensity of the laser pulse, based on beam characterisation measurements, is $I_1 = (2.0 \pm 0.6) \times 10^{14}$ W cm^{-2}.

rescattered ATI electrons have been observed in the case of linear polarisation, and mostly to better quantify the maximum electron energy detected, the angular distributions of the photoelectron signals were examined also in this case. The resulting angular distributions are shown in Fig. 2.15. In the case of circular polarisation (red lines), the photoelectron emission is found strongly localised around the polarisation plane ($\theta = 0°$) at electron energies in the ranges of (4 - 7) eV and (9 - 12) eV. For photoelectron energies higher than (14 ± 2) eV, the angular distribution of the photoelectron generated with the circularly polarised probe pulse becomes indistinguishable from the noise. This is consistent with the lack of a rescattered component in the electron signal in this case. Since only direct electrons arrive on the detector in this case, the cut off in ATI signal is expected to be found at 2 U_p [182]. As a consequence, from this measurement it can be determined that U_p lies in the range of 6 - 7 eV, corresponding to a laser intensity $I_{1c} = (1.09 \pm 0.08) \times 10^{14}$ W cm^{-2}. Although this does not perfectly match with the estimation of the average intensity based on beam characterisation measurements ($I_1 = (2.0 \pm 0.6) \times 10^{14}$ W cm^{-2}), it is in reasonably agreement with this value. In the case of linear polarisation (black lines), it is found that the electron signal is strongly peaked around the laser polarisation axis (0 degrees)

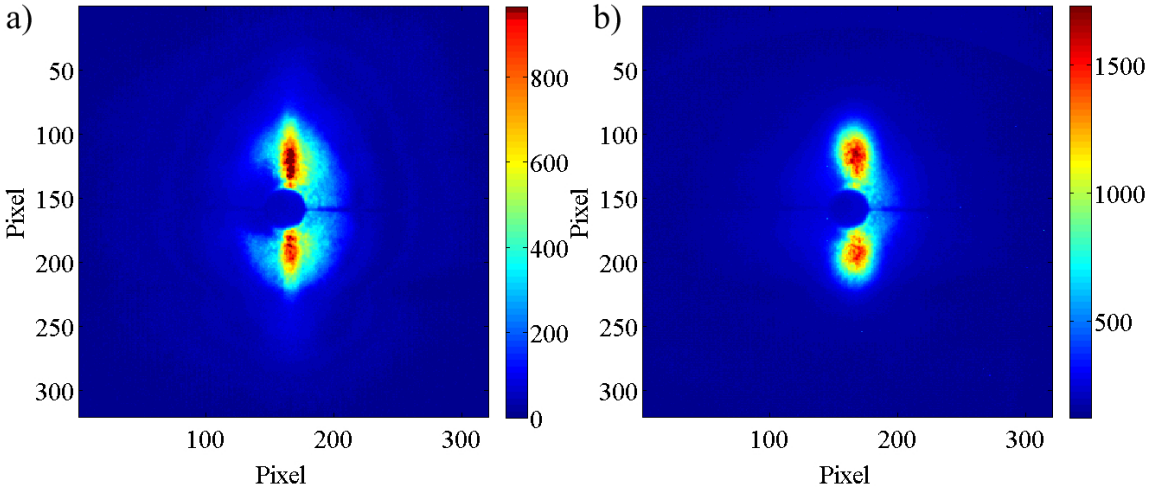

Figure 2.16: Images obtained from a sample of xenon with: a) linear polarisation; b) circular polarisation of the laser pulse. The estimated average intensity of the laser pulse, based on beam characterisation measurements, is $I_2 = (4.1 \pm 0.5) \times 10^{14}$ W cm^{-2}

for energies lower than (70 ± 3) eV, while at higher energies the signal becomes indistinguishable from the noise. This is consistent with the energy at which the cut-off appears in the energy spectrum. Furthermore, considering that the cut-off energy corresponds to 10 U_p [149], the result obtained is also in agreement with the estimation of the U_p coming from the analysis of the angular distributions obtained for the circular polarisation case.

In order to check if higher energy electrons could be detected with this VMI spectrometer, images were acquired with an intensity of the laser pulse which is twice as high as in the previous case, $I_2 = (4.1 \pm 0.5) \times 10^{14}$ W cm^{-2} (estimated from the focal spot measurement). The images, shown in Fig. 2.16, were analysed as described above for the previous measurements. The energy distributions, shown in Fig. 2.17, were calculated for both linearly (black line) and circularly (red line) polarised laser beams. Also in this case, from the comparison between the two spectra it is evident that rescattered photoelectrons are detected in the case of linear polarisation, in which the maximum detected electron energy is of (105 ± 3) eV. Instead, for the circularly polarised laser beam, the maximum electron energy at which the electron emission is still strongly localised around the polarisation plane (0 degrees) is found to be (21 ± 2) eV, which corresponds to a value of U_p of (10.5 ± 1) eV. Thus, the laser intensity is found to be in the range $I_{2c} = (1.8 \pm 0.2) \times 10^{14}$ W cm^{-2}, which although not in agreement with the estimation of the average intensity based on beam characterisation measurements ($I_2 = (4.1 \pm 0.5) \times 10^{14}$ W cm^{-2}), is twice as high as the intensity calculated in the previous measurements (I_{1c}), as expected.

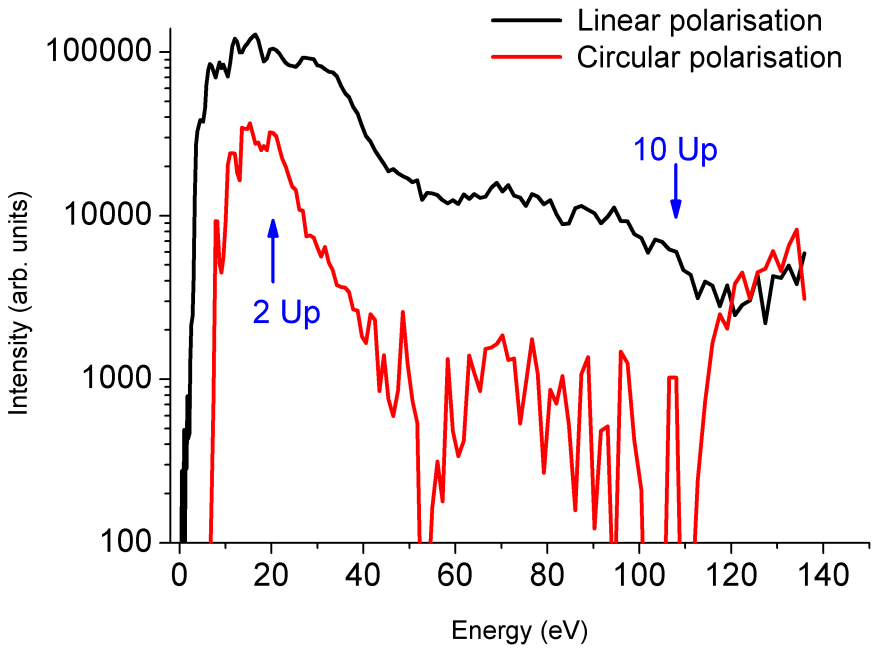

Figure 2.17: Retrieved electron energy distributions obtained by integrating the signal of the inverted image over $\theta \in [0°, 10°]$. The estimated average intensity of the laser pulse, based on beam characterisation measurements, is $I_2 = (4.1 \pm 0.5) \times 10^{14}$ W cm^{-2}. The black curve refers to the linearly polarised laser pulse and the red curve to the circularly polarised laser pulse. The arrows mark ATI cut-offs at 105 eV and 21 eV corresponding respectively to 10 U_p and 2 U_p.

2.6.4 Summary

The preliminary results obtained from the experiment described in the previous section show that the VMI technique can be used to detect and distinguish high energy rescattered photoelectrons. In particular, photoelectron energies as high as (105 ± 3) eV have been detected with this VMI spectrometer. However, it is expected that by employing higher electrode voltages, and by increasing the intensity of the laser pulse, even higher electron energies can be detected.

These preliminary measurements pave the way to future experiments aiming to detect rescattered photoelectrons from aligned molecules by using the VMI technique. The interest in this kind of experiment is due to the fact that, as explained in chapter 1, the rescattered photoelectrons encode information about the molecular structure [49].

Chapter 3

A regularised matrix inversion algorithm for velocity map images with application to Coulomb explosion imaging

3.1 Introduction to inversion of VMI images

Images obtained in a typical VMI experiment are projections of a three dimensional (3D) cloud of charged particles (ions or electrons) onto a two dimensional (2D) detection plane. Therefore, in order to reconstruct the initial 3D velocity and angular distributions of the charged particles, an inversion of the 2D projected image is necessary.

In the past decades many inversion methods have been developed [77–85]. All these methods are based on the assumptions that the original 3D cloud of particles has an axis of cylindrical symmetry lying in a plane parallel to the detection plane, and the initial kinetic energy of the particles is small compared to the kinetic energy they acquire in the accelerating electric field. Under these circumstances for a given energy, all the particles lying on a 2D cross section of the 3D original cloud, perpendicular to the cylindrical symmetry axis, are projected on a straight line perpendicular to the symmetry axis on the

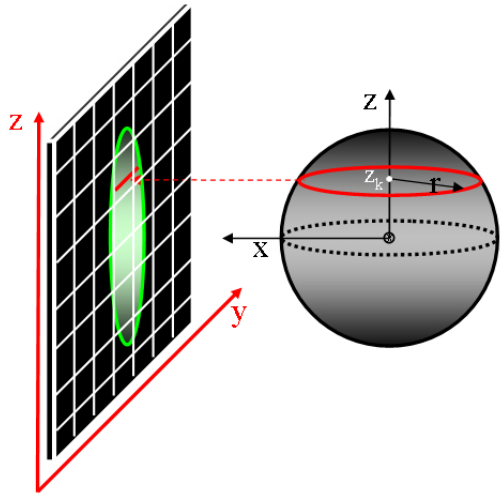

Figure 3.1: Projection of a 3D original ion cloud, cylindrically symmetric about the z axis, on a 2D detector. A 2D cross section of the ion cloud (red curve on the sphere) is projected on a straight line on the detector (red line).

2D detector [83], as illustrated in Fig. 3.1. Therefore, the relation between the original 3D distribution $P(x, y, z)$, that can be represented as a function of only two coordinates $P(r, z)$ in a cylindrical polar coordinate system, and the 2D projected image $I(y, z)$ can be expressed through the Abel integral [183]:

$$I\,(y,z) \;=\; 2\int_{y}^{\infty} \frac{r\,P\,(r,z)}{\sqrt{r^2\,-\,y^2}}\,\mathrm{d}r \tag{3.1}$$

where the z axis is the axis of cylindrical symmetry. This equation represents a direct problem since it allows to determine the result of a measurement ($I(y, z)$) from the knowledge of a model distribution ($P(r, z)$). The main characteristic of direct problems is that their solutions define a transition from a physical quantity with a certain information content, in this case $P(r, z)$, to another quantity with smaller information content, in this case $I(y, z)$ [184]. On the contrary, inverse problems aim to reconstruct the model distribution from the acquired data, and so accomplish a transformation that corresponds to a gain in information. This can cause inverse problems to be ill-posed, that is they do not satisfy all the conditions that define a well-posed problem, which are the existence of a solution for any data, the uniqueness of the solution, and the continuous dependence of the solution on the data [185].

The recovery of the 3D distribution from its 2D projection is an inverse problem, and

it is expressed by the inverse Abel transform given by [183]:

$$P(r,z) = -\frac{1}{\pi}\int_r^\infty \frac{\partial I(y,z)/\partial y \, \mathrm{d}y}{\sqrt{y^2-r^2}} \tag{3.2}$$

This problem is ill-posed because of the singularity at $y^2 = r^2$. However, since experimental images $I(y,z)$ are discretely sampled on a 2D grid, Eq. 3.2 needs to be discretized, and it can be proved that the discrete version of the inverse Abel transform is a well-posed problem [186]. This is because in this case, the fact that uniqueness of the solution holds true implies that a solution of the discrete problem exists and depends continuously on the data. However, this solution can be completely corrupted by noise because discrete ill-posed problems are generally ill-conditioned [187]. This means that their condition numbers, representing the error propagation from the data to the solution, are very large ($\gg 1$), implying that even a small error in the acquired data may cause a large error in the restored solutions. Therefore, a consequence of the ill-conditioned nature of the inverse Abel problem is that the experimental noise tends to be magnified in the inversion process [186]. Besides this problem, the evaluation of Eq. 3.2 is difficult because the estimation of the derivative of a noisy function is required $\partial I(y,z)/\partial y$.

The problem of the singularity at $y^2 = r^2$ and the estimation of the derivative can be avoided by representing the inverse Abel transform as the Hankel transform of the Fourier transform of the 2D projected image. This is the procedure followed in the Fourier-Hankel method [78, 188–190]. This inversion method makes possible the evaluation of the inverse Abel integral. Yet, the main drawback of this algorithm is the magnification of the experimental noise which accumulates along the centreline of the recovered distribution, as well as the artifacts introduced in the retrieved distribution. As a result, the inversion of very noisy images cannot be performed with high accuracy by this method [189].

The problem of the artifacts in the retrieved image has been overcome by other inversion methods, such as BASEX, introduced by Dribinski and co-workers [191]. The essential idea of this method is to represent the original 3D distribution as an expansion in a well-behaved basis set. The projection of this basis set on the detection plane, represented by its Abel integral (Eq. 3.1), forms a basis set in the space of the 2D projected image. As a consequence, the 2D projected image can be represented as an expansion in the projected basis set through the same series expansion coefficients of the 3D distribution. The inversion problem is thus converted into a simple problem of finding expansion coefficients.

Although this method performs better than the Fourier-Hankel in the inversion of noisy images, the centreline noise is still present in the inverted images.

Garcia and co-workers developed another inversion method, pBASEX, essentially based on the BASEX algorithm. The only difference is the choice of the coordinate system. While in the BASEX method the inversion is performed in a Cartesian coordinate system, spherical polar coordinates are used in the pBASEX algorithm [84]. The use of polar basis sets results in a better reconstruction of the 3D original distribution. This distribution, in fact, does not suffer from the centre line noise since in this algorithm the noise is projected toward the centre of the reconstructed image.

Similarly to the pBASEX method, also an iterative inversion procedure, developed by Vrakking [85], has the advantage of accumulating the noise in a central spot of the inverted image. This method makes use of the similarity between a 2D slice of the original 3D distribution and the projected 2D detected image, and calculates iteratively the 2D projection from a guessed initial distribution [85]. The main disadvantages of this method are that the choice of the guessed initial distribution is empirical, there is no criterion to determine the optimal number of iterations, and no proof of convergence exists.

Another method known as onion-peeling, which is based on the back projection approach, can be followed in order to invert 2D projected images [82, 83]. The basic premises behind this inversion is that at a given radius $\tilde{R}$ on the detector, corresponding to a kinetic energy of the ejected particles $\tilde{E}$, all the particles ejected with a kinetic energy larger than $\tilde{E}$ contribute to the signal. Therefore, the signal at the outer pixel ($i_{\max}$, $j_{\max}$) of the image, where i and j are the index over the y and z axes of the detector (with z parallel to the axis of cylindrical symmetry), corresponds to the particles ejected with the maximum initial kinetic energy $E_{\max}$ at an azimuth angle (angle about the axis of cylindrical symmetry) of $\phi = 0$. From the number of particles found at this outer pixel, the contribution that particles with $E_{\max}$ and emitted *at any angle* ϕ make to the signal at the pixels of the line $j_{\max}$ can be calculated, due to the cylindrical symmetry. This signal is added to the retrieved distribution at the pixel ($i_{\max}$, $j_{\max}$) and subtracted from the 2D projected image at all the pixels (i, $j_{\max}$), with $i < i_{\max}$. This procedure is followed for each pixel (i, $j_{\max}$), with $i < i_{\max}$, until the centre of the image is reached. Then the procedure is repeated for each line $j < j_{\max}$, till the whole original distribution is retrieved. A consequence of the inversion procedure from the outer region to the inner region of the image is that the noise accumulates inwards, that is on the central line of the image. This problem

has been overcome by some methods which perform an onion-peeling of the projected image in polar coordinates [192, 193]. In fact, in these methods the experimental noise is accumulated in the centre of the inverted image.

Despite the existence of all these inversion methods, we have developed a different algorithm, based on a matrix inversion method. The implementation of a new inversion method is motivated by the need for an algorithm that allows inclusion of a non-uniform detection function in a straightforward manner since in Coulomb explosion imaging experiments the probe laser does not ionise all molecules with the same probability due to an orientational dependence of ionisation [87]. In these experiments, the resulting ion clouds do not have an axis of cylindrical symmetry, and so none of the algorithms described in this section can be used to invert the corresponding 2D projected image. The approach followed to perform the inversion of such images is to first record an image for the probe laser pulse alone for an isotropic sample of molecules. Inversion of this image yields the molecular orientation dependence of the Coulomb explosion probe. This probe molecular orientation dependence is then deconvoluted from images obtained for aligned molecules in order to quantitatively extract the molecular axis distribution. This is discussed in more detail in Chapter 4.

In this chapter the algorithm used to invert the first image, that is the one obtained by the interaction of the laser pulse with an isotropic sample of molecules, is described. This algorithm is a modified version of the matrix inversion method developed by T Cho and S-J Na [86]. The advantage of using this inversion method is that the relationship between the original 3D distribution and its 2D projection is expressed through a detection matrix, that can easily be incorporated in the inversion process of the second image, obtained by the interaction of the probe laser pulse with the aligned sample of molecules. The inversion process of this second image will be described in the next chapter. The limitation of the Cho-Na algorithm is that it does not handle noisy images with high accuracy, since it is based on the solution of an ill-conditioned problem. For this reason, we have implemented a regularisation method in order to improve the performance of the algorithm.

The chapter is organised as follows. Firstly, the matrix inversion method developed by T Cho and S-J Na [86] is described, then the results of some tests done to evaluate the performance of this algorithm are presented. Finally, the regularised algorithm is described and the resulting inversion of simulated and experimental images obtained with both algorithms are presented.

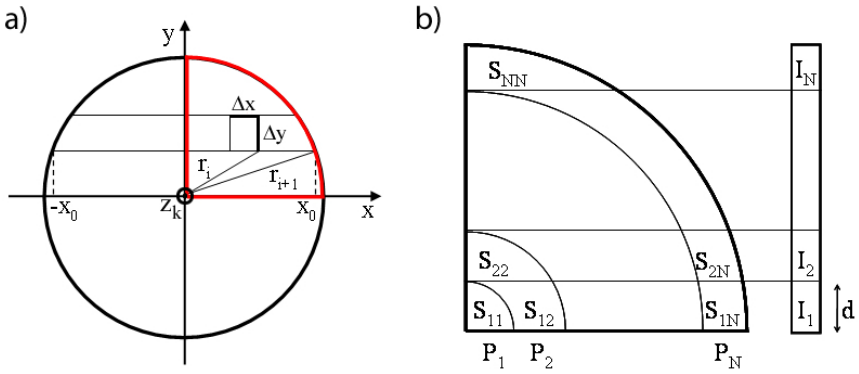

Figure 3.2: a) 2D slice of the original 3D distribution perpendicular to the z axis and passing through z_k. The red line represents the quarter of this slice which is used in the inversion process. b) Illustration of the inversion process and definition of the S matrix.

3.2 Matrix inversion of VMI images

3.2.1 Description of the Cho-Na method

A matrix inversion method, based on the Abel inversion, was introduced by Y T Cho and S-J Na in 2005 [86]. They implemented an algorithm to perform a fast calculation of the Abel inversion in order to reconstruct the emission of circularly and elliptically symmetric plasma radiation sources. This method is based on the consideration that, since a 2D projected image is a discrete distribution measured on an evenly spaced grid of CCD pixels, a matrix expression of the Abel integral can be written for each line of the image perpendicular to the symmetry axis. Assuming that z is the symmetry axis, for each value z_k the intensity of the 2D detected image, $I(y_i)$, at the pixel $(y_i,\ z_k)$ is given by the following expression:

$$I\,(y_i)\ \Delta y\ \Delta z\ =\ \sum_{j\,=\,-x_0}^{x_0}\ P\,(r_j)\ \Delta x\ \Delta y\ \Delta z \tag{3.3}$$

where $P(r_j)$, represented in cylindrical coordinates, is the intensity at the radius r_j of the 2D slice of the original 3D distribution, perpendicular to the z axis and passing through z_k as it is illustrated in Fig. 3.2. The product $\Delta x\ \Delta y\ \Delta z$ on the right side represents the volume element of the 3D original distribution having intensity $P(r_j)$. The corresponding surface element on the detector is represented by the product $\Delta y\ \Delta z$ on the left side, where Δy and Δz are the pixel bin sizes along the y and z directions of the detector. By considering that a slice of the 3D distribution of thickness equal to Δz, perpendicular to the axis of cylindrical symmetry is projected in a stripe of the same thickness on the

detector, the above equation becomes:

$$I\,(y_i)\;\Delta y\;=\;2\;\sum_{j\,=\,0}^{x_0} P\,(r_j)\;\Delta x\,\Delta y \tag{3.4}$$

where it has also been taken into account that, because of the cylindrical symmetry, summing over $j \in [-x_0,\ x_0]$ is equivalent to sum twice over $j \in [0,\ x_0]$. Although the intensity of each pixel y_i of the z_k line satisfies the previous equation, if only half of the pixels y_i with $i \in [1,\ N]$ are considered, then one single quarter of the 2D original slice corresponding to $y > 0$ and $x > 0$ (represented in Fig. 3.2), is involved in the inversion process and, for each quarter of the acquired image, the following matrix expression can be obtained:

$$d\begin{bmatrix} I_1 \\ I_2 \\ \vdots \\ I_N \end{bmatrix} = 2\begin{bmatrix} S_{11} & S_{12} & \dots & S_{1N} \\ 0 & S_{22} & \dots & S_{2N} \\ \vdots & \vdots & \ddots & \vdots \\ 0 & 0 & \dots & S_{NN} \end{bmatrix}\begin{bmatrix} P_1 \\ P_2 \\ \vdots \\ P_N \end{bmatrix} \tag{3.5}$$

where d is the pixel bin size along the y direction. By inverting this equation, the original intensity $[P]$ is obtained and it is expressed by the following linear matrix equation:

$$[P]\;=\;\frac{d}{2}\;[S]^{-1}\,[I] \tag{3.6}$$

The matrix S is an upper triangular matrix of size $[N \times N]$, with N representing the number of pixels along the y direction as shown in Fig. 3.2. Each element of this matrix represents the area of a section of the considered slice of the 3D distribution. This section is defined by the intersection of the i-th line of the measured image and the j-th radius of the 2D slice, as shown in Fig. 3.2 (b). Therefore, each element $S_{i\,j}$ is given by:

$$S_{i\,j} = \begin{cases} (A_{i,\,j} - A_{i+1,\,j}) - (A_{i,\,j-1} - A_{i+1,\,j-1}) & \text{if } i \;\leq\; j \\ 0 & \text{if } i \;>\; j \end{cases} \quad \text{with } i \text{ and } j \;\geq 1 \tag{3.7}$$

where a new matrix A has been introduced. Each element $A_{i\,j}$ of this matrix represents the area contained between the upper border of the i-th line and the upper border of the

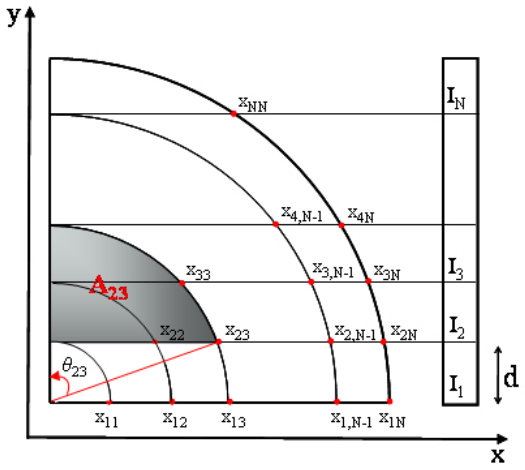

Figure 3.3: Representation of the process to construct the S matrix. The element $A_{2\,3}$ of the A matrix is illustrated (grey area) and represents the area contained between the upper border of the 2nd line and the upper border of the 3th line. $x_{i\,j}$ points, defined as the intersection point between the bottom border of the ith line of the acquired image and the jth radius of the 2D slice of the original distribution, are drawn. Also it is illustrated $\theta_{2\,3}$, which is the angle between the y axis and the line connecting the origin with the point $x_{2\,3}$.

j-th line as shown in Fig. 3.3 and can be expressed as:

$$A_{i\,j} = \begin{cases} \frac{1}{2}\left[(j\,d)^2\ \theta_{i\,j} - ((i-1)\ d)^2\ \tan\left(\theta_{i\,j}\right)\right] & \text{if } i \leq j \\ 0 & \text{if } i > j \end{cases} \quad \text{with } i \text{ and } j \geq 1 \tag{3.8}$$

where $\theta_{i\,j}$ is the angle between the y axis and the line connecting the origin with the point $x_{i\,j}$. This point is the intersection point between the bottom border of the i-th line of the acquired image and the j-th radius of the 2D slice of the original distribution, as indicated in Fig. 3.3. The expression of $\theta_{i\,j}$ is:

$$\theta_{i\,j} = \begin{cases} \arccos\left(\frac{i-1}{j}\right) & \text{if } i \leq j \\ 0 & \text{if } i > j \end{cases} \quad \text{with } i \text{ and } j \geq 1 \tag{3.9}$$

Summarising, the S matrix, which is constructed through geometrical relationships, depends only on the number of pixels N and on the pixel size d of the CCD. Therefore, this matrix can be calculated in advance and stored in a computer to help saving time in order to perform the inversion of the acquired images in real time. By knowing the S matrix, Eq. 3.6 can be solved for each line of the image perpendicular to the symmetry axis, thus retrieving a 2D vertical slice $P(r, z)$ of the original 3D distribution, lying in a

plane parallel to the detection plane corresponding to $\phi = 0$ (where ϕ is the azimuthal angle around the symmetry axis).

3.2.2 Extraction of angular and velocity distributions

The retrieved 2D distribution $P(r, z)$ incorporates the original velocity and angular distributions of the charged particles. In order to extract these distributions it is convenient to express $P(r, z)$ in spherical polar coordinates. The coordinate transformation, given by $R = \sqrt{r^2 + z^2}$, $\theta = \arctan(r/z)$, and $\phi = \phi$, allows to obtain the distribution $P_{\text{sph}}(R, \theta)$ for each given angle ϕ. In order to calculate the intensity of the distribution in spherical coordinates, a new 2D grid of size $Z = \min\{\text{N,M}\}$, with N and M representing the number of pixels on the y and z directions of the CCD respectively, needs to be created. The rows of this new grid represent the R coordinate and the columns the θ coordinate. For each element $(l,\ m)$ of the new grid the corresponding value of the distribution is given by $P_{\text{sph}}(R_l, \theta_m) = W_l\, P(r_j, z_k)$ where $P(r_j, z_k)$ represents the distribution at the position $(r_j = R_l\ \sin\theta_m, z_k = R_l\ \cos\theta_m)$, and is calculated by a bicubic spline interpolation of the values of $P(r, z)$ around that position. The weighting factor W_l is equal to R_l, being it the Jacobian of the transformation from cylindrical to spherical coordinates:

$$J \;=\; \begin{vmatrix} \frac{\partial r}{\partial R} & \frac{\partial r}{\partial \theta} \\ \frac{\partial z}{\partial R} & \frac{\partial z}{\partial \theta} \end{vmatrix}$$

The advantage of expressing the retrieved distribution in spherical coordinates is that $P_{\text{sph}}(R_l, \theta_m)$ is linked to the velocity distribution $G(R_l)$ and the angular distribution $A(\theta_m; R_l)$ through a simple relation:

$$P_{\text{sph}}(R_l, \theta_m) \;=\; G(R_l)\, A(\theta_m; R_l) \tag{3.10}$$

From this equation, the velocity distribution can be extracted by integrating $P_{\text{sph}}(R, \theta)$ across both the polar angle θ and the azimuthal angle around the symmetry axis ϕ:

$$G(R_l) \;=\; \sum_{m=0}^{Z-1} R_l \sin\theta_m P_{\text{sph}}(R_l, \theta_m) \tag{3.11}$$

where $R_l \sin\theta_m$ is the scale factor due to the integration across ϕ in spherical coordinates. For each peak in the velocity distribution, the corresponding angular distribution

$A(\theta_m; R_l)$ can be calculated by integrating the intensities $P_{\text{sph}}(R_l, \theta_m)$ over the radii $R \in [R_{\min}, R_{\max}]$:

$$A(\theta_m; R_l) = \sum_{l=l_{\min}}^{l=l_{\max}} P_{\text{sph}}(R_l, \theta_m) \tag{3.12}$$

where $l_{\min}$ and $l_{\max}$ represent the pixel indexes relative to $R_{\min}$ and $R_{\max}$, respectively. These radii define the range of velocities where the peak in the velocity distribution is found.

3.3 Performance of the method with simulated images

The algorithm was first tested with simulated images in order to compare the retrieved angular and velocity distributions with known input distributions.

3.3.1 Generation of simulated images

In order to simulate an image to be inverted, first a randomly sampled 3D distribution of charged particles with given velocity and angular distributions was generated. The charge, the mass, the source position, the kinetic energy and the initial velocity direction of each charged particle of the 3D distribution were generated through a computer code. In particular, the velocities of the particles were sampled by using the Box-Muller method [194] that allowed generating random velocity deviates with a Gaussian distribution centred on v_0 and with a σ width:

$$G(v) = \frac{1}{\sigma\sqrt{2\pi}} \exp\left(-\frac{(v - v_0)^2}{2\sigma^2}\right) \tag{3.13}$$

Then, for each velocity the corresponding kinetic energy was calculated.

For the purpose of trajectory calculation, the initial velocity direction of each charged particle was specified by azimuth (Az) and elevation (El) angles, which are the complementary angles respectively of azimuthal (ϕ) and polar (θ) angles defined in a spherical coordinate reference system. All these angles and the coordinate system in which charged particles are defined, are shown in Fig. 3.4.

The angles θ and ϕ were sampled by using the rejection method [194], which allowed generating random θ and ϕ deviates with a known and computable distribution function

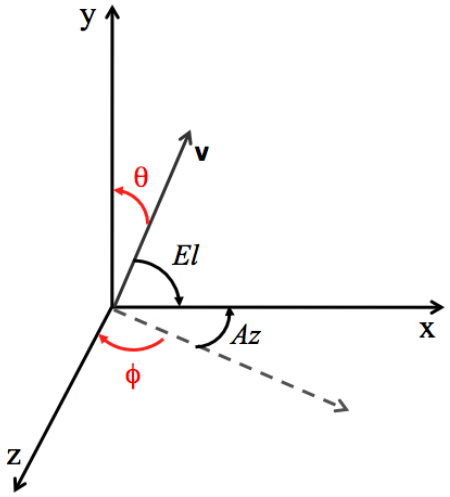

Figure 3.4: Definition of azimuth (Az), elevation (El), polar (θ), and azimuthal (ϕ) angles. The symmetry axis is y.

$A(\theta,\phi)$ given by a combination of spherical harmonics, $Y_{LM}(\theta,\phi)$:

$$A(\theta,\phi) = \sum_{l=0}^{L_{\max}} \beta_{LM} Y_{LM}(\theta,\phi) \tag{3.14}$$

where β_{LM} are called anisotropy coefficients. The corresponding Az and El angles were then calculated. All the other parameters (charge, mass, source position) had constant values for all the generated particles.

Once the 3D distribution was calculated, its 2D projection on the detection plane was obtained by means of a 3D ion trajectory simulation package (Simion 8) [195]. Details about the projection process are given in Appendix A. This procedure was used to generate synthetic images without noise (clean images) and containing single rings, corresponding to a single peak velocity distribution. Projected images corresponding to particle spheres with multi-peak Gaussian distributions were created by summation of projected images that contained single rings. In order to simulate the noisy images, which are more representative of experimental images, random noise was added to the 2D clean images in the following way. A 2D array of the same size as the simulated clean image was generated. The intensities of the pixels of each row of the 2D array were randomly sampled and varied in the range of $[-B,\ B]$, being B chosen by the user. The resulting array was then summed to the array representing the clean image and the positivity constraint was imposed, i.e. each pixel of the noisy image having a negative value was set equal to zero.

3.3.2 Calibration of the simulated VMI system

Once simulated, the 2D projected clean and noisy images were inverted using the algorithm described in section 3.2.1. The retrieved velocity and angular distributions were compared with the distributions used for the trajectory simulations to assess the program performance.

The retrieved angular distribution was fitted to a function of the form given by Eq. 3.14, and the resulting coefficients β_l were compared to those used to simulate the angular distribution of the original 3D cloud of charged particles.

The retrieved velocity distribution was fitted to a curve expressed by the following equation:

$$y = y_0 + \sum_{i=1}^{T} \frac{A_i}{w_i\sqrt{\pi/2}} \exp\left(-2\frac{(x-(x_0)_i)^2}{2w_i^2}\right) \tag{3.15}$$

where T is the number of peaks in the distribution. From this fit the peak position x_0, the width w and the area A relative to each peak of the retrieved velocity distribution were obtained. These parameters were compared to those for the simulated 2D slice of the 3D ion sphere lying in a plane parallel to the detection plane ($\phi = 0$). For comparison, this 2D slice was also created directly for the randomly sampled distribution through the simulation program described in section 3.3.1. The velocity of the particles generated by this program is expressed in millimetres per second, whereas the velocity in the retrieved distribution is expressed in pixels. Therefore, in order to be able to make a comparison between the simulated and the retrieved velocity distributions, the conversion factor (N) from millimetres per second to pixels has to be calculated. For this purpose a 2D vertical slice of an isotropic 3D original distribution, having a velocity distribution given by a combination of eight Gaussian distributions was simulated. The particles forming this slice were accelerated in the electrostatic lens, described in Appendix A, towards the detector. Then, the radial distribution of this image was calculated and the corresponding peak centre positions were plotted as a function of the peak centre positions of the original velocity distribution, as shown in Fig. 3.5. Finally, the coefficient N was obtained by applying a linear fit to the data (red line).

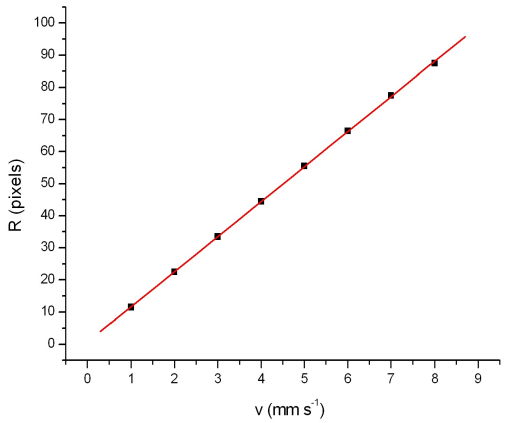

Figure 3.5: Plot of the values of the radii corresponding to the peak centre positions of the detected radial distribution as a function of the velocities corresponding to the peak centre positions of the simulated velocity distribution (square symbols). The red line shows the linear fit to the data. The slope of the fitted line, expressed in pixel $\mathrm{mm}^{-1}\,\mathrm{s}$ represents the calibration factor between the radius of the detected 2D image and the velocity of the 2D vertical slice.

3.3.3 Inversion of images without noise

The algorithm was first tested with noise free simulated images. The input images were chosen in order to examine the sensitivity of the algorithm to the number of counts per pixel and the ratio between the initial kinetic energy of the charged particles and the kinetic energy they acquire in the accelerating electric field (R_{KE}). The results of these tests are discussed below.

Effect of the number of counts per pixel

First, simulated images differing from each other only for the number of trajectories were used as input for the algorithm in order to test its sensitivity to the number of counts per pixel. The 2D input images were VMI projections on a 256×256 pixels detector of 3D ion spheres with Gaussian velocity distributions and $A(\theta) = \cos^2(\theta)$ angular distributions. These images are displayed together with the inverted distributions and the retrieved velocity and angular distributions in Fig. 3.6.

As expected, the reconstructed images present a central line noise. The intensity of this noise is comparable with the intensity of the reconstructed ring when the number of trajectories is less than or about 100000. This is the reason why in this case, the velocity and angular distributions are reconstructed with very low accuracy. By using a higher

number of trajectories, the retrieved velocity and angular distributions fit better with the distributions used for the velocity trajectories (red line in the image). For number of trajectories ≥ 1000000, the reconstructed velocity distributions do not depend on the number of ions per pixel anymore, while the accuracy in reconstructing the angular distributions keep improving with the number of trajectories. Even so, the angular distributions retrieved for a number of trajectories of 1500000 and 2000000 are very similar as it can be observed by comparing the distributions retrieved from images (e) and (f).

Effect of the ratio between the final and initial kinetic energy of the particles

Another interesting point to be tested is the behaviour of the algorithm for different ratios between the kinetic energy that the particles acquire in the electric field and their kinetic energy at the explosion, R_{KE}. This test allows determining the minimum value of R_{KE} for which the Abel integral is still a valid formulation to link the 2D projected image to the original 3D sphere. The validity of the Abel integral, in fact, is based on the assumption that the ratio R_{KE} is big.

For this purpose a 2D projected image was generated by accelerating a 3D ion sphere in the simulated VMI system (described in appendix A) with $V_{\mathrm{R}} = 1000$ V and $V_{\mathrm{E}} = 752$ V towards a detector plane constituted of 256×256 pixels. The velocity distribution of the ion sphere was given by a combination of four Gaussian distributions, each consisting of 1000000 trajectories, with a width of $\sigma = 2.8 \times 10^3$ m s^{-1}, and centred on velocity values corresponding to the kinetic energies given in table 3.1. In this table also the ratios (R_{KE}) relative to each Gaussian peak are listed. The angular distribution corresponding to each velocity peak had a $A(\theta) = \cos^2(\theta)$ distribution.

The simulated 2D image and the corresponding inverted distribution are shown together with the retrieved velocity distribution in Fig. 3.7. By comparing the retrieved velocity distribution with that used to simulate the trajectories (red line), it can be observed that the two curves overlap very well for high ratios R_{KE} (first two peaks), then as the ratio increases the overlap gets slightly worse (third peak) and much worse for the 4th

Figure 3.6 *(following page)*: In each row, from left to right, the 2D simulated projected image, the corresponding inverted image, velocity and angular distributions are shown. The 2D simulated images are projections on a 256×256 pixels detector of 3D ion spheres with Gaussian velocity distributions and $\cos^2(\theta)$ angular distributions. The retrieved velocity and angular distributions (black lines) are compared to the simulated distributions (red lines).

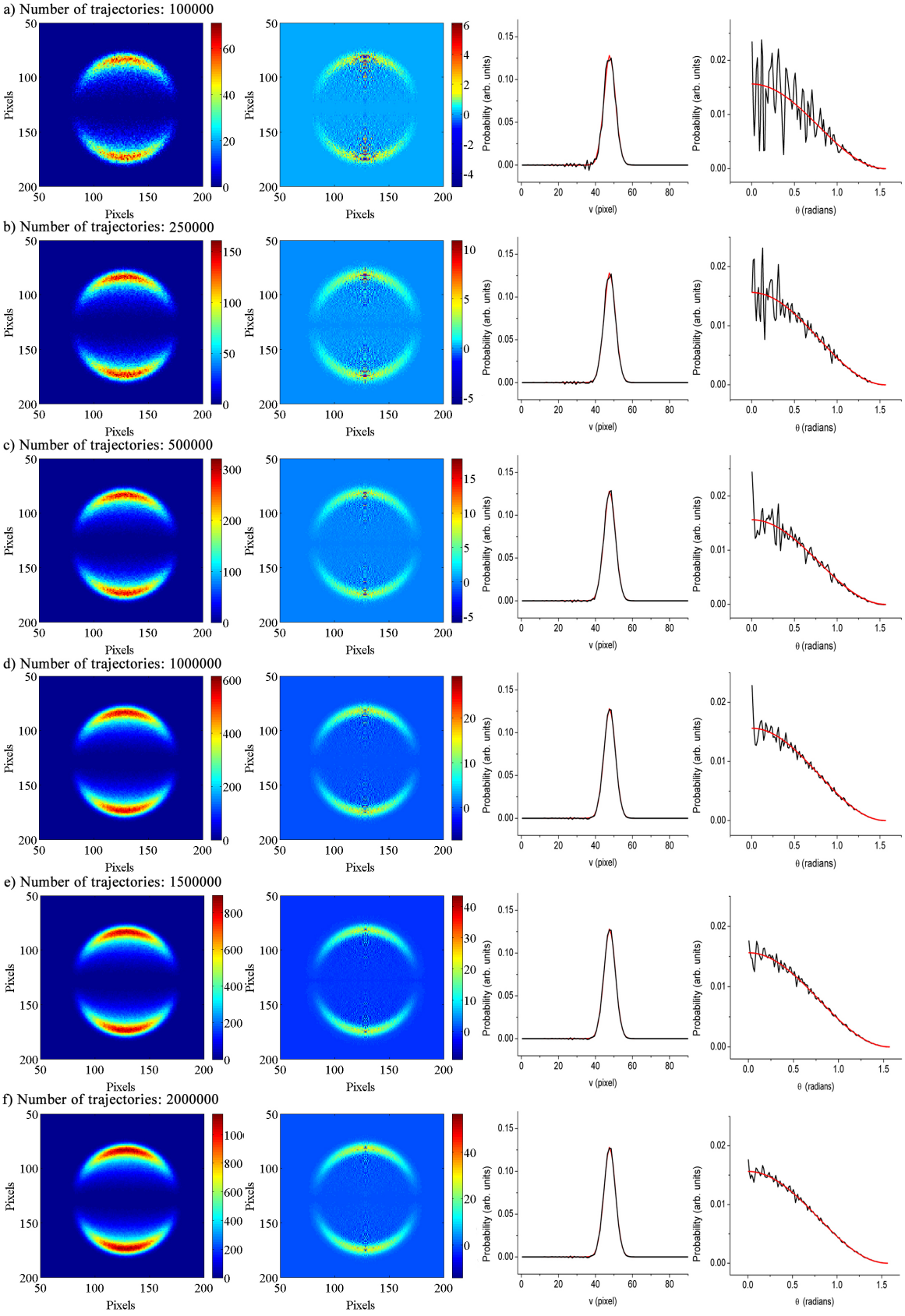
a) Number of trajectories: 100000
b) Number of trajectories: 250000
c) Number of trajectories: 500000
d) Number of trajectories: 1000000
e) Number of trajectories: 1500000
f) Number of trajectories: 2000000
Pixels
Probability (arb. units)
v (pixel)
θ (radians)

Gaussian peak	KE (eV)	R_{KE}
1	0.5	2000
2	4.5	222
3	12.5	80
4	24.5	40

Table 3.1: Kinetic energies KE expressed in eV and corresponding ratios R_{KE} for each Gaussian peak of the velocity distribution of the 3D simulated ion sphere.

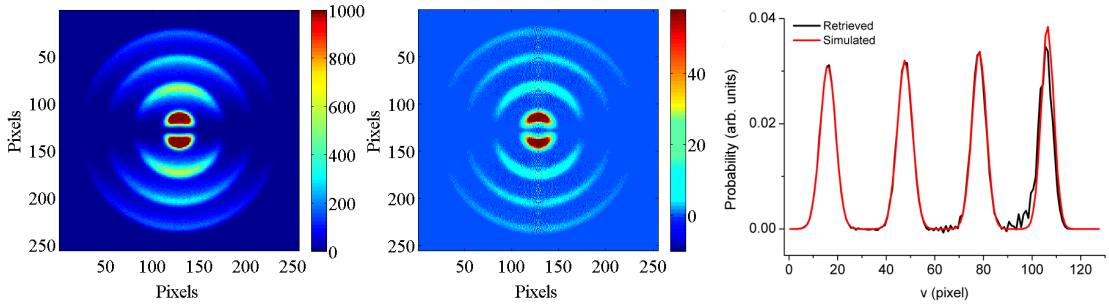

Figure 3.7: From left to right a simulated 2D projected image, the corresponding inverted image and the retrieved velocity distribution (black line) compared to the simulated distribution (red line) are shown. The simulated image is the projection on a detector of a 3D ion sphere having a velocity distribution given by a combination of four Gaussian distributions centred on velocity values corresponding to the kinetic energies given in table 3.1.

Gaussian peak. To better quantify the deviation of the retrieved velocity distribution from the simulated velocity distribution, the procedure presented in section 3.3.2 was followed. Thus, the retrieved velocity distribution was fitted to a curve expressed by Eq. 3.15 and the extracted centre positions and widths were subtracted from the values corresponding to the velocity distribution of the simulated 2D vertical slice of the 3D original distribution, in order to calculate the peak deviations. Instead, the Gaussian areas extracted from the fit were first normalised to the maximum value and then subtracted from the normalised areas of the simulated Gaussian velocity distributions, in order to calculate the peak area deviation. The resulting deviations, plotted as a function of the ion velocity, are shown in Fig. 3.8. The absolute values of the peak and width centre deviations increase with the velocity and so with decreasing R_{KE}. Also, the slope of the curves becomes steeper as the velocity increases. This is in agreement with one of the assumptions in which the validity of the Abel integral is based, *i.e* the initial kinetic energy of the particles has to be small compared to the kinetic energy they acquire in the accelerating electric field (see section 3.1). A different behaviour is followed by the peak area deviation, that although increasing slightly at the fourth peak, stays at a very low value (< 0.03) for all the velocities as

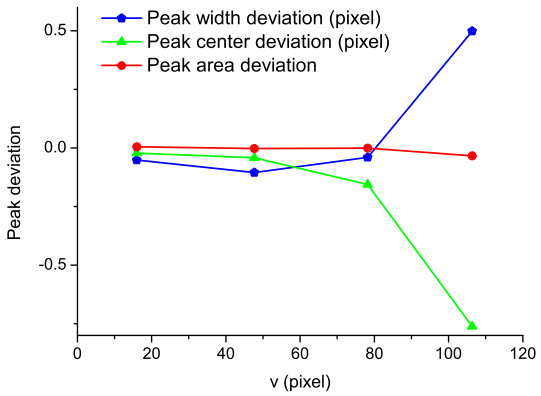

Figure 3.8: Deviation of the recovered peak centre (green line), peak width (blue line), and peak area (red line) from the corresponding values relative to the velocity peak of the 2D slice of the original 3D distribution, plotted as a function of the ion velocity.

expected since the number of ions under the retrieved peaks is unchanged.

The retrieved angular distribution was fitted to a nonlinear curve expressed by Eq. 3.14, and the obtained beta parameters, $(\beta_{00}$ and $\beta_{20})_{\text{fit}}$, were compared to those used for the trajectory simulations, $(\beta_{00}$ and $\beta_{20})_{\text{sim}}$. The resulting beta deviation $\Delta\beta$, defined as:

$$\Delta\beta = \frac{(\beta_{20})_{\text{fit}}}{(\beta_{00})_{\text{fit}}} - \frac{(\beta_{20})_{\text{sim}}}{(\beta_{00})_{\text{sim}}} \tag{3.16}$$

is plotted as a function of the velocity in Fig. 3.9. It can be observed that $\Delta\beta$ does not depend on the ratio R_{KE} in the same way as the peak width and the peak centre deviations. In fact, apart from the highest value of R_{KE} at which $\Delta\beta$ is ≈ 0.03, for the other values of R_{KE}, $\Delta\beta$ stays around the same value ≈ -0.05, implying that the angular distributions are retrieved with high accuracy even for smaller R_{KE} ratios.

3.4 Improving the performance of the algorithm: Regularisation

In the previous section it has been shown that the inversion algorithm implemented by Cho *et al.* allows retrieval of the angular and the velocity distributions from 2D projected clean images with a high accuracy if the number of particles forming the 3D sphere is of the order of 10^6 and $R_{\text{KE}} \geq 10^2$. Even if these conditions are satisfied, the algorithm does not perform so well in the case of noisy images since it is based on a straightforward solution

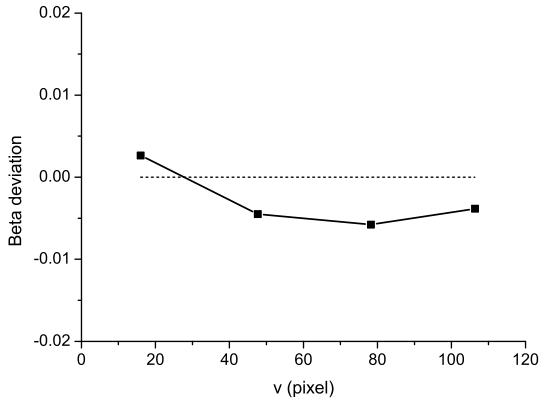

Figure 3.9: Deviation of the ratio of the beta parameters relative to the retrieved angular distribution from the ratio of the beta parameters used for the trajectory simulations.

of the inverse Abel integral, which is an ill-conditioned problem. Thus, its main drawback is the magnification of the experimental noise which is accumulated in the central line of the retrieved distributions.

In order to reduce the noise amplification the problem has to be regularised. The principle of regularisation methods is to use additional information in order to improve the condition number of the problem, thus to construct a family of approximate solutions. These solutions, that depend on a regularisation parameter (which in the case of iterative processes corresponds to the number of iterations) approach an optimal solution of the problem at a specific value of the regularisation parameter, and then diverge. This is the main property of the regularisation methods and it is known as semi convergence [196]. The use of a priori information compensate the loss of information that happens during the projection process allowing to cure the ill-posed/ill-condition nature of the inverse Abel integral.

3.4.1 Inversion of VMI images with regularisation

The regularisation routine we implemented to solve the inverse Abel problem expressed by Eq. 3.5 is based on an iterative method known as the projected Landweber method [184, 197]. The advantage of using this iterative method is that a priori information about the solution can be easily taken into account through the use of a projection operator P_C that projects the approximate solutions onto a set C of functions having the a priori known property. In the case of VMI images the a priori information is the positivity of the 3D original distribution.

The solution of the problem expressed by Eq. 3.5 is found iteratively:

$$p_{k+1} \;=\; P_C\left[p_k + \tau\left(S^T i - S^T S p_k\right)\right] \tag{3.17}$$

where k represents the number of iterations, p and i are row vectors perpendicular to the cylindrical symmetry axis of the reconstructed distribution $P(r,z)$, and acquired image $I(y,z)$ respectively, and S^T is the transpose of the S matrix. P_C is the projection operator onto the set C, and it is chosen in order to satisfy the positivity constraint expressed by:

$$\left(P_C f\right)(t) \;=\; \begin{cases} f(t) & f(t) > 0 \\ 0 & f(t) \leq 0 \end{cases} \tag{3.18}$$

τ, which is called *relaxation parameter*, has to satisfy the following condition:

$$0 \;<\; \tau \;<\; \frac{2}{\|S\|^2} \tag{3.19}$$

in order to ensure the convergence of the iterative method [197]. Therefore, τ is one of the parameters to be chosen by the user of the regularisation routine. Its effects on the solution of the problem were investigated by inverting the 2D simulated noisy image shown in Fig. 3.10 for different values of τ, and with the value of the column vector at the first iteration (p_0) equal to zero for all elements. For each τ the relative norm of the restoration error δ, defined as:

$$\delta \;=\; \frac{\left\|p_k - p^{(0)}\right\|}{\left\|p^{(0)}\right\|} \tag{3.20}$$

was plotted as a function of the number of iterations (see Fig. 3.10 (b)). In the previous equation $p^{(0)}$ represents the "exact" solution of the problem in the case of noise-free data, and for synthetic images it corresponds to the 2D simulated vertical slice of the 3D original distribution, obtained by following the procedure described in section 3.3.2. Therefore, the more accurate the reconstructed image is, the smaller is the relative norm of the restoration error.

From Fig. 3.10 (b) it can be observed that for all the τ values, the restoration error decreases steeply until reaching the same minimum value ($\delta_{\min} = 0.3443$) and then increases again - this property is referred to as "semi-convergence". The number of iterations (k_{opt}) corresponding to $\delta_{\min}$ obtained for each value of τ are reported in table 3.2. It can be

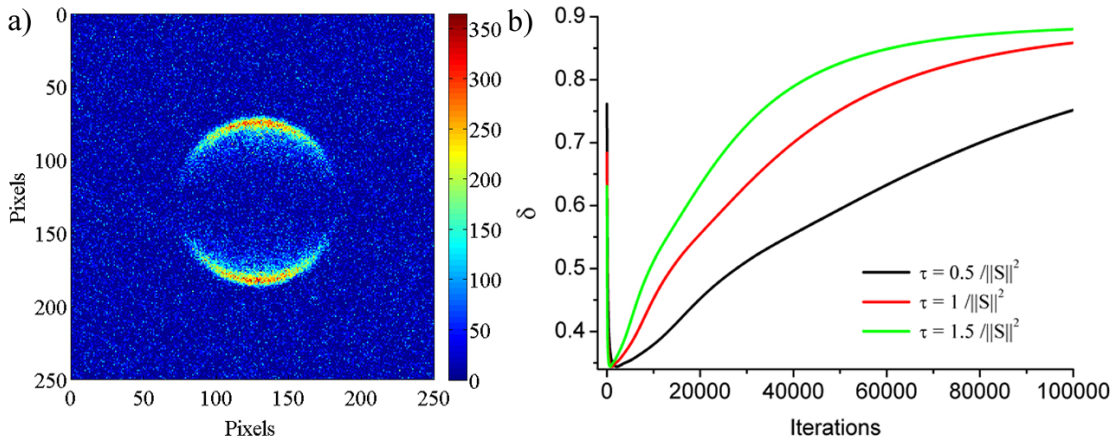

Figure 3.10: a) Simulated noisy image to be inverted. b) Behaviour of the restoration error as a function of the number of iterations resulting from the inversion of the image shown in panel a) by using different values of τ: $\tau = 0.5/\left\|S\right\|^2$ (black line), $\tau = 1/\left\|S\right\|^2$ (red line), and $\tau = 1.5/\left\|S\right\|^2$ (green line). The vector columns used for the first iterations are $p^{(0)}$

τ	k_{opt}
$0.5/\left\|S\right\|^2$	2140
$1/\left\|S\right\|^2$	1060
$1.5/\left\|S\right\|^2$	720

Table 3.2: Optimal number of iterations obtained for different values of τ.

observed that by increasing τ in the range defined by Eq. 3.19, the optimal number of iterations decreases and so the convergence process is accelerated. In order to ensure the convergence of the process a value of τ not too close to the upper limit of the convergence range ($\tau = 1/\left\|S\right\|^2$) was used to perform the inversions presented in this thesis.

The initial guess p_0 is another parameter that has to be chosen. The influence of p_0 on the solution was investigated by inverting the image shown in Fig. 3.10 with different p_0 and analysing the behaviour of the restoration error. The behaviour of the restoration errors as a function of the number of iterations are shown in Fig. 3.11, while the values of δ_{min} and the corresponding k_{opt} for all the p_0 used in the inversions are listed in table 3.3.

From this analysis it emerges that the inverted distributions obtained with p_0 set to either the image to be inverted or the image inverted with the non regularised method are not very accurate. In these cases δ_{min} is very high compared to that obtained in the other two cases, and is reached after few iterations, i.e the resulting image corresponds to an

p_0	$\delta_{\min}$	k_{opt}
0 for all elements	0.344	1080
1 for all elements	0.364	1260
image to be inverted	0.676	20
image inverted without the regularisation routine	0.828	20

Table 3.3: Values of $\delta_{\min}$ and the corresponding k_{opt} obtained for all the different p_0 used to test the inversion algorithm.

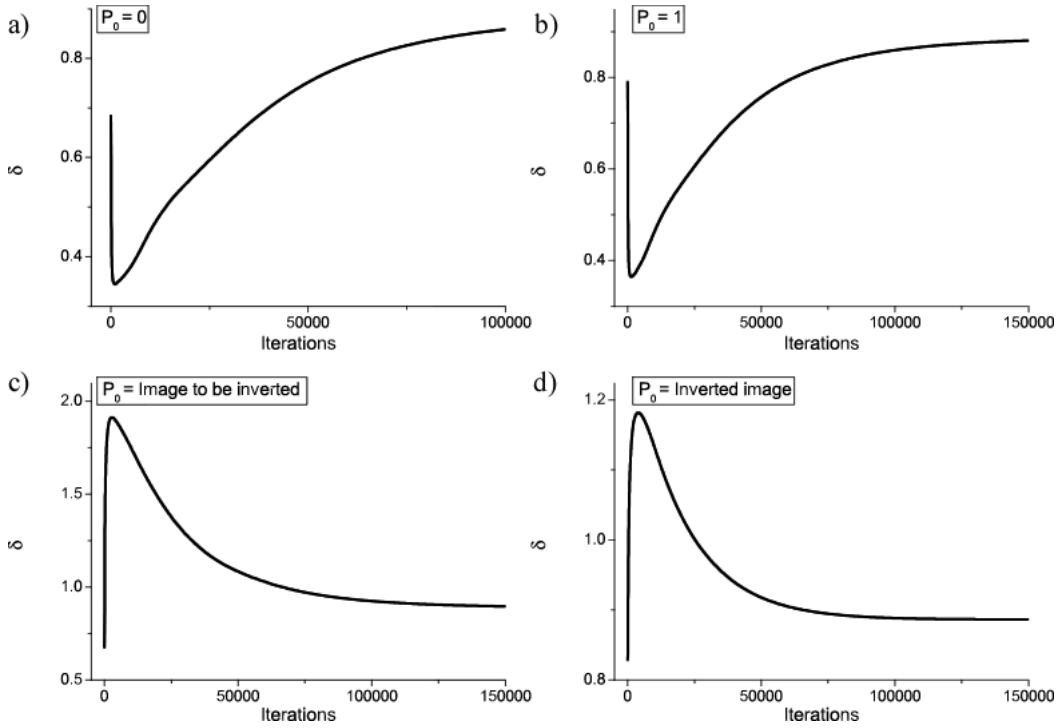

Figure 3.11: Behaviour of the restoration error as a function of the number of iterations, obtained by using a value of the relaxation parameter of $\tau = 1/\|S\|^2$ for different vector columns corresponding to the first iteration (p_0), indicated in the picture itself.

image very close to p_0. In fact, in these two cases (see Fig. 3.11 (c) and (d)) the solution of the inversion problem does not exhibit the semi-convergence, which is the main property of the regularised solutions. Better results are obtained in the other two cases. However, p_0 with all the elements equal zero was used as vector column for the first iteration in all the inversions presented in this thesis, since $\delta_{\min}$ obtained in this case is slightly smaller than that obtained by setting all the elements of p_0 equal one.

3.4.2 Convergence criterion for regularisation

In the previous section the restoration error, defined in Eq. 3.20, has been introduced in order to determine the optimum number of iterations k_{opt}. However, for real images the solution of the problem in the case of noise-free data ($p^{(0)}$) is not known, and so the calculation of the restoration error is not possible. Therefore, a different method for estimating k_{opt} is needed.

Many methods ("stopping rules") have been introduced in the past [184, 198]. Some of these methods require a priori knowledge of one of these quantities: i) the square norm of the solution of the problem in the case of noise-free data, $\left\|p^{(0)}\right\|^2$ [184]; ii) the square norm of the difference between the computed image, given by the product between the S matrix and the retrieved distribution P, and the acquired image I, $\|SP - I\|^2$, as in the case of the discrepancy principle [199]; iii) both a bound on $\left\|p^{(0)}\right\|^2$ and on $\|SP - I\|^2$, as in the Miller method [200]. However, very often these quantities are not known, as for example in the case of the experimental images presented in this thesis. Therefore, a method which does not require this kind of information has to be used. One such method is called generalised cross validation [201, 202]. The basic assumption of this method is that the acquired image is symmetric with respect to the origin, so that the acquired image can be partitioned in very similar quarters. One of these quarters is used as a test set to validate the result from the inversion of the other quarters. Since the experimental images analysed in this thesis are not symmetric with respect to the origin, due to damage present on the MCP, this stopping rule cannot be applied.

We used another stopping rule, called the "interactive method" [184], which is based on the intuition of the user in selecting the best restored image. In order to define a criterion for choosing the optimal solution, we investigated the evolution of the solution with the number of iterations for two different simulated input images. The use of simulated images allows having also an independent estimation of the optimal number of iterations from the calculation of the restoration error.

The first test was done by inverting the 2D projected image shown in Fig. 3.12 for different numbers of iterations. The resulting reconstructed images are shown in Fig. 3.13. From this figure it emerges that performing too few iterations results in a loss of resolution in the central line of the inverted image, whilst iterating for too long implies that the noise dominates the central line of the inverted image. This effect is clearer in the retrieved an-

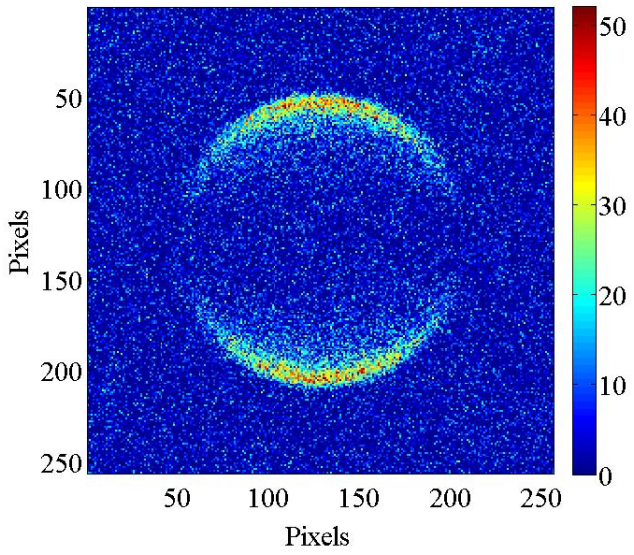

Figure 3.12: Image to be inverted obtained by adding random noise to a simulated clean image, corresponding to the projection of a 3D ion sphere on a detector plane. The ion sphere consists of 500000 trajectories and has a Gaussian velocity distribution centred on a velocity value corresponding to $KE = 12.5$ eV, and with a width $\sigma = 2.8 \times 10^3$ m s^{-1}, and an angular distribution given by $A(\theta) = \cos^2\theta$. The maximum value of the random noise added to the clean image is 15% of the peak intensity of the image itself.

gular distributions (see Fig. 3.14), where it can be noted that for a number of iterations smaller than 2000 the retrieved angular distribution around $\theta = 0$ decreases with the number of iterations, whilst this behaviour is reversed for a number of iterations bigger than 2000. Thus, we consider 2000 as the optimal number of iterations. The optimal number of iterations estimated with this method is in good agreement with that corresponding to the minimum value of the restoration error, which resulted to be 1450. The retrieved angular distributions are shown in Fig. 3.14. This figure confirms that the biggest effect of changing the number of iterations is the reconstruction of the central line of the image. In fact, apart from the case of a very small number of iterations (k = 300), the reconstructed angular distributions differ from each other mainly in their behaviour around the central line of the reconstructed image. Therefore, a zoomed image of the retrieved angular distribution around $\theta = 0$ is shown in Fig. 3.14 (b). In conclusion, the optimal solution is obtained when the behaviour of the retrieved angular distribution around $\theta = 0$ reverses by increasing the number of iterations.

In order to check if this definition holds true in the case where the velocity distribution of the 3D ion cloud has many Gaussian peaks, a noisy image with a velocity distribution

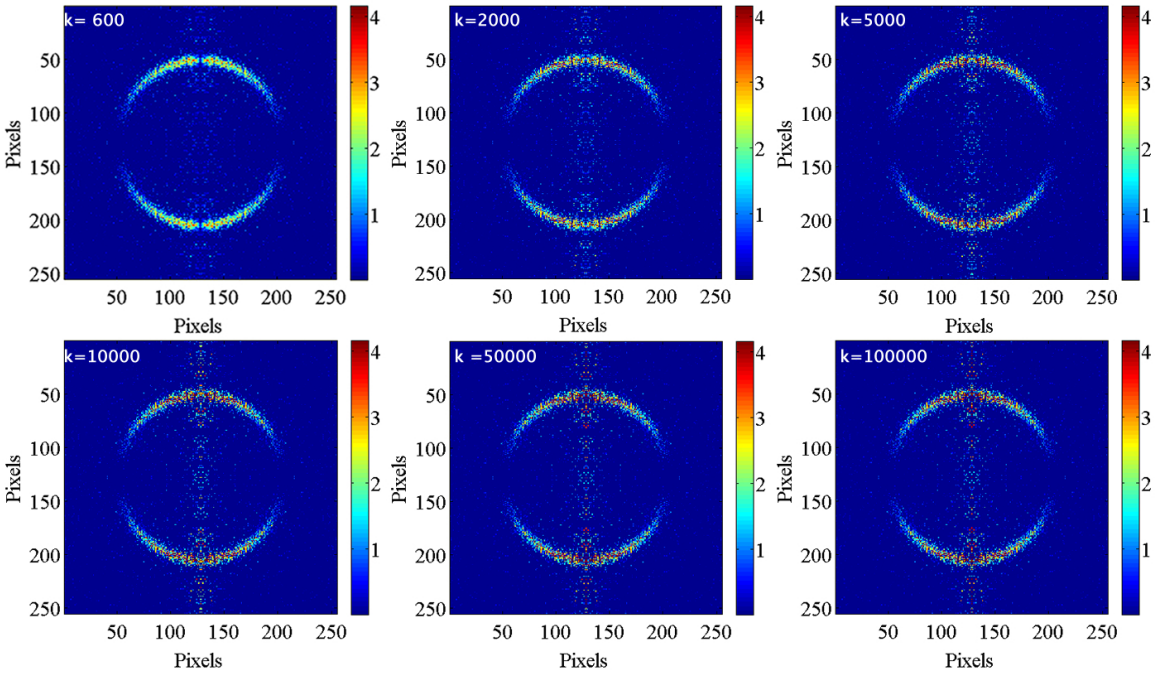

Figure 3.13: Inverted images, reconstructed by using the regularised algorithm, for different numbers of iterations (k). The 2D image to be inverted is shown in Fig. 3.10

given by a combination of three Gaussian distributions, shown in Fig. 3.15, was inverted for different numbers of iterations. The reconstructed images are shown in Fig. 3.16. In this case the minimum value of the restoration error was obtained after 68800 iterations. Again, the most evident effect on the inverted images is the reconstruction of the central line. In particular the lower the energy of the ions is, the more sensitive is the reconstructed angular distribution to the number of iterations. The angular distributions relative to each velocity peak, retrieved for different numbers of iterations, and zoomed in around $\theta = 0$ are shown in Fig. 3.17. An interesting effect can be observed in this figure. The angular distribution corresponding to the ring with the lowest energy (panel (a) in the figure) behaves in the same way as the angular distribution shown in Fig. 3.14. In particular, also in this case, the optimal number of iterations chosen with the interactive method coincides with the value that minimises the restoration error. However, the angular distributions corresponding to the other rings do not give the same result. The farther the ring is from the centre, the smaller is the number of iterations which gives the optimal solution according to the criteria defined above. This effect shows that the experimental noise in the reconstructed image accumulates in the central line, and increases from the outer ring towards the centre of the image with increasing number of iterations.

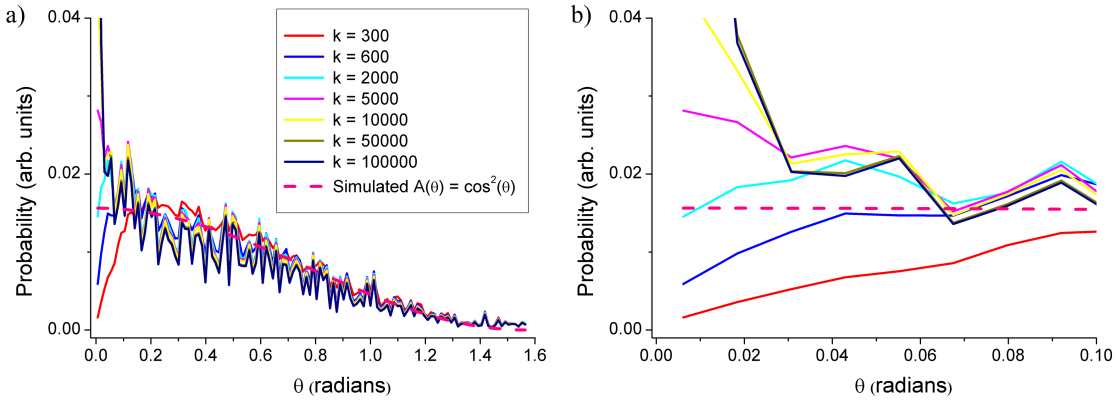

Figure 3.14: a) Angular distributions retrieved from Fig. 3.10, by using the regularised algorithm, for different number of iterations. b) Zoom of the retrieved angular distributions around $\theta = 0$.

Gaussian peak	KE (eV)	R_{KE}	Angular distribution
1	0.5	4000	$\cos^2\theta$
2	4.5	444	$\cos^4\theta$
3	12.5	160	$\cos^6\theta$

Table 3.4: Kinetic energy KE expressed in eV, ratio R_{KE} and angular distribution relative to each peak of the velocity distribution of the 3D simulated ion sphere.

In conclusion, for images with multi peak velocity distributions, the interactive stopping rule was applied by analysing the behaviour of the angular distribution corresponding to the inner ring of the image.

3.4.3 Performance of the regularised method with simulated images

As expected, the use of the regularised method to perform the inversion of noiseless images gives very similar results as in the case when the non-regularised algorithm is used. On the other hand, a remarkable improvement is obtained by regularising the problem for noisy input images. In order to show this, the results of the inversion of a noisy image, obtained by using both algorithms are presented. The image is obtained by adding random noise to a 2D projected clean image corresponding to a 3D sphere with a velocity distribution given by a combination of three Gaussian distributions. The characteristics of each Gaussian distribution are listed in table 3.4.

The peak intensity of the random noise added to this clean image is 10% of the peak intensity of the image itself. This noisy image is shown together with the resulting inverted distributions in Fig. 3.18. The noise is not amplified in the image inverted with the

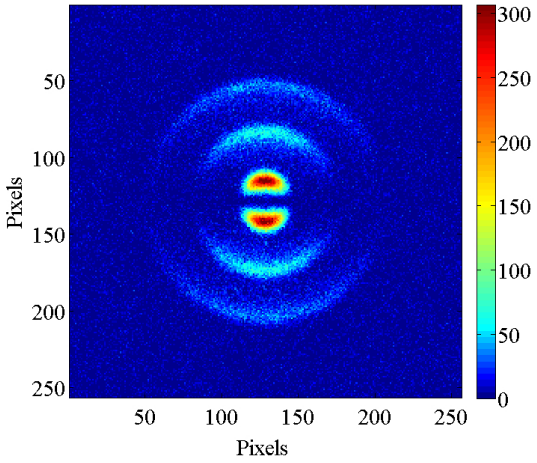

Figure 3.15: Image to be inverted, obtained by adding random noise to a simulated clean image, corresponding to the projection of a 3D ion sphere on a detector plane. The velocity distribution of the ion sphere is given by a combination of three Gaussian distributions, each consisting of 500000 trajectories, with a width of $\sigma = 2.8 \times 10^3$ m s^{-1}, and centred on velocity values corresponding to kinetic energies of 0.5 eV, 4.5 eV, 12.5 eV, respectively. The angular distribution corresponding to each velocity peak had a $A(\theta) = \cos^2(\theta)$ distribution. The maximum value of the random noise added to the clean image is 15% of the peak intensity of the image itself.

regularised algorithm, where the central line noise is much less intense than in the image inverted with the other algorithm. Also in the regularised retrieved image, the contrast between the reconstructed rings and the background is much higher. These are the reasons why the velocity distribution retrieved with the regularised method is much less noisy. The retrieved velocity distributions obtained by using both algorithms are shown in Fig. 3.19, while the retrieved angular distributions corresponding to each Gaussian peak obtained by inverting the image with non regularised (top panels) and regularised (bottom panels) algorithms are shown in Fig. 3.20. It can be observed that a big improvement is obtained in the retrieved angular distributions by using the regularised algorithm. The angular distributions retrieved with the regularised algorithm are, in fact, much less noisy than those obtained with the non regularised algorithm, since the noise is not amplified toward the central line of the retrieved image when regularisation is used.

3.5 Application to Coulomb explosion imaging

In order to test the performance of both the Cho-Na and the regularised algorithms in inverting experimental images, we acquired some data by using the experimental setup

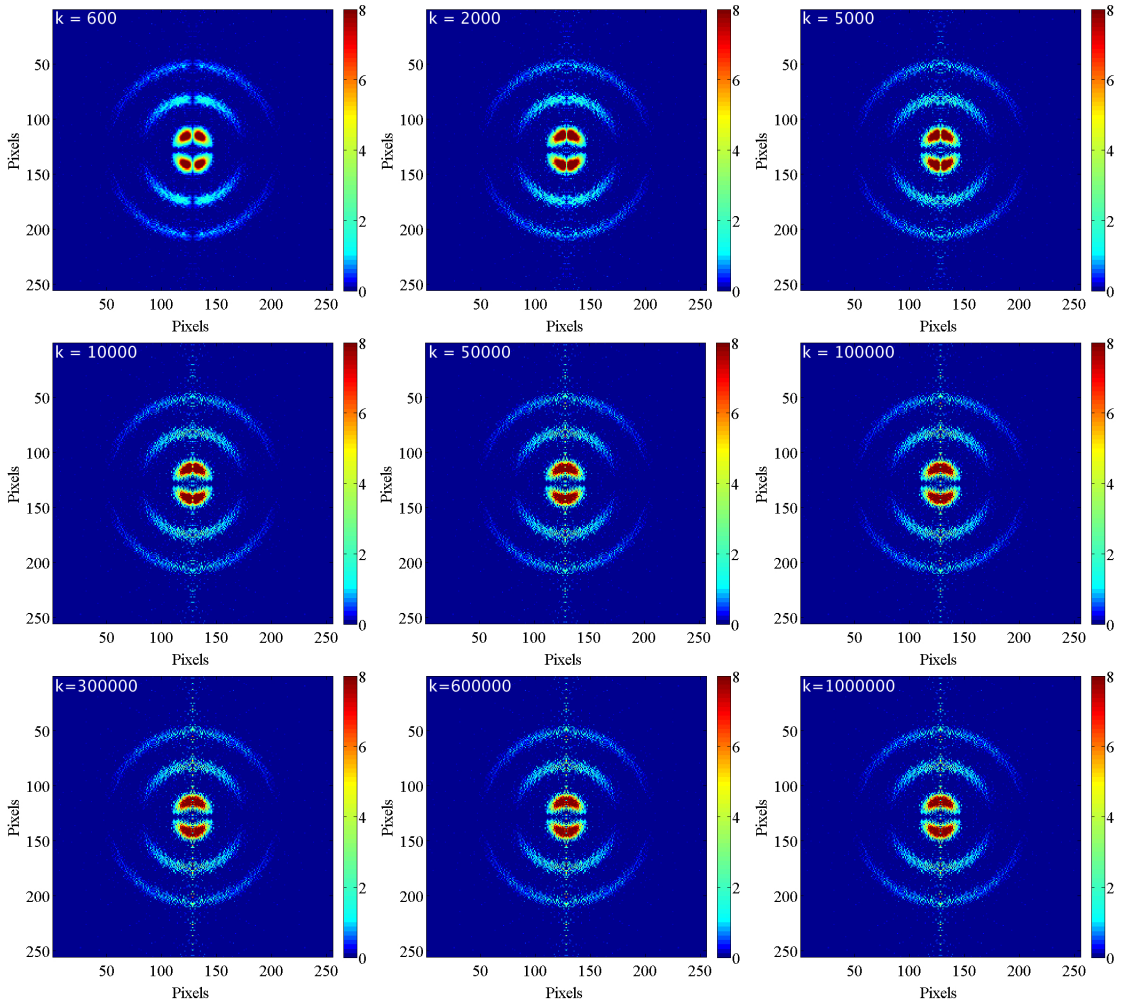

Figure 3.16: Inverted images, reconstructed by using the regularised algorithm, for different numbers of iterations (k). The 2D image to be inverted is shown in Fig. 3.15

described in Chapter 2. In particular, only the hollow fibre compressed beam was used in this experiment to initiate Coulomb explosion of a sample of isotropic N_2 molecules. The backing pressure of the N_2 molecular gas was $P_b = 1.2$ bar, and the gas jet operated at a repetition rate of 100 Hz with an opening time of 200 μs. Images were acquired for both linear and circular polarisation of the laser pulse, whose intensity at the interaction point was $I = (1.7\pm0.5)\times10^{15}$ W cm^{-2} for circular polarisation and $I = (5\pm0.3)\times10^{14}$ W cm^{-2} for linear polarisation. The temporal duration of the probe laser pulse was measured with a SHG FROG and resulted to be $\tau_{\text{probe}} = (13.5\pm0.5)$ fs for both polarisations. The Coulomb exploded ions, generated during the interaction of the laser pulse and the molecular beam, were accelerated towards the detector in the electric field generated by applying $V_R = 1$ kV and $V_E = 0.75$ kV voltages on the VMI electrodes. The MCP was gated in time in order to

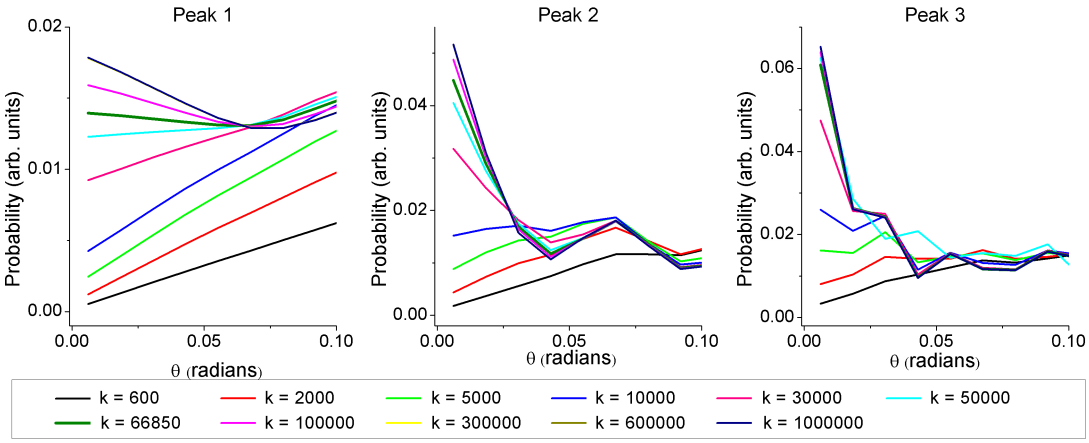

Figure 3.17: Zoom around $\theta = 0$ of the angular distributions relative to the velocity peaks of the inverted images shown in Fig. 3.16. Peak 1, peak 2, and peak 3 are centred on velocity values corresponding to kinetic energies of 0.5 eV, 4.5 eV, 12.5 eV, respectively. The angular distributions are retrieved by using the regularised algorithm, for different number of iterations.

detect only the N^+ ions, and operated at a repetition rate of 100 Hz. Each acquired image corresponded to an average over $2{\times}10^4$ laser shots interacting with the same number of molecular gas pulses. Two typical images acquired with a linearly or circularly polarised laser pulse, and with background subtracted (image acquired without the gas jet firing), are shown in Fig. 3.21 (a) and (b), respectively. The mask placed after the TOF tube to protect the MCP (see Chapter 2 for details) as well as the damaged areas of the MCP are clearly visible at the centre of both images. In particular, two horizontal lines corresponding to a low sensitivity of the MCP and having a vertical thickness of a few pixels, are visible. One horizontal line lies on the top part of the image at a vertical position around 150 pixels, while the other line, thicker than the previous, lies on the bottom of the image at a vertical position around 270 pixels. By comparing the two images, it can be noted that the angular distribution of the ions is different in the two cases. Although the sample of molecules is isotropic, the ion distribution is peaked along the polarisation direction of the laser pulse (vertical axis) in the case of linear polarisation, since in this case the ionisation rate is maximum along the direction of the laser field. In the case of circular polarisation, instead, the ion distribution is more isotropic. Before performing the inversions, the centre position of the images were determined through the algorithm described in Appendix B. Then, each quarter of the images was inverted separately.

We first present the analysis of the image acquired with a linearly polarised laser pulse

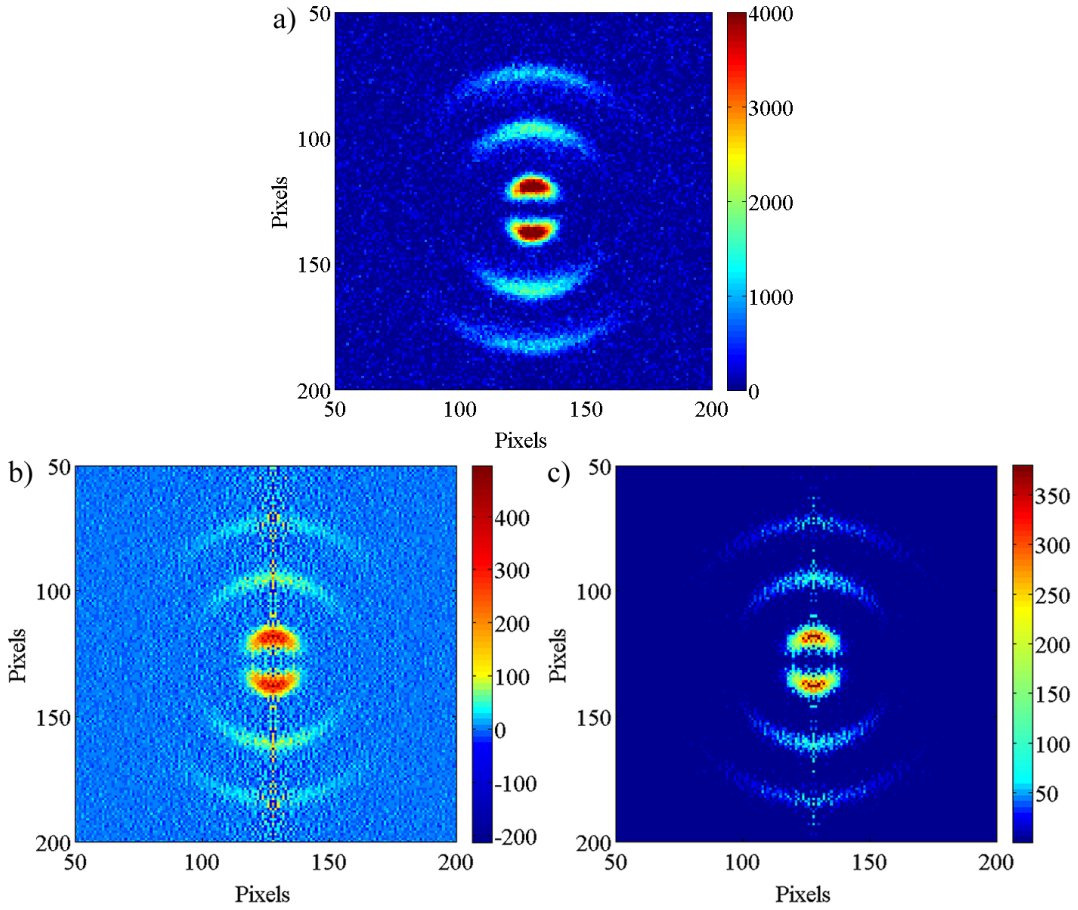

Figure 3.18: (a) Simulated 2D projected noisy image to be inverted. Inverted images obtained by using the non regularised inversion algorithm (b) and the regularised inversion algorithm (c).

(Fig. 3.21 (a)). The inverted images obtained by using the Cho-Na and the regularised algorithm are shown in Fig. 3.22 (a) and (b), respectively. The most striking differences between the two images are in the central parts. When the regularised algorithm is used, no noise is accumulated in the inner part of the ion distribution where all pixel intensities are zero (Fig. 3.22 (b)). On the contrary, the image obtained by using the Cho-Na algorithm is very noisy in the central part where the protecting mask is visible and the central line noise is very intense (Fig. 3.22 (a)). In this case the signal to noise ratio is much lower than when the regularised algorithm is used, which is in agreement with the results obtained from the inversion of simulated images.

From each quarter of the inverted images the radial and angular distributions were extracted. The radial distributions are shown in Fig. 3.23, where the black and red lines refer to the radial distribution retrieved from the image inverted with the Cho-Na and the regularised algorithms, respectively. The radial distributions obtained by using the

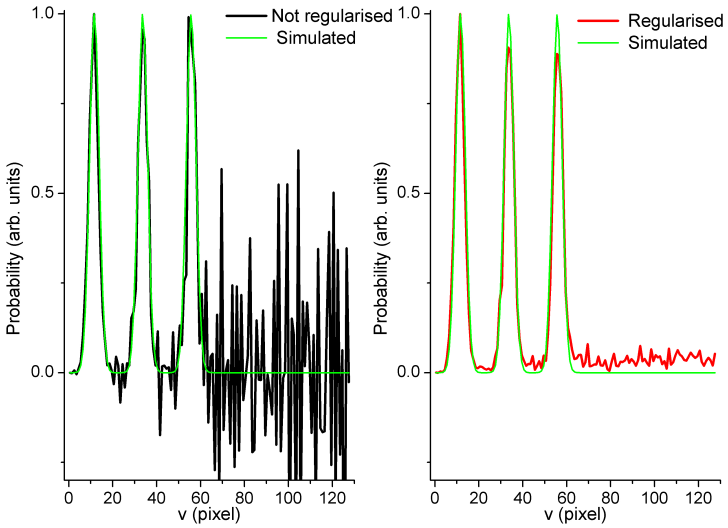

Figure 3.19: Retrieved velocity distribution from the inverted images shown in Fig. 3.18. a) Velocity distribution retrieved by using the non regularised algorithm. b) Velocity distribution obtained by means of the regularised algorithm. The simulated velocity distribution is represented by the green line in both panels.

regularised algorithm are zero for the central part of the inverted image, $R \in [0,\ 75)$, whilst the distributions obtained by using the Cho-Na algorithm assume zero values for the radii corresponding to the presence of the mask ($R \in [0,\ 20]$), and then the distributions assume negative values for the radii $R \in (20,\ 75)$, due to the noise in the reconstructed image, as already observed in Fig. 3.22 (a). For higher values of the radii, the same modulations of the radial distributions are obtained with both algorithms. However, the damaged lines of the MCP are more evident in the radial distributions obtained with the Cho-Na method, particularly for quadrants III) and IV) of the image (see Fig. 3.23) where the bumps at a radius of around 90 pixels are more pronounced with respect to those reconstructed through the regularised algorithm. Also, it can be noted that for $R > 130$ pixels, the radial distributions reconstructed with the Cho-Na algorithm are noisier.

The improvement of the inverted images obtained by using the regularised algorithm is more evident in the angular distributions retrieved from each quadrant of the images of Fig. 3.22. These distributions are plotted as functions of the angle θ, defined as the angle between the ion position and the axis of cylindrical symmetry, in Fig. 3.24. It can be noted, particularly in quadrants I and IV, that the centre line noise is much less intense when the regularised algorithm (red lines) is used. In this case in fact, the angular distribution around $\theta = 0$ does not decrease steeply as it happens when the Cho-Na algorithm is used (black lines). Furthermore, it can be observed that the angular distributions retrieved

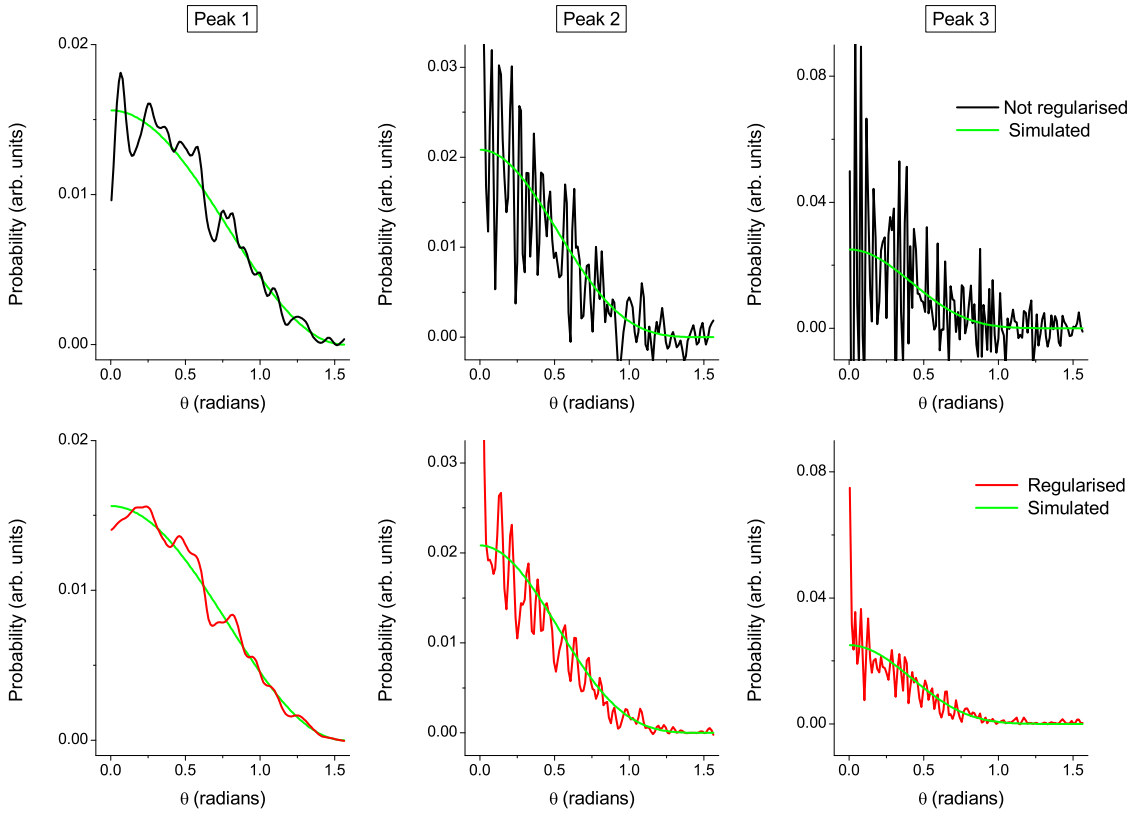

Figure 3.20: Retrieved angular distributions relative to each ring of the inverted images shown in Fig. 3.18, obtained by using the non regularised algorithm (black lines), or the regularised algorithm (red lines). The simulated angular distributions are represented by the green lines.

from the four quadrants are very different from each other, due to the poor quality of the images acquired.

We performed the same analysis for the image acquired with a circularly polarised laser pulse (Fig. 3.21 (b)), and obtained similar results. The inverted images obtained by using the Cho-Na or the regularised algorithm are shown in Fig. 3.25 (a) and (b), respectively. Since in this case the axis of cylindrical symmetry is parallel to the direction of propagation of the laser pulse, the noise accumulates towards the horizontal central line of the image in correspondence to the metallic bars holding the mask. As for the case of linear polarisation, also in this case a big improvement in the inverted image is obtained when the regularised algorithm is used. This can be observed in particular by looking at the retrieved angular distributions shown in Fig. 3.26. Regarding the retrieved radial distributions shown in Fig. 3.27, the same observations made in the case of linear polarisation hold true also in this case.

In conclusion, the inversion of experimental images confirm the results obtained from

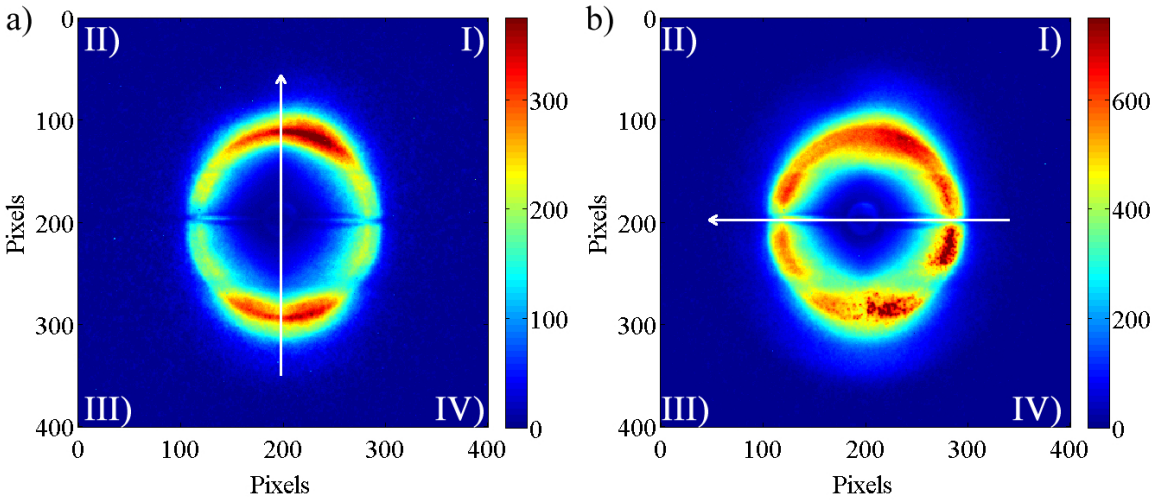

Figure 3.21: Experimental images acquired from a sample of N_2 molecules with: a) linear polarisation; b) circular polarisation of the laser pulse. The estimated average intensity of the laser pulse, based on beam characterisation measurements, is a) $I = (5 \pm 0.3) \times 10^{14}$ W cm^{-2} and b) $I = (1.7 \pm 0.5) \times 10^{15}$ W cm^{-2}. The arrows represent the axes of cylindrical symmetry. The four quadrants of each image are indicated.

the inversion of simulated images, i.e the use of the regularised algorithm allows reconstructing the original ion distribution with a higher accuracy than that obtained when the Cho-Na method is employed.

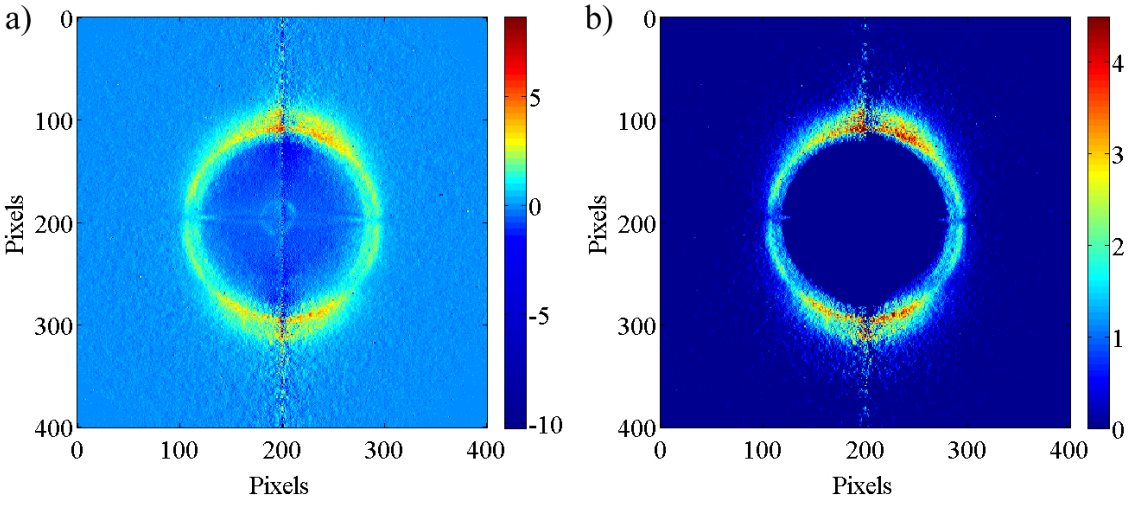

Figure 3.22: Reconstructed 2D slices of the 3D ion cloud, obtained by inverting the acquired image shown in Fig. 3.21 (a) by using a) the Cho-Na algorithm, b) the regularised algorithm

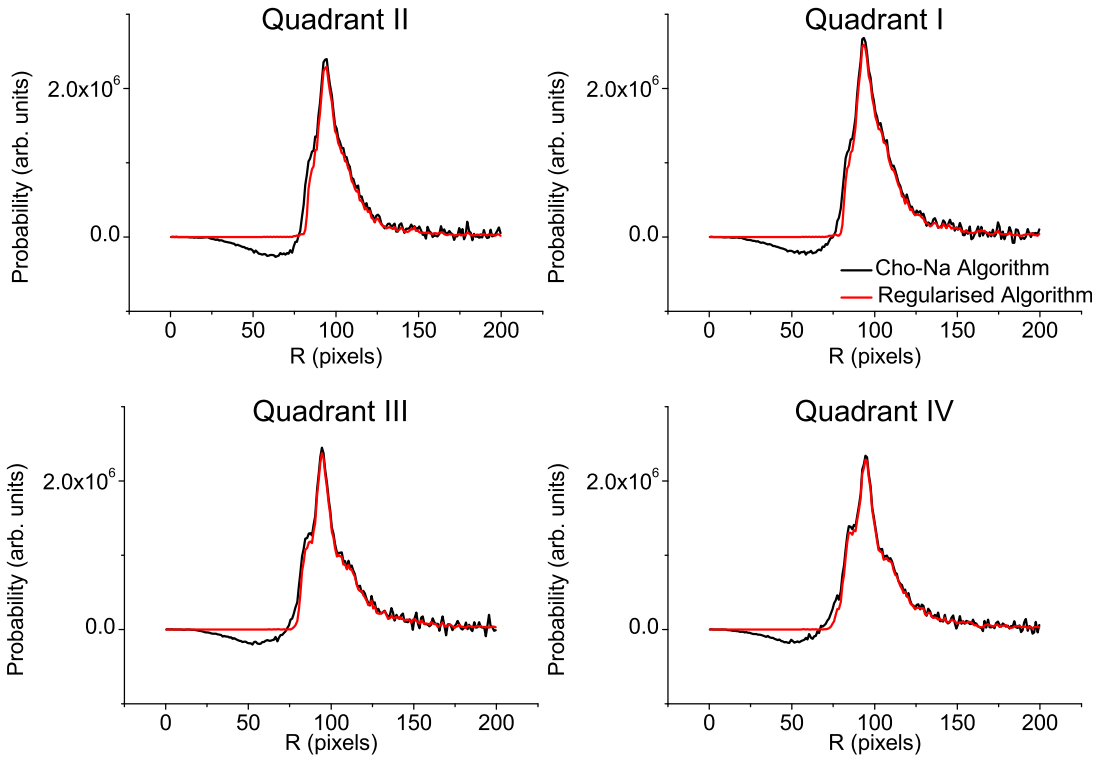

Figure 3.23: Retrieved radial distributions extracted from each quadrant of the image shown in Fig. 3.22, inverted with the Cho-Na algorithm (black lines) and the regularised algorithm (red lines)

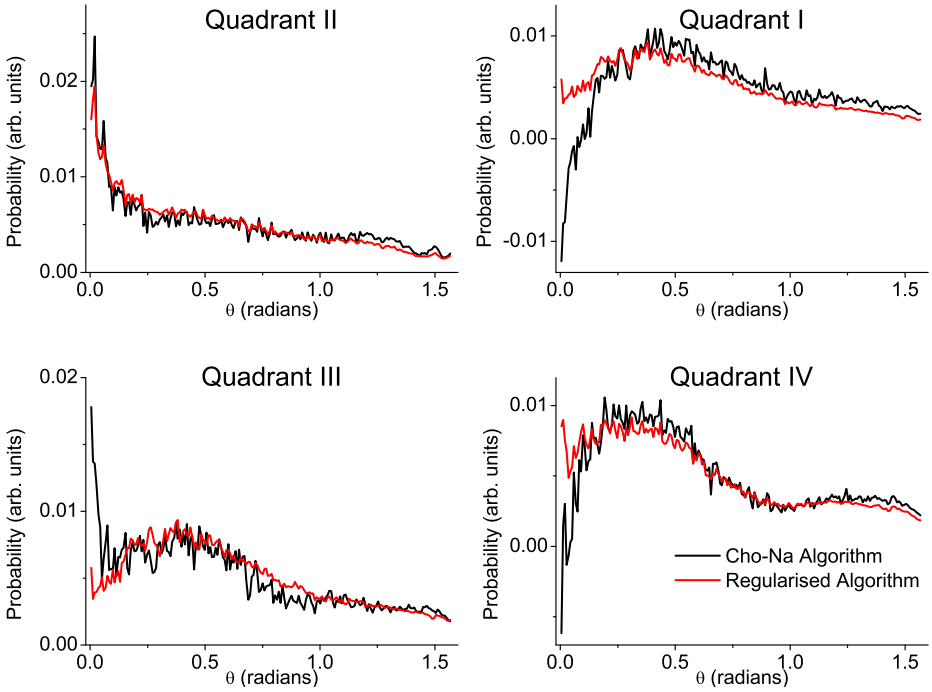

Figure 3.24: Retrieved angular distributions extracted from each quadrant of the image shown in Fig. 3.22, inverted with the Cho-Na algorithm (black lines) and the regularised algorithm (red lines)

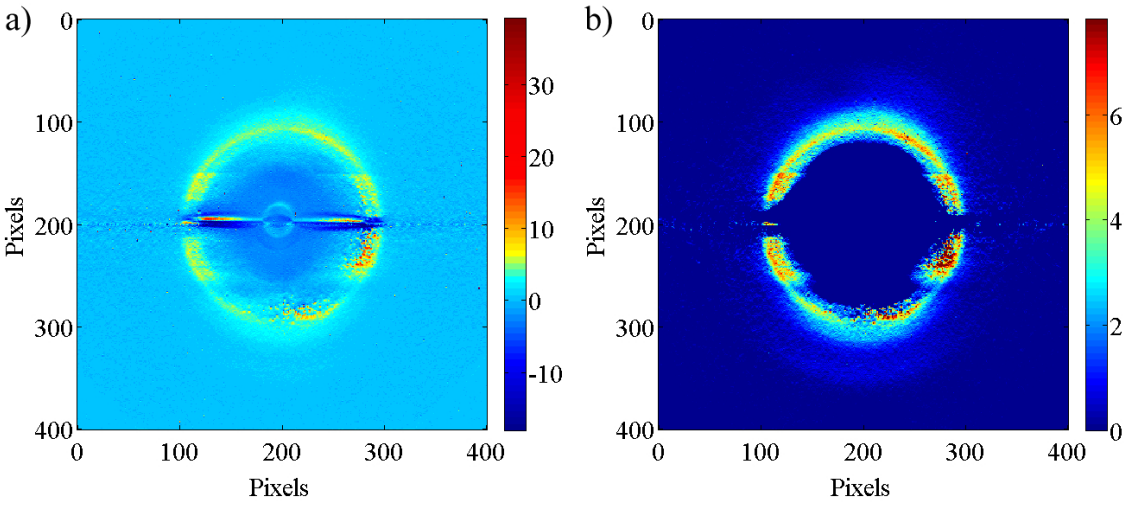

Figure 3.25: Reconstructed 2D slices of the 3D ion cloud, obtained by inverting the acquired image shown in Fig. 3.21 (b) by using a) the Cho-Na algorithm, b) the regularised algorithm

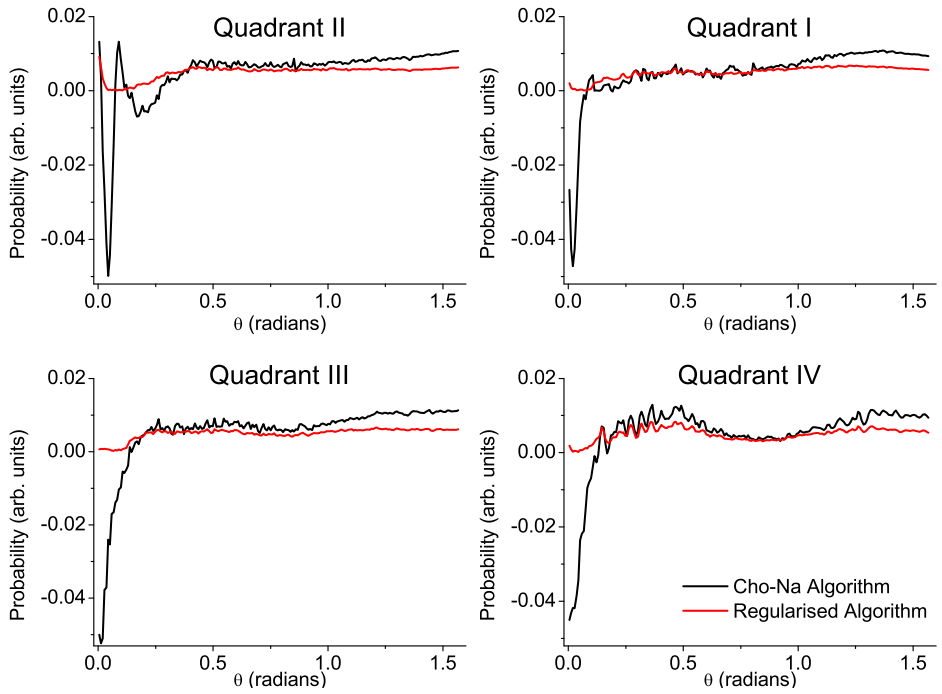

Figure 3.26: Retrieved angular distributions extracted from each quadrant of the image shown in Fig. 3.25, inverted with the Cho-Na algorithm (black lines) and the regularised algorithm (red lines)

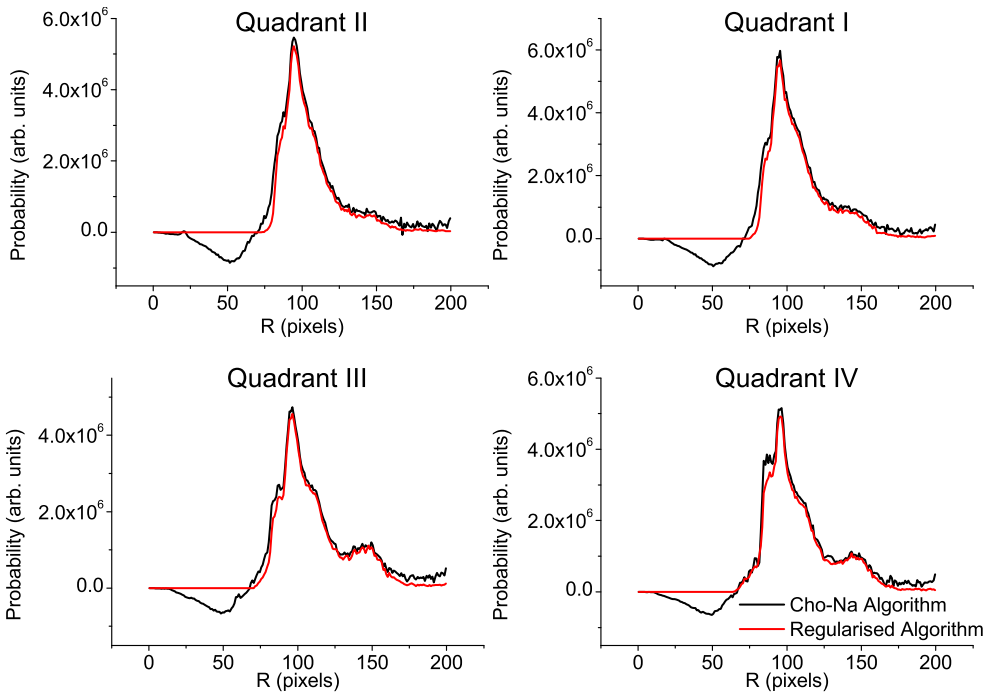

Figure 3.27: Retrieved radial distributions extracted from each quadrant of the image shown in Fig. 3.25, inverted with the Cho-Na algorithm (black lines) and the regularised algorithm (red lines)

Chapter 4

Retrieval of molecular axis alignment from Coulomb explosion imaging experiments

In the last decade many experiments aiming to probe laser induced molecular axis alignment have been performed [32–39, 46]. Frequently the alignment was probed by velocity map imaging of the Coulomb exploded ions generated following the interaction of the probe laser field with a sample of aligned molecules [37–39, 46]. In order to obtain the molecular axis distribution, the VMI image needs to be inverted. The inversion could be performed by using one of the existing inversion algorithms [77–86] if the 3D cloud of ions had an axis of cylindrical symmetry lying in a plane parallel to the detection plane. However, due to an orientational dependence of ionisation [87], the probe laser pulse does not ionise all the molecules with the same probability. As a consequence, the angular distribution of ions retrieved corresponds to the convolution of the molecular axis distribution and the molecular orientation dependence of the Coulomb explosion probe. In order to minimise this problem, many experiments have been performed by using a probe laser beam circularly polarised [37–39], since such a polarisation has the advantage of a uniform detection efficiency for each possible direction of the molecular axis in the polarisation plane for linear molecule, but it is still not uniform for all the molecular orientations. Therefore, even in this case the true molecular axis distribution prior to Coulomb explosion cannot be

extracted. Similar issues arise for linear probe polarisations for measuring 3D alignment [46]. As such, to date CEI-VMI studies of molecular axis alignment have relied entirely on quantitative analysis of the raw velocity map images rather than obtaining the true molecular axis distribution.

We have implemented an algorithm which allows the inclusion of a non-uniform detection function, leading to the retrieval of the molecular axis distribution deconvoluted from the molecular orientation dependence of the Coulomb explosion probe. This algorithm can retrieve the molecular axis distribution from a 2D VMI image even if this image corresponds to a Coulomb exploded cloud of ions which is not cylindrically symmetric about any axis. The only requirements are that the molecular axis distribution of interest is cylindrically symmetric about an axis lying in a plane parallel to the detector, that an *a priori* measurement of the detection function is available, and that the probe has an axis of cylindrical symmetry (not necessarily in the detector plane), i.e. it is not elliptically polarised. The approach followed to extract the molecular axis distribution from a VMI image can thus be described in two steps:

1. An image is acquired by allowing only the probe laser pulse to interact with an isotropic sample of molecules, and is inverted by using either the Cho-Na algorithm or its regularised version (see Chapter 3). The inversion of this image yields the molecular orientation dependence of the Coulomb explosion probe.

2. The probe molecular orientation dependence is deconvoluted from the image acquired when the probe laser pulse interacts with an aligned sample of molecules in order to quantitatively extract the molecular axis distribution.

A detailed description of this algorithm is given in section 4.1. The results of some of the tests done to evaluate the performance of this algorithm with simulated input images are presented in sections 4.2 and 4.3. Finally, the inversions of experimental images are presented in sections 4.4 and 4.5.

4.1 Description of the inversion method

An image acquired when the probe laser pulse interacts alone with an isotropic sample of molecules corresponds to the VMI projection of a 3D cloud of ions that has an axis of cylindrical symmetry. This axis coincides with the laser polarisation direction if the laser

pulse is linearly polarised, or with the propagation direction if the laser pulse is circularly polarised. In both cases, if the axis of cylindrical symmetry lies in a plane parallel to the detector, any 2D acquired image $I(y,\ z)$ can be inverted by using the Cho-Na method or its regularised version described in Chapter 3, in order to obtain a 2D slice $P(r,\ z)$ of the 3D original distribution lying in a plane parallel to the detector. It is important to realise that this retrieved detection function is expressed in a frame of reference (PF) defined by the probe laser. In order to deconvolute this detection function it needs to be expressed in the frame of reference (AF) defined by the alignment laser. Also, it is only the angular dependence of the detection function we wish to deconvolute. Since the retrieved probe-alone distribution also contains the radial distribution function (determined by CEI), we first need to separate the probe alone distribution into radial and angular parts to isolate the probe molecular orientation dependence.

For this purpose, it is convenient to express $P(r,\ z)$ in spherical coordinates $P_{\mathrm{sph}}(R_l,\ \theta_m)$, where the indexes l and m refer to the $(l,\ m)$ pixel of the 2D grid, whose rows and columns correspond to R and θ coordinates, respectively. Considering the transformation from cylindrical to spherical coordinates, which is given by:

$$\begin{aligned} R &= \sqrt{r^2 + z^2} \\ \theta &= \arctan\left(r/z\right) \\ \phi &= \phi \end{aligned} \tag{4.1}$$

the distribution $P_{\mathrm{sph}}(R_l,\ \theta_m)$ can be obtained by following the procedure described in section 3.2.2. As stated in Chapter 3, the advantage of using spherical coordinates is that at each pixel $(l,\ m)$, the retrieved distribution $P_{\mathrm{sph}}(R_l,\ \theta_m)$ is linked to the corresponding velocity distribution $G\left(R_l\right)$ and angular distribution $A\left(\theta_m;\ R_l\right)$ through a simple relation:

$$P_{\mathrm{sph}}\left(R_l,\ \theta_m\right) \ = \ G\left(R_l\right) A\left(\theta_m;\ R_l\right)$$

and the velocity distribution $G\left(R_l\right)$ is given by (see section 3.2.2 for details):

$$G\left(R_l\right) \ = \ \sum_{m=0}^{Z-1} R_l \sin\theta_m P_{\mathrm{sph}}\left(R_l,\ \theta_m\right)$$

Thus, the value of the corresponding probe molecular orientation dependence $A\left(\theta_m; R_l\right)$

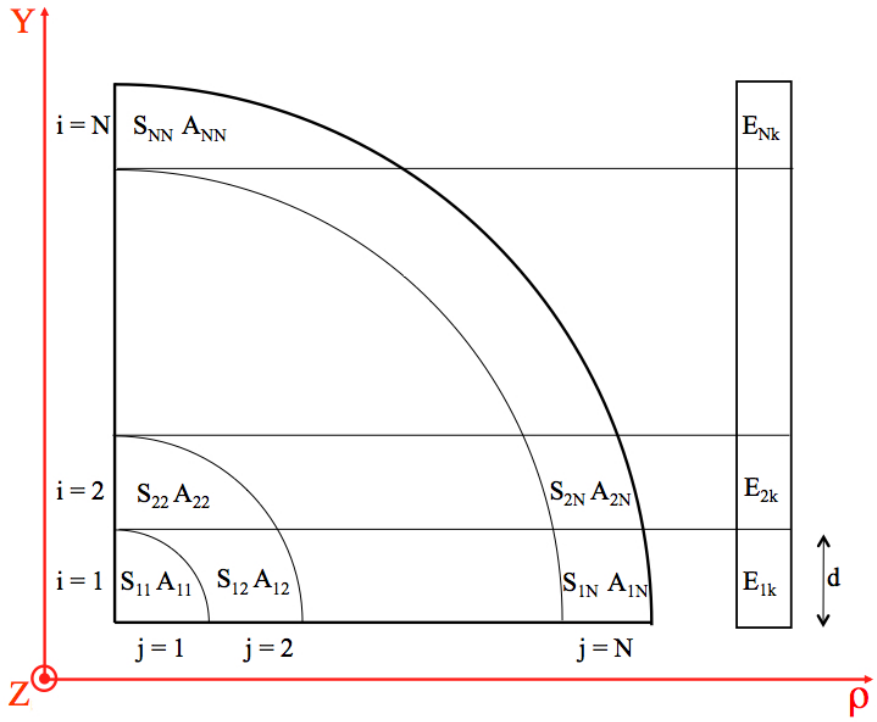

Figure 4.1: Illustration of the inversion process of the k-th column of the image $E(Y,\ Z)$, acquired for an aligned sample of molecules and definition of the D^k matrix.

at each pixel $(l,\ m)$ can be obtained through the relation:

$$A\left(\theta_m;\ R_l\right) = \begin{cases} \frac{P_{\text{sph}}(R_l,\ \theta_m)}{G(R_l)} & \text{if } P_{\text{sph}}\left(R_l,\ \theta_m\right) \neq 0 \text{ and } G\left(R_l\right) \neq 0 \\ 0 & \text{if } P_{\text{sph}}\left(R_l,\ \theta_m\right) = 0 \text{ and/or } G\left(R_l\right) = 0 \end{cases} \tag{4.2}$$

Subsequently, the probe molecular orientation dependence must be deconvoluted from the image that is acquired for an aligned sample of molecules, in order to retrieve the molecular axis distribution. In order to apply the Cho-Na approach, the molecular orientation dependence of the probe process needs to be included in the S matrix, defined in Eq. 3.7 in Chapter 3.

Thus, for each line k of the acquired image, perpendicular to the polarisation of the pump laser pulse, a detection matrix D^k, having the same size as the S matrix, must be constructed. This matrix is defined in the AF, whose axes are indicated with upper case letters (XYZ) to distinguish them from the (xyz) axes defining the PF. Each element $D^k_{i\,j}$ of this matrix represents the product between the area $S_{i\,j}$ of the $(i,\ j)$ pixel of a 2D slice of the original 3D ion cloud and the corresponding value of the probe molecular orientation dependence at that pixel, as shown in Fig. 4.1. The 2D slice considered lies perpendicular

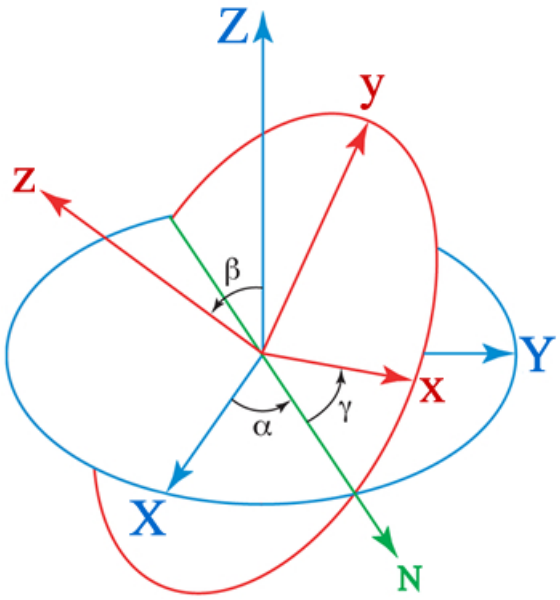

Figure 4.2: Schematic of the relation between the probe frame PF, represented in red, and the alignment frame AF, represented in blue, defined through the Euler angles (α, β, γ). The green line N, represents the line of nodes, defined as the intersection of the xy plane of the probe frame and the XY plane of the pump frame.

to the Z axis at $Z = k$. The indeces i and j refer to the i-th Y line, perpendicular to the Z axis, of the acquired image, and the j-th radius (ρ) of the 2D slice. Therefore, each element $D^k_{i\,j}$ of this matrix is given by:

$$D^k_{i\,j} \;=\; S_{i\,j}\; A^k_{i\,j} \tag{4.3}$$

where $A^k_{i\,j}$ represents the element (ij) of the k-th 2D slice of the probe molecular orientation dependence expressed in cylindrical coordinates in the AF.

In order to obtain $A^k_{i\,j}$ in the AF from the $A\,(\theta_m;\; R_l)$ defined in the PF through Eq. 4.2, two steps have to be followed. First, each element $A\,(\theta_m;\; R_l)$ needs to be expressed in cylindrical coordinates $(r,\; z)$ in the PF. This is done by following the procedure described in section 3.2.2 of Chapter 3 with the inverse of equations 4.1. The resulting probe molecular orientation dependence next needs to be rotated into AF.

In order to perform this rotation, it is taken into account that two generic Cartesian reference frames, one rotated with respect to the other, can be overlapped by means of three successive finite rotations given by the Euler angles α, β, γ as shown in Fig. 4.2. Therefore, a generic vector in the reference frame $(X\;Y\;Z)$ can be expressed in the reference

frame ($x\ y\ z$) through this expression:

$$\begin{bmatrix} x \\ y \\ z \end{bmatrix} = \mathbf{R} \begin{bmatrix} X \\ Y \\ Z \end{bmatrix} \tag{4.4}$$

where $\mathbf{R}$ is the *direction cosine matrix* and is expressed as [203]:

$$\mathbf{R} = \begin{bmatrix} \cos\alpha\ \cos\beta\ \cos\gamma\ -\ \sin\alpha\ \sin\gamma & -\cos\alpha\ \cos\beta\ \sin\gamma\ -\ \sin\alpha\ \cos\gamma & \cos\alpha\ \sin\beta \\ \sin\alpha\ \cos\beta\ \cos\gamma\ +\ \cos\alpha\ \sin\gamma & -\sin\alpha\ \cos\beta\ \sin\gamma\ +\ \cos\alpha\ \cos\gamma & \sin\alpha\ \sin\beta \\ -\sin\beta\ \cos\gamma & \sin\beta\ \sin\gamma & \cos\beta \end{bmatrix} \tag{4.5}$$

By means of this direction cosine matrix the probe molecular orientation dependence can be rotated from the PF into the AF by following these steps:

- A 3D equi-spaced grid ($Y,\ \rho,\ Z$), is created in the AF.
- For each pixel of the grid ($Y,\ \rho,\ Z$), the corresponding Cartesian coordinates ($X,\ Y,\ Z$) are calculated through the following equations:

$$\begin{aligned} X &= \begin{cases} \sqrt{\rho^2 - Y^2} & \text{if } \rho > Y \\ 0 & \text{if } \rho \leq Y \end{cases} \\ Y &= Y \\ Z &= Z \end{aligned} \tag{4.6}$$

  It should be noted that setting $X = 0$ for $\rho \leq Y$ does not limit the generality of the problem since the probe molecular orientation dependence at each pixel ($Y,\ \rho$) needs to be multiplied for the corresponding element of the S matrix, which is 0 for $\rho \leq Y$.

- The coordinates ($x,\ y,\ z$) in the PF are calculated by using Eq. 4.4.
- The corresponding cylindrical coordinates ($r,\ z$) are calculated in the PF, using the

following equations:

$$\begin{aligned} r &= \sqrt{y^2 + x^2} \\ z &= z \end{aligned} \tag{4.7}$$

- For each value of Y the value of the probe molecular orientation dependence at the point $(r,\ z)$ corresponding to $(Y,\ \rho,\ Z)$ is obtained by a bicubic spline interpolation of the values of $A(r,\ z)$ around that position.

Once the detection matrices D^k are constructed for each quarter of the acquired image an expression similar to Eq. 3.6 can be used to relate every column $[E]$ of the acquired image, $E(Y,\ Z)$ to the corresponding column $[T]$ of the inverted image, $T(\rho,\ Z)$:

$$[T] \ = \ \frac{d}{2} \ \left[D^k\right]^{-1} [E] \tag{4.8}$$

Since the $[D^k]$ matrix is usually near-singular we used the singular value decomposition (SVD) method [184] to carry the pseudo-inverse of the $[D^k]$ matrix. Furthermore, a second approach based on the projected Landweber regularisation method, which is widely described in section 3.4 of Chapter 3, was also used to calculate the vector column $[T]$.

By solving Eq. 4.8 for each column vector $[E]$ of the acquired image, the distribution $T\,(\rho,\ Z)$ is obtained, and then, by following the procedure described in section 3.2.2 of Chapter 3, the corresponding molecular axis distribution can be retrieved.

In the next section, the performance of the algorithm is tested in the cases when the SVD or the projected Landweber methods are used.

4.2 Performance of the method with noise free simulated images

The algorithm was first tested with noise free simulated images in order to compare the retrieved molecular axis distributions with the known corresponding input distributions. The probe-alone input images were generated by following the procedure described in Section 3.3 of Chapter 3, while the procedure followed to incorporate the probe molecular orientation dependence into the pump-probe input images is described in Appendix C. The same Gaussian velocity distribution of the ions was generated for the probe-alone

	$M(\theta) = \cos^2\theta$	$M(\theta) = \cos^4\theta$	$M(\theta) = \cos^6\theta$	$M(\theta) = \cos^8\theta$
$\Delta\beta_2$	-2.932×10^{-1}	9.9×10^{-3}	1.52×10^{-2}	9.9×10^{-3}
$\Delta\beta_4$	2.33×10^{-2}	3.21×10^{-2}	2.46×10^{-2}	4.33×10^{-2}
$\Delta\beta_6$	2.04×10^{-2}	2.87×10^{-2}	2.11×10^{-2}	3.15×10^{-2}
$\Delta\beta_8$	3.59×10^{-2}	-1.43×10^{-2}	1.72×10^{-2}	1.87×10^{-2}
$\Delta\beta_{10}$	9.7×10^{-3}	1.35×10^{-2}	-9.4×10^{-3}	-3.5×10^{-3}

Table 4.1: Values of $\Delta\beta_l$ calculated through Eq. 4.10 for each molecular axis distribution, retrieved from the images inverted with the SVD method and shown in Fig. 4.5.

and the pump-probe images, since this distribution is determined by the CEI process. All the velocity Gaussian distributions used in the following tests have the same width ($\sigma = 2.8 \times 10^3$ m s^{-1}). The simulated input images, corresponding to 1D alignment of a sample of linear molecules, were chosen to test the performance of the algorithm in different situations. In particular, the sensitivity of the algorithm to the molecular axis distribution for a given molecular orientation dependence of the Coulomb explosion probe was tested. Also, the ability of the algorithm to retrieve the same molecular axis distribution for different molecular orientation dependences of the Coulomb explosion probe was examined. The results of these tests are discussed below.

4.2.1 Effect of the molecular axis distribution.

In order to examine the sensitivity of the algorithm to the molecular axis distribution, for a given molecular orientation dependence of the Coulomb explosion probe, a set of 2D images was simulated. Each image corresponded to a different molecular axis distribution, and represented the VMI projection of a 3D ion cloud generated following the interaction of the probe laser field with a sample of aligned molecules. Both the alignment and the Coulomb explosion laser beams were assumed to be linearly polarised along the same direction lying in a plane parallel to the detector. As such the probe and the alignment reference frames were coincident. In order to extract the molecular axis distribution from each image, the knowledge of the probe molecular orientation dependence was needed. For this purpose, a 2D image representing the VMI projection of a 3D ion cloud generated from a sample of isotropic molecules was simulated, and is shown in Fig. 4.3 (a).

The 3D ion cloud consisted of 1000000 trajectories, with a Gaussian velocity distribution and a probe molecular orientation dependence $A(\theta) = \cos^2(\theta)$. The 2D VMI image, was inverted by using the non-regularised version of the Cho-Na inversion method. This was used since it gives the same result as the regularised version in performing the inversion

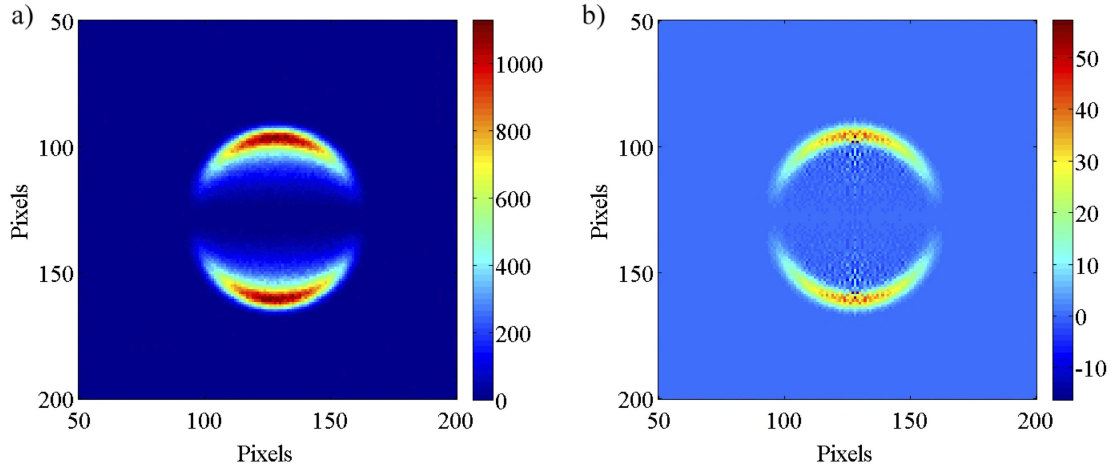

Figure 4.3: a) Simulated 2D projected image, corresponding to the VMI projection on a 256 × 256 pixels detector of a 3D ion sphere consisting of 1000000 trajectories, with a probe molecular orientation dependence given by $A(\theta) = \cos^2(\theta)$, and a Gaussian velocity distribution whose centre corresponds to a kinetic energy of 4.5 eV. b) Reconstructed 2D slice of the 3D original ion sphere, obtained by using the Cho-Na inversion method described in Chapter 3. From this image the probe molecular orientation dependence can be extracted.

	$M(\theta) = \cos^2\theta$	$M(\theta) = \cos^4\theta$	$M(\theta) = \cos^6\theta$	$M(\theta) = \cos^8\theta$
$\Delta\beta_2$	-1.375×10^{-1}	1.62×10^{-2}	8.5×10^{-3}	4.5×10^{-3}
$\Delta\beta_4$	7.5×10^{-3}	9.4×10^{-3}	4.1×10^{-3}	2.60×10^{-2}
$\Delta\beta_6$	-1.37×10^{-2}	-4.2×10^{-3}	-6.0×10^{-3}	3.8×10^{-3}
$\Delta\beta_8$	3.89×10^{-2}	7.9×10^{-3}	-7×10^{-4}	-1.2×10^{-2}
$\Delta\beta_{10}$	-2.09×10^{-2}	-3.0×10^{-3}	-1.81×10^{-2}	-2.84×10^{-2}

Table 4.2: Values of $\Delta\beta_l$ calculated through Eq. 4.10 for each molecular axis distribution, retrieved from the images inverted with the regularisation method and shown in Fig. 4.5

of a clean image, as shown in Chapter 3. Then, the corresponding probe molecular orientation dependence was extracted, and included in the detection matrices used to perform the inversion of the 2D images corresponding to the projection of the 3D ion clouds generated from aligned samples of molecules. The angular distribution of each 3D ion cloud was obtained by analytically incorporating the probe molecular orientation dependence into the molecular axis distribution induced by the alignment laser pulse, as described in Appendix C. The 2D VMI images are shown in Fig. 4.4, together with the images inverted by using both the SVD and the regularisation methods. The corresponding retrieved molecular axis distributions are shown in Fig. 4.5. It can be noted that both the inversion processes are able to reproduce the molecular axis distribution. Also, the accuracy in retrieving this distribution improves with the localisation of the molecules around the axis of cylindrical

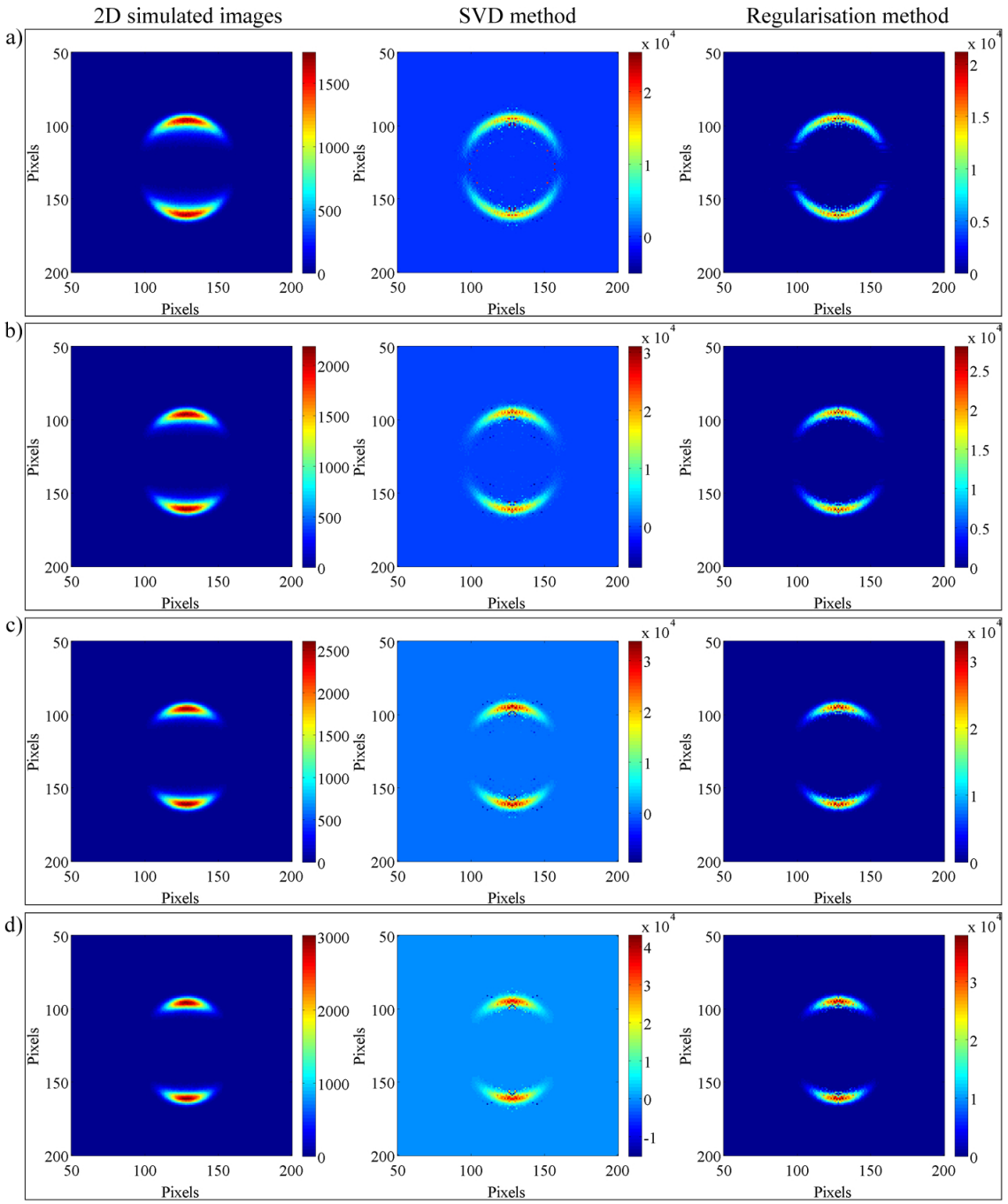

Figure 4.4: In each row, from left to right, the 2D simulated projected image to be inverted, the reconstructed 2D slices of the 3D original ion cloud obtained by using the SVD, or the regularisation methods, are shown. The probe molecular orientation dependence used as input for the inversion algorithms, is retrieved from image (b) of Fig. 4.3. The angular distribution of each 2D image to be inverted is obtained by analytically convoluting the probe angular response, $A(\theta) = \cos^2(\theta)$, and the molecular axis distribution given by: a) $M(\theta) = \cos^2(\theta)$; b) $M(\theta) = \cos^4(\theta)$; c) $M(\theta) = \cos^6(\theta)$; d) $M(\theta) = \cos^8(\theta)$.

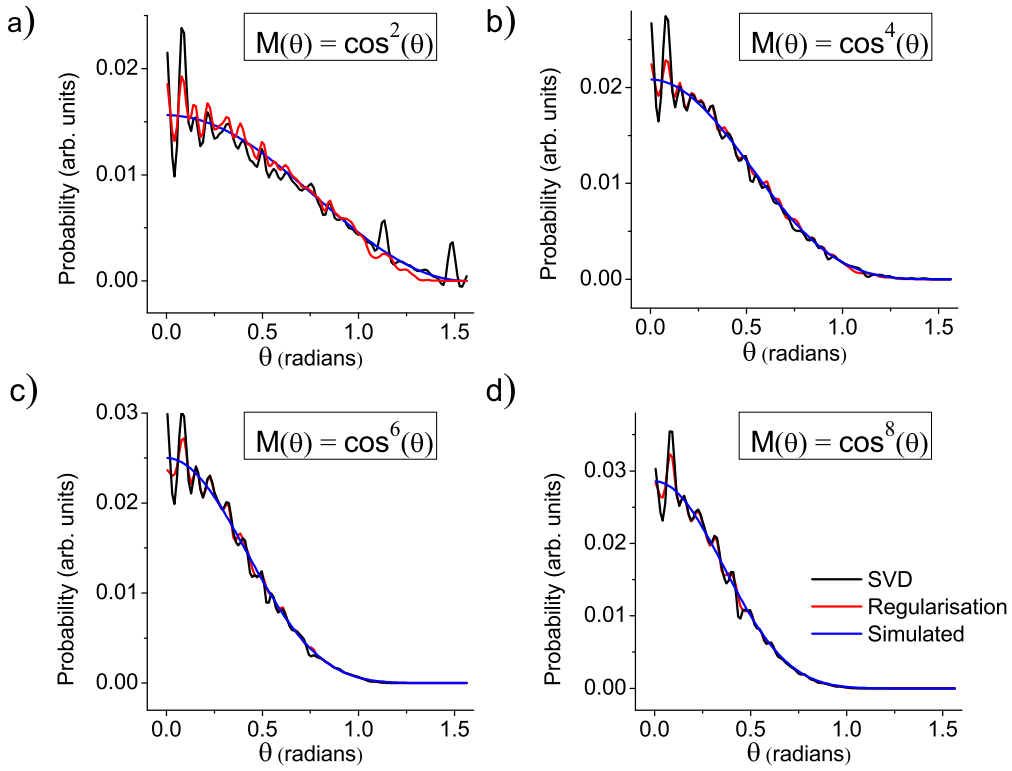

Figure 4.5: Molecular axis distributions retrieved from the corresponding inverted images shown in Fig. 4.4, obtained by using the SVD (black lines), or the regularisation methods (red lines).

symmetry. In order to quantify this observation, the retrieved angular distributions were fitted to the equation:

$$M(\theta) = \sum_{l=0}^{2n} \gamma_l P_l(\cos\theta) \quad \text{with } n = 1, 2, ..., 5 \tag{4.9}$$

and the extrapolated γ_l coefficients, were compared to those used as input for the trajectory simulations, β_l. The resulting beta deviations, $\Delta\beta_l$, defined as:

$$\Delta\beta_l = \frac{(\gamma_l)}{(\gamma_0)} - \frac{(\beta_l)}{(\beta_0)} \tag{4.10}$$

are listed in Tables 4.1, and 4.2 for all the molecular axis distributions retrieved with the SVD and the regularised method, respectively.

It can be noted that the highest $\Delta\beta_l$ values are obtained for the inversion of image (a) of Fig. 4.4, which corresponds to the case where the probe molecular orientation dependence and the molecular axis distributions are both given by $A(\theta) = \cos^2\theta$. For the other images, the retrieved angular distributions reproduce the simulated distributions

$M(\theta)$	$A(\theta)$	O
$M(\theta) = \cos^2\theta$	$A(\theta) = \cos^2\theta$	0.6
$M(\theta) = \cos^4\theta$	$A(\theta) = \cos^2\theta$	0.71
$M(\theta) = \cos^6\theta$	$A(\theta) = \cos^2\theta$	0.78
$M(\theta) = \cos^8\theta$	$A(\theta) = \cos^2\theta$	0.82

Table 4.3: Values of the sample parameter O calculated through Eq. 4.12 for each molecular axis distribution $M(\theta)$ and probe molecular orientation dependence $A(\theta)$ used to simulate the images shown in Fig. 4.5

with high accuracy $\Delta\beta_l \leq 10^{-2}$. and similar results are obtained with the two inversion methods. Therefore, the molecular axis distribution is retrieved with greatest accuracy when a substantial fraction of the molecules are ionised.

More precisely, introducing a sampling-parameter O defined as the fraction of ionised molecules for a given molecular axis distribution and angular dependence of ionisation:

$$O = \int_0^{2\pi} \int_0^{\pi} A(\theta,\ \phi)\ M(\theta,\ \phi)\ \sin\theta\ d\theta\ d\phi \tag{4.11}$$

where the probe molecular orientational dependence $A(\theta,\ \phi)$ is normalised to its maximum value, and the molecular axis distribution $M(\theta,\ \phi)$ is normalised to the area:

$$\int_0^{2\pi} \int_0^{\pi} M(\theta,\ \phi)\ \sin\theta\ d\theta\ d\phi = 1 \tag{4.12}$$

it can be concluded that the accuracy in retrieving the molecular axis distribution increases with the sampling-parameter O, whose values for the images presented above are listed in table 4.3. The maximum value of O is 1 and corresponds to the case where the probe molecular orientational dependence is isotropic.

Furthermore, since the molecular axis distribution is retrieved with a higher accuracy by using the regularisation method rather than the SVD method, only the results obtained with the regularised algorithm will be shown in the rest of the chapter.

4.2.2 Effect of the probe orientational response

A set of images was used to test the sensitivity of the algorithm in retrieving the same molecular axis distribution for different molecular orientation dependences of the Coulomb explosion probe. Two different probe molecular orientation dependences, defined by the physics of the Coulomb explosion process for linear molecules, were considered. One was

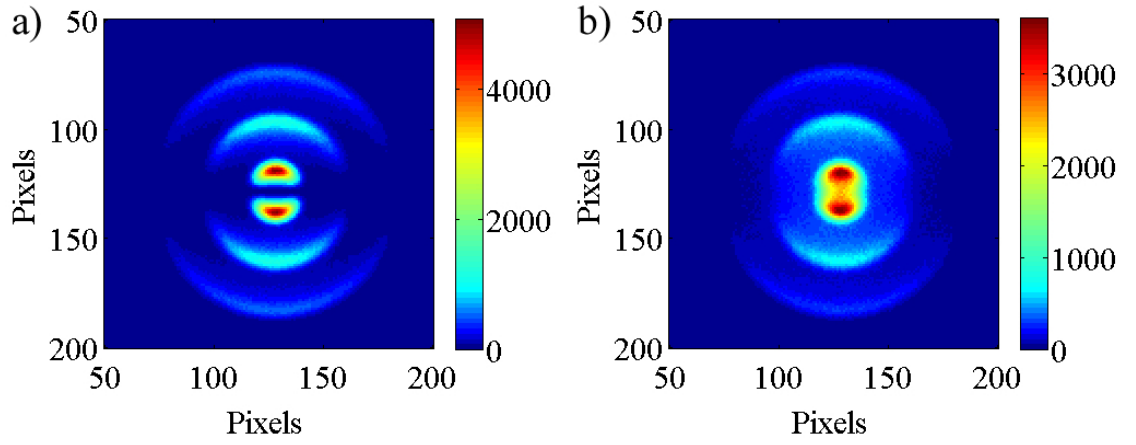

Figure 4.6: Simulated 2D probe-alone images, corresponding to the VMI projections on a 256×256 pixels detector of 3D ion spheres with velocity distributions given by combinations of three Gaussian distributions, each consisting of 1000000 trajectories and having a probe molecular orientation dependence given by a) $A_1(\theta) = \cos^2(\theta)$; and b) $A_2(\theta, \phi) = 1 - \sin^2(\theta)\cos^2(\phi)$.

given by $A_1(\theta) = \cos^2(\theta)$ in the AF, and modelled the case where the probe laser pulse was linearly polarised along an axis lying in a plane parallel to the detection plane. Since also the alignment beam was assumed to be linearly polarised along the same direction, the PF and the AF coincided in this case. The other probe molecular orientation dependence modelled the case of circular polarisation of the probe laser pulse, and was given by $A_2(\eta) = \sin^2(\eta)$ in the PF, η being the angle between the ion position and the propagation direction of the probe laser pulse. In this case, the alignment laser polarisation was perpendicular to the propagation direction of the probe laser beam in a plane parallel to the detector. As such, the probe molecular orientation dependence was given by $A_2(\theta, \phi) = 1 - \sin^2(\theta)\cos^2(\phi)$ in the AF.

Two 2D probe-alone images each corresponding to the VMI projection on a 256 × 256 pixels detector of a 3D ion cloud were simulated. The velocity distribution of each 3D ion cloud was given by a combination of three Gaussian distributions, each consisting of 1000000 trajectories and having an angular distribution of $A_1(\theta)$ or $A_2(\theta, \phi)$. The resulting simulated images are shown in Figs. 4.6 (a) and (b) respectively. These images were inverted by using the Cho-Na inversion method described in Chapter 3.

The corresponding probe molecular orientation dependences were extracted and included in the detection matrices to perform the inversion of the 2D images corresponding to the projection of the CEI ion clouds from aligned samples of molecules. The angular

Gaussian peak	v_0 (m s^{-1})	σ (m s^{-1})	R_{KE}	Number of trajectories	$M(\theta)$
1	1.4×10^4	2.8×10^3	4000	10^6	$\cos^6(\theta)$
2	4.2×10^4	2.8×10^3	445	10^6	$\cos^2(\theta)$
3	12.5×10^4	2.8×10^3	160	10^6	$\cos^4(\theta)$

Table 4.4: Central velocity v_0, width σ, ratios between the final and initial kinetic energies of the particles R_{KE}, number of trajectories, and corresponding molecular axis distributions $M(\theta)$ relative to each Gaussian peak of the velocity distribution of the 3D simulated ion sphere.

distributions of the CEI ion clouds were given by the analytical convolutions of the probe molecular orientation dependences and the molecular axis distributions. Details about the velocity and molecular axis distributions are listed in table 4.4, while the 2D simulated images are shown in Figs. 4.7 (a) and (c).

The 2D simulated images were inverted by using the regularised algorithm. Since in the case of linear polarisation of the probe laser pulse the probe and the alignment frames coincide, the Euler angles were set equal to 0° in Eq. 4.5 to perform the inversion of image (a) of Fig. 4.7. Instead, the probe molecular orientation dependence needed to be rotated into the alignment frame in the case of circular polarisation of the probe laser pulse (image (c) of Fig. 4.7). In this case, rotation of the probe frame into the alignment frame was obtained by setting all Euler angles equal to 90° in Eq. 4.5 (see Fig. 4.8). The images resulting from these inversions are shown in Figs. 4.7 (b) and (c) respectively. The reconstructed molecular axis distributions corresponding to Gaussian peaks 1, 2, and 3, are shown in Figs. 4.7 (e), (f), and (g) respectively. The retrieved molecular axis distributions are in good agreement with the corresponding simulated distributions (blue line), in particular in the case of Gaussian peak 1 (e), which corresponds to the most localised molecular axis distribution. From the $\Delta\beta_l$ values extracted from the curves fitted to the retrieved molecular axis distributions, and listed in tables 4.5 and 4.6 it can be noted that the molecular axis distributions are retrieved with a slightly higher accuracy in the case where the probe angular response is given by $A_1(\theta)$ rather than $A_2(\theta,\phi)$.

In conclusion this test proves that the inversion algorithm we have implemented is capable of retrieving the molecular axis distribution deconvoluted from the probe molecular orientation dependence also in the case when the CEI cloud of ions does not have a cylindrical axis of symmetry, i.e the probe laser pulse is circularly polarised.

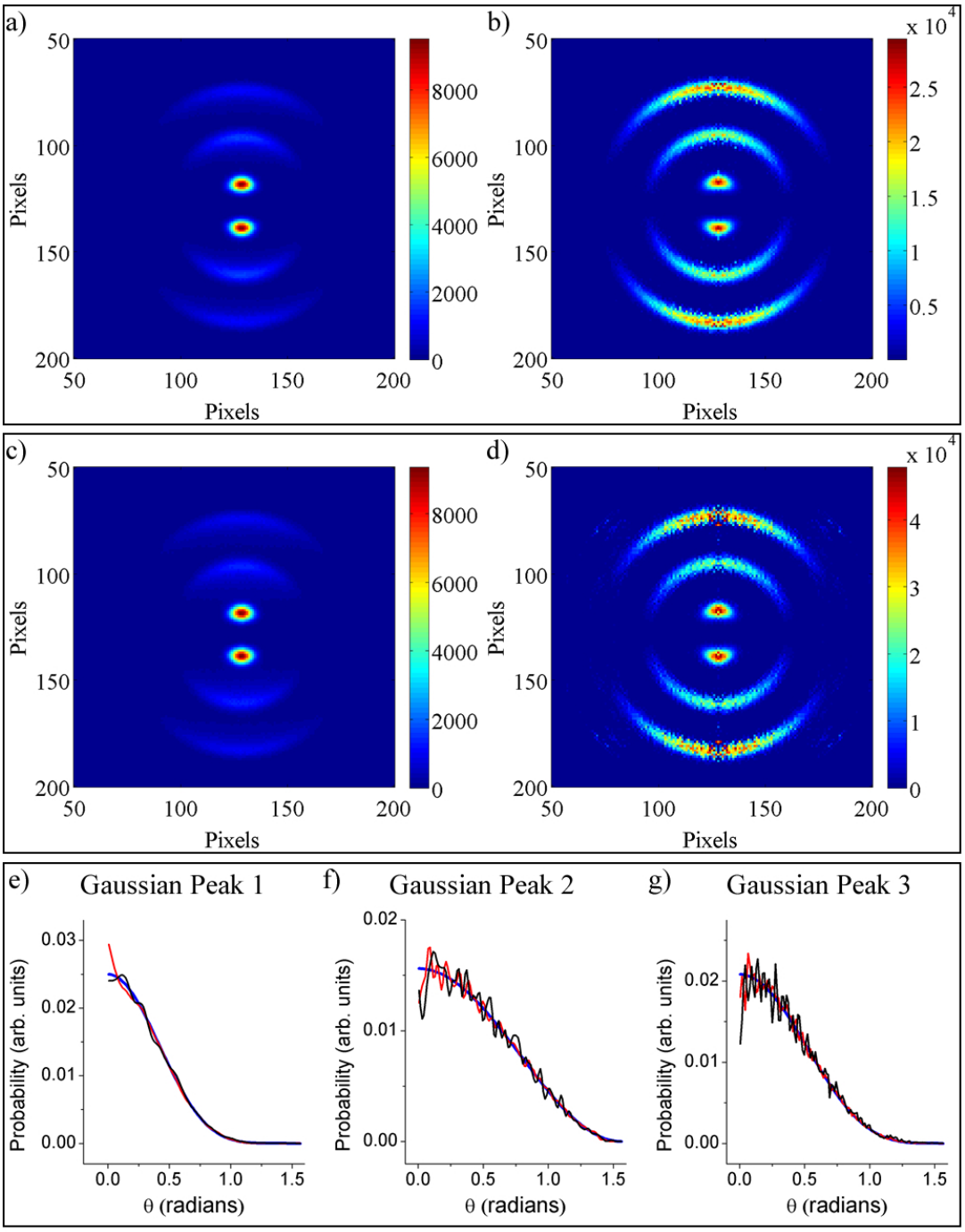

Figure 4.7: Top and middle panels refer to the cases where the probe molecular orientation dependences are given in the AF by $A_1(\theta) = \cos^2(\theta)$ and $A_2(\theta, \phi) = 1 - \sin^2(\theta)\cos^2(\phi)$, respectively. In both panels the 2D projected images to be inverted (a) and (c), and the corresponding reconstructed 2D slices of the 3D ion clouds (b) and (d) are shown. In the bottom panel the retrieved molecular axis distributions deconvoluted from $A_1(\theta)$ (red lines), or $A_2(\theta, \phi)$ (black lines), and relative to: e) Gaussian peak 1, f) Gaussian peak 2, and g) Gaussian peak 3, are shown. For comparison, also the simulated molecular axis distributions, listed in table 4.4, are plotted (blue lines).

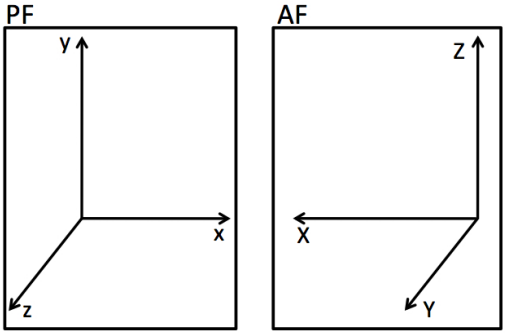

Figure 4.8: Schematic of the probe and alignment reference frames in the case of circular polarisation of the probe laser pulse. The z axis of the PF represents the direction of propagation of the probe laser pulse, while the Z axis in the AF represents the direction of polarisation of the linearly polarised pump laser pulse.

	Peak 1 ($M(\theta) = \cos^6\theta$)	Peak 2 ($M(\theta) = \cos^2\theta$)	Peak 3 ($M(\theta) = \cos^4\theta$)
$\Delta\beta_2$	2.0×10^{-3}	-2.200×10^{-1}	-3.7×10^{-3}
$\Delta\beta_4$	1.7×10^{-3}	-3.6×10^{-3}	-3.5×10^{-3}
$\Delta\beta_6$	5.6×10^{-3}	2.9×10^{-3}	-5.0×10^{-3}
$\Delta\beta_8$	1.81×10^{-2}	-4.9×10^{-3}	-8.9×10^{-3}
$\Delta\beta_{10}$	3.21×10^{-2}	-1.72×10^{-2}	-2.33×10^{-2}

Table 4.5: Values of $\Delta\beta_l$ calculated through Eq. 4.10 for the retrieved molecular axis distributions deconvoluted from $A_1(\theta) = \cos^2(\theta)$ probe angular response, and shown in Fig. 4.7 with red lines.

4.3 Performance of the method with simulated noisy images

The performance of the algorithm was also analysed in the inversion of noisy images. For this purpose random noise was added to the noise free 2D projected images shown in section 4.2.2, following the procedure described in section 3.3 of Chapter 3. Two sets of images, characterised by different probe angular responses were analysed. The first set of images is where the pump and probe laser pulses would be linearly polarised along the

	Peak 1 ($M(\theta) = \cos^6\theta$)	Peak 2 ($M(\theta) = \cos^2\theta$)	Peak 3 ($M(\theta) = \cos^4\theta$)
$\Delta\beta_2$	-1.72×10^{-2}	-2.162×10^{-1}	-3.32×10^{-2}
$\Delta\beta_4$	-2.26×10^{-2}	-8.6×10^{-3}	-2.92×10^{-2}
$\Delta\beta_6$	-6.6×10^{-3}	-1.38×10^{-2}	-1.73×10^{-2}
$\Delta\beta_8$	3.8×10^{-3}	-1.13×10^{-2}	-2.37×10^{-2}
$\Delta\beta_{10}$	1.07×10^{-2}	-3.27×10^{-2}	-4.58×10^{-2}

Table 4.6: Values of $\Delta\beta_l$ calculated through Eq. 4.10 for the retrieved molecular axis distributions deconvoluted from $A_2(\theta, \phi) = 1 - \sin^2(\theta)\cos^2(\phi)$ probe angular response, and shown in Fig. 4.7 with black lines.

same direction, and the probe molecular orientation dependence in the AF is given by a $\cos^2\theta$ distribution. The probe-alone image corresponding to the VMI projection of a CEI ion cloud from an isotropic sample of molecules was obtained by adding random noise to the image shown in Fig. 4.6 (a). The peak intensity of the random noise added to this clean image is 10% of the peak intensity of the image itself, and the resulting 2D noisy image is shown in Fig. 4.9 (a). The corresponding inverted images obtained by using the non-regularised or the regularised versions of the Cho-Na method are shown in Fig. 4.9 (b) and (c), respectively. As predicted from the tests presented in Chapter 3, image (b) is much noisier than image (c). In order to test the performance of the algorithm in both cases, the probe molecular orientation dependence retrieved from each image was used for the inversion of the simulated 2D image from a sample of aligned molecules. This image was obtained by adding random noise, of amplitude that was 10% of the peak intensity of the image itself, to the clean image shown in Fig. 4.7 (a). The resulting noisy image is shown in Fig. 4.9 (d). The inverted images obtained by deconvoluting the probe molecular orientation dependence retrieved from image (b) or (c), are shown in Figs. (e) and (f), respectively. The regularisation method was used to perform both inversions, and the optimum number of iterations needed to minimise the restoration error (see Eq. 3.20) was very different in the two cases. In particular, about 1000000 iterations were done to obtain image (e), while only 1000 iterations were needed for image (f). It is interesting to observe that image (c) was obtained after 100000 iterations. The corresponding retrieved molecular axis distributions are shown in the bottom panel of the same figure. It can be noted that the retrieved molecular axis distributions are very noisy in both cases, particularly for the outer ring since the signal to noise ratio in the simulated 2D image decreases with increasing distance from the centre.

Figure 4.9 *(following page)*: Top left panel refers to the probe-alone images: a) VMI image obtained by adding random noise to the image shown in Fig. 4.6 (a), b) and c) reconstructed 2D slices of the 3D ion clouds obtained by using the Cho-Na algorithm or its regularised version, respectively. Top right panel refers to the pump-probe images: d) VMI image, obtained by adding random noise to the image shown in Fig. 4.7 (a), d) and e) reconstructed 2D slices of the 3D ion clouds obtained by using the probe molecular orientation dependences extracted from images (b) or (c) respectively. In the bottom panel the molecular axis distributions retrieved from image (e) (black line) or (f) (red line) and relative to: g) Gaussian peak 1, h) Gaussian peak 2, i) Gaussian peak 3, are shown. For comparison, also the corresponding simulated molecular axis distributions are plotted (blue lines).

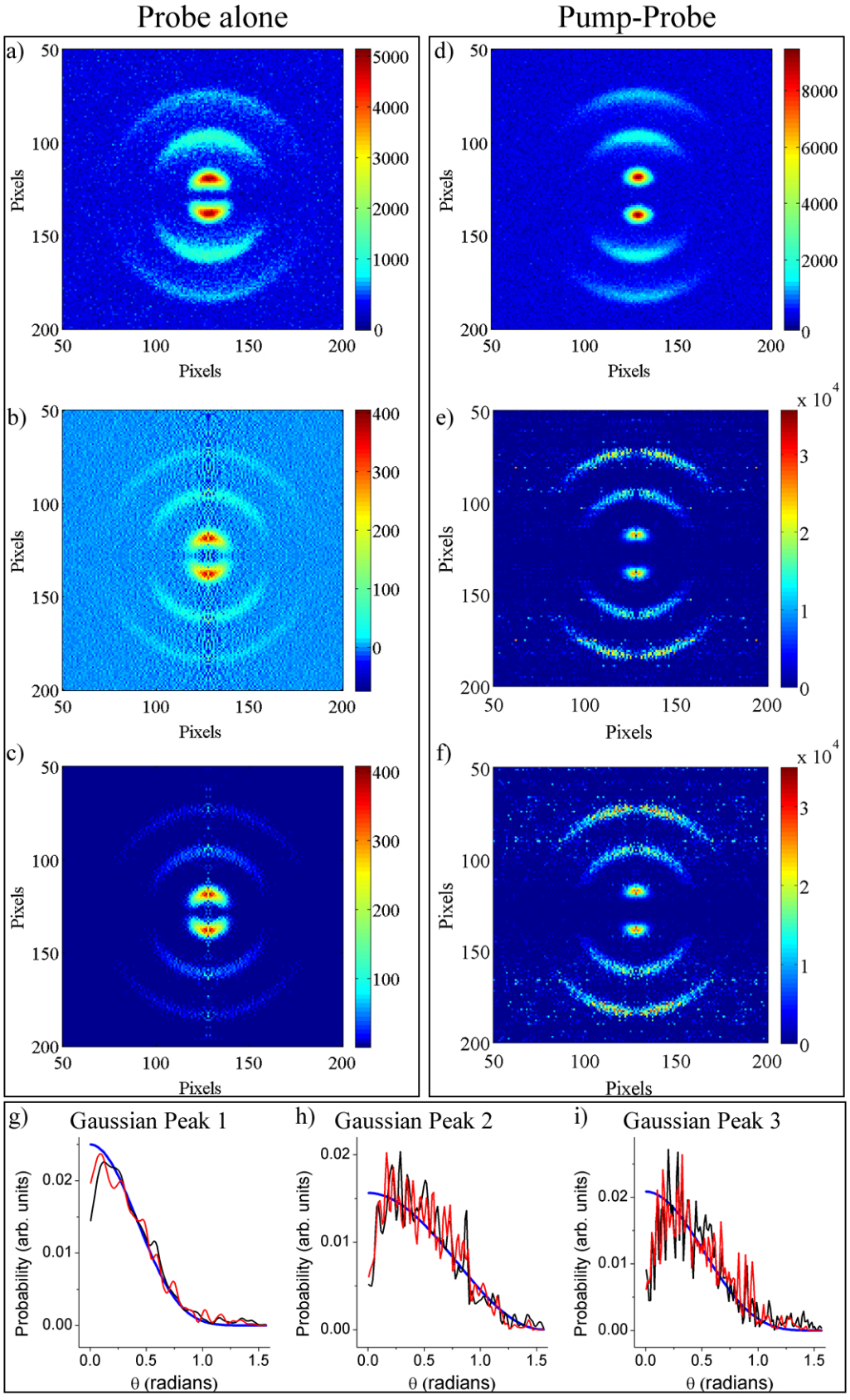
Probe alone
Pump-Probe
a)
b)
c)
d)
e)
f)
Pixels
x 10^4
g) Gaussian Peak 1
h) Gaussian Peak 2
i) Gaussian Peak 3
Probability (arb. units)
θ (radians)

We now consider the case where the pump laser pulse is linearly polarised and the probe laser pulse is circularly polarised. The probe molecular orientation dependence is given by $A_2(\theta, \phi) = 1 - \cos^2\theta \sin^2\phi$. The noisy images were obtained by adding the same random noise distribution used in the previous test to the clean images represented in Fig. 4.6 (b), and 4.7 (c). The corresponding noisy images are shown in Figs. 4.10 (a) and (d). Also in this case, both the non-regularised and regularised versions of the Cho-Na method were used to extract the probe molecular orientation dependences from Figs. 4.10 (b) and (c). The resulting retrieved images were used as input for the algorithm to invert the image (d) relative to the case when the probe laser pulse interacts with a sample of aligned molecules. The corresponding inverted images, shown in Figs. 4.10 (e) and (f), were obtained by using the regularisation method, with the same number of iterations used in the previous test. The retrieved molecular axis distributions, which are very noisy and not as accurate as in the case of the clean images are shown in the bottom panel of Fig. 4.10. Also in this case, the molecular axis distribution retrieved with the highest accuracy corresponds to Gaussian peak 1. The reason for that is that the signal to noise (S/N) ratio corresponding to Gaussian peak 1, is the highest of the three peaks. In fact, although all the Gaussian peaks have the same number of trajectories, the ions under Gaussian peak 1 are the most localised around the axis of polarisation of the pump laser.

In order to obtain a quantitative estimation of the accuracy in retrieving the molecular axis distribution from noisy images, the restoration error δ defined as:

$$\delta = \frac{\left\|T - T^{(0)}\right\|}{\left\|T^{(0)}\right\|} \tag{4.13}$$

with T and $T^{(0)}$ being the inverted image and the 2D simulated slice of the CEI cloud of ions respectively, was calculated for inverted images corresponding to different signal

Figure 4.10 *(following page)*: Top left panel refers to the probe-alone images: a) VMI image obtained by adding random noise to the image shown in Fig. 4.6 (b), b) and c) reconstructed 2D slices of the 3D ion clouds obtained by using the Cho-Na algorithm or its regularised version, respectively. Top right panel refers to the pump-probe images: d) VMI image, obtained by adding random noise to the image shown in Fig. 4.7 (c), d) and e) reconstructed 2D slices of the 3D ion clouds obtained by using the probe molecular orientation dependences extracted from images (b) or (c) respectively. In the bottom panel the molecular axis distributions retrieved from image (e) (black line) or (f) (red line) and relative to: g) Gaussian peak 1, h) Gaussian peak 2, i) Gaussian peak 3, are shown. For comparison, also the corresponding simulated molecular axis distributions are plotted (blue lines).

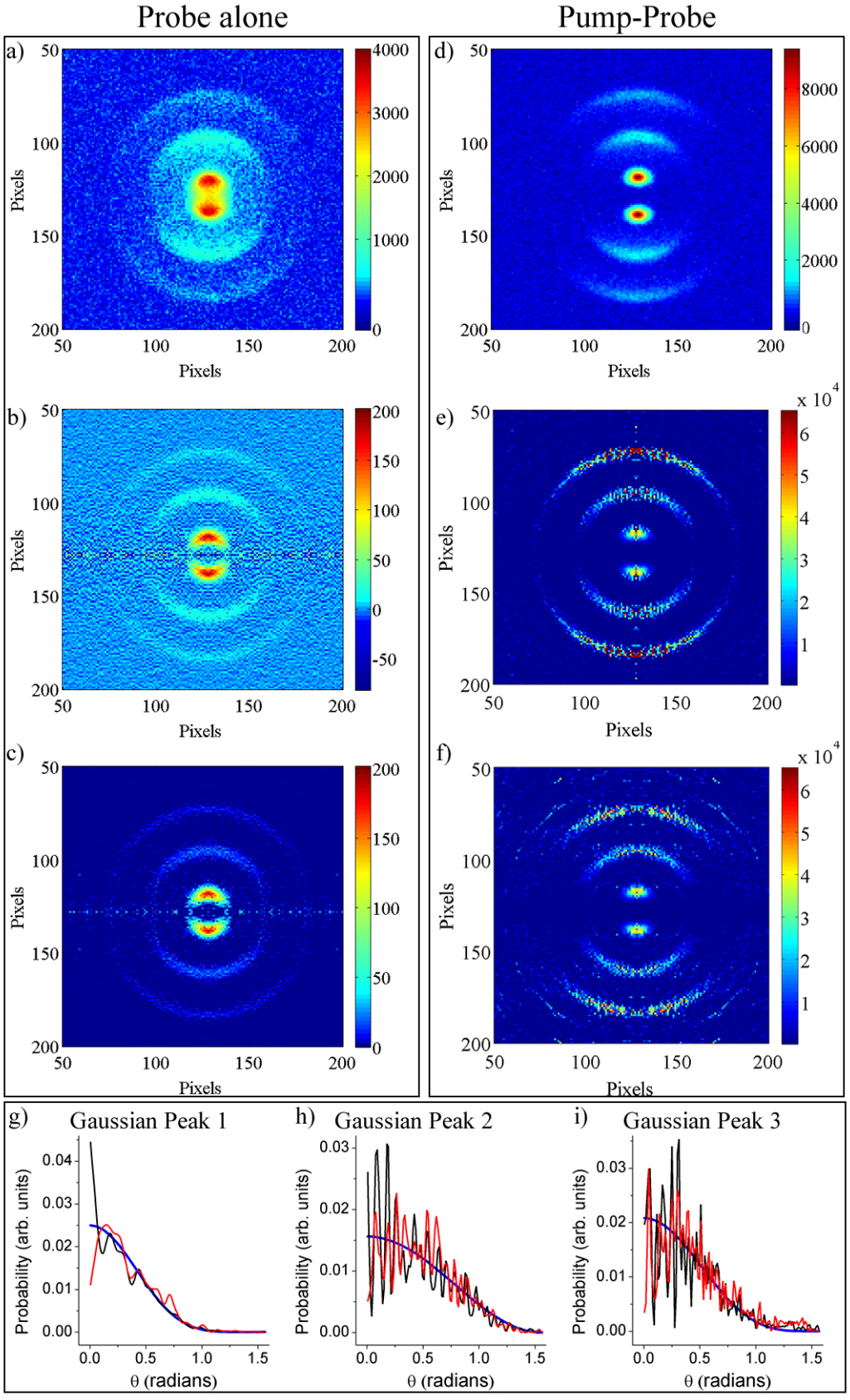
Probe alone
Pump-Probe
a)
b)
c)
d)
e)
f)
Pixels
x 10^4
g) Gaussian Peak 1
h) Gaussian Peak 2
i) Gaussian Peak 3
Probability (arb. units)
θ (radians)

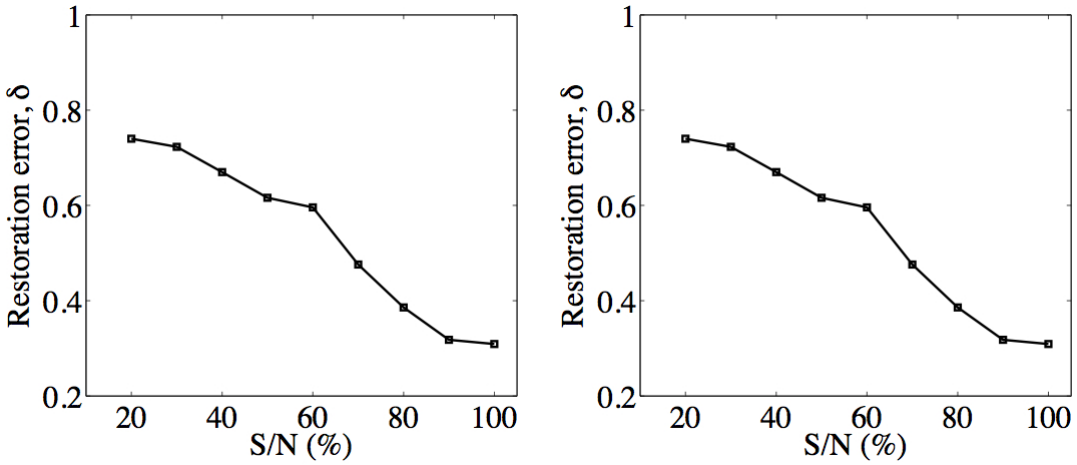

Figure 4.11: Restoration errors plotted as a function of S/N ratios, obtained by inverting noisy VMI images for the case of linear (left panel) or circular (right panel) polarisation of the probe laser pulse. Smaller values of δ correspond to most accurate retrieval.

to noise ratios of VMI simulated images. These images were obtained by adding different amplitude random noise to the same simulated clean image. The clean image corresponded to the VMI projection of a CEI ion cloud consisting of 1000000 trajectories, with a Gaussian velocity distribution whose centre corresponded to a kinetic energy of 12.5 eV. The angular distribution of the CEI ion cloud was given by the convolution of the molecular axis distribution ($M(\theta) = \cos^4(\theta)$) and the probe molecular orientation dependence which was given by A_1, or A_2 in case of linear or circular polarisations of the probe laser pulses. The resulting values of the restoration error are plotted as a function of S/N ratio, for the case of linear (left panel) or circular (right panel) polarisation of the probe laser pulse. It can be observed that the restoration error decreases steeply with increasing of the S/N ratio. In particular, a very similar restoration error is obtained in the case of a clean image ($S/N = 100\%$), and for $S/N = 90\%$. An error bigger than 1.5 times the error made in reconstructing the clean image is obtained for values of the S/N ratio smaller than 70%. It can be concluded that the accuracy in retrieving the molecular axis distribution increases with the S/N ratio.

4.4 Retrieving the molecular axis alignment from CEI experimental images

Once the algorithm was tested with simulated images, experimental images were acquired in order to test the performance of the program in retrieving the molecular axis distribution

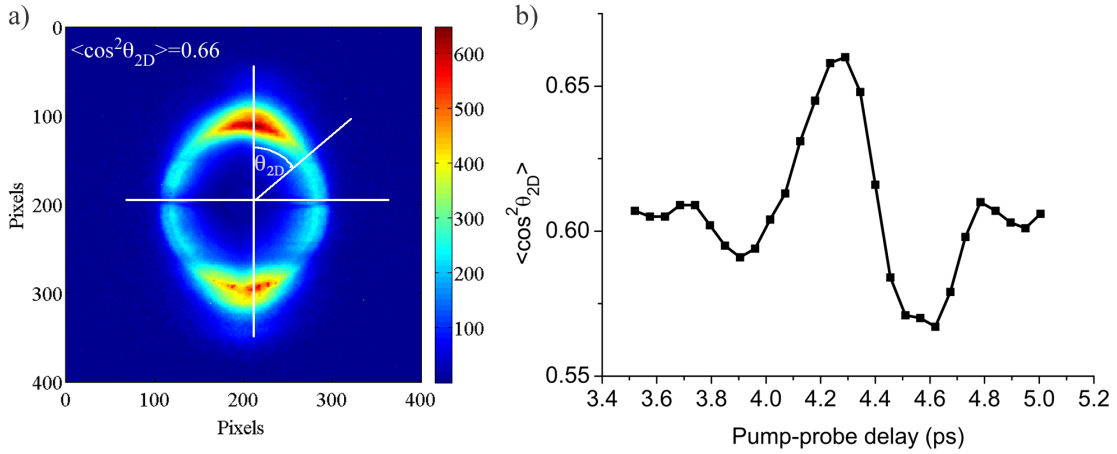

Figure 4.12: a) Definition of θ_{2D} as the angle between the projection of the ion position on the detector plane and the polarisation of the alignment laser pulse. b) Plot of $\langle \cos^2 \theta_{2D} \rangle$ as a function of the delay between the pump and the linearly polarised probe laser pulses.

from CEI experimental images. A pump-probe experiment was carried out, by using the experimental setup described in detail in Chapter 2. The pump laser pulse induced impulsive alignment on a sample of N_2 molecules, which were then Coulomb exploded through the interaction with the probe laser pulse. In order to show that the algorithm is able to deconvolute the probe orientational response from the molecular axis distribution, two sets of images were acquired. The first set was obtained by letting a linearly polarised probe laser pulse interact with a sample of N_2 molecules, aligned along the same direction as the polarisation of the probe laser pulse, while the second set of images was acquired by using a circularly polarised probe laser pulse. In both sets of measurements the same molecular axis distribution was induced by the pump laser pulse, with an intensity of $(3.5 \pm 0.6) \times 10^{13}$ W cm^{-2} and a Full Width at Half Maximum (FWHM) temporal duration of (45 ± 1) fs, and with the same gas conditions. The same FWHM temporal duration probe laser pulse, (13.5 ± 0.5) fs, was used in both cases, and the intensity of the probe laser pulse along the direction of pump laser linear polarisation was kept at the same value by means of a combination of a polariser and a waveplate (see Chapter 2), in order to achieve comparable signal levels. Since in the case of circular polarisation the laser field has also a component along the axis perpendicular to the direction of the field in case of linear polarisation, in an ideal situation the probe laser intensity in the case of circular polarisation should have been twice as high as in the case of linear polarisation. In the experiment, the estimated average probe laser intensities based on beam characterisation measurements, were $(1.7 \pm 0.5) \times 10^{15}$ W cm^{-2} and $(5 \pm 0.3) \times 10^{14}$ W cm^{-2}, for

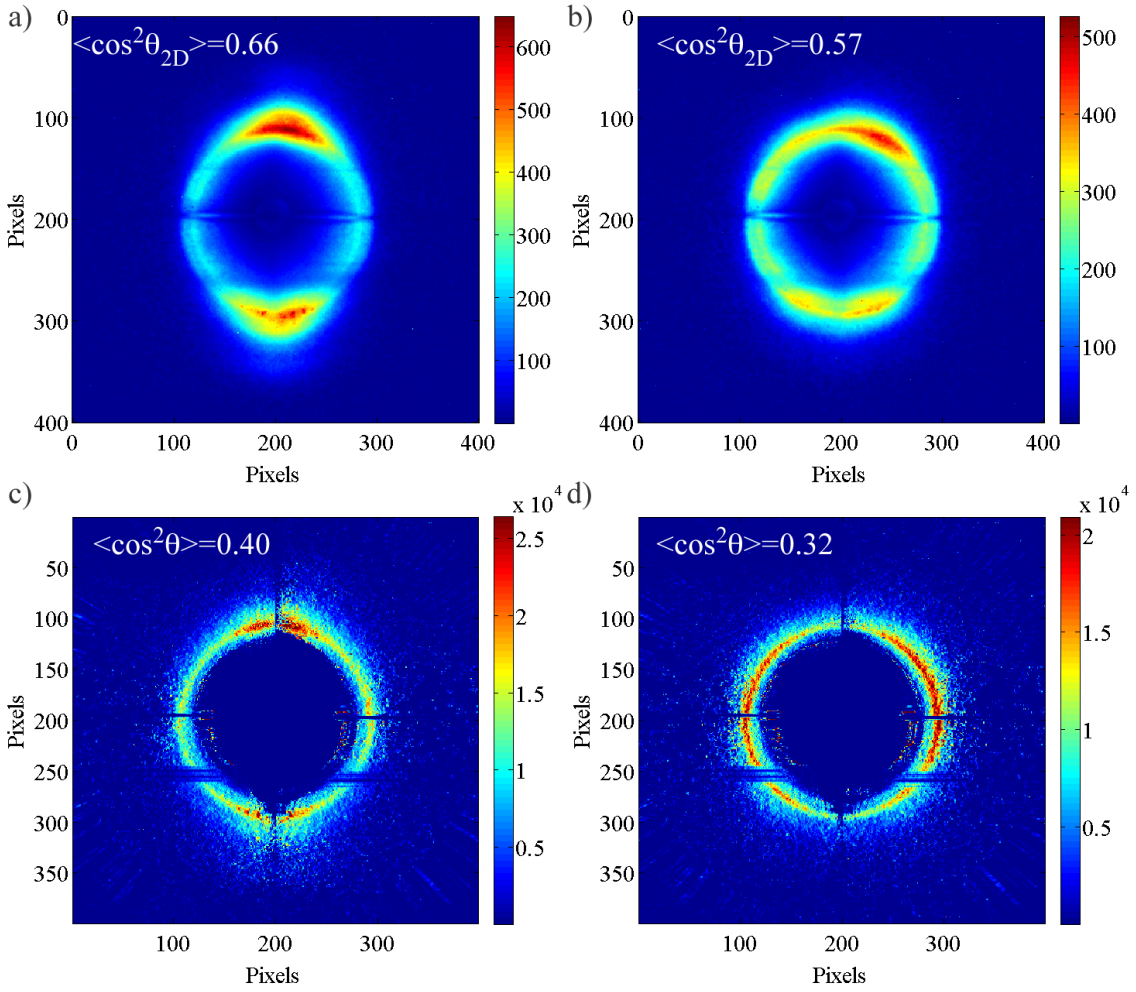

Figure 4.13: Images obtained from a sample of N_2 molecules by using the linearly polarised probe laser pulse, delayed with respect to the pump laser pulse of: a) $\approx$ 4.3 ps, and b) $\approx$ 4.6 ps, corresponding to the alignment and the anti-alignment peaks, respectively. The corresponding reconstructed 2D slices of the 3D cloud of ions are shown in panels c) and d).

circular and linear polarisations respectively. The ions produced by Coulomb explosion were accelerated towards the detector in the electric field generated by applying $V_R = 1$ kV and $V_E = 0.75$ kV voltages on the VMI electrodes. Only the N^+ ions were detected by temporally gating the MCP gain. The MCP was gated at a repetition rate of 100 Hz, which was the same as the gas jet valve (see section 2.5.1 of Chapter 2 for timing details). In order to measure the probe molecular orientation dependence, for each set of measurements an image was acquired by allowing only the probe laser pulse interact with an isotropic sample of N_2 molecules. These images, shown in Chapter 3 (Fig. 3.21), were inverted and the corresponding retrieved probe molecular orientation dependences were extracted (see

Section 3.5 of Chapter 3). Images were then recorded around the half revival time. For N_2 molecules this occurs at about 4.2 ps after the interaction of the alignment laser pulse with the molecules, since the rotational period of N_2 is T_{rot} = 8.4 ps. The first image was acquired at a delay between the pump and probe laser pulses of about 3.5 ps. The other images were acquired by increasing the delay of the probe laser pulse 55 fs at a time. Each recorded image corresponded to an average over 2×10^4 laser shots interacting with the same number of molecular gas pulses. In order to have a rough estimation of the degree of alignment, the raw images were analysed. The degree of alignment, quantified by $\langle\cos^2\theta_{2D}\rangle$ where θ_{2D} is the angle between the projection of the ion position on the detector plane and the polarisation of the alignment laser pulse (see Fig. 4.12 (a)), was calculated for each acquired image, by using the algorithm described in Appendix D. The behaviour of $\langle\cos^2\theta_{2D}\rangle$ as a function of the delay between the pump and probe laser pulses is plotted in Fig. 4.12 (b) for the case of linear polarisation of the probe laser pulse. The effect of molecular axis alignment is observed as a modulation in the $\langle\cos^2\theta_{2D}\rangle$ when the delay between the pump and the probe pulses is varied. In order to retrieve the molecular axis distributions, deconvoluted from the probe angular response, the acquired images needed to be inverted. Only two images, acquired at the alignment and the anti-alignment peaks are shown in Fig. 4.13 (a) and (b). A background image acquired without the gas jet firing was subtracted from these and the other acquired images presented in this section. As already discussed in Section 3.5 of Chapter 3, the MCP response is not uniform. In particular there are some areas with very low sensitivity especially on the bottom part of the images. The centres of these images were calculated by using the algorithm described in Appendix B, and each quarter of each image was inverted separately, by using the regularised version of the algorithm presented in section 4.1. The probe angular responses used as inputs for the inversions were retrieved from each quarter of the inverted image shown in Fig. 3.24, and since the pump and probe laser pulses were polarised along the same direction, all the Euler angles were set to 0° in Eq. 4.5. The resulting 2D slices of the original 3D ion clouds are shown in panel (c) and (d) of Fig. 4.13. Apart from the centre line noise, it can be observed that the line corresponding to a lower sensitivity of the MCP in the bottom part of the image is much more visible after the inversion process. For each quarter of the inverted images, the value of the $\langle\cos^2\theta\rangle$ was calculated through the algorithm described in Appendix D, and the value averaged over the four quarters of each image was plotted as a function of the pump-probe delay. The resulting plot is

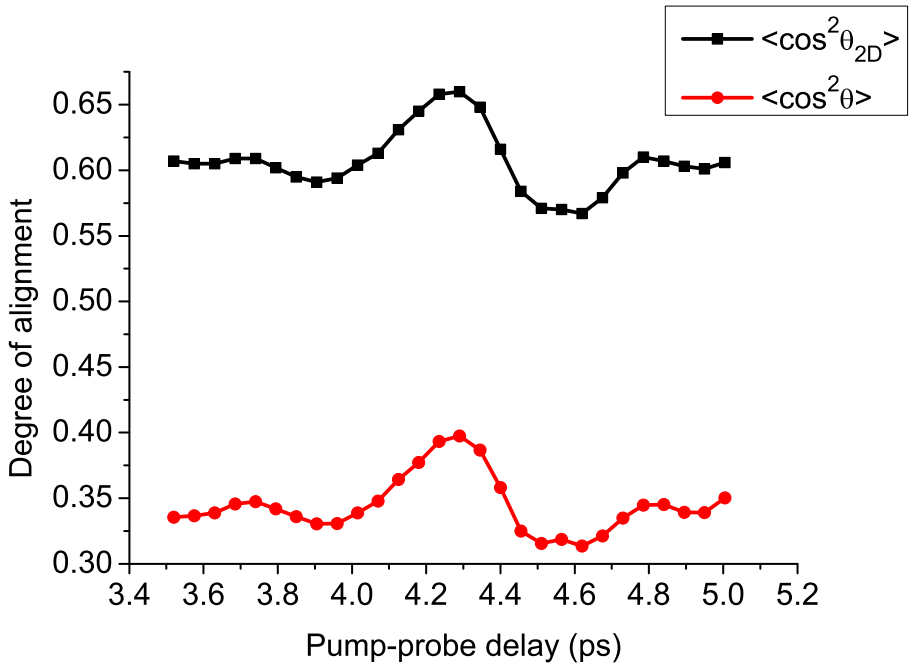

Figure 4.14: Plots of $\langle \cos^2 \theta_{2D} \rangle$ (black line), and $\langle \cos^2 \theta \rangle$ (red line) as a function of the delay between the pump and the linearly polarised probe laser pulses.

shown in Fig. 4.14, where for comparison also the $\langle \cos^2 \theta_{2D} \rangle$ curve is plotted. It can be noted that the degree of alignment induced by the pump laser pulse is not very high, since the maximum value of $\langle \cos^2 \theta \rangle \approx 0.40$ is only slightly raised from the value of 0.33, corresponding to an isotropic distribution.

Furthermore, the values of $\langle \cos^2 \theta_{2D} \rangle$ are much higher than the $\langle \cos^2 \theta \rangle$ values due to the fact that the inversion algorithm is able to take into account two effects, one of which is related to the projection process and hence affects any VMI image, whilst the other effect depends on the probe angular response:

1. The first effect is due to the fact that for each angle θ, all the ions lying on a slice of the Newton sphere perpendicular to the symmetry axis and corresponding to a value of the angle ϕ between 0 and 2π are projected into a line on the detector, as shown in Chapter 3 (see Fig. 3.1). As a consequence the resulting 2D image intensity is increased towards $\theta = 0°$, and hence the $\langle \cos^2 \theta_{2D} \rangle$ value is higher than the $\langle \cos^2 \theta \rangle$ value. This effect is shown in Fig. 4.15 where a simulated 2D slice of a 3D Newton sphere having a $A(\theta) = \cos^2 \theta$ angular distribution is compared to the corresponding 2D projected distribution. The $\langle \cos^2 \theta \rangle$ and the $\langle \cos^2 \theta_{2D} \rangle$ values extracted from these images resulted to be 0.59 and 0.75, respectively.

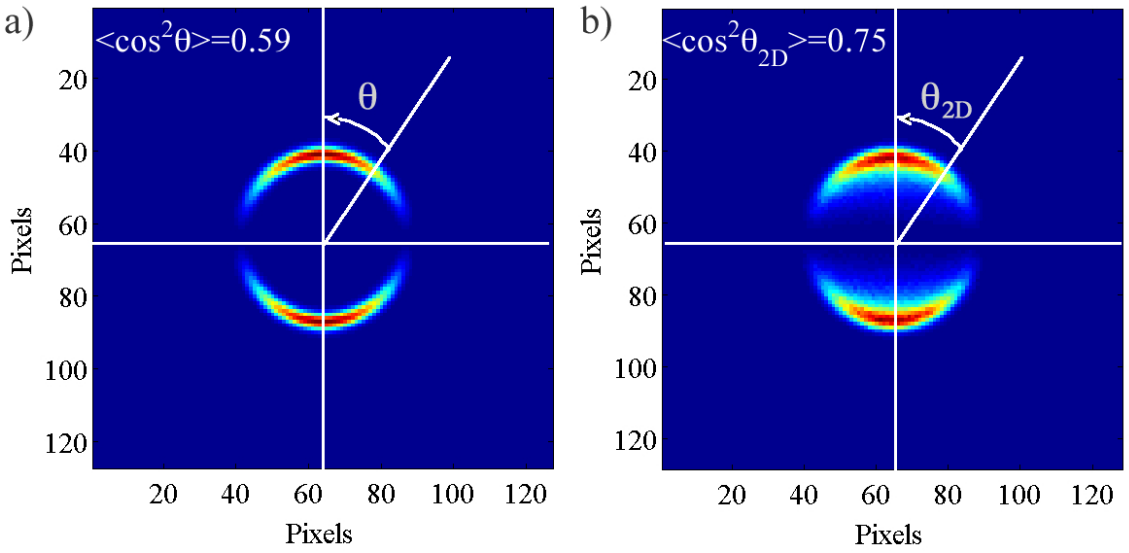

Figure 4.15: a) Simulated 2D slice, and b) VMI 2D projected image of a 3D Newton sphere having a $A(\theta) = \cos^2\theta$ angular distribution.

2. The second effect is due to the fact that the probe angular response is not uniform, as can be seen from the image acquired with only the probe laser pulse interacting with the molecular sample, and shown in the last section of Chapter 3 (see Fig. 3.21), where it can be noted that the ions are more localised along the vertical axis. This non uniformity of the detection function leads to higher detection efficiency for molecules aligned along the vertical axis ($\theta = 0°$), which are parallel to the direction of polarisation of the alignment laser pulse. Therefore, the images acquired when the probe laser pulse interacts with samples of aligned molecules are more peaked toward $\theta = 0°$. This results in an overestimation of the degree of alignment extracted from the raw images $\langle\cos^2\theta_{2D}\rangle$.

A second set of images was acquired with the circularly polarised probe laser pulse, and the same analysis described above was performed on these images. In Fig. 4.16 the images corresponding to the alignment and the anti-alignment peaks are shown in panel (a) and (b), while the corresponding reconstructed 2D slices of the 3D ion clouds are shown in panels (c) and (d). The quality of the acquired images is even worse than that of the images acquired with the linearly polarised laser pulse. Although the same voltages were applied on the MCP plates in both set of measurements, it seems that the MCP was saturating in some points when the circularly polarised probe laser beam was used. This effect, together with the fact that the gain of the MCP was not uniform, resulted

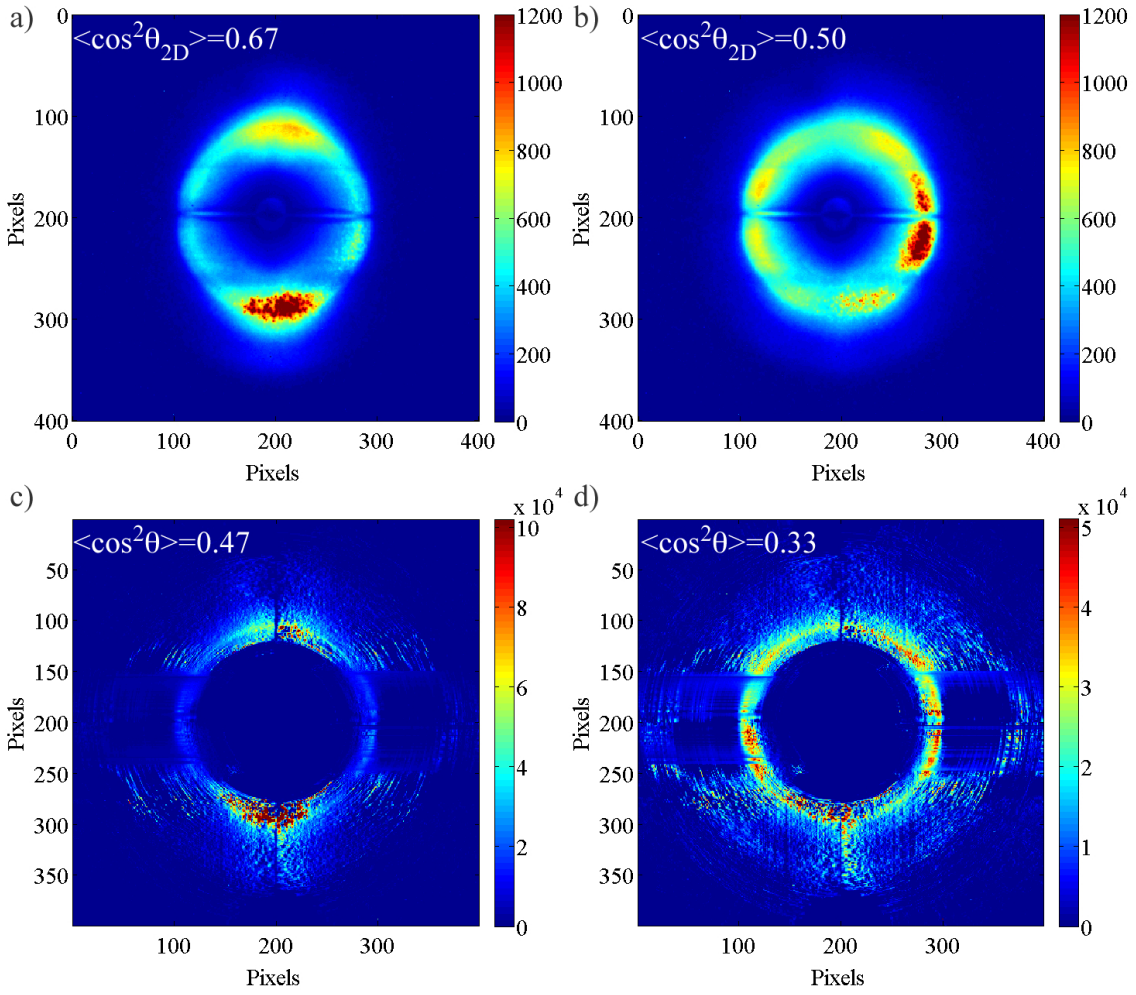

Figure 4.16: Images obtained from a sample of N_2 molecules by using the circularly polarised probe laser pulse, delayed with respect to the pump laser pulse of: a) ≈ 4.3 ps, and b) ≈ 4.6 ps, corresponding to the alignment and the anti-alignment peaks, respectively. The corresponding reconstructed 2D slices of the 3D cloud of ions are shown in panels c) and d).

in a low quality of the inverted images. Even so, the reconstruction of the molecular axis distribution is reasonably accurate. Both the $\langle \cos^2 \theta \rangle$ and $\langle \cos^2 \theta_{2D} \rangle$ are plotted as functions of the pump-probe delay in Fig. 4.17. It can be observed that the distribution at the anti-alignment peak is entirely isotropic since the corresponding $\langle \cos^2 \theta_{2D} \rangle$ and $\langle \cos^2 \theta \rangle$ values are 0.5 and 0.33, respectively. A higher degree of alignment is extracted from all the other acquired and inverted images. This represents an overestimation of the degree of alignment induced by the pump laser pulse, which could be related to the poor quality of the acquired images.

In conclusion, these measurements show the ability of the algorithm in retrieving the

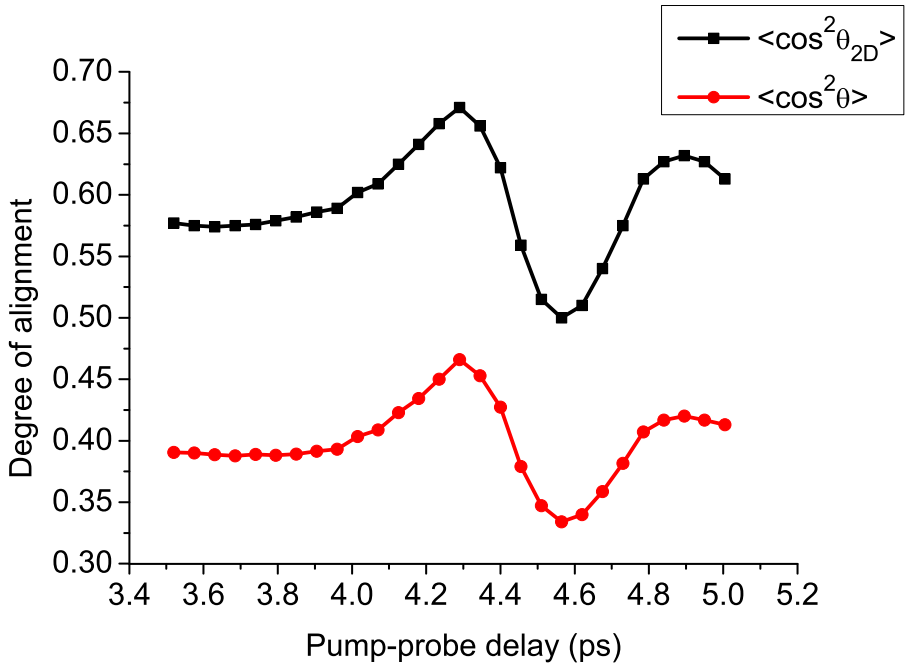

Figure 4.17: Plots of $\langle \cos^2 \theta_{2D} \rangle$ (black line), and $\langle \cos^2 \theta \rangle$ (red line) as a function of the delay between the pump and the circularly polarised probe laser pulses.

molecular axis distribution from velocity map images even in the case of poor quality images with highly non uniform detection, and low degree of alignment. However, due to the low degree of alignment, we were not able to compare the molecular axis distributions retrieved from the two sets of measurements taken by using either a linearly or circularly polarised probe laser pulse.

4.5 Retrieving the molecular axis alignment from Stapelfeldt experimental images

In order to show the ability of the algorithm in inverting images in the case where the Coulomb explosion cloud does not have a cylindrical symmetry, we tested it with some VMI high quality images acquired for us by Henrik Stapelfeldt's group in Aarhus. Two laser systems, an injection-seeded, 20 Hz, 10 ns Nd:YAG laser operating at 1064 nm, and a regeneratively amplified, 130 fs, 2.3 mJ/pulse, 1 kHz Ti:sapphire laser operating at 800 nm, were used for the generation of the images. The 1064 nm laser beam was linearly polarised, and was used as a pump to induce molecular axis alignment on a sample of molecules. Given the long temporal duration (10 ns) of the alignment laser pulses, adiabatic alignment

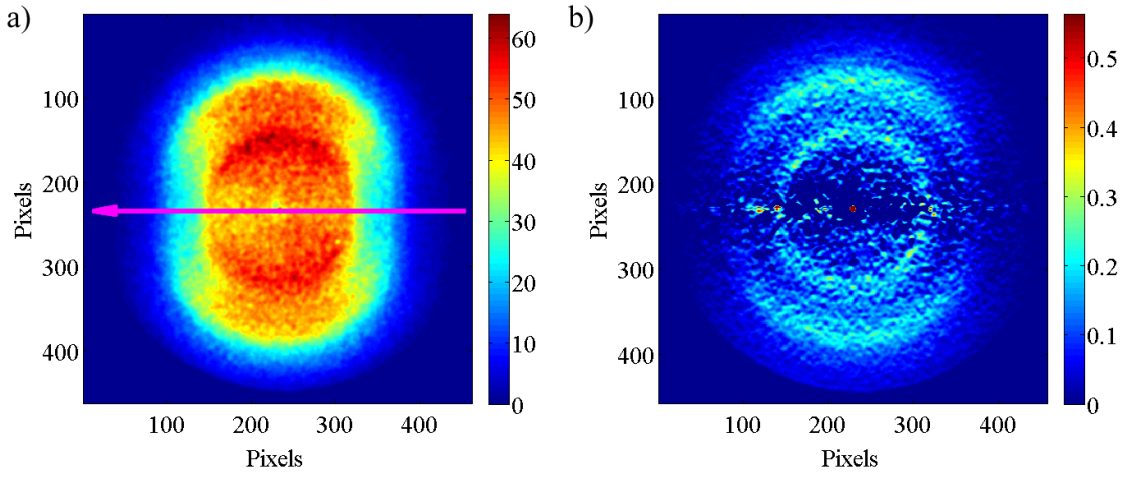

Figure 4.18: a) Experimental image acquired through the interaction of the circularly polarised probe laser beam with an isotropic sample of 1,4-diiodobenzene molecules. b) Corresponding reconstructed 2D slice of the 3D ion cloud, obtained by using the regularised algorithm described in Chapter 3. The arrow in image a) indicates the propagation direction of the probe laser beam.

was generated [15]. This alignment was probed by a circularly polarised 800 nm laser pulse, which arrived at the peak of the alignment laser pulse and generated Coulomb explosion of the molecules. The ions produced in this process were accelerated in a VMI system towards a detector system. The molecular species investigated are 1,4-diiodobenzene, and iodobenzene.

We first present the results obtained by analysing the images acquired with the 1,4-diiodobenzene molecules. A first image was acquired by letting only the probe laser beam interact with an isotropic sample of molecules. This image is shown in Fig. 4.18 together with the corresponding inverted image, obtained by using the regularised algorithm described in Chapter 3. The probe angular response extracted from the inverted image was rotated by setting the Euler angles equal to 90° in Eq. 4.5, and then deconvoluted from two images acquired for different intensities of the alignment laser beam $I_1 = 7.7\times10^{11}$ W cm^{-2} and $I_2 = 1.53 \times 10^{11}$ W cm^{-2}. These images are shown in Fig. 4.19 (a) and (c) together with the corresponding inverted images (Fig. 4.19 (b) and (d), respectively) obtained by using the regularised algorithm described in Section 4.1. The expectation values of $\langle\cos^2\theta\rangle$, which indicate the degree of molecular alignment induced by the alignment laser pulses, were extracted from the inverted images and compared to the expectation values $\langle\cos^2\theta_{2D}\rangle$ extracted from the raw images. The procedure that was followed to calculate $\langle\cos^2\theta\rangle$ and $\langle\cos^2\theta_{2D}\rangle$, whose resulting values are listed in table 4.7, is described in Appendix D.

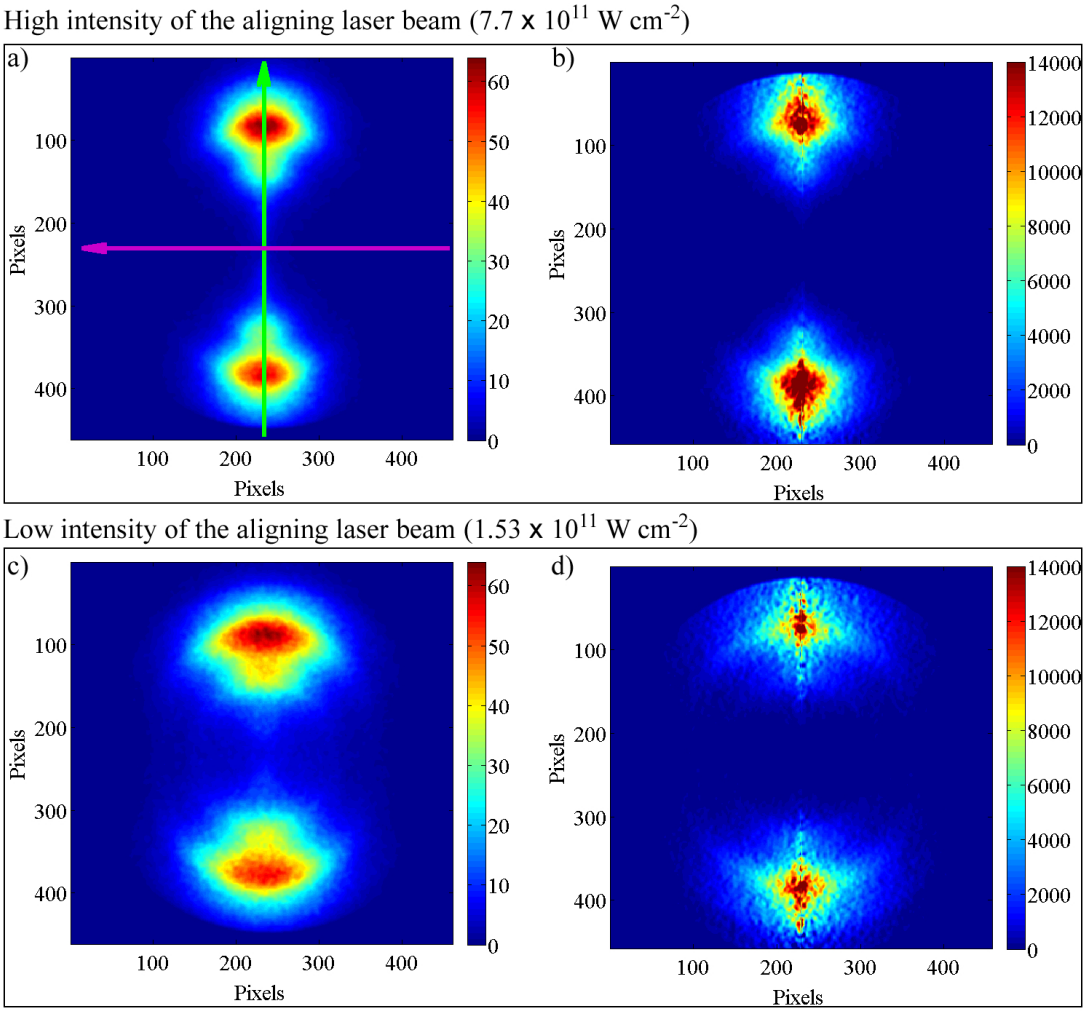

Figure 4.19: Images acquired at two different intensities of the alignment laser beam a) $I_1 = 7.7 \times 10^{11}$ W cm^{-2}, or c) $I_2 = 1.53 \times 10^{11}$ W cm^{-2} (b). The reconstructed 2D slices of the 3D ion clouds are shown in panel b) and d) and are obtained by inverting images a) and c), respectively. The arrows in image a) indicate the propagation direction of the probe laser beam (magenta) and the polarisation direction of the alignment laser beam (green).

From this table it can be noted that for both images the $\langle \cos^2 \theta \rangle$ value is smaller than the corresponding $\langle \cos^2 \theta_{2D} \rangle$ value extracted from the raw images. This is in agreement with what we expected, considering the two effects discussed in the previous section. It is clear that the probe angular response is not uniform, as can be seen from both the acquired and inverted images in Fig. 4.18, where it is evident that the ions are more localised along the vertical axis. This is also confirmed by the expectation value of $\cos^2 \theta$ extracted from the inverted image, $\langle \cos^2 \theta \rangle \approx 0.5$, that is bigger than the value corresponding to an isotropic distribution, 0.33. Therefore, also for these experimental images, the non

Intensity of alignment laser	$\langle\cos^2\theta\rangle$	$\langle\cos^2\theta_{2D}\rangle$
I_1	0.88	0.92
I_2	0.75	0.82

Table 4.7: Expectation values of $\langle\cos^2\theta\rangle$, and $\langle\cos^2\theta_{2D}\rangle$ calculated for the inverted and raw images, respectively, and corresponding to the images acquired with both pump laser intensities: $I_1 = 7.7 \times 10^{11}$ W cm^{-2} and $I_2 = 1.53 \times 10^{11}$ W cm^{-2}.

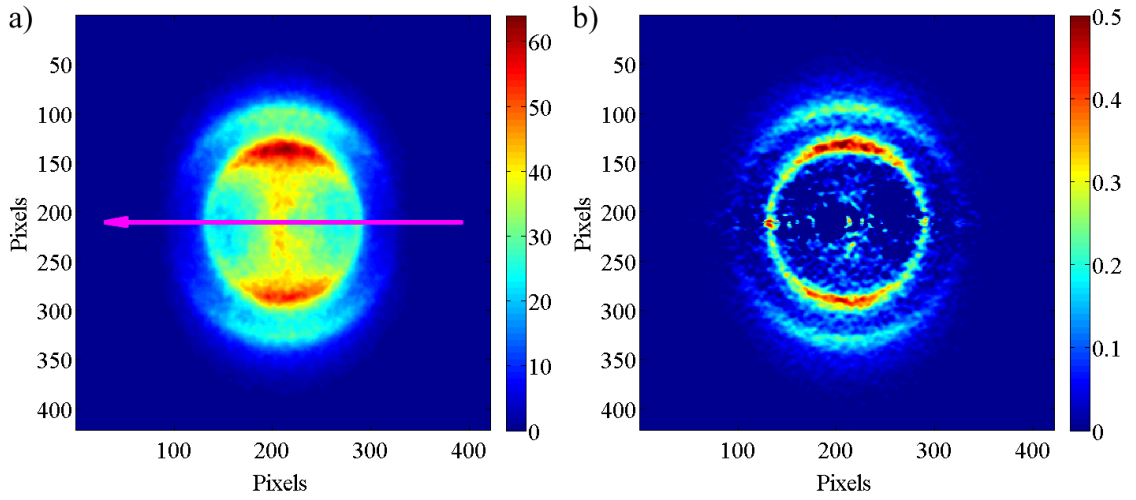

Figure 4.20: a) Experimental image acquired through the interaction of the circularly polarised probe laser beam ($I = 3.1 \times 10^{14}$ W cm^{-2}) with an isotropic sample of iodobenzene molecules. b) Corresponding reconstructed 2D slice of the 3D ion cloud, obtained by using the regularised algorithm described in Chapter 3. The arrow in image a) indicates the propagation direction of the probe laser beam.

uniformity of the detection function leads to a higher detection efficiency for molecules aligned along the vertical axis ($\theta = 0°$), which is parallel to the direction of polarisation of the alignment laser pulse. Therefore, the images acquired when the probe laser pulse interacts with samples of aligned molecules are more peaked toward $\theta = 0°$. This leads to an overestimation of the degree of alignment extracted from the raw images $\langle\cos^2\theta_{2D}\rangle$.

Another proof that the inversion algorithm presented in this chapter performs the inversion of good quality experimental images, allowing the inclusion of a non-uniform detection function, is given by the analysis of the images acquired for an aligned sample of iodobenzene molecules. The probe-alone image is shown in Fig. 4.20 together with the corresponding inverted image, obtained by using the regularised algorithm described in Chapter 3. The probe angular response extracted from the inverted image was rotated by setting the Euler angles equal to 90° in Eq. 4.5, and then deconvoluted from two images acquired for different intensities of the alignment laser beam $I_3 = 1.24 \times 10^{12}$ W cm^{-2}

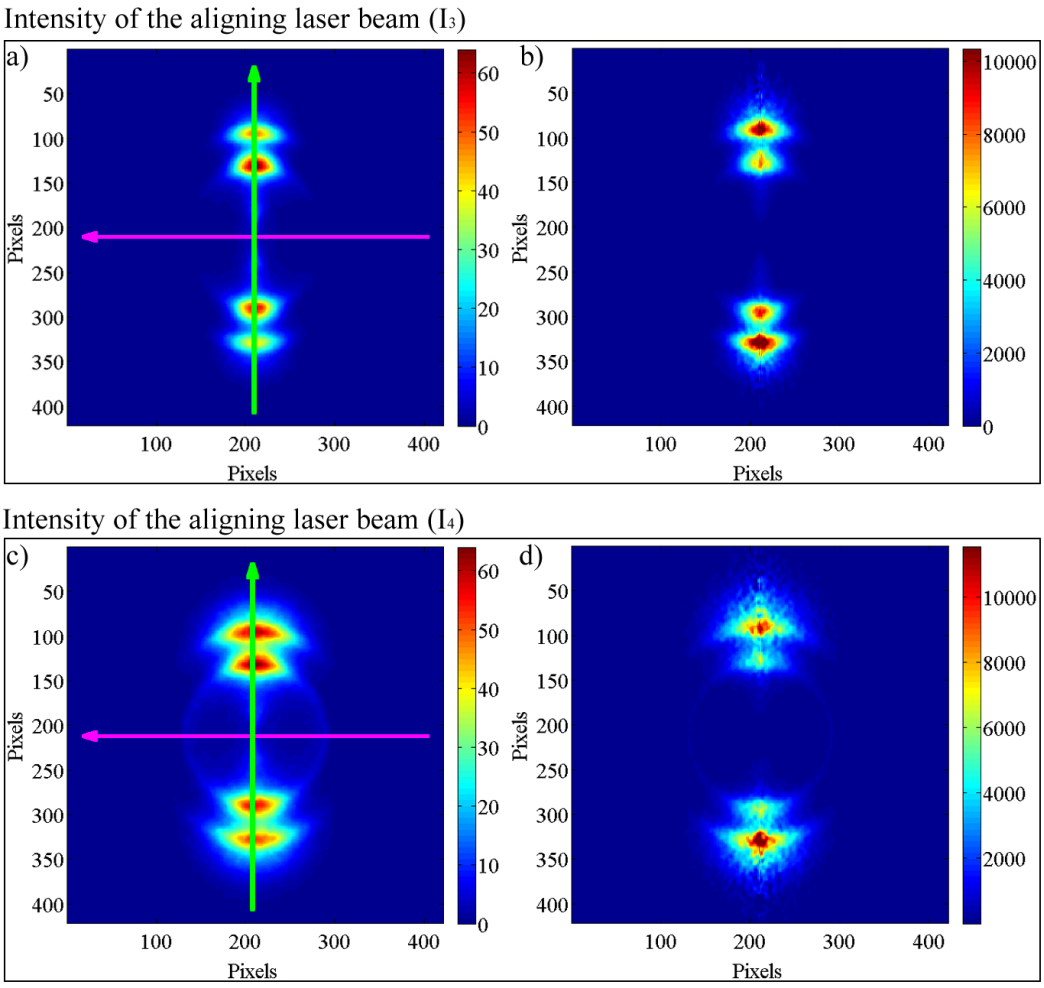

Figure 4.21: Images acquired at two different intensities of the alignment laser beam a) $I_3 = 1.24 \times 10^{12}$ W cm^{-2}, and c) $I_4 = 2.5 \times 10^{11}$ W cm^{-2}. The corresponding reconstructed 2D slices of the 3D ion clouds are shown in panel b), and d), respectively. The arrows in image a) indicate the propagation direction of the probe laser beam (magenta) and the polarisation direction of the alignment laser beam (green).

and $I_4 = 2.5 \times 10^{11}$ W cm^{-2}. These images are shown in Fig. 4.21 (a), and (c) together with the corresponding inverted images (Fig. 4.21 (b), and (d) respectively) obtained by using the regularised algorithm described in Section 4.1. The degrees of alignment, quantified by the expectation values of $\langle \cos^2 \theta \rangle$, were extracted from the inverted images by integrating over the radii relative to the outer channel ($R \in [100, 170]$) and compared to the corresponding expectation values $\langle \cos^2 \theta_{2D} \rangle$ extracted from the raw images. The resulting values are listed in table 4.8. For both images the $\langle \cos^2 \theta \rangle$ value is smaller than the corresponding $\langle \cos^2 \theta_{2D} \rangle$ value extracted from the raw images. This is in agreement with what we expected, considering the two effects discussed in the previous section.

Intensity of alignment laser	$\langle\cos^2\theta\rangle$	$\langle\cos^2\theta_{2D}\rangle$
I_3	0.94	0.97
I_4	0.88	0.93

Table 4.8: Expectation values of $\langle\cos^2\theta\rangle$, and $\langle\cos^2\theta_{2D}\rangle$ calculated for the inverted and raw images, respectively, and corresponding to the images acquired with pump laser intensities: $I_3 = 1.24 \times 10^{12}$ W cm^{-2} and $I_4 = 2.5 \times 10^{11}$ W cm^{-2}.

These tests show that the inversion algorithm presented in this chapter allows the retrieving of the molecular axis distribution induced by the alignment laser beam also in the case where the Coulomb exploded ion cloud does not have an axis of cylindrical symmetry.

4.6 Conclusions

In this chapter we have presented a new inversion algorithm which allows the inclusion of a non-uniform detection function, leading to the retrieval of the molecular axis distribution deconvoluted from the molecular orientation dependence of the Coulomb explosion probe. The tests performed show that the algorithm is able to retrieve the molecular axis distribution with high accuracy in the case of clean images as long as the the probe molecular orientation dependence is sufficiently broad so as to ionise a substantial fraction of the aligned molecules. The accuracy in retrieving the molecular axis distribution decreases with decreasing of signal to noise ratio. Furthermore, inversion of experimental velocity map images have been presented. These inversions have shown that the algorithm works well also in the case of poor quality images with highly non uniform detection, and low degree of alignment. The accuracy in retrieving the molecular axis distribution increases with the increasing of the quality of the experimental acquired images.

Chapter 5

High-order harmonic generation in aligned molecules from mid-IR fields

5.1 Introduction

High-order harmonic generation in atomic and molecular gases has been extensively studied during the past few decades, both theoretically and experimentally. The initial interest in this field was triggered by the idea of using the harmonic radiation as a new coherent extreme ultraviolet (XUV) source [204–207], since the harmonic radiation preserves the spatial and temporal coherence of the driving laser pulse [208–211], and also because the harmonics are emitted as a train of sub-femtosecond pulses, thus opening the possibility of measuring and controlling electron dynamics in atoms, molecules and solids with attosecond time resolution [212]. Initially, experiments were conducted in atomic gases and the dependence of the high-order harmonic efficiency and the cutoff position on different rare gases and laser parameters were studied. It was found that the highest order of the generated harmonics, corresponding to the cutoff in the spectrum, increases with the ionisation potential (I_p) through the relation $E_{\text{cutoff}} \approx I_p + 3.2\ U_p$, where $U_{\text{p}} \approx I\ \lambda^2$ is the ponderomotive energy depending on the laser intensity I, and wavelength λ [205]. This experimental observation was in agreement with the quasi-classical theory formulated by

Kulander *et al.* [105], and by Corkum [133], that describes the HHG as a three step process, as discussed in detail in Chapter 1. Also, was observed that the conversion efficiency of the HHG in atomic gases increases with the atomic mass, being favoured by higher atomic polarisabilities and lower ionisation potentials [205].

This last observation motivated a series of experiments aiming to generate high-order harmonics in molecules in order to find the optimal conditions to improve and control coherent XUV light emission [204, 206, 207]. Calculations based on the solution of the time dependent Schrödinger equation (TDSE) were done in order to simulate HHG spectra from molecules. Lappas *et al.* [213] found in calculations that the efficiency of some high-order harmonics generated in H_2^+ and H_3^{2+} with the laser field perpendicular to the molecular axis is up to three orders of magnitude higher than when the two are parallel. They attributed this effect to the fact that the perpendicular orientation of the molecule provides a higher recollision cross section for the electrons. The prediction of the dependence of HHG on the angle between the molecular axis and the polarisation direction of the driving laser field (θ) was soon confirmed by a first experiment performed by Velotta *et al.* on adiabatically aligned molecules of CS_2 and N_2 [50], and then by other experiments [51, 52], that showed a modulation of the HHG yield as a result of alignment in the molecular ensemble.

The observation of the dependence of HHG on the molecular axis orientation was important, not only because it could be a way to control the intensity of the XUV generated source, but also because it paved the way for the use of HHG in molecules for the investigation of molecular structure with sub-Angstrom spatial resolution and sub-femtosecond temporal resolution [53–55, 57]. The investigation of the molecular structure is possible because the harmonic spectrum generated by the interaction of a linearly polarised laser field with a molecule is proportional to the Fourier transform of the time-dependent expectation value of the dipole moment $D(t)$ [53], which is related to the properties of the ground state wavefunction Ψ_0 and the continuum Ψ_c, through the equation [56, 134]:

$$D(t) = \langle \Psi_c | - e\mathbf{r} | \Psi_0 \rangle \tag{5.1}$$

obtained by using the Single Active Electron (SAE) approximation and Strong Field Approximation (SFA). The SAE approximation assumes that only one electron, the one described by the Highest Occupied Molecular Orbital (HOMO), is involved in the HHG process [137]. The SFA assumes that the bound electrons are unaffected by the laser

field, and that after the ionisation the electron moves in the laser field unaffected by the Coulomb potential [56]. Furthermore, in the strong field approximation the continuum wavefunctions are expressed as a superposition of plane waves and then, in principle, the ground state wavefunction can be retrieved from complete measurements of the harmonic dipole phase and amplitude [56]. A more correct theory should imply antisymmetric multielectronic wavefunctions, which include indistinguishability of electrons and Pauli exclusion principle. In that case the orbital reconstructed from the HHG spectra is the Dyson orbital. However, in small molecules where the relaxation of orbitals upon ionisation can be neglected (i.e. when Koopmans' theorem applies [214]), the HOMO is a good approximation to the Dyson orbital [215].

Information about the structure and symmetry of the HOMO, are encoded in the HHG spectra since two of the three steps of the HHG process (ionisation and recombination) depend on the shape of the HOMO. Experimental and theoretical work have demonstrated that for molecules aligned along the polarisation direction of a linearly polarised driving laser field, ionisation is suppressed when the electronic cloud lies perpendicular to the molecular axis (laser field polarisation), and it is enhanced when the electronic cloud lies parallel to the molecular axis [63–65, 87, 122, 216]. The suppression of ionisation results in the ionisation saturation[1] being reached at a higher intensity, implying an extension of the harmonic cutoff as obtained by Shan *et al.* in O_2 [217].

The other step affected by the symmetry of the HOMO is the recombination, which has been widely investigated, first theoretically and then experimentally [52–59, 94, 143, 218]. Numerical calculations of HHG for H_2^+ and H_2 molecules in linearly polarised laser pulses showed the appearance of intensity minima in the HHG spectra for certain harmonic orders [94, 136]. Also, the location of the minimum depends on the angle between the molecular axis and the driving harmonic laser field [65, 94, 136], as shown in Fig. 5.1. The appearance of these minima was explained as the result of the interference between the dipole amplitude from the two indistinguishable atomic centres in the molecule when they are separated by half the de Broglie wavelength λ_{dB} of the returning electron [94]. The positions of the minima found in the spectra verified the double-slit-type interference conditions (see Fig. 5.2), given in the following equations for constructive and destructive

[1]The expression "ionisation saturation" is used to indicate the situation when all the sample molecules have been ionised, and thus no more ionisation can occur.

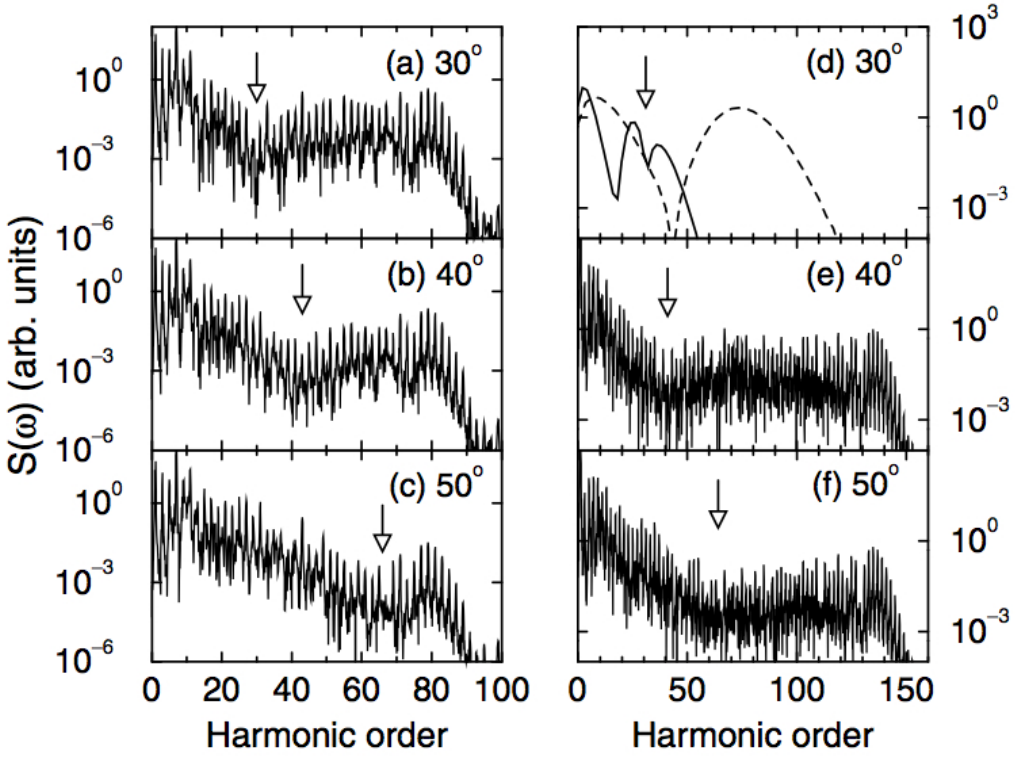

Figure 5.1: Spectra of harmonics polarised parallel to the laser field for 2D H_2^+. The angle between the molecular axis and the polarisation axis is as indicated. Left: 780 nm pulses of 5.3×10^{14} W cm^{-2} intensity. Panel (d): Recollisions corresponding to the 31st (solid line) and 75th harmonic (dashed line). Panels (e),(f): 780 nm pulses of 5.3×10^{14} W cm^{-2} intensity. The arrows point out the position of the interference minimum. Taken from [94].

interference, respectively:

$$\begin{aligned} \mathrm{R}\cos\theta &= (n\,\lambda_{\mathrm{dB}}) \\ \mathrm{R}\cos\theta &= \left(n+\frac{1}{2}\right)\lambda_{\mathrm{dB}} \end{aligned} \tag{5.2}$$

with R being the internuclear distance, θ being the angle between the molecular axis and the driving laser field, and n being an integer. In antisymmetric orbitals the π phase difference between the lobes centred in each atom adds to the phase of the recombining electron wavefunctions, reversing the interference conditions *i.e* the first condition corresponds to destructive and the second to constructive interference. These equations, which assume the single active electron and the strong field approximations, allow in principle measurement of the internuclear distance of the molecules with ultrafast time resolution.

The experimental confirmation of the two-centre interference effect was obtained by two different groups [54, 55] that investigated the HHG in non-adiabatically aligned samples of

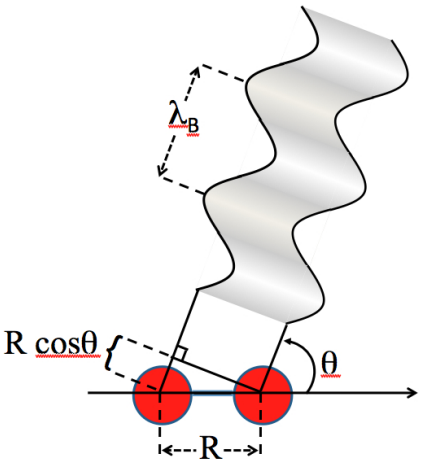

Figure 5.2: Schematic of the two point emitters model for a diatomic molecule. λ_{dB} is the de Broglie wavelength of a free electron, θ is the angle between the molecular axis and the driving laser field, R and $R\cos\theta$ are the internuclear distance and its projection, respectively. In the recombination process, the destructive or constructive interference takes place depending on the conditions defined in Eq. 5.2.

CO_2 molecules. Although CO_2 is a triatomic molecule, it was considered a good candidate for the observation of the interference minimum since it is linear, its π_g HOMO can be regarded as a combination of two atomic p-orbitals centred at each oxygen atom, and also because the distance between the two oxygen atoms is larger than the distance between atoms in common diatomic molecules, making the conditions for the observation of the interference effect favourable [137]. Kanai *et al.* measured simultaneously the ionisation yield and the HHG spectra, and observed that HHG was suppressed in a particular region of the spectrum (around the 27th harmonic) where the ionisation was enhanced [54]. This result suggested that the minimum found in the HHG spectrum at the 27th harmonic originated only from the recombination process. A similar experiment was performed by Vozzi *et al.* [55], who observed a minimum in the HHG spectrum from CO_2 at a different harmonic order, 33rd harmonic. These different results raised some doubts about the approximations used to simulate and interpret the interference minimum. Recently, calculations of HHG in aligned sample of CO_2 [93, 96] have shown that the minimum found in the HHG spectrum cannot be simply predicted by Eq. 5.2, since multiple electron orbitals are involved in the HHG process, therefore the SAE is not a valid approximation. A consequence of this result is the dependence of the position of the minimum on the intensity of the harmonic driving laser pulse [93, 96], which could explain the different position of the minimum observed by Sakai and Vozzi groups. On the other hand, acquiring HHG spectra in aligned molecules for different laser intensities in order to monitor the

behaviour of the position of the minimum is a challenging task. This and other challenges in HHG spectroscopy are discussed in the next section.

5.1.1 Challenges in HHG spectroscopy

Different parameters related either to the laser beam or to the molecular target are fundamental in HHG experiments. As stated before, the modulations of HHG spectra, which are related to the angle θ between the molecular axis and the polarisation direction of the driving laser field, encode the structure and symmetries of molecular orbitals. Therefore, one of the key steps in observing these structures is controlling the angle θ, i.e fixing the orientation of the molecular sample with respect to the driving laser beam. This can be done by inducing impulsive molecular axis alignment on the molecular sample by letting the isotropic sample of molecules interact first with an aligning laser pulse [12]. In order to obtain a high degree of alignment the molecular sample has to be rotationally cold. However, the distance between the nozzle of the gas jet and the interaction point has to be set in order to obtain a molecular sample at the interaction point not only rotationally cold, but also dense enough ($>10^{16}$ molecules cm^{-3}) in order to generate sufficient HHG signal.

The spatial resolution for the extraction of the structural information encoded in HHG spectra is determined by the de Broglie wavelength of the recolliding electron. The shorter this wavelength, or the higher is the generated harmonic order, the better is the spatial resolution. In particular, in order to record structural features arising from typical internuclear distances of 1 - 2 Å, a harmonic spectrum reaching significantly more than 50 eV is required. Since the highest harmonic generated corresponds to an energy of the returning electron of ≈ 3.2 U_p, where the ponderomotive energy $U_p \approx I\lambda^2$ (with I and λ intensity and wavelength of the laser pulse, respectively), the choice of the intensity and wavelength of the laser beam is crucial for optimising the spatial resolution.

The highest laser intensity that can be used to generate harmonics is limited by the ionisation saturation intensity [219]. Since the ionisation saturation intensity increases with the ionisation potential of the molecule [56], previous experiments, performed using a standard 800 nm Ti:Sapphire laser, have focused on the study of few molecular systems with relatively high ionisation potentials ($\geq$13 eV), typically N_2 and CO_2 [51–55]. For these molecules, in fact, intensities as high as 3×10^{14} W cm^{-2} can be used allowing the generation of harmonic spectra extending above 50 eV. However, the requirement of such

a high intensity for the investigation of these molecules limits the capabilities of intensity-dependent studies as the full structural contribution to the harmonic spectrum cannot be probed at the lower intensities. More recently, some experiments have been performed by using very short laser pulses (10 fs) to generate high-order harmonics in aligned sample of organic polyatomic molecules, having lower ionisation saturation intensities ($\approx 1.5 \times 10^{14}$ W cm^{-2}) [59]. Due to the intensity limitation, only harmonics up to 46 eV were detected, preventing the extraction of structural and dynamical information from the analysis of the HHG spectra acquired in aligned samples of these complex molecules.

The other crucial parameter is the laser wavelength. In principle, by increasing λ it is possible to extend the harmonic cutoff to higher photon energies whilst keeping the laser intensity below the saturation intensity [105, 133]. However, using a longer wavelength implies that after the ionisation the electron spends more time in the continuum before recombining with the parent molecule, and since the electronic wavepacket spreads in the continuum, the recombination probability decreases when using longer wavelengths. In particular, the harmonic efficiency scales as λ^{-5} or λ^{-6} [135].

Based on these considerations we carried out an experiment aiming to investigate the HHG in aligned samples of N_2, CO_2, N_2O, and C_2H_2, by using a driving laser beam with a wavelength of 1300 nm, longer with respect to that used in previous experiments (800 nm). The experimental apparatus and all the aspects of the experiment are explained in details in the following section, while the results of the experiment are presented and discussed in sections 5.3, 5.4, 5.5.

5.2 Experimental apparatus

This experiment was performed at the Artemis facility at Rutherford Appleton Laboratory. The optical setup, the molecular beam, and the detection system used in the experiment are described in this section.

5.2.1 Optical setup

A 1 kHz CPA Ti:Sapphire laser system comprising a two-stage laser amplifier system was used in this experiment (Red Dragon, KMLabs). The first amplification stage consists of a fourteen pass amplifier, which is pumped by a frequency doubled Nd:YLF laser from Photonics Industries. The second amplifier is a two pass amplifier pumped by two lasers

identical to the pump laser of the first amplifier. The output pulses have a central wavelength of 780 nm, an energy of about 14 mJ, and a near transform limited duration of 80 fs, which was measured with a SHG-FROG.

A schematic of the optical setup is shown in Fig. 5.3. The output laser beam was split in two by a 85/15 beam splitter. The reflected 85% beam was used to seed a commercial optical parametric amplifier (OPA), a HE-TOPAS-C from Light Conversion. The OPA output beam, which was used as the driving beam for high-order harmonic generation, consisted of pulses of 1300 nm, having an energy of 1 mJ and a temporal duration of 40 fs, as measured with a second order autocorrelator. The transmitted 15% beam was used as the pump beam to induce impulsive molecular alignment. This beam was sent to a motorised delay stage in order to control its delay with respect to the harmonic driving beam. The relative polarisation angle θ between the two laser beams was controlled by a half-waveplate, inserted in the pump beam path. The beams were recombined through a normal incidence dichroic mirror and sent collinearly into the vacuum chamber where they were focused onto the molecular beam through a 30 cm focal length lens. The corresponding foci were imaged through a CCD camera, and it was found that due to chromatic aberrations and different divergences, the two beams focused 5 mm away from each other. In order to compensate for this, a telescope with -500 mm and 1000 mm focal length lenses was inserted in the harmonic driving beam path. The second lens of the telescope was mounted on a translation stage so that the divergence of the beam was controlled in order to obtained the spatial overlap of the foci. Furthermore, this telescope was used to make the focus of the harmonic driving beam smaller than that of the aligning beam in order to probe a homogeneously aligned sample. The spatial overlap was checked by diverting the beams at the chamber entrance through a flip up mirror towards a lens, placed at an identical distance to the lens inside the chamber, and imaging the foci with a CCD camera.

The temporal overlap was obtained in two stages. First, a time overlap with a precision of few hundred fs was obtained by focusing the two beams through a lens and imaging the 1300 nm beam profile through a CCD camera placed some distance after the focus, whilst the 800 nm beam was blocked by a filter placed in front of the CCD. The 1300 nm far field pattern, which was monitored as a function of the delay between the two beams, changed if the 800 nm pulse arrived before or after it. This is due to the plasma created at the focus of the 800 nm beam distorting the 1300 nm beam. Once the temporal overlap

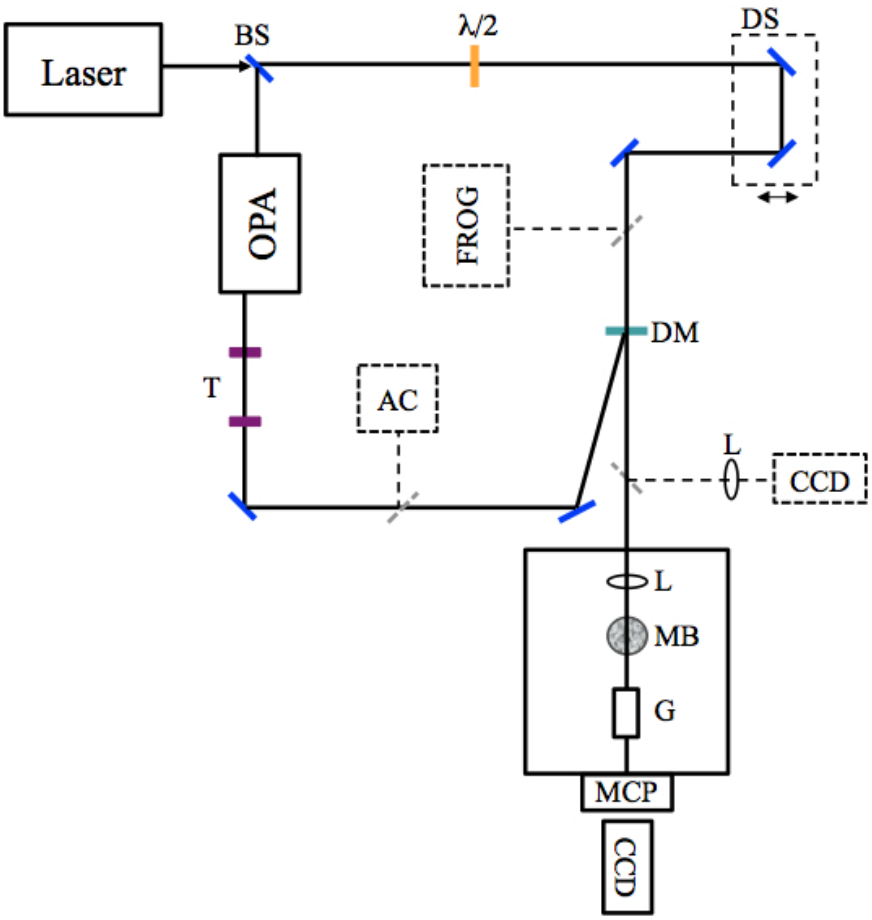

Figure 5.3: Schematic of the optical setup. Abbreviations: BS beam splitter (85/15); $\lambda/2$ half-waveplate; DS motorised delay stage; DM dichroic mirror; OPA optical parametric amplifier; T telescope composed of two lenses with focal lengths $f = -500$ mm and $f = 1000$ mm (represented in purple); L lens with a focal length $f = 300$ mm; MB molecular beam; G grating; MCP multichannel plates. The pump beam can be deviated through a flip mirror towards the FROG [167], while the probe can be deviated towards an autocorrelator (AC) for pulse duration measurements (dashed lines). Both beams can be deviated (dashed line) towards a lens L, before the vacuum chamber, for checking the spatial overlap.

was narrowed to this smaller range, a more precise overlap was obtained on a daily basis by focusing both beams into a gas jet of argon for harmonic generation. The 800 nm beam was apertured down until no detectable harmonics were present on the MCP. The beams were then temporally scanned in 25 fs steps and the intensity of the harmonics generated by the 1300 nm beam were monitored. A sharp increase in harmonic intensity was observed when the two beams overlapped, as discussed in detail in [220].

5.2.2 Molecular beam

A homemade nozzle obtained by drilling a 100 μm diameter hole in the middle of a Swagelok plug was used to generate a continuous cooled molecular beam by expanding the gas with a backing pressure of 2 bar through the hole into a vacuum chamber.

The vacuum chamber, which was pumped by a 2000 $\mathrm{l\,s^{-1}}$ turbo pump, consisted of the target area and the detection area. These areas were separated by a 2 mm differential pumping hole, which allowed to keep a sufficiently low pressure (below 10^{-5} mbar) in the detection area during the measurements, whilst the pressure in the target chamber was about 10^{-3} mbar. The temperature of the molecular beam at the interaction point, which lay at 180 μm below the nozzle, was estimated to be about 90 K [179], sufficiently cold to obtain a significant degree of molecular axis alignment.

Different species of linear molecules, with different ionisation potentials (I_p) and electronic structures, were used to produce the molecular beam: nitrogen (N_2), acetylene (C_2H_2), carbon dioxide (CO_2), and nitrous oxide (N_2O). Apart from N_2O, all the other molecules have been widely analysed in HHG experiments performed with a 800 nm harmonic driving laser beam [54, 55, 57, 59]. As a consequence, a comparison of the results obtained from the experiment described in this chapter and those obtained from previous experiments can be easily made. The choice of analysing also N_2O was determined by its similarity with CO_2. Both molecules, in fact, have a similar HOMO symmetry (π_g) and the same internuclear distance between the nitrogen atoms in N_2O and the oxygen atoms in CO_2. The relevant parameters of these molecules are summarised in table 5.2.2, while the highest occupied orbitals, which as explained in section 5.1 are responsible for the HHG spectrum features, are shown in Fig. 5.4. These HOMOs were calculated by Ricardo Torres using the package General Atomic and Molecular Electronic Structure System (GAMESS-UK), based on the Density Functional Theory (DFT), with the 3-21 G basis set [221].

Molecule	T_{rot} (ps)	I_p (eV)	Internuclear distance (Å)	HOMO symmetry
N_2	8.4	15.6	1.1	σ_g
C_2H_2	14.2	11.4	1.2	π_u
CO_2	42.7	13.8	2.3	π_g
N_2O	39.8	12.9	2.3	$\approx \pi_g$

Table 5.1: Relevant parameters for the molecules investigated in this experiment. Abbreviations: T_{rot} fundamental rotational period of the molecule; I_p ionisation potential. The internuclear distance corresponds to the distance between the carbon atoms, the oxygen atoms, and the oxygen and the outermost nitrogen atoms, for C_2H_2, CO_2, and N_2O, respectively.

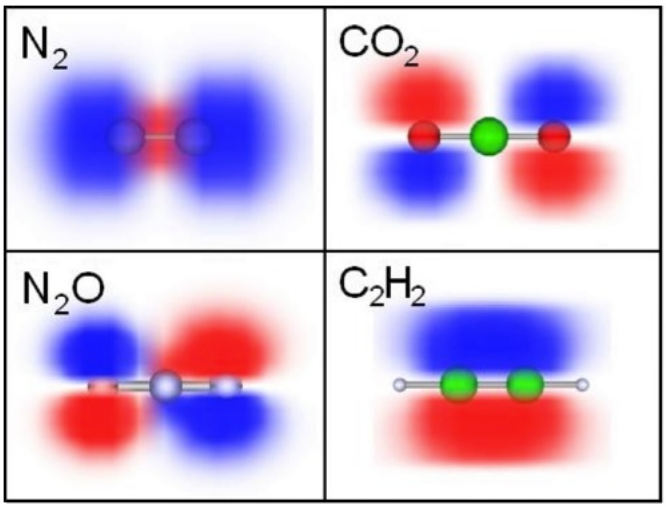

Figure 5.4: Highest occupied molecular orbital of the molecules investigated, calculated by DFT using GAMESS-UK with the 3-21G basis set. Blue and red colours correspond to positive and negative lobes of the orbital.

5.2.3 Detection and data acquisition system

The harmonics, generated by the interaction of the driving laser field with the molecular beam, propagated through the 2 mm diameter hole into the detection area towards a flat-field XUV spectrometer. This spectrometer consisted of a near grazing incidence (3°), 1200 lines/mm, curved grating and a detector. The main characteristic of the grating is that the grooves are not uniformly spaced, so that the spectrally dispersed radiation was focused onto a plane rather than onto a cylindrical section [222, 223]. The line spacing was arranged in such a way that the focal plane, where the detector was placed, was 20 cm away from the grating.

The position sensitive detector consisted of two imaging micro-channel plates (MCPs), mounted in a Chevron configuration, followed by a P46 phosphor screen (PS), which emitted green light and had a decay time of the order of 300 ns. A CCD camera (FDI

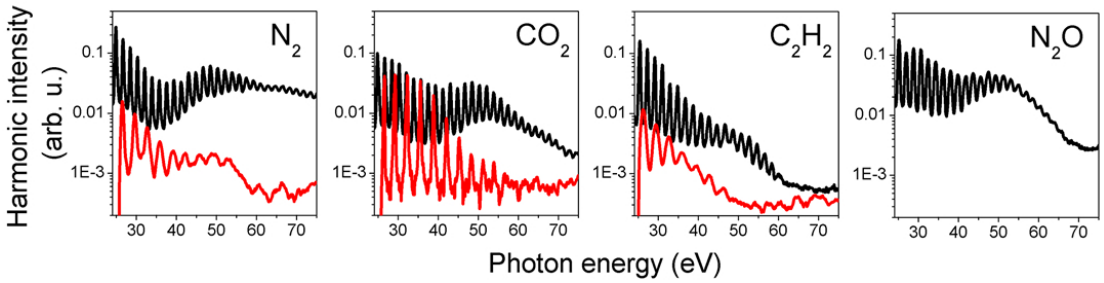

Figure 5.5: Harmonic spectra obtained from different unaligned molecular systems with 1300 nm (black lines), and 800 nm (red lines). The intensities of the driving laser beams at the interaction region for all the molecules investigated are listed in table 5.3.1. The harmonic intensity has been offset for clarity. Taken from [58]

Coolview) was placed behind the PS in order to record the HHG spectra and store them on a computer.

5.3 Results

5.3.1 Extension of the HHG cutoff

HHG spectra were first acquired from isotropic samples of molecules in order to investigate their shapes and in particular the cutoff energies. Therefore, only the 1300 nm driving laser beam was allowed to interact with each of the molecular species investigated. The acquired harmonic spectra, having the typical shape described in Chapter 1, are shown with black lines in Fig. 5.5. In the case of N_2 and CO_2 the cutoffs are not shown in the acquired spectra, since their energies are higher than the maximum detectable energy obtained with the experimental configuration used for all the measurements, which was 80 eV. For the other molecules, C_2H_2 and N_2O, the highest harmonic generated corresponded to an energy of 60 eV where the cutoffs can be clearly identified in the spectra. For comparison, also the harmonic spectra of N_2, CO_2, and C_2H_2, obtained in a previous experiment performed by Torres *et al.* [57, 59] using a 800 nm driving laser beam, are shown in red lines in the same figure. In this last case much lower cutoff energies, about 60 eV for N_2 and CO_2 and about 45 eV for C_2H_2, were obtained even though the laser intensities were typically higher than the ones used at 1300 nm (see table 5.3.1).

The advantage of the cutoff extension is evident particularly in the case of the C_2H_2 where the region of interest for observation of interference features is at about 50-55 eV. As can be seen from the acquired spectra, no harmonics are generated in this region by

Molecule	$I_{1300\,nm}$ (W cm^{-2})	$I_{800\,nm}$ (W cm^{-2})	$E_{1300\,nm}$ (eV)	$E_{800\,nm}$ (eV)
N_2	1.7×10^{14}	2.1×10^{14}	$>$ 80	$\approx$ 60
CO_2	1.4×10^{14}	2.1×10^{14}	$>$ 80	$\approx$ 60
C_2H_2	1.0×10^{14}	1.8×10^{14}	$\approx$ 60	$\approx$ 45
N_2O	1.0×10^{14}	//	$\approx$ 60	//

Table 5.2: Intensities of both the 1300 nm and the 800 nm driving laser beams at the interaction region for all the molecules investigated, and corresponding cutoff energies extracted from the harmonic spectra.

using the 800 nm laser beam at the ionisation saturation intensity, whilst photon energies up to 60 eV are detected in the case of 1300 nm at an intensity lower than the ionisation saturation intensity.

Although the harmonic efficiency was lower in the case of 1300 nm laser beam, the high repetition rate of the driving laser beam in the present experiment (1 kHz) helped somewhat to compensate the lower efficiency, improving the signal to noise ratio by averaging the signal over more laser shots. Therefore, the 1300 nm wavelength was considered a good compromise between cutoff energy and efficiency.

In a recent experiment we also observed that the harmonic efficiency could be increased while keeping the characteristic high cutoff energy of a long wavelength driving field by using a Superposition of Multiple UnRelated Frequency (SMURF) [220]. With a superposition of two laser fields of similar intensity and wavelengths of 1300 nm and 800 nm, we obtained an increase in the yield of the mid-plateau harmonics of more than two orders of magnitude compared to using the 1300 nm field alone. Theoretical calculations have shown that the enhancement in the harmonic efficiency is due to a modification of the electron trajectories in the sum field leading to an earlier return time [220]. This experiment has been further described in the thesis of Thomas Siegel (Imperial College London) [224].

5.3.2 HHG from aligned sample of molecules

In order to exploit the advantages of using longer wavelength driving fields in investigating the structure of molecules, and in making time resolved measurements of electron dynamics, HHG generated in aligned samples of molecules was investigated. Non-adiabatic molecular axis alignment was induced by the 800 nm pump beam, while the 1300 nm probe beam was used to generate high-order harmonics containing the structural information about the target molecules. The intensity of the pump laser beam was set in order

to optimise the degree of alignment without generating any harmonics in the monitored spectral region, and was set to $I_{\text{pump}} = 5 \times 10^{13}$ W cm^{-2}. The intensities of the probe beams used for each molecular species were chosen in order to generate the optimum harmonic spectra in terms of cutoff and efficiency. Both laser beams were linearly polarised along the same direction, so that the angle between the molecular axis and the polarisation direction of the driving laser beam, θ, was zero.

HHG spectra were acquired as a function of the delay between the driving and the aligning pulses, in order to investigate the modulations in the harmonic signals, which correspond to revivals of the aligned state of the molecules. These revivals occur at times corresponding to multiples of the fundamental rotational period of the molecules, T_{rot}, as explained in Chapter 1. In this experiment the delay range was set around the half-revival, corresponding to $T_{\text{rot}}/2$. Spectra were also recorded in the absence of an aligning field under identical condition in order to extract the signal ratio between the harmonics generated from aligned and isotropic samples of the investigated molecules. For each molecular species, a plot of the harmonic signal ratio as a function of photon energy (harmonic order) and delay time between the aligning and the driving laser pulses is shown in Fig. 5.6. Evidence of the dependence of the HHG signal on the structure of the HOMO, emerging from both the modulation and the presence/absence of an interference minimum in the harmonic signal, is encoded in these measurements.

The modulations found on the harmonic spectra generated in CO_2 and N_2O are very similar. In both cases, in fact, the modulation of the harmonic signal with respect to the time delay between the aligning and the driving laser pulses (t_{delay}) is much more pronounced at higher photon energies, precisely around the spectral region where two centre interference is expected (≈ 60 eV). A completely opposite situation is obtained in the case of N_2, where the intensity of the modulation of the HHG signal with respect to t_{delay} decreases with increasing photon energy. In the case of C_2H_2, instead, a quite similar modulation of the HHG signal as a function of t_{delay} is obtained for all photon energies. The similarity in the harmonic signal modulations for CO_2 and N_2O reflects the similarity of their electronic structure. In order to extract the relationship between this modulation and the molecular axis alignment, the degree of alignment, expressed as the average of the cosine squared of the angle θ between the polarisation direction of the driving laser beam and the molecular axis ($\langle \cos^2 \theta \rangle$), was calculated by Ricardo Torres by solving the time-dependent Schrödinger equation for the experimental conditions [23]. The

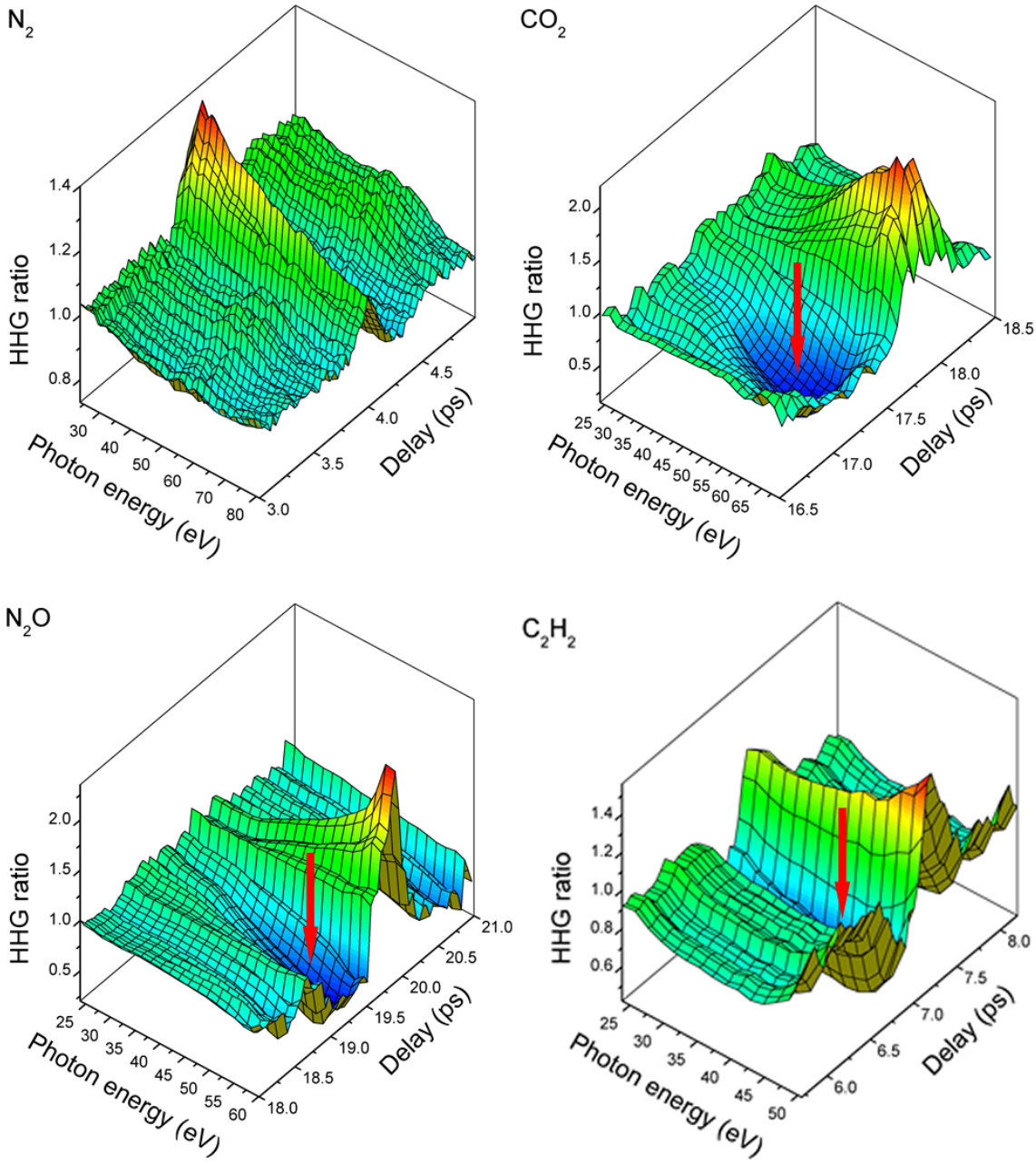

Figure 5.6: Ratio of harmonic signal between aligned and unaligned samples of N_2, CO_2, N_2O, and C_2H_2 as a function of photon energy (harmonic order) and of delay time between the aligning and the driving laser pulses. The laser intensities of the 1300 nm laser beams are: $I_{N_2} = 1.7 \times 10^{14}$ W cm^{-2}, $I_{CO_2} = 1.1 \times 10^{14}$ W cm^{-2}, $I_{N_2O} = 0.9 \times 10^{14}$ W cm^{-2}, $I_{C_2H_2} = 0.9 \times 10^{14}$ W cm^{-2}. The arrows mark the position of the minima.

resulting degree of alignment is plotted as a function of the delay time between the pump and probe laser pulses for each molecular species, as shown in Fig. 5.7. For comparison, the harmonic signal ratio of one harmonic (51st) in the plateau region, is plotted on the same graph for each molecular species. For N_2 the harmonic signal ratio is enhanced in

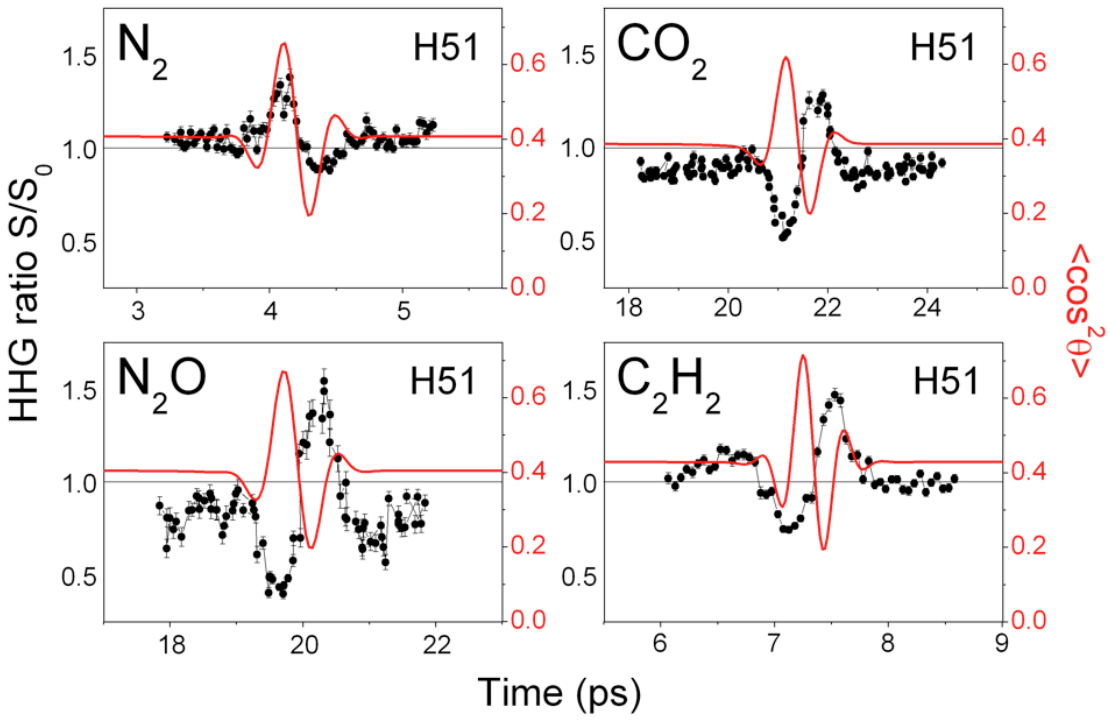

Figure 5.7: Black dots represent the ratio of 51st harmonic signal between aligned and unaligned molecular samples as a function of the delay between the driving and aligning pulses. Red lines represent the degree of alignment calculated by Ricardo Torres for the same experimental conditions.

correspondence with the maximum degree of alignment and suppressed when the degree of alignment is minimum (anti-alignment), that is when the molecular axis is localised around a plane perpendicular to the driving laser field. For the other molecules investigated, the modulation of the harmonic signal ratio is opposite to that of the degree of alignment. The reason for this behaviour is the presence of a nodal plane along the molecular axis direction in the HOMO of CO_2, C_2H_2, and N_2O molecules (see Fig. 5.4), that suppresses the ionisation when the driving field is parallel to the molecular axis.

The modulation in the harmonic spectra shown here are characteristic of the molecular orbital structure. Therefore, although it is not possible to extract the orbital structure from these measurements, this experiment shows that HHG has the power to distinguish different orbital symmetries. Also, since HHG spectra encode information on the attosecond time scale, HHG spectroscopy has the capability to track changes in electronic structure (electron dynamics) with attosecond time resolution.

Apart from the modulation of the spectra, a very interesting feature observed in Fig. 5.6 is a minimum in the harmonic signal ratio for CO_2, C_2H_2, and N_2O. This has already been

observed for CO_2 [54, 55], and recently also for N_2O [225], yet this is the first evidence of such a feature in the C_2H_2 HHG spectrum. The presence of this minimum can be interpreted as a structural feature due to the characteristic two centre structure of the HOMO of these molecules. In particular, as explained in section 5.1, the recombination amplitude from the two centres can interfere constructively or destructively if the returning electrons have a momentum p_e ($p_e = h/\lambda_{\mathrm{dB}}$, where h is the Planck's constant) corresponding to a de Broglie wavelength (λ_{dB}) that satisfies the condition expressed by Eq. 5.2. In the case of C_2H_2, which has a symmetric orbital, the first destructive interference occurs when the two centres are separated by half a de Broglie wavelength in the direction of electron propagation, which is the direction of polarisation of the driving laser beam. Therefore, considering that the internuclear distance between the two carbon atoms, which represent the two centres of interference, is 1.2 Å, destructive interference should be seen for electrons returning with a wavelength of 2.4 Å if the molecular axis is parallel to the driving laser field (i.e. $\theta = 0°$). Since in our experimental condition the most probable alignment angle of the molecules with respect to the driving field is $\approx 30°$, corresponding to the degree of alignment $\langle \cos^2\theta \rangle = 0.72$ (see Fig. 5.7), the condition of destructive interference is satisfied for a λ_{dB} approximately equals to 2.1 Å. This wavelength corresponds to an energy of the recombining electron, and so of the generated harmonic of 46 eV ($E = p_e^2/2m_e + I_p$, where m_e is the electron mass, and I_p is the ionisation potential), which is in perfect agreement with the minimum energy obtained from the experimental acquired spectrum. In previous experiments, the observation of the minimum in C_2H_2 spectrum was not possible since the use of a 800 nm driving laser beam only allowed the generation of harmonics up to 40 eV [57, 59].

In the case of CO_2 and N_2O the first destructive interference is expected when the two centres are one de Broglie wavelength apart (n = 2), since their HOMOs are π_g and similar to π_g, respectively. Since for both molecules the internuclear distance between the two centre interference atoms is 2.3 Å, the resulting minimum in the harmonic spectrum is expected at around 52 eV, in the experimental conditions. This result is obtained by using Eq. 5.2, which, as stated before, is obtained in the frame of a single active electron in the strong field approximation. Calculations done by using the strong-field eikonal- Volkov approximation [226], which includes electron exchange correlation and takes into account the angle dependent ionisation probability, predict the interference minimum in CO_2 at 60 eV [227]. Both values are compatible with the position of the minimum observed in

the experimental spectrum.

In the case of N_2, as predicted in some theoretical calculations [228, 229], no minimum is observed in the harmonic signal ratio due to the mixed symmetry of the N_2 HOMO.

The positions of the minima in the acquired spectra are in good agreement with the expected values calculated by using Eq. 5.2. If the minima in the spectra shown here are entirely determined by the nuclear structure of the molecules we expect their position to be independent of laser intensity.

5.3.3 Beyond the single active electron approximation

In order to establish the nature of the minimum in the harmonic spectrum generated from aligned samples of CO_2, different driving laser intensities in the range of (0.8 - 1.6)$\times 10^{14}$ W cm^{-2} were used to investigate HHG in this molecular species. The use of the 1300 nm driving laser allowed the generation of harmonic spectra with photon energies reaching beyond 60 eV for all the intensities used, facilitating the investigation of the dynamical interference model [93, 96] in the region of interest (40-70) eV, i.e the plateau, where the two centre interference minimum (referred to as "structural minimum") appeared. The dynamical interference model, recently proposed by Smirnova *et al.* [93, 96], is based on the observation that tunnel ionisation can populate several ionic states creating a multielectron wave-packet. This wave-packet, which can be visualised as a hole left in the valence shell of the molecule, evolves on an attosecond time-scale between the ionisation and the recombination process. During the recombination the contributions from different ionic states can interfere destructively, giving rise to a minimum in the HHG spectrum. The spectral position of this minimum does not depend on the nuclear structure of the molecule, but on the recollision time. As such, this minimum is laser intensity dependent. This theory has been confirmed by an experiment performed with a 800 nm driving laser [93], which has shown that the minimum in the harmonic spectrum from aligned molecules in CO_2 depends on the laser intensity, and shifts by $\approx$ 20 eV for laser intensities of (0.5 - 2.0)$\times 10^{14}$ W cm^{-2}. According to this model, at longer wavelengths the interference minima should appear at lower photon energies.

The acquired HHG spectra normalised to those obtained from isotropic samples of CO_2, are plotted as a function of photon energy and delay time between the aligning and the driving laser pulses in Fig. 5.8, for four different intensities. Surprising results are obtained from these measurements. First of all the interference minimum does not

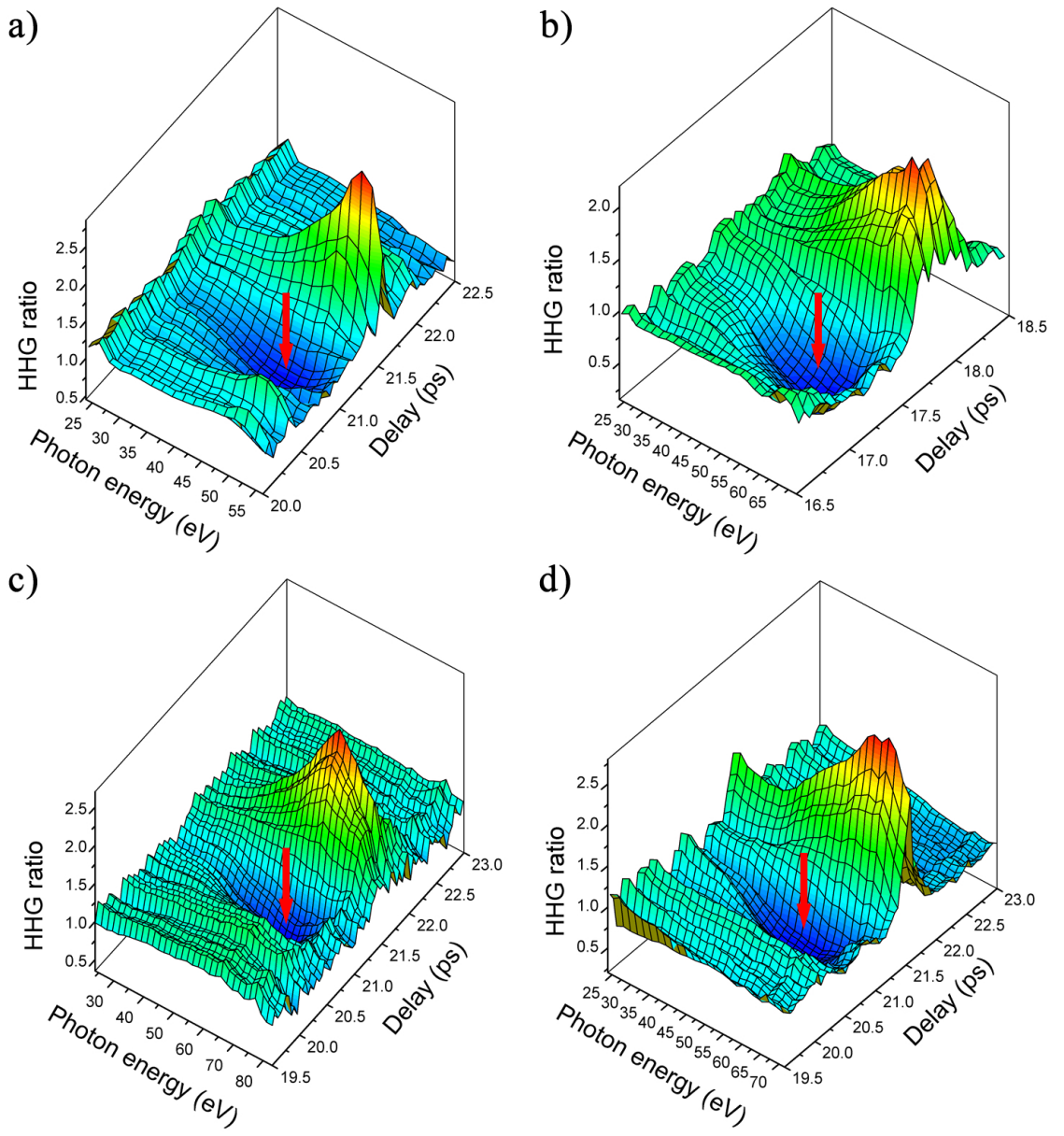

Figure 5.8: HHG ratios between aligned and unaligned CO_2 molecules as a function of photon energy and delay time between the aligning and the driving laser pulses for intensities of : a) $I = 0.8 \times 10^{14}$ W cm^{-2}, b) $I = 1.0 \times 10^{14}$ W cm^{-2}, c) $I = 1.2 \times 10^{14}$ W cm^{-2}, d) $I = 1.6 \times 10^{14}$ W cm^{-2} .

appear at lower photon energies as expected from Smirnova's model for longer wavelengths (1300 nm). This demonstrates that something was lacking in that model. Furthermore, the position of the minimum varies with the intensity of the laser pulse in a non-monotonic way, as shown in Fig. 5.9 where the behaviour of the position of the interference minimum is plotted as a function of laser intensity. The minimum appears around 47 eV for the lowest intensity ($I = 0.8 \times 10^{14}$ W cm^{-2}), then increases up to 55 eV at a laser intensity

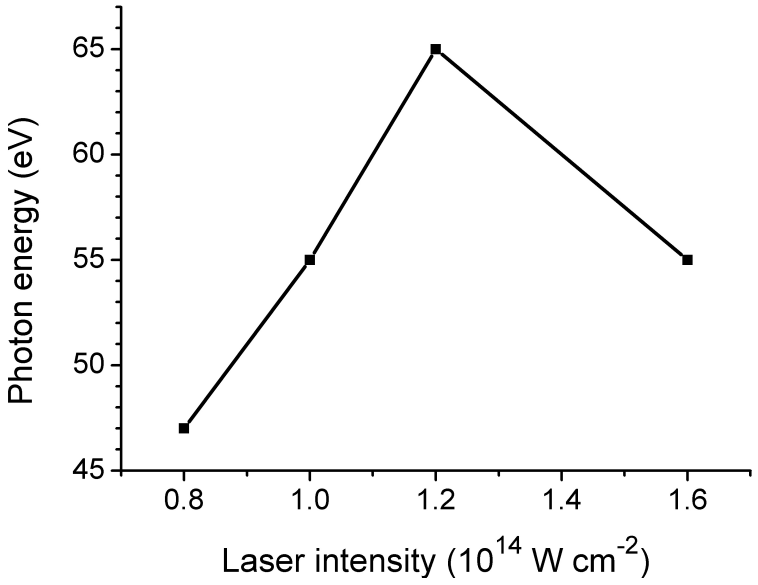

Figure 5.9: Position of the interference minimum as a function of laser intensity.

$I = 1.0\times10^{14}$ W cm^{-2}, reaching the maximum value of 65 eV at $I = 1.2\times10^{14}$ W cm^{-2} and finally it returns to 55 eV at $I = 1.6\times10^{14}$ W cm^{-2}. Such an intensity dependence suggests that the minimum in the HHG spectrum is not due only to a dynamical interference. In order to understand the reason of such behaviour, the theoretical analysis developed by Smirnova *et al.* [93, 96] is followed.

The critical factors in strong-field tunnel ionisation, which is the first step of the HHG process, are the ionisation potential I_p and the geometry of the ionising orbital [87, 96, 121]. The tunnel ionisation rate Γ depends exponentially on the ionisation potential I_p of the molecule through the following equation [87, 104, 114, 115]:

$$\Gamma \approx 4I_p \left[\frac{2\,(2I_p)^{3/2}}{E}\right]^{2n^*-|m|-1} \exp\left(-\frac{2\,(2I_p)^{3/2}}{3E}\right)$$

n^*, l, and m are the effective principal quantum number and the angular and magnetic quantum numbers of the ionising electron, and E is the electric field experienced by the electron. For this reason, it is usually assumed that during the ionisation process the electron is removed only from the HOMO (SAE approximation). However, in the case of CO_2 the nodal structure of the HOMO (see Fig. 5.10 (a)) suppresses ionisation for molecules aligned parallel ($\theta = 0°$) or perpendicular ($\theta = 90°$) to the laser polarisation. Thus, at these angles the ionisation from lower lying orbitals with higher I_p becomes

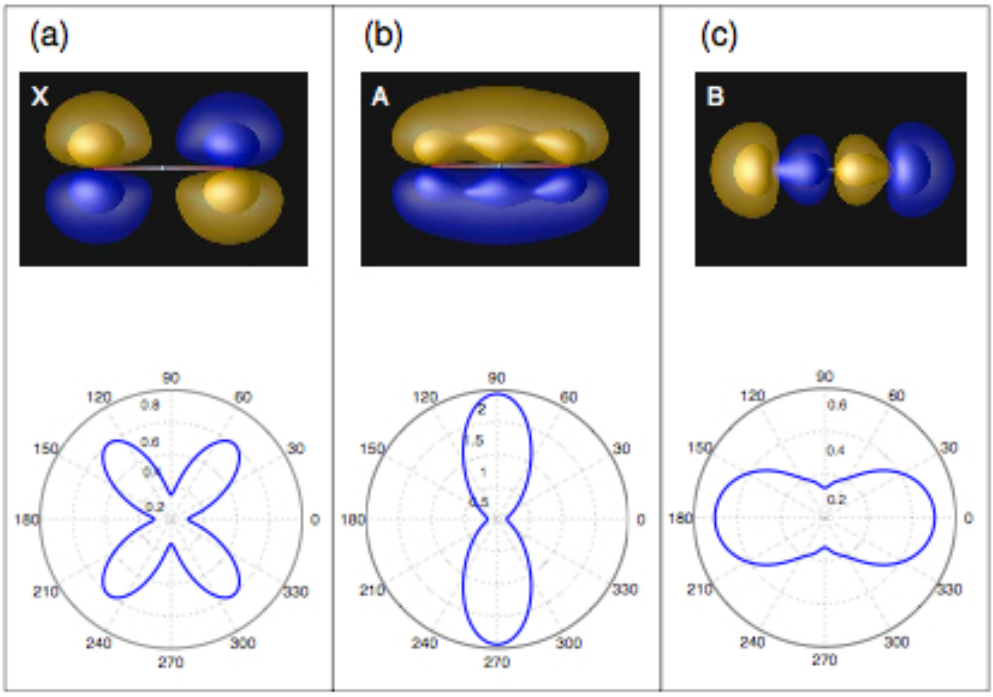

Figure 5.10: HOMOs (top) and angular dependences of strong-field ionisation rates (bottom) for different final states of CO_2^+, normalised to a single atomic orbital with the same ionisation potential. Blue and yellow colours correspond to positive and negative lobes of the orbital. (a) Ionisation with ion left in the ground state, channel X. (b) Ion left in the first excited electronic state, channel A. (c) Ion left in the second excited electronic state, channel B. Taken from [93]

comparatively important. In the case of CO_2 the ionisation potential from the HOMO-1 and HOMO-2 is 17.3 eV and 18.1 eV, respectively. Therefore, the ion CO_2^+ can be created by removing one electron from the HOMO (channel X), or the HOMO-1 (channel A), or the HOMO-2 (channel B), and the ionisation rate of each channel depends on the angle between the molecular axis and the polarisation direction of the laser pulse. The HOMOs and angular dependences of strong-field ionisation rates for different final states of CO_2^+ were calculated by Smirnova *et al.* in [93]. The results of these calculations are shown in Fig. 5.10, which is taken from [93]. From this figure it can be observed that HOMO-1 has a π_u symmetry with a nodal plane along the molecular axis direction, which implies an ionisation suppression along this direction, whilst HOMO-2 has a σ_u symmetry which corresponds to an ionisation enhancement for a driving laser beam parallel to the molecular axis direction.

In our experimental conditions, where the polarisation direction of the driving laser beam is parallel to the molecular axis, the B channel contributes to the ionisation with

a similar amplitude to the X channel [96]. The presence of two competing ionisation channels leaves a superposition of holes in the ion. As the energy difference between the two ionic states is ΔE, the superposition of holes evolves with a phase $\Phi = (\Delta E/\hbar)\tau + \Phi_0$ with Φ_0 being the relative phase at the time of ionisation. Therefore, the phase difference between the two channels contributing to harmonic emission is $\Phi = (\Delta E/\hbar)\tau + \Phi_0$, where τ is the time the electron spends in the continuum, that is the time between ionisation and recombination. The initial phase Φ_0 can be estimated from the intensity dependent position of the interference minimum, and for CO_2 it was found to be 0 in the experiment presented in Smirnova et al. [93]. The two ionisation channels will interfere constructively or destructively when the time-dependent relative phase between the ionisation channels, Φ, is an even or odd multiple of π, respectively. Given the energy separation between the B and X channels of 4.3 eV, the condition for constructive interference is satisfied at times after ionisation around 0.6 fs and 1.6 fs (see Fig. 5.11 (a) light background shading), while the condition for destructive interference is satisfied at around 1.2 fs and 2.2 fs (see Fig. 5.11 (a) dark background shading) for photon energies below the structural interference in the X channel. These conditions are reversed above the structural minimum due to the π phase shift of the recombination matrix element for the X channel [136]. Since the position of the dynamical interference is locked to the time spent by the electron in the continuum, only short trajectories were selected by positioning the gas jet after the laser focus [212] in the experimental apparatus. The selection of short trajectories allows linking each generated harmonic to a single electron excursion time [153].

The relation between the time spent by the electron in the continuum and the harmonic photon energy was estimated through a classical calculation for our experimental conditions ($\lambda = 1300$ nm) for five different laser intensities ((0.8 - 1.6)$\times 10^{14}$ W cm^{-2}), as shown in Fig. 5.11 (a) (black lines). From this plot, it can be observed that an increase in the laser intensity causes a shift in the dynamical minima toward higher photon energies, while the structural minimum stays at fixed energy. Therefore, it could be expected that the photon energy of the dynamical minimum increases monotonically with the laser intensity. However, in order to obtain a detectable modulation in the HHG spectrum due to this dynamical interference, the two ionisation channels should generate harmonics with comparable amplitudes. This requirement is satisfied only for photon energies around the structural minimum (in a range of (50-75) eV (see Fig. 5.11 (b))), which provides a natural window into lower molecular orbitals. For this reason, although for all the considered

intensities the two ionisation channels go through two dynamical minima, only the second dynamical minimum contributes to the modulation in the HHG spectrum. In particular, the first minimum occurs for an electron excursion time of ≈ 1.2 fs corresponding to photon energies between 15 eV and 25 eV, outside the range of interest and detection. The second minimum, instead is estimated to be in the region of interest for intensities in the range of (0.8-1.2)$\times 10^{14}$ W cm^{-2}, whilst for higher laser intensities, the dynamical minimum should occur at photon energies higher than 75 eV. For this reason, the position of the minimum in the total harmonic yield, calculated by taking into account the contributions from the two channels, goes from 53 eV to 65 eV and down to 43 eV for increasing laser intensities (due to the π phase shift of the recombination matrix element for the X channel after the two-centre interference), as shown in Fig. 5.11 (c). This behaviour of the minimum position in HHG spectra as a function of the laser intensities is in good agreement with our experimental results (see Fig. 5.9).

It can be concluded that the use of a 1300 nm wavelength allowed us to elucidate the mechanism of interference in HHG. The interference is not purely structural nor dynamical but an interplay between them. By disentangling both mechanisms it is possible to obtain information about the internuclear distance and electron-hole dynamics between the ionisation and recombination process at the same time.

5.4 Conclusions and outlook

The use of a 1300 nm driving laser has allowed obtaining the first evidence of a structural minimum in a high harmonic spectrum generated from C_2H_2, which is an organic molecule with a low I_p (11.4 eV) as compared with the I_p of CO_2 or N_2 (13.8 and 15.5 eV, respectively). This is because a longer wavelength implies a cutoff extension in the HHG spectrum. The use of the 1300 nm driving laser also allowed the generation of harmonic spectra from CO_2 with photon energies reaching beyond 60 eV for different driving laser intensities, elucidating the understanding of the interference mechanisms in the HHG process. The interesting achievement from this experiment is that the dip in the HHG spectrum is the result of an interplay between structural and dynamical interferences. Since the dynamical interference is due to the participation of different molecular orbitals in the HHG process, this experiment gives an evidence that the SAE approximation is not adequate to describe the HHG process in molecular systems.

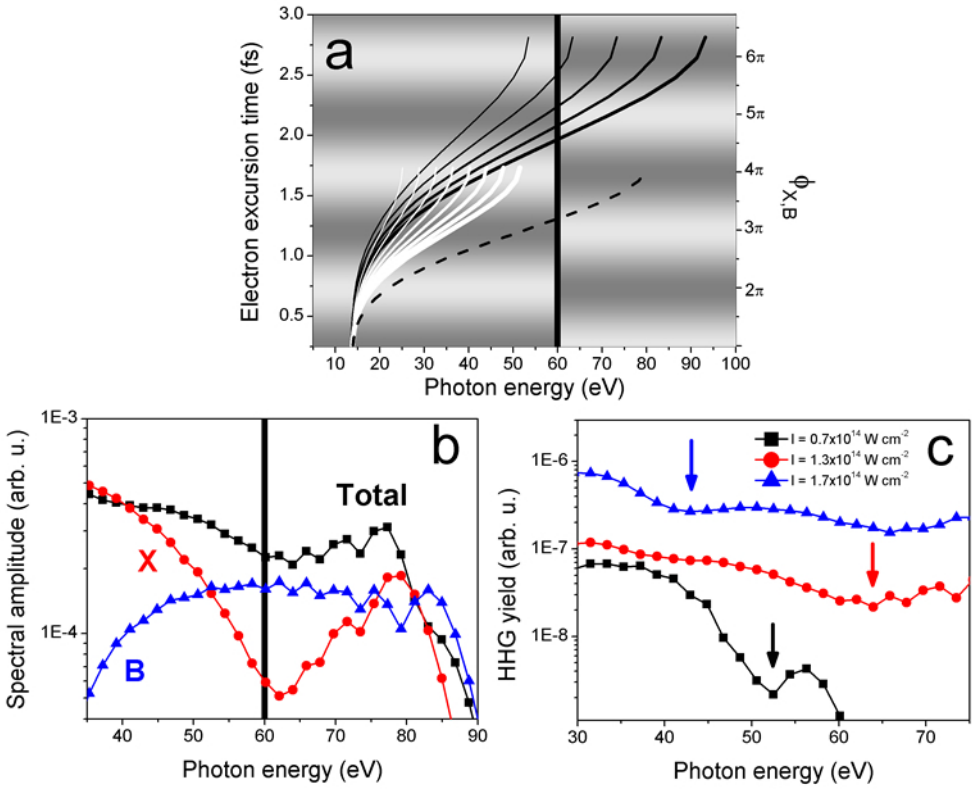

Figure 5.11: (a) Electron excursion time vs photon energy (short trajectories) calculated classically for CO_2. Black and white solid lines correspond to the conditions of the present work and those of Ref. [93] respectively. Increasing thickness represents increasing intensity (0.8 - 1.6)$\times 10^{14}$ W cm^{-2} (black) and (0.6 - 2.0)$\times 10^{14}$ W cm^{-2} (white). The dashed line corresponds to the experiment of Ref. [55], at 3.5×10^{14} W cm^{-2} . The background shading represents the dynamical interference between X and B channels: constructive (light) or destructive (dark). The vertical lines in (a) and (b) show the position of the structural minimum. (b) Calculated harmonic amplitudes in CO_2 with 1300 nm drive field and an intensity of 1.3×10^{14} W cm^{-2} for the X (circles) and B (triangles) channels as well as the total amplitude (squares). (c) Calculated total harmonic yield at three intensities spanning the range used in this work. Taken from [60]

Chapter 6

Conclusions

The present thesis deals with laser induced alignment of molecules in gas phase. The laser techniques of molecular alignment provide a useful tool for studying the dependence of many basic phenomena like chemical reactions or light-matter interactions on the spatial orientation of molecules.

Particular attention has been dedicated to the detection and measurement of the degree of alignment. In this thesis a method based on Coulomb explosion imaging (CEI) in conjunction with the velocity map imaging (VMI) technique has been used to detect the alignment, i.e. the fragments generated from the Coulomb explosion have been accelerated in an electrostatic lens towards a 2D detector, where a projection of the Coulomb explosion cloud of ions was formed. Although this method has been widely used in the past, to date there are no inversion algorithms that allow retrieving the molecular axis distribution from a CEI-VMI image, due to a molecular orientational dependence of ionisation.

We have presented an algorithm that allows for the first time the inclusion of a non-uniform detection function, leading to the retrieval of the molecular axis distribution deconvoluted from the molecular orientation dependence of the Coulomb explosion probe. In order to test the performance of the algorithm, we induced non-adiabatic molecular axis alignment on a sample of N_2 molecules through a strong non-resonant linearly polarised laser field and detected it by Coulomb exploding the aligned molecules with a circularly polarised laser pulse and acquiring the image formed on the detector by the resulting fragments. Although the quality of the resulting 2D images was very poor, the algorithm

was able to retrieve the molecular axis distribution from the images corresponding to Coulomb exploded clouds of ions which are not cylindrically symmetric about any axis. The inversion of high quality images acquired from Stapelfeldt's group has shown that the accuracy in retrieving the molecular axis distribution increases with the quality of the VMI images.

Future works focusing on measurement of molecular axis alignment, would thus benefit from the use of the inversion algorithm presented in this thesis for the analysis of the acquired data. Measuring molecular axis alignment is of fundamental importance for the development of new techniques aiming to optimise the degree of alignment obtainable following the interaction of a sample of isotropic molecules with a linearly polarised laser pulse. A strong degree of alignment is critical in some applications of aligned molecules in order to gain insight into molecular structures and dynamics, therefore measuring and optimising molecular alignment is essential.

One of these applications of molecular axis alignment is high-order harmonic generation (HHG) spectroscopy. Over the last few years there has been some effort to extend HHG spectroscopy to molecules of interest (which have typically $I_p < 10$ eV) and there have been basically two approaches: 1) using ultrashort pulses to minimise the effect of saturation of ionisation and 2) using wavelength longer that 800 nm which has proven more successful. The demonstration of large harmonic spectra from molecules with relatively low I_p paves the way to the application of HHG spectroscopy to large molecules and to study such processes as charge transfer in biomolecules with time resolution. The implementation of HHG spectroscopy in molecules has found some theoretical difficulties even in small molecules like CO_2, where the assumptions of the strong field (SFA) and single-active electron (SAE) approximations, used originally to interpret the experimental observation have proven to be too simplistic. A complete theoretical picture of the HHG in molecules is therefore essential if one wants to establish HHG spectroscopy as a general technique to extract useful information from molecules of interest.

The experimental approach presented in this thesis, where a mid-IR driving laser field was used to generate high-order harmonics, has allowed us to gain structural information of C_2H_2 and to identify the interplay between structural and dynamical interferences in HHG from CO_2. This experiment has thus helped to elucidate some controversies regarding the SAE approximation and its development in the future will help in testing and improving the current theoretical models.

Appendix A

Projection of 3D simulated distributions

We used a 3D ion trajectory simulation package (Simion 8) [195] to project a simulated 3D ion sphere on a detection plane. This software allowed simulating the electrostatic lens through which the charged fragments were accelerated. In Fig. A.1 a schematic diagram of the imaging lens is shown together with equipotential surfaces. The best ratio between the voltages on the repeller V_{R} and on the extractor V_{E} was determined in order to obtain the optimal focusing at the detection plane. In order to do this, a bunch of twelve ions having the same kinetic energy and with a 1 mm separation along the axis of propagation of the laser pulse was generated. These ions were directed with the same elevation and azimuthal angles and accelerated in the electrostatic lens. They arrived on the detector at different positions along a line parallel to the direction of the propagation of the laser pulse. These positions were recorded for different values of the extractor voltage by keeping the repeller at the same voltage (V_R = 2000 V), and the width of the trajectories, given by the distance between the two farthest ions on the detector, was plotted as a function of the ratio $V_{\mathrm{R}}/V_{\mathrm{E}}$, as shown in Fig. A.2. From this figure it can be seen that the best voltage ratio, that corresponds to the minimum value of the width of the trajectories, is $V_{\mathrm{R}}/V_{\mathrm{E}} = 75.2\%$. Therefore, this voltage ratio was used to obtain the 2D projected images used to test the inversion algorithm.

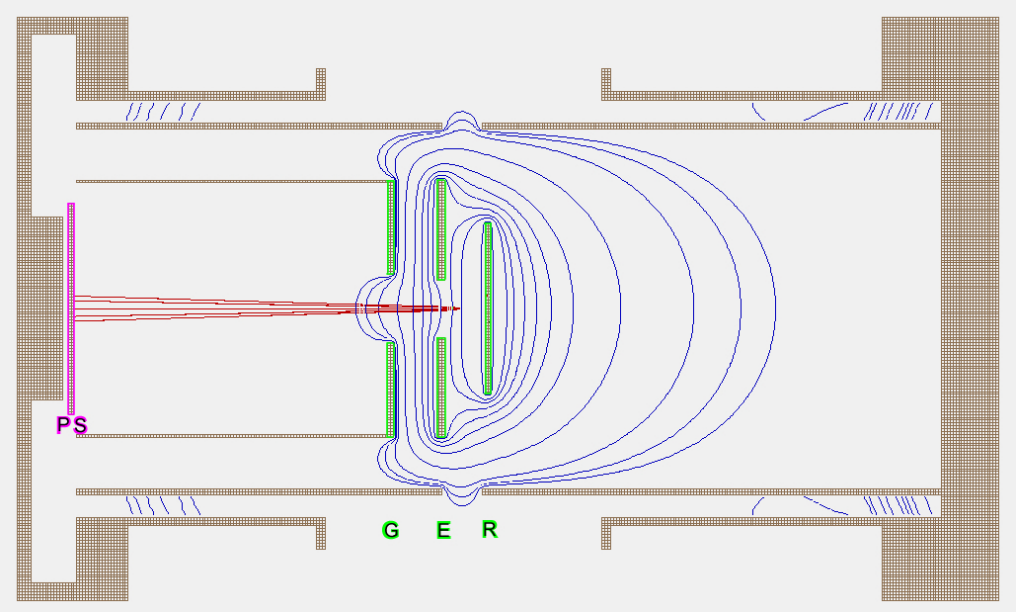

Figure A.1: Schematic diagram of a workbench simulated using SIMION. The imaging lens consisting of three electrodes (highlighted in green), called respectively repeller (R), extractor (E) and ground (G), is shown together with equipotential surfaces (blue curves). The trajectories of ions (red lines) accelerated in this VMI device towards the phosphor screen (PS) (highlighted in pink) are also shown.

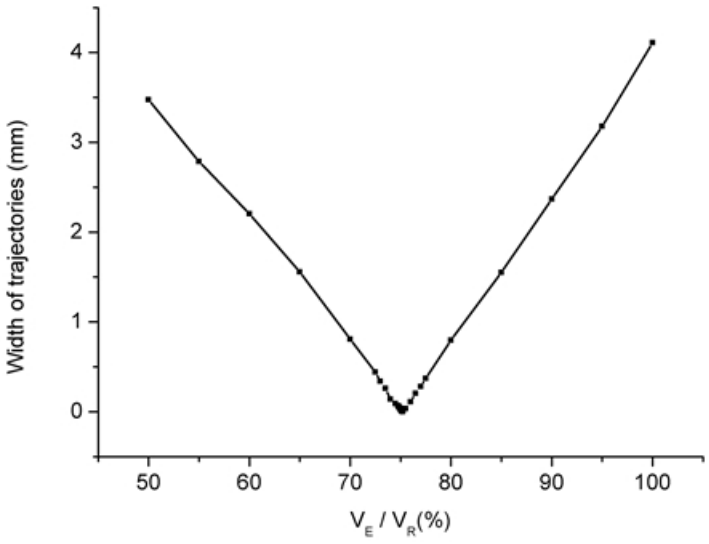

Figure A.2: Plot of the width of the trajectories, given by the distance between the two farthest ions on the detector, as a function of the ratio $V_{\mathrm{R}}/V_{\mathrm{E}}$. Twelve ions having the same kinetic energy and with a 1 mm separation along the axis of propagation of the laser pulse were considered. The minimum value of the width of the trajectories corresponds to the optimal focus condition of the VMI device and it is obtained for $V_{\mathrm{R}}/V_{\mathrm{E}} = 75.2\%$.

Appendix B

Centre of an experimental image

In order to determine the centre of an experimental image, we followed the procedure described by Bordas *et al.* [83], that can be schematised in few steps.

- Identification of an area T of the image where a guessed centre could lie.
- Calculation of the function $F(x_0, y_0)$ defined as:

$$F(x_0, y_0) = \sum_p I(x_p,y_p)\, I(2x_0 - x_p,2y_0 - y_p) \qquad \forall \quad (x_0, y_0) \in T \tag{B.1}$$

  where $I(x_p,y_p)$ represents the intensity of the acquired image in the pixel position specified by p, and $I(2x_0 - x_p,2y_0 - y_p)$ corresponds to the intensity of an image obtained by mirroring the original image at the trial centre position (x_0, y_0). The index p runs over all the pixels of the acquired image.

- Calculation of the maximum value of the $F(x_0, y_0)$ function.

The pixel (x_0, y_0) corresponding to the maximum value of $F(x_0, y_0)$ represents the centre position of the acquired image.

Appendix C

Simulation of a pump-probe VMI image

In order to generate a pump-probe VMI image which incorporates the probe molecular orientation dependence, the following procedure was followed. First a 3D randomly sampled distribution of charged particles with given velocity and angular distributions was generated. The velocities of the particles were sampled in the same way as for the probe-alone image (see section 3.3 of Chapter 3).

The initial velocity direction of each charged particle was specified in the alignment frame by azimuthal (ϕ) and polar (θ) angles defined in a spherical polar coordinate system in the alignment frame. These angles were sampled by using the rejection method [194], which allowed generating random θ and ϕ deviates with a known and computable distribution function $Z(\theta, \phi)$ given by:

$$Z(\theta,\phi) = M(\theta,\ \phi)\, A(\theta,\ \phi) \tag{C.1}$$

where $M(\theta,\ \phi)$ and $A(\theta,\ \phi)$ are the molecular axis distribution and the probe molecular orientation dependence respectively, both expressed in the alignment frame. The molecular axis distribution was given by a combination of spherical harmonics, $Y_{LM}(\theta, \phi)$:

$$M(\theta,\phi) = \sum_{l=0}^{L_{\max}} \beta_{LM} Y_{LM}(\theta, \phi) \tag{C.2}$$

where β_{LM} are the anisotropy coefficients.

The probe molecular orientation dependence was also given by a combination of spherical harmonics $Y_{LM}(\eta, \zeta)$, where η and ζ are the polar and azimuth angles defined in a spherical polar coordinate system in the probe frame, and are obtained from each pair of angles θ and ϕ through the following process:

- For each pair of angles θ and ϕ randomly sampled in the alignment frame, the corresponding Cartesian coordinates (X, Y, Z) were calculated through equations:

$$\begin{aligned} X &= \sin\phi \sin\theta \\ Y &= \cos\phi \sin\theta \\ Z &= \cos\theta \end{aligned} \tag{C.3}$$

- The corresponding Cartesian coordinates (x, y, z) in the probe frame were calculated by using Eq. 4.4 defined in section 4.1 of Chapter 4.

- The corresponding spherical coordinates ($\eta,\ \zeta$) were calculated in the probe frame trough the following equations:

$$\begin{aligned} \alpha &= \tan^{-1}\left(\frac{x^2+y^2}{z}\right) \\ \beta &= \tan^{-1}\left(\frac{y}{x}\right) \end{aligned} \tag{C.4}$$

The probe molecular orientation dependence was given by:

$$A\left(\theta,\ \phi\right) = A\left(\eta(\theta,\ \phi), \zeta(\theta,\ \phi)\right) = \sum_{l=0}^{L_{\max}} \xi_{LM} Y_{LM}(\eta, \zeta) \tag{C.5}$$

where ξ_{LM} are the anisotropy coefficients.

The resulting 3D distribution of charged particles was finally projected onto a 2D detector by means of a 3D ion trajectory simulation package (Simion 8) [195], as for the probe-alone image.

Appendix D

Calculation of the degree of alignment

As discussed in section 1.1 of Chapter 1, the degree of alignment is quantified by $\langle \cos^2 \theta \rangle$ with θ being the angle between the direction of the alignment laser field and the molecular axis. The value of $\langle \cos^2 \theta \rangle$ can be extracted from a normalised inverted distribution $P(R_l,\ \theta_m)$ by integrating over the angles θ and ϕ_n and the radii R:

$$\langle \cos^2 \theta \rangle = \sum_{l=0}^{R_{\max}} \sum_{m=0}^{2\pi} \sum_{n=0}^{\pi} R_l\, P(R_l,\ \theta_m)\, \sin \theta_m\, \cos^2 \theta_m \tag{D.1}$$

being $R_{\max}$ chosen from the user, and $R_l \sin \theta_m$ the scale factor due to the integration across ϕ. The distribution $P(R_l,\ \theta_m)$ is obtained from the inverted image expressed in cylindrical coordinates by following the procedure described in section 3.2.2 of Chapter 3.

The $\langle \cos^2 \theta \rangle$ cannot be extracted directly from the acquired images because the ion images do not measure the real molecular orientation, but instead its projection on the detector plane. Therefore, each ion hit on the detector defines an angle θ_{2D} between the projection of the molecular orientation and the polarisation of the alignment laser pulse. By averaging over all the ions an estimation of the $\langle \cos^2 \theta_{2\mathrm{D}} \rangle$, which quantifies the degree of alignment for raw images, can be obtained through the following equation:

$$\langle \cos^2 \theta_{2D} \rangle = \sum_{l=0}^{R_{\max}} \sum_{m=0}^{\pi} I(R_l,\ \theta_{2D}^m)\, \cos^2 \theta_{2D}^m \tag{D.2}$$

where $I\left(R_l,\ \theta_{2D}^m\right)$ represents the normalised acquired image in polar coordinates, and is related to the acquired image $I\left(y_u,\ z_v\right)$ expressed in Cartesian coordinates through this expression:

$$I\left(R_l, \theta_{2D}^m\right) = R_l\, I\left(y_u, z_v\right) \tag{D.3}$$

being R_l the Jacobian of the transformation from Cartesian to polar coordinates ($R_l = \sqrt{y_u^2 + z_v^2}$, and $\theta_{2D}^m = \tan^{-1}\left(y_u / z_v\right)$).

Bibliography

[1] P. R. Brooks, J. S. McKillop, and H. G. Pippin, *Molecular beam reaction of K atoms with sideways oriented CF_3I*, Phys. Lett. **66**, 144 (1979).

[2] S. R. Gandhi, T. J. Curtiss, and R. B. Bernstein, *Asymmetry of the polarized-laser-induced photofragmentation of oriented CH_3I molecules*, Phys. Rev. Lett. **59**, 2951–2954 (1987).

[3] S. Kaesdorf, G. Schönhense, and U. Heinzmann, *Experimental angular-resolved photoelectron spectroscopy of free oriented CH_3I molecules*, Phys. Rev. Lett. **54**, 885–888 (1985).

[4] D. A. Baugh, D. Y. Kim, V. A. Cho, L. C. Pipes, J. C. Petteway, and C. D. Fuglesang, *Production of a pure, single ro-vibrational quantum-state molecular beam*, Chem. Phys. Lett. **219**, 207 (1994).

[5] S. I. lonov and M. E. LaVilla, *Probing the molecule-surface interaction via inversion symmetry changes in the scattering of state-selected ND_3 on graphite (0001)*, J. Chem. Phys. **97**, 9379 (1992).

[6] J. M. Alvariño and A. Lagana, *Orientation effects and reaction mechanisms for the H + ICl reaction*, J. Phys. Chem. **91**, 5487 (1987).

[7] V. A. Cho and R. B. Bemsteint, *Tight focusing of beams of polar polyatomlc molecules via the electrostatic hexapole lens*, J. Phys. Chem. **95**, 8129 (1991).

[8] J. Bulthuis, J. J. van Leuken, and S. Stolte, *Hexapole state selection and focusing vs. brute force orientation of beam molecules*, J. Chem. Soc. Faraday. Trans. **91**, 205 (1995).

[9] H. J. Loesch and A. Remscheid, *Brute force in molecular reaction dynamics: A novel technique for measuring steric effects*, J. Chem. Phys. **93**, 4779 (1990).

[10] B. Friedrich and D. Herschbach, *On the possibility of orienting rotationally cooled polar molecules in an electric field*, Z. Phys. D - Atoms, Molecules and Clusters **18**, 153 (1991).

[11] M. Wu, R. J. Bemish, and R. E. Miller, *Photodissociation of molecules oriented by DC electric fields: Determining photofragment angular distributions*, J. Chem. Phys. **101**, 9447 (1994).

[12] H. Stapelfeldt and T. Seideman, *Colloquium: Aligning molecules with strong laser pulses*, Rev. Mod. Phys. **75**, 543 (2003).

[13] J. P. Heritage, T. K. Gustafson, and C. H. Lin, *Observation of coherent transient birefringence in CS_2 vapor*, Phys. Rev. Lett. **34**, 1299 (1975).

[14] B. A. Zon and B. G. Katsnelson, *Nonresonant scattering of intense light by a molecule*, Sov. Phys. JETP **42**, 595 (1976).

[15] B. Friedrich and D. Herschbach, *Alignment and trapping of molecules in intense laser fields*, Phys. Rev. Lett. **74**, 4623 (1995).

[16] B. Friedrich and D. Herschbach, *Polarization of molecules induced by intense nonresonant laser fields*, J. Phys. Chem. **99**, 15686 (1995).

[17] T. Seideman, *Rotational excitation and molecular alignment in intense laser fields*, J. Chem. Phys. **103**, 7887 (1995).

[18] W. Kim and P. M. Felker, *Spectroscopy of pendular states in optical-field-aligned species*, J. Chem. Phys. **104**, 1147 (1996).

[19] F. Rosca-Pruna and M. J. J. Vrakking, *Experimental observation of revival structures in picosecond laser-induced alignment of I_2*, Phys. Rev. Lett. **87**, 153902 (2001).

[20] J. Ortigoso, M. Rodríguez, M. Gupta, and B. Friedrich, *Time evolution of pendular states created by the interaction of molecular polarizability with a pulsed nonresonant laser field*, J. Chem. Phys. **110**, 3870 (1999).

[21] T. Seideman, *Revival structure of aligned rotational wave packets*, Phys. Rev. Lett. **83**, 4971 (1999).

[22] T. Seideman, *On the dynamics of rotationally broad, spatially aligned wave packets*, J. Chem. Phys. **115**, 5965 (2001).

[23] R. Torres, R. de Nalda, and J. P. Marangos, *Dynamics of laser induced molecular alignment in the adiabatic and impulsive regime: a direct comparison*, Phys. Rev. A **72**, 023420 (2005).

[24] V. Renard, M. Renard, S. Guérin, Y. T. Pashayan, B. Lavorel, O. Faucher, and H. R. Jauslin, *Postpulse molecular alignment measured by a weak field polarization technique*, Phys. Rev. Lett. **90**, 153601 (2003).

[25] C. M. Dion, A. Keller, O. Atabek, and A. D. Bandrauk, *Laser-induced alignment dynamics of hcn: Roles of the permanent dipole moment and the polarizability*, Phys. Rev. A **59**, 1382 (1999).

[26] M. Machholm and N. E. Henriksen, *Field-free orientation of molecules*, Phys. Rev. Lett. **87**, 193001 (2001).

[27] J. G. Underwood, M. Spanner, M. Y. Ivanov, J. Mottershead, B. J. Sussman, and A. Stolow, *Switched wave packets: A route to nonperturbative quantum control*, Phys. Rev. Lett. **90**, 223001 (2003).

[28] J. G. Underwood, B. J. Sussman, and A. Stolow, *Field-free three dimensional molecular axis alignment*, Phys. Rev. Lett. **94**, 143002 (2005).

[29] S. Guérin, L. P. Yatsenko, H. R. Jauslin, O. Faucher, and B. Lavorel, *Orientation of polar molecules by laser induced adiabatic passage*, Phys. Rev. Lett. **88**, 233601 (2002).

[30] W. Kim and P. M. Felker, *Ground-state intermolecular spectroscopy and pendular states in benzeneargon*, J. Chem. Phys. **107**, 2193 (1997).

[31] W. Kim and P. M. Felker, *Optical-field-induced pendular states and pendular band contours in symmetric tops*, J. Chem. Phys. **108**, 6763 (1998).

[32] H. Stapelfeldt, *Laser aligned molecules: Applications in physics and chemistry*, Physica Scripta. **T110**, 132 (2004).

[33] E. Péronne, M. D. Poulsen, C. Z. Bisgaard, H. Stapelfeldt, and T. Seideman, *Nonadiabatic alignment of asymmetric top molecules: Field-free alignment of Iodobenzene*, Phys. Rev. Lett. **91**(4), 043003 (2003).

[34] P. W. Dooley, I. V. Litvinyuk, K. F. Lee, D. M. Rayner, M. Spanner, D. M. Villeneuve, and P. B. Corkum, *Direct imaging of rotational wave-packet dynamics of diatomic molecules*, Phys. Rev. A **68**, 023406 (2003).

[35] K. Miyazaki, T. Shimizu, and D. Normand, *Femtosecond-laser-induced alignment in Coulomb explosion of N_2*, J. Phys. B: At. Mol. Opt. Phys. **37**, 753 (2004).

[36] F. Légaré, K. F. Lee, A. D. Bandrauk, D. M. Villeneuve, and P. B. Corkum, *Laser Coulomb explosion imaging for probing ultra-fast molecular dynamics*, J. Phys. B: At. Mol. Opt. Phys. **39**, S503 (2006).

[37] J. J. Larsen, H. Sakai, C. P. Safvan, I. Wendt-Larsen, and H. Stapelfeldt, *Aligning molecules with intense nonresonant laser fields*, J. Chem. Phys. **111**, 7774 (1999).

[38] J. J. Larsen, K. Hald, N. Bjerre, H. Stapelfeldt, and T. Seideman, *Three dimensional alignment of molecules using elliptically polarized laser fields*, Phys. Rev. Lett. **85**, 2470 (2000).

[39] M. D. Poulsen, T. Ejdrup, H. Stapelfeldt, E. Hamilton, and T. Seideman, *Alignment enhancement by the combination of a short and a long laser pulse*, Phys. Rev. A **73**, 033405 (2006).

[40] T. Suzuki, Y. Sugawara, S. Minemoto, and H. Sakai, *Optimal control of nonadiabatic alignment of rotationally cold N_2 molecules with the feedback of degree of alignment*, Phys. Rev. Lett. **100**, 033603 (2008).

[41] M. Muramatsu, M. Hita, S. Minemoto, and H. Sakai, *Field-free molecular orientation by an intense nonresonant two-color laser field with a slow turn on and rapid turn off*, Phys. Rev. A **79**, 011403 (2009).

[42] H. Tanji, S. Minemoto, and H. Sakai, *Three-dimensional molecular orientation with combined electrostatic and elliptically polarized laser fields*, Phys. Rev. A **72**, 063401 (2005).

[43] H. Sakai, S. Minemoto, H. Nanjo, H. Tanji, and T. Suzuki, *Controlling the orientation of polar molecules with combined electrostatic and pulsed, nonresonant laser fields*, Phys. Rev. Lett. **90**, 083001 (2003).

[44] L. Cai, J. Marango, and B. Friedrich, *Time-dependent alignment and orientation of molecules in combined electrostatic and pulsed nonresonant laser fields*, Phys. Rev. Lett. **86**, 775 (2001).

[45] A. Goban, S. Minemoto, and H. Sakai, *Laser-field-free molecular orientation*, Phys. Rev. Lett. **101**, 013001 (2008).

[46] I. Nevo, L. Holmegaard, J. H. Nielsen, J. L. Hansen, H. Stapelfeldt, F. Filsinger, G. Meijerd, and J. Küpper, *Laser-induced 3D alignment and orientation of quantum state-selected molecules*, Phys. Chem. Chem. Phys. **11**, 9912 (2009).

[47] Y. Sugawara, A. Goban, S. Minemoto, and H. Sakai, *Laser-field-free molecular orientation with combined electrostatic and rapidly-turned-off laser fields*, Phys. Rev. A **77**, 031403 (2008).

[48] O. Ghafur, A. Rouzée, A. Gijsbertsen, W. K. Siu1, S. Stolte, and M. J. J. Vrakking, *Impulsive orientation and alignment of quantum-state-selected NO molecules*, Nature Physics **5**, 289 (2009).

[49] M. Meckel, D. Comtois, D. Zeidler, A. Staudte, D. Pavičić, H. C. Bandulet, H. Ppin, J. C. Kieffer, R. Drner, D. M. Villeneuve, and P. B. Corkum, *Laser-induced electron tunneling and diffraction*, Science **320**, 1478 (2008).

[50] R. Velotta, N. Hay, M. B. Mason, M. Castillejo, and J. P. Marangos, *High-order harmonic generation in aligned molecules*, Phys. Rev. Lett. **87**, 183901 (2001).

[51] N. Hay, R. Velotta, M. Lein, R. de Nalda, E. Heesel, M. Castillejo, and J. P. Marangos, *High-order harmonic generation in laser-aligned molecules*, Phys. Rev. A **65**, 053805 (2002).

[52] R. d. Nalda, E. Heesel, M. Lein, N. Hay, R. Velotta, E. Springate, M. Castillejo, and J. P. Marangos, *Role of orbital symmetry in high-order harmonic generation from aligned molecules*, Phys. Rev. A **69**, 031804 (2004).

[53] J. Itatani, J. Levesque, D. Zeidler, H. Niikura, H. Pépin, J. C. Kieffer, P. B., and D. M. Villeneuve, *Tomographic imaging of molecular orbitals*, Nature **432**, 867 (2004).

[54] T. Kanai, S. Minemoto, and H. Sakai, *Quantum interference during high-order harmonic generation from aligned molecules*, Nature **435**, 470 (2005).

[55] C. Vozzi, F. Calegari, E. Benedetti, J.-P. Caumes, G. Sansone, S. Stagira, M. Nisoli, R. Torres, E. Heesel, N. Kajumba, J. P. Marangos, C. Altucci, and R. Velotta, *Controlling two-center interference in molecular high harmonic generation*, Phys. Rev. Lett. **95**, 153902 (2005).

[56] J. P. Marangos, S. Baker, N. Kajumba, J. S. Robinson, J. W. G. Tisch, and R. Torres, *Dynamic imaging of molecules using high order harmonic generation*, Phys. Chem. Chem. Phys. **10**, 35 (2008).

[57] R. Torres, N. Kajumba, J. G. Underwood, J. S. Robinson, S. Baker, J. W. G. Tisch, R. de Nalda, W. A. Bryan, R. Velotta, C. Altucci, I. C. E. Turcu, and J. P. Marangos, *Probing orbital structure of polyatomic molecules by high-order harmonic generation*, Phys. Rev. Lett. **98**, 203007 (2007).

[58] R. Torres, T. Siegel, L. Brugnera, I. Procino, J. G. Underwood, C. Altucci, R. Velotta, E. Springate, C. Froud, I. C. E. Turcu, M. Y. Ivanov, O. Smirnova, and J. P. Marangos, *Extension of high harmonic spectroscopy in molecules by a 1300 nm laser field*, Opt. Expr. **18**, 3174 (2010).

[59] N. Kajumba, R. Torres, J. G. Underwood, J. S. Robinson, S. Baker, J. W. G. Tisch, R. de Nalda, W. A. Bryan, R. Velotta, C. Altucci, I. C. E. Turcu, I. Procino, and J. P. Marangos, *Measurement of electronic structure from high harmonic generation in non-adiabatically aligned polyatomic molecules*, New J. Phys. **10**, 025008 (2008).

[60] R. Torres, T. Siegel, L. Brugnera, I. Procino, J. G. Underwood, C. Altucci, R. Velotta, E. Springate, C. Froud, I. C. E. Turcu, S. Patchkovskii, M. Y. Ivanov, O. Smirnova, and J. P. Marangos, *Revealing molecular structure and dynamics through high-order harmonic generation driven by mid-IR fields*, Phys. Rev. A **81**, 051802(R) (2010).

[61] C. B. Madsen, A. S. Mouritzen, T. K. Kjeldsen, and L. B. Madsen, *Effects of orientation and alignment in high-order harmonic generation and above-threshold ionization*, Phys. Rev. A **76**, 035401 (2007).

[62] K. Hoshina, K. Yamanouchi, T. Ohshima, Y. Ose, and H. Todokoro, *Direct observation of molecular alignment in an intense laser field by pulsed gas electron diffraction I: observation of anisotropic diffraction image*, Chem. Phys. Lett. **353**, 27 (2002).

[63] I. V. Litvinyuk, K. F. Lee, P. W. Dooley, D. M. Rayner, D. M. Villeneuve, and P. B. Corkum, *Alignment-dependent strong field ionization of molecules*, Phys. Rev. Lett. **90**, 233003 (2003).

[64] C. Guo, M. Li, J. P. Nibarger, and G. N. Gibson, *Single and double ionization of diatomic molecules in strong laser fields*, Phys. Rev. A **58**, R4271 (1998).

[65] G. Lagmago Kamta and A. D. Bandrauk, *Imaging electron molecular orbitals via ionization by intense femtosecond pulses*, Phys. Rev. A **74**, 033415 (2006).

[66] M. Tsubouchi, B. J. Whitaker, L. Wang, H. Kohguchi, and T. Suzuki, *Photoelectron imaging on time-dependent molecular alignment created by a femtosecond laser pulse*, Phys. Rev. Lett. **86**, 4500–4503 (2001).

[67] P. Johnsson, A. Rouzée, W. Siu, Y. Huismans, F. Lépine, T. Marchenko, S. Düsterer, F. Tavella, N. Stojanovic, A. Azima, R. Treusch, M. F. Kling, and M. J. J. Vrakking, *Field-free molecular alignment probed by the free electron laser in Hamburg (FLASH)*, J. Phys. B: At. Mol. Opt. Phys. **42**, 134017 (2009).

[68] E. R. Peterson, C. Buth, D. A. Arms, R. W. Dunford, E. P. Kanter, B. Krässig, E. C. Landahl, S. T. Pratt, R. Santra, S. H. Southworth, and L. Young, *An X-ray probe of laser-aligned molecules*, Appl. Phys. Lett. **92**, 094106 (2008).

[69] R. Neutze, R. Wouts, D. van der Spoel, E. Weckert, and J. Hajdu, *Potential for biomolecular imaging with femtosecond X-ray pulses*, Nature **406**, 752 (2000).

[70] V. Renard, M. Renard, A. Rouzée, S. Guérin, H. R. Jauslin, B. Lavorel, and O. Faucher, *Nonintrusive monitoring and quantitative analysis of strong laser-field-induced impulsive alignment*, Phys. Rev. A **70**, 033420 (2004).

[71] L. Frasinski, K. Codling, P. Hatherly, J. Barr, I. N. Ross, and W. T. Toner, *Femtosecond dynamics of multielectron dissociative ionization by use of picosecond laser*, Phys. Rev. Lett. **58**, 2424 (1987).

[72] D. Normand, L. A. Lompré, and C. Cornaggia, *Laser-induced molecular alignment probed by a double-pulse experiment*, J. Phys. B: At. Mol.Opt. Phys. **25**, L497 (1992).

[73] F. Légaré, K. F. Lee, I. V. Litvinyuk, P. W. Dooley, S. S. Wesolowski, P. R. Bunker, P. Dombi, F. Krausz, A. D. Bandrauk, D. M. Villeneuve, and P. B. Corkum, *Laser Coulomb-explosion imaging of small molecules*, Phys. Rev. A **71**, 013415 (2005).

[74] H. Stapelfeldt, E. Constant, H. Sakai, and P. B. Corkum, *Time-resolved Coulomb explosion imaging: A method to measure structure and dynamics of molecular nuclear wave packets*, Phys. Rev. A **58**, 426 (1998).

[75] C. Y. Wu, H. Z. Ren, T. T. Liu, R. Ma, H. Yang, H. B. Jiang, and Q. H. Gong, *Field-induced ionization and Coulomb explosion of nitrogen*, Appl. Phys. B **75**, 91 (2002).

[76] A. T. J. B. Eppink and D. H. Parker, *Velocity map imaging of ions and electrons using electrostatic lenses: Application in photoelectron and photofragment ion imaging of molecular oxygen*, Rev. Sci. Instr. **68**, 3477 (1997).

[77] B. Whitaker, *Imaging in Molecular Dynamics. Technology and Applications*, Cambridge University Press, Cambridge, UK, 2003.

[78] S. Candel, *An algorithm for the Fourier-Bessel transform*, Comp. Phys. Comm. **23**, 343 (1981).

[79] R. N. Strickland and D. W. Chandler, *Reconstruction of an axisymmetric image from its blurred and noisy projection*, App.Opt. **30**, 1811 (1991).

[80] A. J. R. Heck and D. W. Chandler, *Imaging techniques for the study of chemical reaction dynamics*, Annu. Rev, Phys. Chem. **46**, 335 (1995).

[81] C. J. Dasch, *One-dimensional tomography: a comparison of Abel, onion-peeling, and filtered backprojection methods*, App.Opt. **31**, 1146 (1992).

[82] S. Manzhos and H.-P. Loock, *Photofragment image analysis via pattern recognition*, Rev. Sci. Instr. **75**, 2435 (2004).

[83] C. Bordas, F. Paulig, H. Helm, and D. L. Huestis, *Photoelectron imaging spectrometry: Principle and inversion method*, Rev. Sci. Instrum. **67**, 2257 (1996).

[84] G. A. Garcia, L. Nahon, and I. Powis, *Two-dimensional charged particle image inversion using a polar basis function expansion*, Rev. Sci. Instrum. **75**, 4989 (2004).

[85] M. J. J. Vrakking, *An iterative procedure for the inversion of two-dimensional ion-photoelectron imaging experiments*, Rev. Sci. Instrum. **72**, 4084 (2001).

[86] Y. T. Cho and S.-J. Na, *Application of Abel inversion in real-time calculations for circularly and elliptically symmetric radiation sources*, Meas. Sci. Technol. **16**, 878 (2005).

[87] X. M. Tong, Z. X. Zhao, and C. D. Lin, *Theory of molecular tunneling ionization*, Phys. Rev. A **66**, 033402 (2002).

[88] T. Morishita, A.-T. Le, Z. Chen, and C. D. Lin, *Accurate retrieval of structural information from laser-induced photoelectron and high-order harmonic spectra by few-cycle laser pulses*, Phys. Rev. Lett. **100**, 013903 (2008).

[89] D. Ray, B. Ulrich, I. Bocharova, C. Maharjan, P. Ranitovic, B. Gramkow, M. Magrakvelidze, S. De, I. V. Litvinyuk, A. T. Le, T. Morishita, C. D. Lin, G. G. Paulus, and C. L. Cocke, *Large-angle electron diffraction structure in laser-induced rescattering from rare gases*, Phys. Rev. Lett. **100**, 143002 (2008).

[90] T. Zuo, A. D. Bandrauk, and P. B. Corkum, *Laser-induced electron diffraction: a new tool for probing ultrafast molecular dynamics*, Chem. Phys. Lett. **259**, 313 (1996).

[91] S. Baker, J. S. Robinson, C. A. Haworth, H. Teng, R. A. Smith, C. C. Chirilă, M. Lein, J. W. G. Tisch, and J. P. Marangos, *Probing proton dynamics in molecules on an attosecond time scale*, Science **312**, 424 (2006).

[92] W. Li, X. Zhou, R. Lock, S. Patchkovskii, A. Stolow, H. C. Kapteyn, and M. M. Murnane, *Time-resolved dynamics in N_2O_4 probed using high harmonic generation*, Science **322**, 1207 (2008).

[93] O. Smirnova, S. Patchkovskii, Y. Mairesse, N. Dudovich, D.Villeneuve, P. Corkum,

and M. Y. Ivanov, *High harmonic interferometry of multi-electron dynamics in molecules*, Nature **460**, 972 (2009).

[94] M. Lein, N. Hay, R. Velotta, J. P. Marangos, and P. L. Knight, *Role of the intramolecular phase in High-Harmonic Generation*, Phys. Rev. Lett. **88**, 183903 (2002).

[95] S. Baker, J. S. Robinson, M. Lein, C. C. Chirilă, R. Torres, H. C. Bandulet, D. Comtois, J. C. Kieffer, D. M. Villeneuve, J. W. G. Tisch, and J. P. Marangos, *Dynamic two-center interference in high-order harmonic generation from molecules with attosecond nuclear motion*, Phys. Rev. Lett. **101**, 053901 (2008).

[96] O. Smirnova, S. Patchkovskii, Y. Mairesse, N. Dudovich, and M. Y. Ivanov, *Strong-field control and spectroscopy of attosecond electron-hole dynamics in molecules*, PNAS **106**, 16556 (2009).

[97] B. Friedrich and D. Herschbach, *Spatial orientation of molecules in strong electric fields and evidence for pendular states*, Nature **353**, 412 (1991).

[98] D. Herschbach, *Chemical physics: Molecular clouds, clusters, and corrals*, Rev. Mod. Phys. **71**, S411 (1999).

[99] T. Seideman and E. Hamilton, *Nonadiabatic alignment by intense pulses*, Ad. At. Mol. Opt. Phys. **52**, 289 (2006).

[100] A. D. Bandrauk, *Atomic and molecular processes with short intense laser pulses*, Plenum Press, New York, 1988.

[101] M. Gavrila, *Atoms in intense laser fields*, Academic Press, New York, 1992.

[102] B. Piraux and K. Rzążewski, *Super-intense laser-atom physics*, Kluwer Academic Publishers, London, 2001.

[103] M. Protopapas, C. H. Keitel, and P. L. Knight, *Atomic physics with super-high intensity lasers*, Rep. Prog. Phys. **60**, 389 (1997).

[104] P. Corkum, M. Y. Ivanov, , and J. S. Wright, *Subfemtosecond processes in strong laser fields*, Annu. Rev. Phys. Chem. **48**, 387 (1997).

[105] K. C. Kulander, K. J. Schafer, and J. L. Krause, *Proceedings of the Workshop, Super Intense Laser Atom Physics (SILAP) III*, Plenum Press, New York, 1993.

[106] R. Bruzzese, A. Sasso, and S. Solimeno, *Multiphoton excitation and ionisation of atoms and molecules*, La Rivista Del Nuovo Cimento **12** (1989).

[107] N. Delone and V. Krainov, *Multiphoton Processes in Atoms*, Springer, Berlin, 2000.

[108] J. H. Eberly and P. Lambropoulos, *Multiphoton processes : proceedings of an international conference at the University of Rochester, Rochester, N.Y., June 6-9, 1977*, John Wiley, New York, 1978.

[109] F. Fabre, G. Petite, P. Agostini, and M. Clement, *Multiphoton above-threshold ionisation of xenon at 0.53 and 1.06μm*, J. Phys. B: At. Mol. Phys. **15**, 1353 (1982).

[110] G. Petite, F. Fabre, P. Agostini, M. Crance, and M. Aymar, *Nonresonant multiphoton ionization of cesium in strong fields: Angular distributions and above-threshold ionization*, Phys. Rev. A **29**, 2677 (1984).

[111] B. H. Bransden and C. J. Joachain, *Introduction to quantum mechanics*, Longman Scientific & Technical ; Wiley, New York, 1989.

[112] Y. Gontier and M. Trahin, *Energetic electron generation by multiphoton absorption*, J. Phys. B: At. Mol. Phys. **13**, 4383 (1980).

[113] N. Milosevic, V. P. Krainov, and T. Brabec, *Semiclassical Dirac theory of tunnel ionization*, Phys. Rev. Lett. **89**, 193001 (2002).

[114] M. Y. Ivanov, M. Spanner, and O. Smirnova, *Anatomy of strong field ionization*, J. Mod. Opt **52**, 165 (2005).

[115] M. V. Ammosov, N. B. Delone, and V. P. Krainov, *Tunnel ionization of complex atoms and atomic ions by an alternating electromagnetic field*, Sov. Phys. JETP **64**, 1191 (1986).

[116] L. V. Keldysh, *Ionization in the field of a strong electromagnetic wave*, Sov. Phys. JETP **20**, 1018 (1965).

[117] E. Mevel, P. Breger, R. Trainham, G. Petite, P. Agostini, A. Migus, J.-P. Chambaret, and A. Antonetti, *Atoms in strong optical fields: Evolution from multiphoton to tunnel ionization*, Phys. Rev. Lett. **70**, 406 (1993).

[118] V. P. Krainov, *Ionization rates and energy and angular distributions at the barrier-suppression ionization of complex atoms and atomic ions*, Chem. Phys. Lett. **14**, 425 (1997).

[119] T. K. Kjeldsen, C. Z. Bisgaard, L. B. Madsen, and H. Stapelfeldt, *Role of symmetry in strong-field ionization of molecules*, Phys. Rev. A **68**, 063407 (2003).

[120] A. Jaroń Becker, A. Becker, and F. H. M. Faisal, *Ionization of N_2, O_2, and linear carbon clusters in a strong laser pulse*, Phys. Rev. A **69**, 023410 (2004).

[121] J. Muth-Böhm, A. Becker, and F. H. M. Faisal, *Suppressed molecular ionization for a class of diatomics in intense femtosecond laser fields*, Phys. Rev. Lett. **85**, 2280 (2000).

[122] A. Talebpour, C.-Y. Chien, and S. L. Chin, *The effects of dissociative recombination in multiphoton ionization of O_2*, J. Phys. B **29**, L677 (1996).

[123] D. Pavičić, K. F. Lee, D. M. Rayner, P. B. Corkum, and D. M. Villeneuve, *Direct measurement of the angular dependence of ionization for N_2, O_2, and CO_2 in intense laser fields*, Phys. Rev. Lett. **98**, 243001 (2007).

[124] M. Ivanov, T. Seideman, P. Corkum, F. Ilkov, and P. Dietrich, *Explosive ionization of molecules in intense laser fields*, Phys. Rev. A **54**, 1541 (1996).

[125] T. Zuo and A. D. Bandrauk, *Charge-resonance-enhanced ionization of diatomic molecular ions by intense lasers*, Phys. Rev. A **52**, R2511 (1995).

[126] T. Seideman, M. Y. Ivanov, and P. B. Corkum, *Role of electron localization in intense-field molecular ionization*, Phys. Rev. Lett. **75**, 2819 (1995).

[127] J. H. Posthumus, L. J. Frasinski, A. J. Giles, and K. Codling, *Dissociative ionization of molecules in intense laser fields: a method of predicting ion kinetic energies and appearance intensities*, J. Phys. B: At. Mol. Opt. Phys. **28**, L349 (1995).

[128] C. Ellert and P. B. Corkum, *Disentangling molecular alignment and enhanced ionization in intense laser fields*, Phys. Rev. A **59**, R3170 (1999).

[129] E. Constant, H. Stapelfeldt, and P. B. Corkum, *Observation of enhanced ionization of molecular ions in intense laser fields*, Phys. Rev. Lett. **76**, 4140 (1996).

[130] K. Codling, L. J. Frasinski, and P. A. Hatherly, *On the field ionisation of diatomic molecules by intense laser fields*, J. Phys. B: At. Mol. Opt. **22**, L321 (1989).

[131] D. M. Villeneuve, M. Y. Ivanov, and P. B. Corkum, *Enhanced ionization of diatomic molecules in strong laser fields: A classical model*, Phys. Rev. A **54**, 736 (1996).

[132] K. Lin, S. Lin, P. Hunt, G. Leroi, and S. Crouch, *Experimental and theoretical study of laser-enhanced ionization and dual-laser ionization of sodium vapor.*

[133] P. B. Corkum, *Plasma perspective on strong-field multiphoton ionisation*, Phys. Rev. Lett. **71**, 1994 (1993).

[134] M. Lewenstein, P. Balcou, M. Y. Ivanov, A. L'Huillier, and P. B. Corkum, *Theory of high-harmonic generation by low-frequency laser fields*, Phys. Rev. A **49**, 2117 (1994).

[135] J. Tate, T. Auguste, H. G. Muller, P. Salières, P. Agostini, and L. F. DiMauro, *Scaling of wave-packet dynamics in an intense midinfrared field*, Phys. Rev. Lett. **98**, 013901 (2007).

[136] M. Lein, N. Hay, R. Velotta, J. P. Marangos, and P. L. Knight, *Interference effects in high-order harmonic generation with molecules*, Phys. Rev. A **66**, 023805 (2002).

[137] M. Lein, *Molecular imaging using recolliding electrons*, J. Phys. B **40**, R135 (2007).

[138] M. Spanner, O. Smirnova, P. B. Corkum, and M. Y. Ivanov, *Reading diffraction images in strong field ionization of diatomic molecules*, J. Phys. B: At. Mol. Opt. Phys. **37**, L243 (2004).

[139] M. Lein, J. P. Marangos, and P. L. Knight, *Electron diffraction in above-threshold ionization of molecules*, Phys. Rev. A **66**(5), 051404 (Nov 2002).

[140] H. Niikura, F. Légaré, R. Hasbani, A. D. Bandrauk, M. Y. Ivanov, D. M. Villeneuve, and P. B. Corkum, *Sub-laser-cycle electron pulses for probing molecular dynamics*, Nature **417**, 917 (2004).

[141] S. N. Yurchenko, S. Patchkovskii, I. V. Litvinyuk, P. B. Corkum, and G. L. Yudin, *Laser-induced interference, focusing, and diffraction of rescattering molecular photoelectrons*, Phys. Rev. Lett. **93**, 223003 (2004).

[142] S. X. Hu and L. A. Collins, *Imaging molecular structures by electron diffraction using an intense few-cycle pulse*, Phys. Rev. Lett. **94**, 073004 (2005).

[143] B. Shan, S. Ghimire, and Z. Chang, *Effect of orbital symmetry on high-order harmonic generation from molecules*, Phys. Rev. A **69**, 021404 (2004).

[144] T. Weber, H. Giessen, M. Weckenbrock, G. Urbasch, A. Staudte, L. Spielberger, O. Jagutzki, V. M. amd M. Vollmer, and R. Dörner, *Correlated electron emission in multiphoton double ionization*, Nature **405**, 658 (2006).

[145] V. R. Bhardwaj, D. M. Rayner, D. M. Villeneuve, and P. B. Corkum, *Quantum interference in double ionization and fragmentation of C_6H_6 in intense laser fields*, Phys. Rev. Lett. **87**, 253003 (2001).

[146] H. Sakai, J. J. Larsen, I. Wendt-Larsen, J. Olesen, P. B. Corkum, and H. Stapelfeldt, *Nonsequential double ionization of D_2 molecules with intense 20-fs pulses*, Phys. Rev. A **67**, 063404 (2003).

[147] B. Walker, B. Sheehy, L. F. DiMauro, P. Agostini, K. J. Schafer, and K. C. Kulander, *Precision measurement of strong field double ionization of helium*, Phys. Rev. Lett. **73**, 1227 (1994).

[148] D. N. Fittinghoff, P. R. Bolton, B. Chang, and K. C. Kulander, *Observation of nonsequential double ionization of helium with optical tunneling*, Phys. Rev. Lett. **69**, 2642 (1992).

[149] G. G. Paulus, W. Nicklich, H. Xu, P. Lambropoulos, and H. Walther, *Plateau in above threshold ionization spectra*, Phys. Rev. Lett. **72**, 2851 (1994).

[150] G. G. Paulus, W. Becker, and H. Walther, *Classical rescattering effects in two-color above-threshold ionization*, Phys. Rev. A **52**, 4043–4053 (1995).

[151] G. G. Paulus, W. Becker, W. Nicklich, and H. Walther, *Rescattering effects in above-threshold ionization: a classical model*, J. Phys. B: At. Mol. Opt. Phys. **27**, L703 (1994).

[152] F. Grasbon, G. G. Paulus, H. Walther, P. Villoresi, G. Sansone, S. Stagira, M. Nisoli, and S. D. Silvestri, *Above-threshold ionization at the few-cycle limit*, Phys. Rev. Lett. **91**, 173003 (2003).

[153] Y. Mairesse, A. de Bohan, L. J. Frasinski, H. Merdji, L. C. Dinu, P. Monchicourt, P. Breger, M. Kovacev, R. Taïeb, B. Carré, H. G. Muller, P. Agostini, and P. Saliières, *Attosecond synchronization of high-harmonic soft X-rays*, Science **302**, 1540 (2003).

[154] K. Kwon and A. Moscowitz, *Molecular ion geometries from inversion of Coulomb explosion imaging data*, Phys. Rev. Lett. **77**, 1238 (1996).

[155] S. Chelkowski, P. B. Corkum, and A. D. Bandrauk, *Femtosecond Coulomb explosion imaging of vibrational wave functions*, Phys. Rev. Lett. **82**, 3416 (1999).

[156] H. Stapelfeldt, E. Constant, and P. B. Corkum, *Wave packet structure and dynamics measured by Coulomb explosion*, Phys. Rev. Lett. **74**, 3780 (1995).

[157] C. Cornaggia, *Ultrafast Coulomb explosion imaging of molecules*, Laser Physics **19**, 1660 (2009).

[158] A. Hishikawa, A. Iwamae, K. Hoshina, M. Kono, and K. Yamanouchi, *Coulomb explosion dynamics of N_2 in intense laser field by mass-resolved momentum imaging*, Chem. Phys. Lett. **231**, 315 (1998).

[159] H. Ren, R. Ma, J. Chen, X. Li, H. Yang, and Q. Gong, *Field ionization and Coulomb explosion of CO in an intense femtosecond laser field*, J. Phys. B: At. Mol.Opt. Phys. **36**, 2179 (2003).

[160] P. Graham, K. W. D. Ledingham, R. P. Singhai, S. M. Hankin, T. McCanny, X. Fang, C. Kosmidis, P. Tzallas, P. F. Taday, and A. J. Langley, *On the fragment ion angular distributions arising from the tetrahedral molecule CH_3I*, J. Phys. B: At. Mol. Opt. Phys. **34**, 4015 (2001).

[161] E. P. Kanter, P. J. Cooney, D. S. Gemmell, K. O. Groeneveld, W. J. Pietsch, A. J. Ratkowski, Z. Vager, and B. J. Zabransky, *Role of excited electronic states in the interactions of fast (MeV) molecular ions with solids and gases*, Phys. Rev. A **20**, 834 (1979).

[162] Z. Vager, R. Naaman, and E. P. Kanter, *Coulomb explosion imaging of small molecules*, SCIENCE **244**, 4903 (1989).

[163] D. S. Gemmell, *Determining the stereochemical structures of molecular ions by*

"Coulomb-explosion" techniques with fast (MeV) molecular ion beams, Chem. Rev. **80**, 301 (1980).

[164] E. Baldit, S. Saugout, and C. Cornaggia, *Coulomb explosion of N_2 using intense 10- and 40-fs laser pulses*, Phys. Rev. A **71**, 021403 (2005).

[165] C. Cornaggia, M. Schmidt, and D. Normand, *Coulomb explosion of CO_2 in an intense femtosecond laser field*, J. Phys. B: At. Mol.Opt. Phys. **27**, L123 (1994).

[166] C. Rullière, *Femtosecond Laser Pulses: Principles and Experiments*, Springer, New York, USA, 1998.

[167] R. Trebino and D. J. Kane, *Using phase retrieval to measure the intensity and phase of ultrashort pulses: frequency-resolved optical gating*, J. Opt. Soc. Am. A **10**, 1101 (1993).

[168] M. Nisoli, S. D. Silvestri, and O. Svelto, *Generation of high energy 10 fs pulses by a new pulse compression technique*, Appl. Phys. Lett. **68**, 13 (1996).

[169] M. Nisoli, S. Stagira, S. D. Silvestri, O. Svelto, S. Sartania, Z. Cheng, M. Lenzner, C. Spielmann, and F. Krausz, *A novel-high energy pulse compression system: generation of multi gigawatt sub-5-fs pulses*, Appl. Phys. B **65**, 189 (1997).

[170] C. Vozzi, M. Nisoli, G. Sansone, S. Stagira, and S. D. Silvestri, *Optimal spectral broadening in hollow-fiber compressor systems*, Appl. Phys. B **80**, 285 (2005).

[171] G. P. Agrawal, *Nonlinear Fiber Optics*, Academic Press, San Diego, USA, 2001.

[172] F. Shimizu, *Frequency broadening in liquids by a short light pulse*, Phys. Rev. Lett. **19**, 1097 (1967).

[173] R. H. Stolen and C. Lin, *Self phase modulation in silica optical fibers*, Phys. Rev. A **17**, 1448 (1978).

[174] J. Robinson, C. A. Haworth, H. Teng, R. A. Smith, J. P. Marangos, and J. W. G. Tisch, *The generation of intense, transform-limited laser pulses with tuneable duration from 6 to 30 fs in a differentially pumped hollow fibre*, Appl. Phys. B **85**, 525 (2006).

[175] I. Procino, R. Velotta, C. Altucci, S. Amoruso, R. Bruzzese, X. Wang, V. Tosa, G. Sansone, C. Vozzi, and M. Nisoli, *Hollow-fiber compression of visible, 200 fs laser pulses to 40 fs pulse duration*, Opt. Lett. **32**, 1866 (2007).

[176] M. Nurhuda, A. Suda, K. Midorikawa, M. Hatayama, and K. Nagasaka, *Propagation dynamics of femtosecond laser pulses in a hollow fiber filled with argon: constant gas pressure versus differential gas pressure*, J. Opt. Soc. Am. B **20**, 2002 (2003).

[177] M. Nurhuda, A. Suda, K. Midorikawa, and H. Budiono, *Control of self-phase modulation and plasma-induced blue shifting of high-energy, ultrashort laser pulses in an argon-filled hollow fiber using conjugate pressure-gradient method*, J. Opt. Soc. Am. B **22**, 1757 (2005).

[178] R. Szipöcs, K. Ferencz, C. Spielmann, and F. Krausz, *Chirped multilayer coatings for broadband dispersion control in femtosecond lasers*, Opt. Lett. **19**, 201 (1994).

[179] G. Scoles, *Atomic and Molecular Beam Methods*, Oxford University Press, Oxford, 1988.

[180] D. Irimia, R. Kortekaas, and M. H. M. Janssen, *In situ characterization of a cold and short pulsed molecular beam by femtosecond ion imaging*, Phys. Chem. Chem. Phys. **11**, 3958 (2009).

[181] D. Proch and T. Trickl, *A high-intensity multi-purpose piezoelectric pulsed molecular beam source*, Rev. Sci. Instrum. **60**, 713 (1989).

[182] H. B. van Linden van den Heuvell and H. G. Muller, *Multiphoton processes*, Cambridge University Press, Cambridge, UK, 1988.

[183] R. N. Bracewell, *The Fourier Transform and its Applications*, McGraw-Hill, New York, 1978.

[184] M. Bertero and P. Boccacci, *Introduction to Inverse Problems in Imaging*, Institute of Physics, Bristol, 1998.

[185] J. Hadamard, *Lectures on Cauchys problem in linear partial differential equations*, Yale University Press, New Haven CT, 1923.

[186] M. Bertero, T. A. Poggio, and V. Torre, *Ill-posed problems in early vision*, Proc. IEEE **76**, 869 (1988).

[187] C. Hansen, *Analysis of discrete ill-posed problems by means of the L-curve*, SIAM Rev. **34**, 561 (1992).

[188] E. W. Hansen, *Fast Hankel transform algorithm*, IEEE Trans. Acoust. Speech, Sig. Proc. **33**, 666 (1985).

[189] B. Whitaker, *Image Reconstruction: The Abel transform*, chapter 5, pages 68–86, American Chemical Society, Washington, DC, 2000.

[190] L. M. Smith, D. R. Keefer, and S. I. Sudharsanan, *Abel inversion using transform techniques*, J. Quant. Spectrosc. Radial. Transfer **39**, 367 (1988).

[191] V. Dribinski, A. Ossadtchi, V. A. Mandelshtam, and H. Reislera, *Reconstruction of Abel-transformable images: The Gaussian basis-set expansion Abel transform method*, Rev. Sci.lnstrum. **73**, 2634 (2002).

[192] K. Zhao, T. Colvin, W. T. Hill, and G. Zhang, *Deconvolving two-dimensional images of three-dimensional momentum trajectories*, Rev. Sci. Instr. **73**, 3044 (2002).

[193] G. M. Roberts, J. L. Nixon, J. Lecointre, E. Wrede, and J. R. R. Verlet, *Toward real-time charged-particle image reconstruction using polar onion-peeling*, Rev. Sci.lnstrum. **80**, 053104 (2009).

[194] W. H. Press, S. A. Teukolsky, W. T. Vetterling, and B. P. Flannery, *Numerical recipes: The Art of Scientific Computing*, Cambridge University Press, New York, 2007.

[195] D. A. Dahl, J. E. Delmore, and A. D. Appelhans, *SIMION PC/PS2 electrostatic lens design program*, Rev. Sci.lnstrum. **61**, 607 (1990).

[196] F. Natterer, *The Mathematics of Computerized Tomography*, Society for Industrial and Applied Mathematics, Philadelphia, 2001.

[197] L. Landweber, *An iteration formula for Fredholm integral equations of the first kind*, Am. J. Math. **73**, 615 (1951).

[198] T. Elfving and T. Nikazad, *Stopping rules for Landweber-type iteration*, Inverse Problems **23**, 1417 (2007).

[199] V. A. Morozov, *On the solution of functional equations by the method of regularization*, Sov. Math. -Dokl. **7**, 414 (1966).

[200] K. Miller, *Least squares methods for ill-posed problems with a prescribed bound*, SIAM J. Math. Anal. **1**, 52 (1970).

[201] G. Wahba, *Practical approximate solutions to linear operator equations when the data are noisy*, SIAM J. Numer. Anal. **14**, 651 (1977).

[202] F. Renth, J. Riedel, and F. Temps, *Inversion of velocity map ion images using iterative regularization and cross validation*, Rev. Sci.lnstrum. **77**, 033103 (2006).

[203] R. N. Zare, *Angular Momentum*, Wiley, New York, 1988.

[204] C. Lyngå, A. LHuillier, and C.-G. Wahlström, *High-order harmonic generation in molecular gases*, J. Phys. B **29**, 3293 (1996).

[205] A. L'Huillier and P. Balcou, *High-order harmonic generation in rare gases with a 1-ps 1053-nm laser*, Phys. Rev. Lett. **70**, 774 (1993).

[206] Y. Liang, S. Augst, S. L. Chin, Y. Beaudoin, and M. Chaker, *High-order harmonic generation in in atomic and diatomic molecular gases using intense picosecond laser pulses-a comparison*, J. Phys. B **27**, 5119 (1994).

[207] Y. Liang, A. Talebpour, C. Y. Chien, S. Augst, and S. L. Chin, *Comparison of high harmonic conversion efficiency in atomic and diatomic molecular gases*, J. Phys. B **30**, 1369 (1997).

[208] T. Ditmire, E. T. Gumbrell, R. A. Smith, J. W. G. Tisch, D. D. Meyerhofer, and M. H. R. Hutchinson, *Spatial coherence measurement of soft x-ray radiation produced by high order harmonic generation*, Phys. Rev. Lett. **77**, 4756 (1996).

[209] L. Le Déroff, P. Salières, B. Carré, D. Joyeux, and D. Phalippou, *Measurement of the degree of spatial coherence of high-order harmonics using a Fresnel-mirror interferometer*, Phys. Rev. A **61**, 043802 (2000).

[210] C. Lyngå, M. B. Gaarde, C. Delfin, M. Bellini, T. W. Hänsch, A. L' Huillier, and C.-G. Wahlström, *Temporal coherence of high-order harmonics*, Phys. Rev. A **60**, 4823 (1999).

[211] M. Bellini, C. Lyngå, A. Tozzi, M. B. Gaarde, T. W. Hänsch, A. L'Huillier, and C.-G. Wahlström, *Temporal coherence of ultrashort high-order harmonic pulses*, Phys. Rev. Lett. **81**, 297 (1998).

[212] P. Antoine, A. L'Huillier, and M. Lewenstein, *Attosecond pulse trains using high-order harmonics*, Phys. Rev. Lett. **77**, 1234 (1996).

[213] D. G. Lappas and J. P. Marangos, *Orientation dependence of high-order harmonic generation in hydrogen molecular ions*, J. Phys. B **633**, 4679 (2000).

[214] B. N. Plakhutin, E. V. Gorelik, and N. N. Breslavskaya, *Koopmans theorem in the ROHF method: Canonical form for the Hartree-Fock Hamiltonian*, J. Chem. Phys. **125**, 204110 (2006).

[215] S. Patchkovskii, Z. Zhao, T. Brabec, and D. M. Villeneuve, *High harmonic generation and molecular orbital tomography in multielectron systems: Beyond the single active electron approximation*, Phys. Rev. Lett. **97**, 123003 (2006).

[216] M. J. DeWitt, E. Wells, and R. R. Jones, *Ratiometric comparison of intense field ionization of atoms and diatomic molecules*, Phys. Rev. Lett. **87**, 153001 (2001).

[217] B. Shan, X.-M. Tong, Z. Zhao, Z. Chang, and C. D. Lin, *High-order harmonic cutoff extension of the O_2 molecule due to ionization suppression*, Phys. Rev. A **66**, 061401 (2002).

[218] X. X. Zhou, X. M. Tong, Z. X. Zhao, and C. D. Lin, *Alignment dependence of high-order harmonic generation from N_2 and O_2 molecules in intense laser fields*, Phys. Rev. A **74**, 023403 (2006).

[219] V. V. Strelkov, A. F. Sterjantov, N. Y. Shubin, and V. T. Platonenko, *XUV generation with several-cycle laser pulse in barrier-suppression regime*, J. Phys. B: At. Mol. Opt. Phys. **39**, 577 (2006).

[220] T. Siegel, R. Torres, D. J. Hoffmann, L. Brugnera, I. Procino, A. Zaïr, J. G. Underwood, E. Springate, I. C. E. Turcu, L. E. Chipperfield, and J. P. Marangos, *High harmonic emission from a superposition of multiple unrelated frequency fields*, Opt. Expr. **18**, 6853 (2010).

[221] M. F. Guest, I. J. Bush, H. J. J. van Dam, P. Sherwood, J. M. H. Thomas, J. H. van Lenthe, R. W. A. Havenith, and J. Kendrick, *The GAMESS-UK electronic structure package: algorithms, developments and applications*, Molecular Physics **103**, 719 (2005).

[222] T. Harada, K. Takahashi, H. Sakuma, and A. Osyczka, *Optimum design of a grazing-incidence flat-field spectrograph with a spherical varied-line-space grating*, Appl. Opt. **38**, 2743 (1999).

[223] T. Kita, T. Harada, N. Nakano, and H. Kuroda, *Mechanically ruled aberration-corrected concave gratings for a flat-field grazing-incidence spectrograph*, Appl. Opt. **22**, 512 (1983).

[224] T. Siegel, *Imaging of molecular structure and dynamics using laser driven electron recollisions*, PhD thesis, Imperial College, UK, 2010.

[225] R. M. Lock, X. Zhou, W. Li, M. M. Murnane, and H. C. Kapteyn, *Measuring the intensity and phase of high-order harmonic emission from aligned molecules*, Chem. Phys. **366**, 22 (2009).

[226] O. Smirnova, M. Spanner, and M. Y. Ivanov, *Analytical solutions for strong field-driven atomic and molecular one- and two-electron continua and applications to strong-field problems*, PRA **77**, 033407 (2008).

[227] O. Smirnova, S. Patchkovskii, Y. Mairesse, N. Dudovich, D. Villeneuve, P. Corkum, and M. Y. Ivanov, *Attosecond circular dichroism spectroscopy of polyatomic molecules*, PRL **102**, 063601 (2009).

[228] B. Zimmermann, M. Lein, and J. M. Rost, *Analysis of recombination in high-order harmonic generation in molecules*, Phys. Rev. A **71**, 033401 (2005).

[229] M. Gühr, B. K. McFarland, J. P. Farrell, and P. H. Bucksbaum, *High harmonic generation for N_2 anc CO_2 beyond the two-point model*, J. Phys. B **40**, 3745 (2007).